

UNIVERSITY OF CATANIA

PhD Course in Systems Engineering, Energy, Information Technology and
Telecommunications – XXXIII Cycle

PhD Thesis

Performance Optimization of Large
Photovoltaic Plants using Distributed
Converters and Integration of Energy
Storage Systems



Giovanni Nobile

Supervisors

prof. Giuseppe Scarcella
prof. Mario Cacciato

Company tutors

ENEL GREEN POWER

eng. Agnese Di Stefano
eng. Paola Pugliatti
dr. Giuseppe Leotta
eng. Fabrizio Bizzarri

PhD Course Coordinator

prof. Paolo Arena, PhD

September 2020

To my daughter Anna

To my wife Evelina

Acknowledgements

I wish to express my sincere gratitude to my daughter Anna and my wife Evelina. This thesis would not have been possible without their support and patience.

Special thanks go to Prof. Giuseppe Scarcella, Prof. Mario Cacciato and Prof. Giacomo Scelba. Their experience provided many valuable ideas for my research work. Under their guidance I have learned a lot about renewable energy, power electronics and energy storage systems. I extend these thanks to all the colleagues at the laboratory for their support and for creating such a pleasant working environment.

I would also to say thank you to Prof. Dr. Paolo Arena whose coordinator role has been of great help during the PhD course.

I want to thank also my tutors at Enel Green Power Dr. Giuseppe Leotta, Eng. Agnese Di Stefano, Eng. Paola Pugliatti and Eng. Fabrizio Bizzarri. They gave me the opportunity to work on real case studies contributing to my research activities and to my professional growth.

Abstract

This thesis focuses on large or utility-scale photovoltaic (PV) plants. The first target is to improve the energy production by using distributed converters. The second target, which is linked to the first one, is to optimize the management of energy flows by integrating distributed energy storage systems (ESS) realized with several battery packs. The approach is the implementation of innovative energy management strategies supported by suitable models for both PV field and storage system.

In particular, a behavioural model is applied to large PV plants. This model is built in the form of an integrated state-space average model used to compute all the electrical quantities in each section of a PV plant allowing a simple calculation of power, energy, losses, voltage drops, etc. The final model is obtained as the merging of the state-space average models developed for each component of the PV plant. Moreover, this approach leads to a straightforward way to calculate the average DC-link current at the input side of inverters from the direct-sequence components of the AC currents, the latter being state variables. Thanks to this novelty, no any data storage is required to calculate the integral terms of the common formulation of DC-link current, obtaining a significant simplification without decreasing the accuracy level.

About the storage system, estimation of State of Charge (SOC) and State of Health (SOH) of battery packs play a key role for the effective integration of battery packs in large PV plants. Because of the large amount of data to manage for both PV system and ESS, the algorithms developed in this work for the estimation of SOC and SOH aim to keep a low computational effort while ensuring a satisfactory accuracy. Such algorithms belong to two different categories. The first one relates to PI-based observers. The second one, classified as a mixed algorithm, mixes two basic estimation methods in order to benefit from their advantages while compensating their drawbacks.

The core of these estimation algorithms is the equivalent circuit model of the battery pack. An in-depth literature review and extensive experimental tests lead to the selection of proper models to be integrated in algorithms.

Power and energy capability of battery packs represent the link between the model of ESS and the model of PV plant. The justification of this approach deals with the limitation of complexity. In fact, the separation of PV plant model and of ESS estimation algorithm is useful to keep a low computational effort. At the same time, the link based on actual values of power capability allows a suitable integration of the models for the optimal energy management of the entire system.

Validation of the novelties presented in this thesis has been carried out by means of laboratory tests and by processing large databases collected during measurement campaigns carried out in two case studies: a 300 MW PV plant in Brazil and a 2 MW PV plant in Central Italy.

Keywords: Large PV plants, Distributed converters, State-space average modelling, Energy storage systems, Equivalent circuit modelling, SOC estimation algorithms, SOH estimation algorithms, Power capability.

My bibliography

- S. Graziani, G. Nobile, N. Pitrone, N. Savalli, "Education Enhancement on Three-Phase System Measurements", in Proc. 2007 4th WSEAS/IASME International Conference on Engineering Education, pp. 306-310.
- G. Nobile, A. G. Sciacca, M. Cacciato, C. Cavallaro, A. Raciti, G. Scarcella, G. Scelba, "Energy Harvesting in Roped Elevators", in Proc. 2014 International Symposium on Power Electronics, Electrical Drives, Automation and Motion (SPEEDAM), pp. 533-540.
- M. Cacciato, G. Nobile, G. Scarcella, G. Scelba, "Real-time model-based estimation of SOC and SOH for energy storage systems", in Proc. 2015 IEEE 6th International Symposium on Power Electronics for Distributed Generation Systems (PEDG), pp. 1-8.
- M. Cacciato, G. Nobile, G. Scarcella, G. Scelba, A. G. Sciacca, "Energy management optimization in stand-alone power supplies using online estimation of battery SOC", in Proc. 2016 IEEE 18th European Conference on Power Electronics and Applications (EPE), pp. 1-10.
- M. Galad, P. Spanik, M. Cacciato, G. Nobile, "Comparison of common and combined state of charge estimation methods for VRLA batteries", in Proc. ELEKTRO 2016 Conference, pp. 220-225.
- M. Cacciato, L. Finocchiaro, G. Nobile, G. Scarcella, G. Scelba, "Assessment of energy management strategies for battery assisted solar pumping systems", in Proc. 2016 International Symposium on Power Electronics, Electrical Drives, Automation and Motion (SPEEDAM), pp. 575-581.
- M. Cacciato, G. Nobile, G. Scarcella, G. Scelba, "Real-time model-based estimation of SOC and SOH for energy storage systems", IEEE Trans. Power Electronics, vol. 32, no. 1, pp. 794-803, January 2017.
- M. Cacciato, G. Nobile, M. Pulvirenti, A. Raciti, G. Scarcella, G. Scelba, "Energy management in parallel hybrid electric vehicles exploiting an integrated multi-

- drives topology”, in Proc. 2017 International Conference of Electrical and Electronic Technologies for Automotive, pp. 1-8.
- M. Galad, P. Spanik, M. Cacciato, G. Nobile, “Analysis of state of charge estimation methods for smart grid with VRLA batteries”, in Electrical Engineering Journal, vol. 99, pp. 1233-1244, July 2017.
 - G. Nobile, G. Scelba, M. Cacciato, G. Scarcella, “Losses Minimization in an Integrated Multi-Drives Topology devoted to Hybrid Electric Vehicles”, in Proc. 2017 43rd Annual Conference of the IEEE Industrial Electronics Society (IECON), pp. 2059-2066.
 - G. Nobile, M. Cacciato, G. Scarcella, G. Scelba “Performance Assessment of Equivalent-Circuit Models for Electrochemical Energy Storage Systems”, in Proc. 2017 43rd Annual Conference of the IEEE Industrial Electronics Society (IECON), pp. 2799-2806.
 - G. Nobile, M. Cacciato, G. Scarcella, G. Scelba “Multi-criteria experimental comparison of batteries circuital models for automotive applications”, Communications – Scientific Letters of the University of Zilina, vol. 20, no. 1, pp. 96-103, March 2018.
 - G. Nobile, M. Cacciato, G. Scarcella, G. Scelba, L. Salvo “Performance Assessment of a novel Integrated Multi- Drives Topology for Automotive Applications”, in Proc. 2018 International Symposium on Power Electronics, Electrical Drives, Automation and Motion (SPEEDAM), pp. 570-576.
 - G. Nobile, M. Cacciato, G. Scarcella, G. Scelba, A. G. F. Di Stefano, G. Leotta, P. M. Pugliatti, F. Bizzarri “Comparison between central and string inverters performance for the utility-scale PV plant in Nova Olinda Brazil”, in Proc. 2018 European PV Solar Energy Conference and Exhibition EU PVSEC, Brussels, Belgium, pp. 1935-1941.
 - G. Nobile, M. Cacciato, G. Scarcella, G. Scelba, “Losses Minimization Control for an Integrated Multi-Drives Topology devoted to Hybrid Electric Vehicles”, IEEE Trans. Industrial Electronics, vol. 66, issue 11, pp. 8345-8360, November 2019.

- G. Nobile, M. Cacciato, G. Scarcella, G. Scelba, E. Vasta, L. D. Tornello, A. G. F. Di Stefano, G. Leotta, P. M. Pugliatti, F. Bizzarri “A novel model-based approach for the energy management of distributed storage systems in utility-scale PV fields”, in Proc. 2019 IEEE 21st European Conference on Power Electronics and Applications (EPE), pp. 1-10.
- G. Nobile, M. Cacciato, G. Scarcella, G. Scelba, E. Vasta, A. Di Stefano, G. Leotta, P. M. Pugliatti and F. Bizzarri, "Distributed converters in large PV plants: performance analysis supported by behavioral models", ELECTRIMACS 2019 Springer Lecture Notes in Electrical Engineering, vol. 604, pp. 553-566, April 2020.
- G. Nobile, E. Vasta, M. Cacciato, G. Scarcella, G. Scelba, A. G. F. Di Stefano, G. Leotta, P. M. Pugliatti, F. Bizzarri, “Integration of a relaxation voltage prediction function into a PI-based observer to improve the SOC estimation of battery packs in renewable energy applications”, in Proc. 2020 ELEKTRO Conference.
- G. Nobile, E. Vasta, M. Cacciato, G. Scarcella, G. Scelba, A. G. F. Di Stefano, G. Leotta, P. M. Pugliatti, F. Bizzarri, “Mismatch losses in large PV plants: data analysis of a case study and modelling approach”, in Proc. 2020 International Symposium on Power Electronics, Electrical Drives, Automation and Motion (SPEEDAM).
- G. Nobile, E. Vasta, M. Cacciato, G. Scarcella, G. Scelba, “Estimation of SOH for Battery Packs: A Real-Time Mixed Algorithm based on Coulomb Counting Method and Parameter-Varying Circuit Modelling”, in Proc. 2020 IEEE 11th International Symposium on Power Electronics for Distributed Generation Systems (PEDG).
- G. Nobile, E. Vasta, M. Cacciato, G. Scarcella, G. Scelba, A. G. F. Di Stefano, G. Leotta, P. M. Pugliatti, F. Bizzarri, “Performance Assessment of Large Photovoltaic (PV) Plants Using an Integrated State-Space Average Modeling Approach”, MDPI Energies, vol. 13, no. 4777, September 2020.

Contents

List of figures.....	13
List of tables.....	20
Glossary	23
Main symbols in equations.....	26
Chapter 1 - Introduction.....	28
Chapter 2 - PV plants: technology and technical issues	34
2.1 The PV solar source.....	34
2.1.1 PV cells technology and materials	35
2.1.2 Standard technical solutions for PV plants	36
2.2 Underperformance of PV plants: causes and diagnosis	42
2.2.1 PV modules: underperformance effects	42
2.2.2 Strings and arrays: underperformance effects	43
2.2.3 The mismatch	44
2.3 Methods to mitigate the underperformance effects.....	45
Chapter 3 - ESS in PV plants.....	46
3.1 ESS for renewables: state of the art	46
3.2 Batteries in large PV plants.....	47
Chapter 4 - Power electronics converters in PV plants	51
4.1 Power converters in PV plants	51
4.2 Distributed conversion systems	52
4.2.1 Distributed power converters for small PV plants	52
4.2.2 Distributed power converters for large PV plants	52
4.3 Power converters for the integration of ESS in PV plants	54
Chapter 5 - Modelling and simulation of PV plants	56
5.1 State of the art.....	56
5.2 Modelling of large PV fields	56
5.2.1 The proposed modelling approach	57

5.3 Model for PV modules and PV arrays	61
Chapter 6 - Modelling and simulation of ESS	64
6.1 State of the art.....	64
6.2 Equivalent Circuit Modelling.....	65
6.2.1 Main ECM for ESS: features and performance comparison	65
6.3 SOC and SOH estimation algorithms	71
6.4 PI-based observer algorithms.....	73
6.5 ESS state estimation algorithm 1	75
6.6 ESS state estimation algorithm 2	78
6.7 Calculation of PC and EC	82
Chapter 7 - Modelling of converters, transformers and utility grid....	84
7.1 Power converters models.....	84
7.1.1. DC-link current calculation	89
7.2 Transformers and grid models.....	91
Chapter 8 – Integration of PV plant and ESS models.....	92
8.1 PV plant model	92
8.1.1 Control system	95
8.2 Parameters identification	95
8.3 Merging models using PC and EC	97
Chapter 9 - Models validation	99
9.1 Experimental tests for validation of PV modules modelling	99
9.2 Validation of PV plant integrated model	107
9.2.1 Model running	107
9.2.2 Execution time performance	112
9.2.3 Accuracy evaluation	117
9.3 Experimental setup for battery testing	122
9.3.1 Batteries under test	122
9.4 ECM performance assessment and comparison.....	124
9.4.1 Experimental comparison between ECMs	124
9.4.2 Sensitivity to parameters uncertainty	133
9.4.3 Selection of the ECM for this work	136

9.5 Tests for validation of ESS state estimation algorithm 1	138
9.6 Tests for validation of ESS state estimation algorithm 2	144
9.7 Experimental assessment of PC and EC	146
Chapter 10 - Case study 1, PV plant in Brazil	150
10.1 Criteria for performance assessment	153
10.1.1 Relevance of the PV plant model	155
10.2 Mismatch losses assessment.....	157
10.2.1 Mismatch evaluation criteria	158
10.2.2 Mismatch assessment results	161
10.2.3 Investigating the causes of mismatch	167
10.3 Performance assessment	170
10.3.1 Temperature effects and overload ability	172
10.3.2 Energy yield	175
10.4 Technical note on 1500 V_{DC} PV systems	179
Chapter 11 - Case study 2, PV plant in Central Italy.....	183
11.1 Criteria for performance assessment	188
11.1.1 Relevance of the PV plant model	191
11.1.2 Execution time performance	192
11.2 Performance assessment	193
11.2.1 DC cables voltage drops	193
11.2.2 Analysis 1: Inverter EOH from strings data	196
11.2.3 Analysis 2: Inverter EOH from counters	197
11.2.4 Analysis 3: Inverter EOH from monitoring system AC data	198
11.2.5 Analysis 4: Daily PR of PV arrays in experimental subfield	199
11.2.6 Central inverter operation	201
11.2.7 Conclusions on performance assessment	203
11.3 Integration of ESS in case study 2.....	203
11.3.1 Scenario 1	204
11.3.2 Scenario 2	206
Chapter 12 - Conclusions and outlook	209
Appendices.....	211
Appendix 1: Matlab code examples, case study 1.....	211

A.1.1 String inverter energy and peak power	211
A.1.2 Central inverter energy, peak power and internal temperature	213
A.1.3 Irradiance	217
Appendix 2: Matlab code examples, case study 2.....	219
A.2.1 Experimental subfield 4 data processing	219
A.2.2 Irradiance, ambient temperature, module temperature	231
Appendix 3: Strings PR in experimental field of case study 2.....	235
Bibliography	243

List of figures

Figure 1. PV string: series connection of N_S PV modules	36
Figure 2. PV array: parallel connection of N_P PV strings	37
Figure 3. Rough scheme of a small PV plant connected to LV grid	38
Figure 4. Rough scheme of a large PV plant connected to MV grid	38
Figure 5. Orientation of PV module with respect to sun, azimuth and tilt angle	41
Figure 6. Left: example of single-axis tracker, tilt 0° . Center: example of single-axis tracker, tilt 20° . Right: example of dual-axis tracker	41
Figure 7. Left: example of rooftop PV plant. Right: example of ground-mounted PV field.....	41
Figure 8. Left: example of floating PV system. Right: example of flexible PV modules.....	41
Figure 9. From centralized large ESS to distributed small battery packs	49
Figure 10. Generic PV plant configuration for modelling purpose	59
Figure 11. Simplified equivalent circuit used to build the basic state-space representation of PV array	62
Figure 12. ECM comparative analysis based on applications and technologies	70
Figure 13. ECM comparative analysis based on modelling goals and dynamics	71
Figure 14. Runtime circuit model for the PI-based observer algorithm in [125]	74
Figure 15. Real-time PI-based observer scheme in [125]	74
Figure 16. Thevenin ECM being part of the algorithm 1 for ESS state estimation.....	75
Figure 17. PI-based observer scheme including OCV_{relax} prediction function, algorithm 1 for ESS state estimation.....	75
Figure 18. Identification of the OCV_{10s} detection point for the implementation of algorithm 1	77
Figure 19. Estimation of SOH for a Li-Ion battery pack through the implementation of CCM in different discharging operations. The $OCV_{quasi-relax}$ (in quasi-relaxation state) is used to calculate the SOC on the basis of no-load curve $SOC(OCV)$	80
Figure 20. The parameter-varying Randles ECM included in the proposed mixed algorithm.....	81
Figure 21. Flow chart of the proposed mixed algorithm i.e. algorithm 2 for ESS state estimation.....	82

Figure 22. Block diagram of a grid-connected PV system with multi-stage conversion system	84
Figure 23. DC/DC converter basic topology and its state-space form including duty cycle variation	85
Figure 24. Grid connected inverter and AC filtering stage, basic topology.....	87
Figure 25. Schematic representation of the matching between ESS and PV plant models.....	98
Figure 26. PV modules model validation, first session: UNICT laboratory test bench. Legend: 1. programmable DC power supply / PV emulator, 2. power analyzer, 3. DC electronic load, 4. PC with emulator software, 5. PC / LabVIEW.....	99
Figure 27. PV modules model validation, first session: emulation of a PV module through the DC power supply software.....	100
Figure 28. PV modules model validation, first session: LabVIEW front panel.....	101
Figure 29. PV modules model validation, second session: pictures of the test bench. Legend: 1. PV module under test, 2. irradiance sensors, 3. pulsed light emitter, 4. GUI, plot of results	102
Figure 30. Simulation vs measured data for the Solar World SW 255 PV module under test. Charts created automatically by the monitoring system during the second test session. Green curves: I-V and P-V characteristics from simulation, blue curves: measured I-V characteristics, red curves: measured P-V characteristics. Legend: a. $G = 1000 \text{ W/m}^2$, $T_{mod} = 25^\circ\text{C}$, b. $G = 800 \text{ W/m}^2$, $T_{mod} = 25^\circ\text{C}$, c. $G = 700 \text{ W/m}^2$, $T_{mod} = 25^\circ\text{C}$, d. $G = 400 \text{ W/m}^2$, $T_{mod} = 25^\circ\text{C}$	106
Figure 31. Simulation of a 18.9 kW PV array. PV system topology is represented in Fig. 22, technical data of components in Table 13. Irradiance is 1000 W/m^2 , module temperature is 25°C . Comparison between detailed model and integrated state-space average model	109
Figure 32. Simulation of a 18.9 kW PV array. PV system configuration is represented in Fig. 22, technical data of components in Table 14. Irradiance is 800 W/m^2 , module temperature is 45°C . At time 0.1 s the control system forces non null reactive power. Comparison between detailed model and integrated state-space average model.....	110
Figure 33. Example of daily power curves measured in the experimental subfield of case study 1. Proposed model output (simulation) vs measured data. Calculation of percentage relative error	118
Figure 34. Another example of daily power curves measured in the experimental subfield of case study 1. Proposed model output (simulation) vs measured data. Calculation of percentage relative error.....	119

Figure 35. Another example of daily power curves measured in the experimental subfield of case study 1. Proposed model output (simulation) vs measured data. Calculation of percentage relative error.....	120
Figure 36. Another example of daily power curves measured in the experimental subfield of case study 1. Proposed model output (simulation) vs measured data. Calculation of percentage relative error.....	121
Figure 37. UNICT laboratory test bench for the experimental validation of ESS models and algorithms.....	122
Figure 38. Electrical scheme of the 24 V 108 Ah VRLA battery pack under test	124
Figure 39. Test performed by forcing discharge operation for the 24 V 108 Ah VRLA battery pack under test. Comparison between voltage waveform provided by ECM and measured voltage. The relative error is also represented.....	127
Figure 40. Test performed by forcing charge operation for the 24 V 108 Ah VRLA battery pack under test. Comparison between voltage waveform provided by ECM and measured voltage. The relative error is also represented.....	128
Figure 41. Test performed by forcing charge and discharge operation (CC and CP control) for the 24 V 108 Ah VRLA battery pack under test. Comparison between voltage waveform provided by ECM and measured voltage. The relative error is also represented	129
Figure 42. 3D plots of the mean relative error related to the voltage estimation carried out by each ESS equivalent circuit model, for different current rates and SOC values.....	131
Figure 43. Mean relative error vs SOC. Selected current in 3D plots is -2 A.....	132
Figure 44. Mean relative error vs SOC. Selected current in 3D plots is 10 A	132
Figure 45. Mean relative error vs SOC. Selected SOC in 3D plots is 30 %	133
Figure 46. Mean relative error vs SOC. Selected SOC in 3D plots is 80 %	133
Figure 47. ECM comparison based on voltage estimation error sensitivity to parameters uncertainty, perturbation of parameters is $x_{i,p}=1.1$ $x_{i,o}$	135
Figure 48. Circuit models comparison based on voltage estimation error sensitivity to parameters uncertainty, perturbation of parameters is $x_{i,p}=0.9$ $x_{i,o}$	135
Figure 49. Graphical comparison amongs ECM of ESS based on different design requirements. For each criterion, 0 represents the minimum score while 5 is the maximum one.	137
Figure 50. Variation of R_i with SOC during a charge process, battery type 1	138

Figure 51. Variation of R_i with SOC during a discharge process, another battery type 1	139
Figure 52. Variation of R_i with SOC during a discharge process, another battery type 1	139
Figure 53. Comparison between the OCV_{relax} curve after a discharge and the measured one at different time intervals. The polynomial fitting curve for the OCV_{10s} terminal voltage is also shown. Charts are related to two batteries type 1	140
Figure 54. Left: Battery belonging to typology 1, comparison between the OCV_{relax} curve after a charge and the measured one at different time intervals. Right: Battery belonging to typology 3, comparison between the OCV_{relax} curve after a discharge and the measured one at different time intervals. The polynomial fitting curve for the OCV_{10s} terminal voltage is also shown for both batteries	141
Figure 55. Experimental test example. Implementation of the Boolean logic for the identification of the OCV_{10s} value	142
Figure 56. Example of experimental test on a battery type 1. Estimation algorithm 1 provides an estimation of SOC that is very close to the SOC curve calculated by the popular CCM. The proposed method does not suffer from the well-known issues occurring in the implementation of the CCM.....	143
Figure 57. Implementation of the proposed algorithm for a battery type 1. Numerical results for each time period (A to D) are reported in Table 24. Circle areas A1 and A2 in period B: the proper tuning of parameters improves the accuracy of ECM in quasi-relaxation state. If such tuning is not performed, difference between v_{model} and v_{meas} will increase over time, as evident in A1, leading to significant errors in terms of SOH estimation	145
Figure 58. Experimental test performed by forcing discharge operation on a 24 V 108 Ah VRLA battery pack. SOC estimation, provided by the algorithm 1, is superimposed to the SOC calculated via CCM. Estimated SOH is 93%	147
Figure 59. Power capability prediction during discharge. Initial time instant $t_{0,a}$ is pointed out in Fig. 58 (zero current state)	147
Figure 60. Power capability prediction during discharge. Initial time instant $t_{0,b}$ is pointed out in Fig. 58 (non-zero current state)	148
Figure 61. Experimental test performed by forcing charge operation for a 24 V 108 Ah VRLA battery pack. SOC estimation, provided by the algorithm 1, is superimposed to the SOC calculated via CCM. Estimated SOH is 93%	149
Figure 62. Power capability prediction during charge. Initial time instant $t_{0,c}$ is pointed out in Fig. 61 (non-zero current state)	149

Figure 63. Pictures of the 300 MW PV plant in Brazil representing the case study 1 of this work	150
Figure 64. Power system configuration of the 2.5 MW subfield with central inverters	151
Figure 65. Power system configuration of the 2.5 MW subfield with string inverters	152
Figure 66. Data processing of measurements provided by plant dataloggers in case study 1	155
Figure 67. Proposed model output vs measured data for QPCA 1 during a selected day. The integrated state-space average model is able to estimate the theoretical extra energy produced in absence of inverter maximum power threshold.	156
Figure 68. Proposed model output vs measured data of central inverter 1 subfield in a selected day during which a fault occurs in the power supply of solar trackers. The integrated state-space average model is able to estimate the theoretical energy that could be produced in absence of such fault.....	157
Figure 69. Criterion 1 results, database: 47 days selected in the reference period.....	162
Figure 70. Criterion 2 results, database: 70 days selected in the reference period.....	163
Figure 71. Criterion 3 results, database: 62 days selected in the reference period.....	164
Figure 72. Criterion 4 results, database: 34 days selected in the reference period.....	165
Figure 73. Criterion 5 results, database: 200 days selected in the reference period. Pie chart shows the distribution of worst strings in the selected array for the same period.....	165
Figure 74. Graph of the electrical quantities for an array in the string inverter subfield. A tracker fault occurs in string no. 7.....	168
Figure 75. Period from 18 th January to 19 th February 2018: string inverters AC peak power, ambient and module temperature	172
Figure 76. Sunny day in winter 2018: power plots of central inverters, QPCA 1 and QPCA 2. In the central part of the day (high irradiance) the energy flow in string inverters is not limited while the central inverters work at maximum power threshold.....	173
Figure 77. Sunny day in winter 2018: frequency histogram for the instantaneous power of central inverters and QPCAs.....	174
Figure 78. Comparison between central and string inverters in the experimental subfield based on daily energy during a cloudy day	176
Figure 79. Results obtained considering the days during which no any limitation related to inverter peak power thresholds occur. String inverters gain distribution charts and normal density fitting functions: (a) QPCA 1 vs	

central inverter 1, (b) QPCA 1 vs central inverter 2, (c) QPCA 2 vs central inverter 1, (d) QPCA 2 vs central inverter 2, (e) string inverters subfield (QPCA 1 + QPCA 2) vs central inverters subfield (central 1 + central 2). The integrated state-space average model has been used to replace data coming from the monitoring system of the PV plant in case of data issues, unavailability or external constraints	177
Figure 80. Plot of the energy gain components, including the days during which some cases of limitations related to inverter peak power thresholds occur.....	178
Figure 81. Pictures of the ground-mounted 2 MW PV plant in Central Italy representing the case study 2 of this work.....	183
Figure 82. Pictures regarding the assembly of string optimizers. Left: cabling modification at the string box. Right: string optimizers mounted on the back side of the string box	184
Figure 83. Single line diagram of the subfields whose layout maintained the original configuration	185
Figure 84. Single line diagram of the experimental subfield with power optimizers mounted at string level in August 2018.....	185
Figure 85. Data processing of measurements provided by plant dataloggers in case study 2	189
Figure 86. Timeline of data exploited in case study 2. Days in yellow refer to unavailabilities, faults, issues in monitoring system, etc. causing wrong or missing data	190
Figure 87. Comparison between measured power and power curve provided by model during a sunny day in autumn 2018. The behavioral model is used to trace the theoretical power curve during a maintenance shutdown	192
Figure 88. Example of calculation for R_{DC} . Left: first part of the DC line, cable cross section 120 mm^2 , resistance per kilometre $0.16 \text{ } \Omega/\text{km}$, resistance $0.0037 \text{ } \Omega$. Right: second part of the DC line, cable cross section 240 mm^2 , resistance per kilometre $0.080 \text{ } \Omega/\text{km}$, resistance $0.0010 \text{ } \Omega$	194
Figure 89. Calculation of voltage drop during a sunny day in winter 2019. Comparison between the experimental subfield and another subfield with the original configuration	196
Figure 90. Distribution plots of the daily PR in some strings of the experimental subfield for periods bDC and aDC.....	200
Figure 91. Distribution plot of the PR gain in all the arrays of the experimental subfield, time period February 2018 to February 2019.....	201
Figure 92. Main electrical quantities acquired by the datalogger of the central inverter in the experimental subfield during two days close to the installation date of string optimizers	202

Figure 93. Single line diagram for the case study 2 with the integration of distributed ESS.....	204
Figure 94. Example of operating scenario: the ESS is used to store the energy produced by the PV array 1 being part of a string box in the experimental subfield during a maintenance shutdown	205
Figure 95. Example of operating scenario in which the distributed ESS is used to store the produced energy in case of power limitation forced by the PPC.....	207
Figure 96. Recalculation of PC and EC of ESS 4 at time t_l on the basis of the actual SOC value that is continuously estimated by the proposed PI observer algorithm.....	207

List of tables

Table 1. Examples of large PV plants with ESS	48
Table 2. ECM for battery packs.....	66
Table 3. Names usually assigned to the ECM in Table 2. Together with ID, such names are used in this thesis to refer to models.....	67
Table 4. Models comparison based on main requirements and performance	69
Table 5. Features of the main SOC and SOH estimation methods.....	72
Table 6. Basic methods combined in the mixed algorithm i.e. the method 2 for ESS state estimation	78
Table 7. Technical specifications of the Solar World SW 255 PV module	102
Table 8. Example of measurements acquired during the second test session in case of irradiance fixed in a narrow range around 1000 W/m ²	103
Table 9. Preliminary identification of the resistance parameters in single-diode model for the PV module under test.....	103
Table 10. Average value and maximum deviation in measured power for the Solar World SW 255 PV module	104
Table 11. Parameters values provided by the model	104
Table 12. Technical specifications of main power components for simulation of PV array.....	107
Table 13. Parameters list for the simulation shown in Fig. 31	111
Table 14. Parameters list for the simulation shown in Fig. 32	111
Table 15. Execution time performance evaluation, case A (simulation time step is 1·10 ⁻⁶ s for state-space average model and for detailed model), computer 1	113
Table 16. Execution time performance evaluation, case A (simulation time step is 1·10 ⁻⁶ s for state-space average model and for detailed model), computer 2	114
Table 17. Execution time performance evaluation, case B (simulation time step is 2·10 ⁻⁵ s for state-space average model, 1·10 ⁻⁶ s for detailed model), computer 1	115
Table 18. Execution time performance evaluation, case B (simulation time step is 2·10 ⁻⁵ s for state-space average model, 1·10 ⁻⁶ s for detailed model), computer 2.....	116
Table 19. Main technical specifications of the experimental subfield in case study 1, used for the assessment of model accuracy	117

Table 20. Battery under test type 1	123
Table 21. Battery under test type 2	123
Table 22. Battery under test type 3	123
Table 23. ECM parameters for the 24 V 108 Ah VRLA battery pack under test	126
Table 24. Numerical data for time periods in Fig. 57	145
Table 25. Main technical specifications of the experimental subfield in case study 1	152
Table 26. Rated power quantities for strings and arrays	159
Table 27. Criterion 1 formulation	159
Table 28. Criterion 2 formulation	159
Table 29. Criterion 3 formulation	160
Table 30. Criterion 4 formulation	160
Table 31. Criterion 5 formulation	161
Table 32. Daily energy produced by strings in an array of the string inverter subfield. The underperformance of string no. 7, due to the tracker fault, is about 27 %	168
Table 33. Daily energy produced by strings in an array of the string inverter subfield. For each day, the worst string is highlighted in red.....	170
Table 34. Period from January to September 2018: main fault and unavailability events in the subfields under investigation.....	171
Table 35. Rough estimation of the main factors contributing to energy gain obtained by string inverters, including the days during which some cases of limitations related to inverter peak power thresholds occur.....	178
Table 36. Comparison between 1000 V _{DC} and 1500 V _{DC} inverters, database derives from [154].....	180
Table 37. Main technical specifications of the experimental subfield in case study 2.....	184
Table 38. Power configuration of strings in subfield 1.....	186
Table 39. Power configuration of strings in subfield 2.....	187
Table 40. Power configuration of strings in subfield 3.....	187
Table 41. Power configuration of strings in subfield 4.....	188
Table 42. List of the main cases of unavailability in the period under consideration ..	191
Table 43. Execution time performance evaluation for case study 2, state-space average model vs detailed model. Simulation end time instant: 0.3 s. Scenario 1: 1000 W/m ² , 25° C. Scenario 2: 800 W/m ² , 45° C, non-zero	

reactive power is forced after 0.1 s. Computer hardware: Intel Core i3-4005U CPU@1.70 GHz (4 CPUs), RAM 4096 MB, HD SSD 240 GB read speeds up to 545 MB/s, 64 bit.....	193
Table 44. Values of resistance for each DC line in the PV plant.	195
Table 45. Results of analysis 1	197
Table 46. Results of analysis 2	198
Table 47. Results of analysis 3	199

Glossary

AC	Alternate Current
AGM	Absorbed Glass Mat Lead Acid Battery
BMS	Battery Management System
CAPEX	Capital Expenditure
CC	Constant Current
CCM	Coulomb Counting Method
CI	Central Inverter
CP	Constant Power
CPV	Concentrated Photovoltaic
CR	Constant Resistance
CV	Constant Voltage
DC	Direct Current
DIFF	Diffuse Irradiance
DNI	Direct Normal Irradiance
EC	Energy Capability
ECM	Equivalent Circuit Model
EGP	Enel Green Power company
EMI	Electromagnetic Interference
EOH	Equivalent Operating Hours
ESS	Energy Storage System/s - battery packs where not otherwise indicated
EVA	Ethylene-Vinyl Acetate encapsulant
FF	Fill Factor
GaN	Gallium Nitride
G _{TOT}	Global Irradiance
GUI	Graphical User Interface
HCPV	High Concentration Photovoltaic

HV	High Voltage
IC	Incremental Conductance
IGBT	Insulated Gate Bipolar Transistor
I-V	Current-Voltage Characteristic or Current-Voltage Curve
KCL	Kirchhoff Current Law
KF	Kalman Filter
KTL	Kirchhoff Voltage Law
LA	Lead Acid battery
LCOE	Levelized Cost of Electricity
Li-Ion	Lithium Ions Battery
LV	Low Voltage
MPP	Maximum Power Point
MPPT	Maximum Power Point Tracking
MV	Medium Voltage
Ni-MH	Nickel Metal Hydride Battery
NOCT	Normal Operating Cell Temperature
OCV	Open Circuit Voltage
OPEX	Operating Expense
P&O	Perturb and Observe
PC	Power Capability
PID	Potential Induced Degradation
PLL	Phase Locked Loop
PPC	Power Plant Controller
PR	Performance Ratio
PV	Photovoltaic
PWM	Pulse Width Modulation
REFL	Reflected Irradiance
RMS	Root Mean Square
SB	String Box
SI	String Inverter

SiC	Silicon Carbide
SO	String Optimizer
SOC	State of Charge
SOH	State of Health
STC	Standard Test Conditions
UNICT	University of Catania
VRLA	Valve Regulated Lead Acid Battery

Main symbols in equations

C_{act}	Actual capacity depending on battery aging
C_{bulk}	Bulk capacitance in Randles circuit model
C_n or C_{rated}	Rated capacity of a battery
C_R	Battery current rate
d	DC/DC converter duty cycle
E_0 or OCV	No-load or Open Circuit Voltage
EOH	Equivalent operating hours
FF	Fill factor
G	Irradiance
i or i_{meas}	Current measured at battery terminals, positive during discharge
I_{array}	PV array current
i_{DCinv}	DC-link current
I_{MPP}	PV module current at MPP
I_{sc}	Short Circuit Current of a PV module
I_{str}	PV string current
m	DC/AC converter modulation index
$NOCT$	Normal Operating Cell Temperature
N_p	Number of strings in parallel in an array
N_s	Number of modules in series in a string
$OCV(SOC)$	No-load characteristic, $SOC(OCV)$ is an equivalent diction
OCV_{10s}	Open Circuit Voltage, 10 s after load shutdown
$OCV_{quasi-relax}$	Open Circuit Voltage in electrical relaxation state
OCV_{relax}	Open Circuit Voltage in electrochemical relaxation state
P_{array}	Rated power of a PV array
P_{mod}	Rated power of a PV module
PR	Performance ratio
P_{str}	Rated power of a PV string
Q	Total charge during a charge or a discharge process

Rad	Radiation
R_{DC}	DC cables resistance
R_p	Parallel resistance
R_s	Series resistance
SOC	State of Charge
SOH	State of Health
T_{cell} or T_{mod}	Cell or module temperature
V_{array}	PV array voltage
v_{meas}	Voltage measured at battery terminals
v_{model}	Voltage provided by the ECM of a battery
V_{MPP}	PV module voltage at MPP
V_{oc}	Open circuit voltage of a PV module
V_{str}	PV string voltage
η_{mod}	Module efficiency

Chapter 1 - Introduction

The sustainability in electricity production and the contribution coming from renewable energy systems have become very topical in recent years.

Transition from the traditional electricity grid, supplied by large power stations exploiting fossil fuels, to a new grid with a massive presence of renewable energy sources is a slow but unavoidable process. In fact, fossil fuel reserves are dramatically diminishing while their price is continuously increasing as reported in many studies [1]. At the same time, the advances obtained by research activities in the smart management of production, consumption and storage systems create a favourable context for a fast transformation of the traditional electricity grid into smart grids [2].

Some scientists expect that nuclear power plants will represent the main alternative for electricity production in a medium time horizon. A first reason is that the nuclear energy generation is a proven technology. In fact, about 500 big production plants, up to 8 TW, are already operating in 40 countries producing about 10 % of the total electricity generated in the world. A second reason is related to the actual availability of fissile materials that could last more than 100 years at the current extraction rate. [3]. Even if there are some well-known drawbacks, mainly related to waste disposal, nuclear energy is considered the best option to replace traditional fossil fuels. This importance is shared with renewable energy plants.

Among the renewable energy sources, hydro power plants are used to produce electricity since 19th century. Primary source is falling or fast-running water. The nominal power of a single plant can reach 20 TW in presence of very large water basin. Electricity produced by hydro power plants has an impact of about 17 % on the world electricity production and constitutes about 70 % of all renewable electricity. Anyway, the effective exploitation of hydro power sources depends on the morphology of territory [4].

Taking into account all the other renewable sources, their contribution to the electricity production is now about 11 % on a world basis, 18 % is the percentage in Europe. Within this category, the impact of biofuels and waste powered plants is very

significant, over 60 %. The rest of electricity is produced by wind, solar, geothermal and tidal power plants. In a medium time horizon (10 - 20 years), the growth of the latter sources is expected to be much more large with respect to the others renewables and to traditional production systems [5], [6].

Wind and PV plants drive such growth. Referring to big power plants, the number of new installations for both the technologies is continuously increasing year by year. Wind farms give to opportunity to reach tens of MW with minimal occupation of land while PV parks require from 10.000 to 30.000 m² per MW. Typically, the productivity of wind farms is higher thanks to the energy produced during the night.

In contrast, for residential or industrial applications (up to 50 – 100 kW) the number of wind power plants is very low. In this market segment, the uncertainties related to the actual availability of the wind source and the disturbance effect of obstacles and buildings around the generation site create several issues for potential investors. A solution could be a detailed measurement campaign to carry out before the installation, in order to collect wind data useful for a proper design process. Unfortunately, these preliminary activities are often too expensive causing the worsening of the payback time expectations [7].

Two main advantages make PV the leading technology for an extensive utilization in every part of the world and for any size of plants:

- the energy produced is easy to forecast with a satisfactory accuracy from a set of few parameters (see Section 2.1) taking advantage of several solar databases as [8], [9];
- full scalability of the PV plants meaning that similar configurations and technical solutions can be quickly adapted for many different cases.

Since the main disadvantage of large PV plants is the occupied land, research activities in the last years have been conducted searching for innovative solutions able to increase the energy productivity or, more generally, the performance of the plants. Under this perspective, the main lines of research can be listed as in the following:

- increase the efficiency of PV modules so that an higher rated power is obtained for the same external frame [10];

- bifacial modules able to produce power from both sides of the module, the obtained energy is higher than a traditional module but the actual increase depends on the shadowing effects at the rear side [11], [12];
- innovative power configurations including distributed converters which can reduce the mismatch effects recovering significant amount of energy, some examples are in [13]-[16].

This thesis focuses on the implementation of this last solution for large or utility-scale PV plants. Moreover, since the presence of distributed converters makes it possible the creation of a distributed ESS based on multiple electrochemical battery packs, this thesis also focuses such promising research topic. The result is a detailed analysis of the control strategies to implement for a proper energy management of the PV + ESS system.

Matching of renewable energy sources with ESS is one of the best ways to converge to smart grids [17]. For the sake of example, a typical issue related to the renewable energy production is that produced power exhibits large fluctuations during the day affecting grid stability and its reliability. These fluctuations can be effectively compensated by ESS enabling the store of energy during overproduction periods and delivering the same energy to cover load demand periods.

In general terms, ESS can effectively increase the grid efficiency as well as its stability and reliability, contributing to the integration of renewable energy sources and to the rationalization of consumptions. A full list of services provided by ESS in distribution networks is in [18] where an overview regarding storage systems based on various technologies is provided, including electrochemical batteries. Here is brief list of the main services addressed to grid:

- energy time shifting;
- peak power shaving;
- voltage regulation;
- frequency regulation;
- load leveling;
- end-user services;

- energy management services for renewable energy sources, mainly for PV plants.

Referring to the last point, which is a key topic for this thesis, [19]-[21] report information on existing ESS systems, consisting of battery packs integrated in PV plants having different sizes and power configurations.

It is worth noting that there is a consolidated market for ESS in residential and industrial PV plants whose rated power is in the order of tens of kW at most. In this market segment there is no a dominant ESS technology or a fixed power configuration suitable for all cases. In lower power PV plants, the integration of battery packs is limited because of their cost and of uncertainty about their expected service life. Anyway, the number of ESS integrated in low power PV plants is slowly but continuously increasing.

Considering large or utility-scale PV plants, [19], [22], [23] describe some of the existing technical solution for the integration of ESS systems. Some of these large battery packs were installed in recent years for research purpose in order to enlarge the knowledge on most promising technologies and on the proper energy management strategies. There are many possible power configurations under study. For example, even if the basic solution is a centralized large power ESS, the presence of distributed power converters allows the implementation of a distributed ESS system with more batteries having small size. This latter solution ensures more freedom degrees in terms of size, connection points, management strategy and so on [23].

The achievement of benefits related to the presence of ESS in a PV plant strictly depend on the accurate monitoring of the state of the battery pack. Under this point of view, it is necessary to estimate continuously two main parameters: SOC and SOH. From these quantities, it is possible to know the Power Capability (PC) and the Energy Capability (EC) of the ESS [24]. The latters are indexes of the maximum power and energy that the battery can deliver in a given time horizon keeping itself into normal operating zone, with respect to safety too. Under a different point of view, the accurate modelling of ESS is a useful tool for designers giving them the opportunity to size the batteries on the basis of the expected working cycles.

Finally, this thesis investigates on the performance optimization of large or utility-scale PV plants through the installation of distributed converters and the integration of distributed battery packs. This optimization involves the implementation of innovative control strategies supported by suitable modelling approaches as described in-depth in the following chapters. Validation of the novelties presented in this thesis is carried out by means of:

- experimental laboratory tests;
- elaboration of data collected in extensive measurement campaigns carried out in a 300 MW PV plant in Brazil and in a 2 MW PV plant in Central Italy.

The thematic areas of this thesis and the related Chapters are summarized here:

- Overview on PV systems and on integration of ESS:
 - o Chapter 2: PV technology, large PV plants, underperformance effects and mitigation
 - o Chapter 3: Integration of ESS in PV plants
 - o Chapter 4: Power converters in PV plants, distributed converters
- Modelling and simulations:
 - o Chapter 5: Modelling of PV modules and arrays
 - o Chapter 6: Modelling of ESS, equivalent circuits, SOC and SOH estimation algorithms, calculation of PC and EC
 - o Chapter 7: Modelling of power converters, transformers, filters and utility grid
 - o Chapter 8: Integration of models
- Experimental validation:
 - o Chapter 9: Validation of PV models, ESS models and battery state estimation algorithms
- Case studies:
 - o Chapter 10: Case study 1, 300 MW PV plant in Brazil, comparison between central and string inverters performance using a multi-criteria approach, validation of the proposed models, mismatch assessment

- Chapter 11: Case study 2, 2 MW PV plant in Central Italy, comparison between central inverter and string optimizers performance using a multi-criteria approach, validation of the proposed models, integration of ESS

Chapter 2 - PV plants: technology and technical issues

2.1 The PV solar source

The impact of the renewable power plants on the world electricity production is continuously increasing. Among the main available technologies, the PV plants represent the most relevant contribution to this growth thanks to their wide spread for both residential and industrial buildings. At the same time, in the last years, starting from the years 2008 - 2009, the number of large or utility-scale PV fields has grown exponentially reaching, in some countries, significant results in terms of contribution to the overall electricity produced and distributed by utilities [25], [26].

It is well-known that the primary source of every PV systems is the electromagnetic energy coming from the nuclear fusion processes occurring in the sun. The basic phenomenon exploited to produce electricity from such energy, received as sun light, is the photoelectric effect. For the latter, the PV effect used to capture energy in PV cells represents a particular sub-effect. The PV effect was first observed by Alexandre-Edmond Becquerel in 1839. Subsequently, in 1946 the first modern solar cell made of silicon was invented by Russel Ohl [27].

The total solar irradiance G_{TOT} on a given surface as a PV module, usually measured in W/m^2 , is the sum of three components: Direct Normal (DNI), Diffuse (DIFF) and Reflected irradiance (REFL). In terms of energy G_{TOT} is usually transposed in Wh/m^2 or kWh/m^2 , in this case it is also named radiation or solar energy [28].

Considering a certain PV plant, the average value of solar radiation and its variation over time depend on some main factors:

- latitude;
- longitude;
- azimuth angle;
- tilt angle;
- albedo of the ground (or roof) surface;
- horizon map showing potential shading from obstructions.

Details about the influence of these factors are in [29].

During the planning process of new PV plants, designers make extensive use of large databases created from the collection of solar irradiance data in most countries for several years. Representative examples of solar databases available in the web are [8], [9].

2.1.1 PV cells technology and materials

The modern PV technology is based on the principle of electron hole creation in each cell composed of two different layers (p-type and n-type materials) of a semiconductor material. When a photon of sufficient energy impinges on the p-type and n-type junction, an electron is ejected by gaining energy from the striking photon and moves from one layer to another. This creates an electron and a hole in the process and by this process electrical power is generated [27].

The common types of materials applied for PV cells include silicon (single crystal, multi-crystalline, amorphous silicon), cadmium-telluride, copper-indium-gallium-selenide, and copper-indium-gallium-sulfide. Depending on the material, the photovoltaic solar cells are categorized into various classes [27]. Anyway, for some technical and economical reasons the most used technology is the crystalline one, especially the multi-crystalline. In some specific applications, for which coloured panels or flexible panels are required, the crystalline technology is unsuitable. In these cases the modules are usually realized using amorphous cells or other different types.

Another technology developed in last years is the Concentrated PV (CPV). The use of cost-efficient concentrating optics dramatically reduces the cells area allowing for the use of more expensive, high-efficiency cells and potentially a Levelized Cost of Electricity (LCOE) competitive with standard flat-plate PV technology in certain sunny areas with high DNI. The available CPV systems are classified according to the concentration factor of the technology configuration. More than 90 % of the CPV capacity that has been publicly documented to be installed in the last years is in the form of high concentrated PV (HCPV) with two-axis tracking. Despite of the high efficiency

of this technology, the number of CPV plants is very low. The main challenge reported by the industries is the difficulty of CPV to compete with crystalline PV modules on cost. CPV companies expect that this technology can compete on an LCOE basis with flat-plate PV when installed in sunny areas, but the road to scale is difficult [30].

Various other typologies of high efficiency PV cells are under development such as bifacial and HJT cells. Some information on these and others promising technologies are in [12], [29], [31].

2.1.2 Standard technical solutions for PV plants

Thanks to their scalability, PV systems can be realized for a wide range of power rate, from few kW for residential applications to hundreds of MW for utility-scale electricity production.

The basic element of a PV module is the cell. More cells in series form a sub-module or a module, that is sometimes called panel. Bypass diodes prevents the current flowing from good, well-exposed to sunlight solar cells overheating and burning out weaker or partially shaded solar cells by providing a current path around the bad cells.

The open circuit voltage V_{oc} of a PV module is typically about 40 V. The voltage at module terminals in presence of a load is normally a little lower than V_{oc} . The operating voltage is too low for the direct connection of the module to the input side of the DC/AC converters. It is necessary to reach higher voltage by creating a string, Fig. 1, so that the total voltage of the series of modules is:

$$V_{str} = V_1 + V_2 + \dots + V_{N_S} \quad (1)$$

where N_S is the number of modules in series.

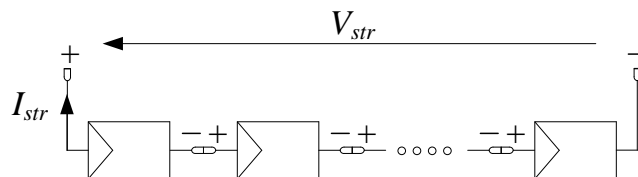


Figure 1. PV string: series connection of N_S PV modules

If, theoretically, all the modules are identical, equation (1) becomes:

$$V_{str} = N \cdot V_i \quad (2)$$

In this case, the string current I_S is equal to the current of each module, considering that the modules are identical each other. In reality, there are always small or big differences in the electrical characteristics of modules, so that the actual string current depends on the modules that generate the lower current. More details on this topic are in following Chapters.

In large PV plants, groups of strings are connected in parallel creating PV arrays, whose voltage V_{array} is fixed by the parallel connection of N_P strings. The total current I_{array} is the sum of the currents supplied by each string:

$$I_{array} = I_1 + I_2 + \dots + I_{N_P} \quad (3)$$

The parallel connection of the strings to form an array is realized in a parallel box or string box, Fig. 2. The portion of PV field connected to such box is usually called subfield. The number of parallel boxes in a PV plants depends on the size of the latter and of the number of strings connected to them.

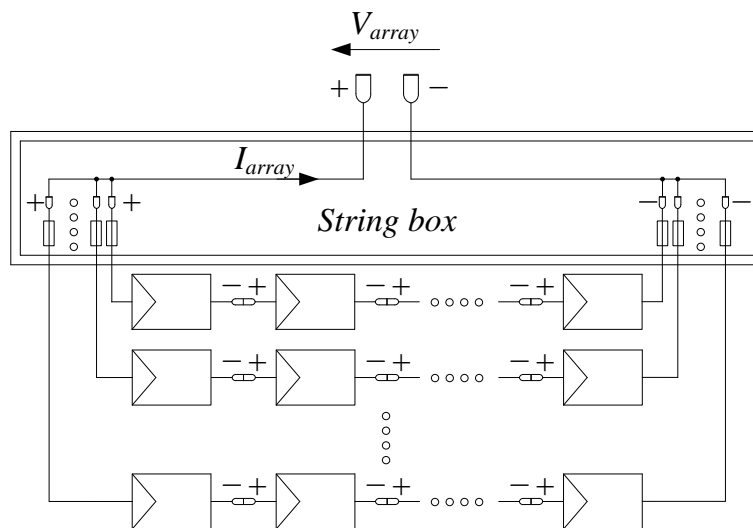


Figure 2. PV array: parallel connection of N_P PV strings

In small plants, until about 6 kW, strings are usually connected directly to the conversion system that is the only interface between the generation system and the low voltage (LV) grid, see Fig. 3. For rated power above 200 kW, the PV plant usually deliver the energy to medium voltage (MV) utility-grid. In this case, a power transformer is placed between the inverters and the grid, see Fig. 4.

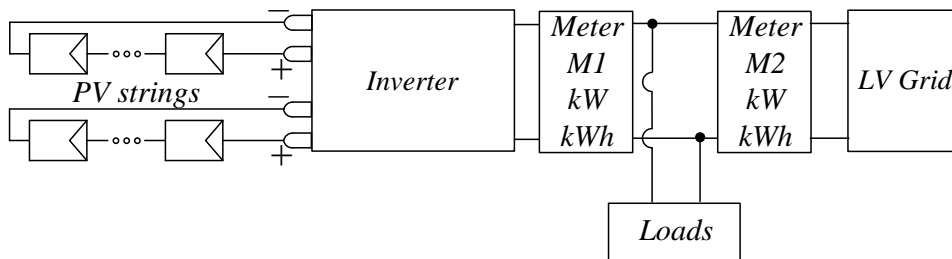


Figure 3. Rough scheme of a small PV plant connected to LV grid

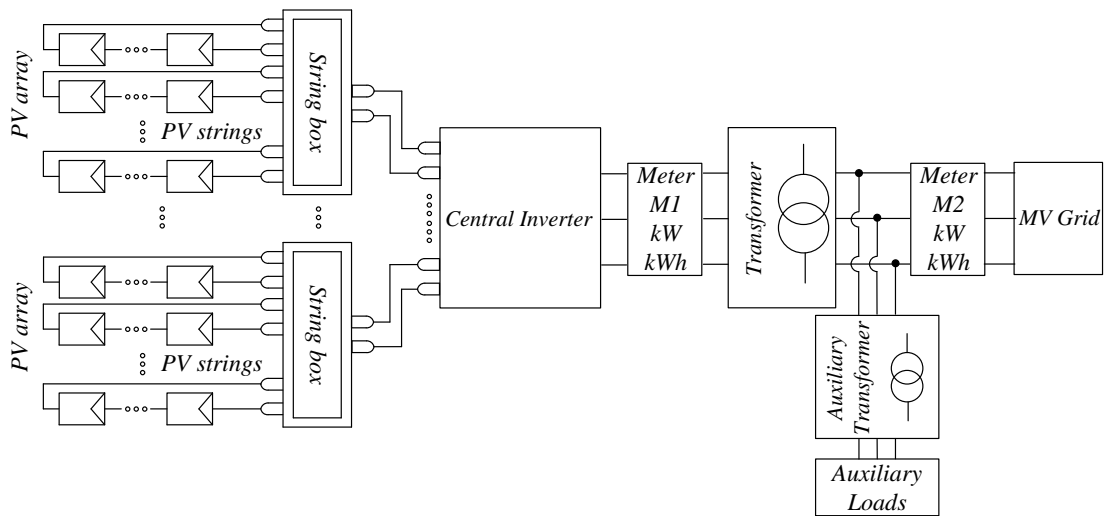


Figure 4. Rough scheme of a large PV plant connected to MV grid

The design of inverters for PV applications takes into account the presence of large fluctuations of voltage at the DC input side. Within a given range of input voltage that has to be as large as possible, the inverter is able to perform the DC/AC conversion in Maximum Power Point Tracking mode (MPPT) transferring the maximum energy that the PV modules can produce at that moment depending on sun irradiance and on

ambient temperature. The most popular MPPT algorithms are the Perturb and Observe (P&O) and the Incremental Conductance (IC) [32].

At the same time, the control system of the inverter has to manage the parallel connection with the grid on the basis of technical specifications fixed by the utility company also in terms of protection settings. The Phase Locked Loop (PLL) control system, together with electronic and electromechanical relays, fulfils these functions [33], [34].

Other converters, DC/DC or DC/AC types, can be integrated in a PV plant with the purpose to increase the energy production. This kind of converters, investigated in this thesis with particular reference to string inverter and string optimizer types, are described in following Chapters.

About the protections placed between the inverter and the grid, there are three main types:

- the Generator Protection (PVGP) that commands the Generator Breaker (PVGB) that is at the output side of the inverter;
- the General Protection (GP) that commands the General Breaker (GB), used to separate the plant from the grid in case of an internal fault;
- the Interface Protection (IP) that commands the Interface Breaker (IB), used to separate the plant from the grid in case of large deviations occurring for the grid voltage and frequency.

This classification is valid in most countries. It is regulated by international standards, in particular ANSI IEEE Standard C37.2 [35]. Anyway, the name and characteristics of each protection item may differ in some cases due to special requirements fixed by the local utility company.

Regarding the meters for the measurement of the produced energy, the common configuration is the one shown in Fig. 3 and Fig. 4.

The meter M1, which is placed close to the output side of the inverter, is used to measure the energy produced by the PV plant. The meter M2 is used to measure the amount of energy delivered to the grid. This latter meter is bidirectional, in fact it is used to measure the energy coming from the grid during the night, too.

During the day, the energy measured by M2 is the difference between the energy production, measured by M1, and the energy consumption of the loads being part of the plant itself. In small plants for residential or industrial applications, the amount of self-consumption can be significant because the primary target is to supply all the loads exploiting the PV source in order to reduce the energy acquired by grid. On the contrary, in large or utility-scale PV plants, the primary target is to deliver the produced energy to grid. In this case, the self-consumption is due to cables losses, transformers losses and internal auxiliary loads. The impact of self-consumption is about 2 - 3 % meaning that the energy measured by M2 is quite close to the entire energy production measured by M1.

In some cases, the configuration of meters could differ, for example:

- in small PV plants, depending on the specific feed-in tariff mechanism, a single meter can be sufficient (M1 or M2);
- in presence of ESS, a third meter could be required to measure the energy flow at the battery pack during charge or discharge processes;
- in some countries, backup meters are required by technical regulations, these meters have to be inserted in case of fault on the primary ones.

Taking into account the orientation of PV modules with respect to the sun, Fig. 5, the ideal situation is to keep continuously the right angle between the module surface and the sunrays. The dual-axis solar trackers can keep this orientation for the modules during the day, getting a large increase of produced energy in comparison to fixed systems. Some examples are in Fig. 6. An intermediate solution is represented by the single-axis solar trackers. For large PV plants, the latter is often the best tracking solution because it ensures a satisfactory extra production but with limited costs for both construction and maintenance. A review of tracking systems for PV modules is in [36].

It is well-known that the main types of PV installations are the rooftop plants for buildings (mainly fixed tilt installations) and the plants mounted on large ground areas (fixed or with trackers), Fig. 7. There are also other particular categories but their utilization is limited to specific applications or to research tests. Some examples are floating PV systems [37] and plants with flexible modules [38], Fig. 8.

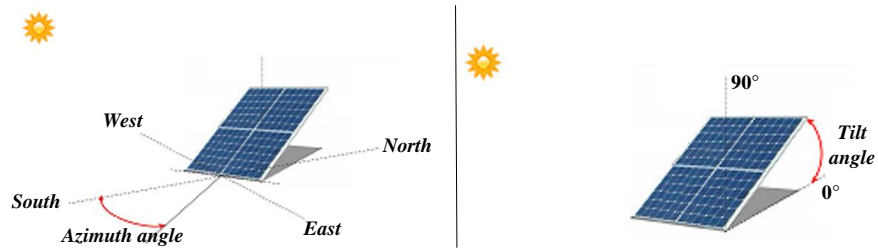


Figure 5. Orientation of PV module with respect to sun, azimuth and tilt angle



Figure 6. Left: example of single-axis tracker, tilt 0° . Center: example of single-axis tracker, tilt 20° . Right: example of dual-axis tracker



Figure 7. Left: example of rooftop PV plant. Right: example of ground-mounted PV field

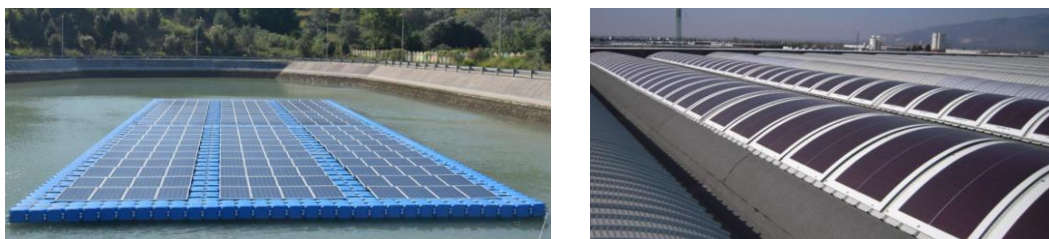


Figure 8. Left: example of floating PV system. Right: example of flexible PV modules

In the last years, the development of new PV plants has been favoured by several policy mechanisms designed to accelerate investment in renewable energy technologies. In particular, the feed-in tariff consisting of fixed electricity prices for each kWh of energy produced or injected into the electricity grid is the most common mechanisms regulated by most of the countries with the purpose to increase the number of new installation while keeping the same in good maintenance state for almost 20 years [39]. With special reference to small PV plants for residential applications, the latest approach is to increase the self-consumption energy with benefits in terms of sizing and efficiency.

2.2 Underperformance of PV plants: causes and diagnosis

This Section provides a brief review on the main underperformance phenomena in PV plants and on techniques to diagnose these issues. Since this is a very broad argument, information in next sections cannot be exhaustive. Readers can delve into the topic from the references within the text.

2.2.1 PV modules: underperformance effects

At module level, the underperformance effect originates from several phenomena, in some cases two or more of these phenomena can occur at the same time.

The main causes are:

- manufacturing defects related to issues in the quality control processes during the assembly of cells or modules;
- local shadowing during sunny hours on one or more cells of the PV module;
- very dirty cells;
- mechanical damages;
- Potential Induced Degradation (PID) effect [40];

- other effects including delamination, discoloration (browning, yellowing, etc.), Ethylene-Vinyl Acetate encapsulant (EVA) degradation, snail trails and so on [41].

The procedures commonly adopted to diagnose the degradation level of a PV module are listed below, from the less precise to the more accurate method:

- visual inspection;
- current measurement during operation;
- open circuit voltage measurement;
- thermographic inspection;
- I-V curve tracing.

These verifications should be periodically performed in order to monitor the degradation over time and the mismatch effects caused by differential aging occurring for modules being part of the same manufacturing stock.

Some reviews on the underperformance effects occurring in PV modules, on diagnostics procedures and on mitigation techniques are in [41], [42].

2.2.2 Strings and arrays: underperformance effects

One or more of the following issues often cause the underperformance effects occurring at string or array level in PV plants:

- one or more modules exhibit one of the faults described in previous Section;
- modules connected together in a string or in an array are affected by different level of aging;
- the electrical configuration, in particular the ground connection, make it possible the presence of leakage currents leading to PID in some cases;
- faults or misalignments in solar trackers;
- other faults, a common example is the presence of a blown fuse that disconnect a string in a parallel box until its replacement.

In most cases, the final result is a mismatch effect at string or at array level

2.2.3 The mismatch

Generally, the mismatch is defined as the underperformance effect occurring for a string when modules exhibit different electric behaviours or for an array when strings have different I-V characteristics [43], [44].

For large or utility-scale PV plants, it is possible to calculate the mismatch also for subareas whose string boxes are connected to the same inverter featuring a single MPPT control. In this case, the cause of mismatch is the non-uniform behaviour of the arrays connected to the string boxes [44]-[46].

One of the main target for the researchers is the evaluation of the actual loss in energy production caused by mismatch effects. Moreover, due to its nature, mismatch can occur in plants not affected by faults. This fact creates further difficulties in diagnosis process. For example, the wrong sorting of PV modules during the assembly of strings, caused by the missing coupling of modules on the basis of their flash reports [47], could lead to significant mismatch effects despite the absence of faults or aging.

This thesis contributes to the knowledge on mismatch phenomena and on its evaluation for large PV plants. In fact, mismatch is calculated on the basis of real data following a multi-criteria approach for the case studies represented by real large PV plants. This analysis takes on particular importance because the literature existing to date on the assessment of mismatch for large plants is limited to few examples [15], [16], [46].

Criteria suitable for the numerical evaluation of mismatch level in large PV plants can be different. For example, calculation can be executed referring to instantaneous power or to produced energy. Alternatively, it is possible to calculate the percentage difference among the currents of the strings connected in parallel to the same string box, controlled by a single MPPT algorithm. There are several similar criteria exploitable for mismatch evaluation but there is no a dominant approach in literature because the selected criteria depend on the expected goals of the performance analysis.

The criteria selected in this work derive from [45], [48], but they have been modified and adapted for the specific case studies.

2.3 Methods to mitigate the underperformance effects

Techniques to increase energy production by mitigating underperformance effects in PV plants fall into two main categories:

- before the construction of the plant: innovative design solutions or innovative manufacturing processes;
- during the operation of the plant: retrofitting activities.

An example of the first category is the arrangement of interconnections of solar cells in crystalline silicon PV modules [49]. In this case, referring to the unevenly distribution of diffuse solar radiation on the surface of a PV module, the target is to reduce the differences in the currents produced by the subgroups of cells searching for the best arrangement and interconnection of solar cells.

Another example for the first category is the selection of the tracker system. The target is to increase the energy production in order to recover the extra cost of trackers in a fast time, with benefits for the entire plant in terms of payback time [36].

About the second category, with special reference to large PV plants, a common retrofitting activity concern the installation of distributed power converters with the purpose to mitigate the mismatch effects. Going back to first category, some technical solutions for distributed converters could be selected during the design process on the basis of the expected extra production. A comprehensive review on distributed power converters used to mitigate the mismatch effects is in Section 4.2.

Chapter 3 - ESS in PV plants

3.1 ESS for renewables: state of the art

In the last years, the integration of ESS in renewable power plants has become a very important topic because of its importance in the transition process from the traditional grid to smart grids. In reality, the installation of ESS in small power renewable systems, particularly in the range 3 – 10 kW, is already an established market in many countries. On the contrary, the integration of ESS in large plants is limited to few cases, most of these are experimental test on new battery technologies [18], [50]-[52].

The battery pack is an essential element in the stand-alone power plants supplied by renewable sources. In such plants, not connected to utility grid, the proper sizing of ESS has fundamental importance because the battery is the heart of the system [53]. In many cases, considering large time horizon consisting in some days or more, the PC and the EC of ESS must be quite high to store the entire energy produced by the PV plant in absence of load. On the other side, ESS should be able to deliver rated power of loads in absence of generation. This last case is frequent during winter in presence of several rainy days in succession.

Sizing calculation of battery packs in stand-alone power plants is difficult because it involves statistical information for weather forecast, the selection of a proper time horizon for the calculation of PC and EC, the precise knowledge of the state of the battery, the availability of information about the expected working cycles and so on.

Interesting overviews regarding the stand-alone PV plants, the common technical solutions and the sizing strategies are in [53], [54].

For grid-connected PV plants category, which includes almost all the existing PV systems, the integration of ESS is not mandatory as for stand-alone plants. Anyway, the presence of battery packs can produce large benefits in the energy management of the PV system obtaining more efficiency, flexibility and reliability.

The high cost for the integration of ESS in small PV plants is often an obstacle because it abnormally enlarges the payback time of the investment. Despite this, there are particular situations for which the extra cost of batteries is justified by specific technical reasons, for example:

- users or loads that experience a wide number of grid black-out over time, in this case the ESS could work as an UPS system. The batteries could be sized for all the users or just for the critical ones;
- power supply of loads that can be connected directly to the battery pack without any conversion system as for some lighting systems or some water heaters;
- users with main loads activated during the night hours. In this case the batteries will provide the energy time shifting services for the energy stored during the sunny hours.

3.2 Batteries in large PV plants

As mentioned before, the integration of batteries in large PV plants is limited to few cases, most of them for experimental test purposes. However, some of these systems operate from several years providing large database of information regarding the management of batteries, the benefits, the drawbacks and the adaptability for future smart grids.

For the sake of example, Table 1 reports some large PV plants with ESS, more details on these installations are in listed references.

For all these existing projects, the power configuration used for the ESS is the connection of large centralized battery packs at the DC-link of inverters (using bidirectional DC/DC converters) or at the grid delivery point (using bidirectional DC/AC converters). Unfortunately, due to high costs, complexity and safety issues, the spread of these solutions is not expected to increase in the market for a relevant number of PV plants in the next years. An additional reason is the absence of an optimal electrochemical technology able to drive this spread.

Plant	ESS size		ESS Technology	Services	References
	MW	MWh			
Zhangbei, China	20	36	Li-Ion	PV and wind energy smoothing, grid stabilization, increased reliability	[55]-[57]
Buzen, Japan	50	300	Sodium-sulphur	Stabilization of power flow and frequency fluctuations caused by renewables	[34]
Mafraq, Jordan	3	12.6	Li-Ion	Peak power shaving, energy shifting	[56]-[58]
Sendai, Japan	40	20	Li-Ion	Minimization of frequency fluctuations caused by PV plants	[34]
Naiyu, Daly River, Australia	0.8	2	Li-Ion	Black start, microgrid capability, energy time shifting	[58], [59]
Yokohama, Japan	1	5	Flow batteries	Electric supply capacity, energy time shifting	[57], [60]
Dangling Rope, USA	0.25	2.4	LA	Renewables capacity firming, energy time shifting	[57]
Puerto Rico	0.25	1.25	Sodium-sulphur	Microgrid capability, energy time shifting	[57]

Table 1. Examples of large PV plants with ESS

It is necessary to find innovative solutions for both technology and power configuration. Focusing on the latter item, this thesis investigates on benefits related to the creation of a distributed ESS for large PV plants in replacement of the traditional centralized storage system. In other words, in the proposed approach there is no longer a big battery pack close to the inverters but several small size batteries connected to strings or to arrays into the field close to PV modules and to string boxes, Fig. 9. This idea is strictly related to distributed converter systems for large PV plant analyzed in this work.

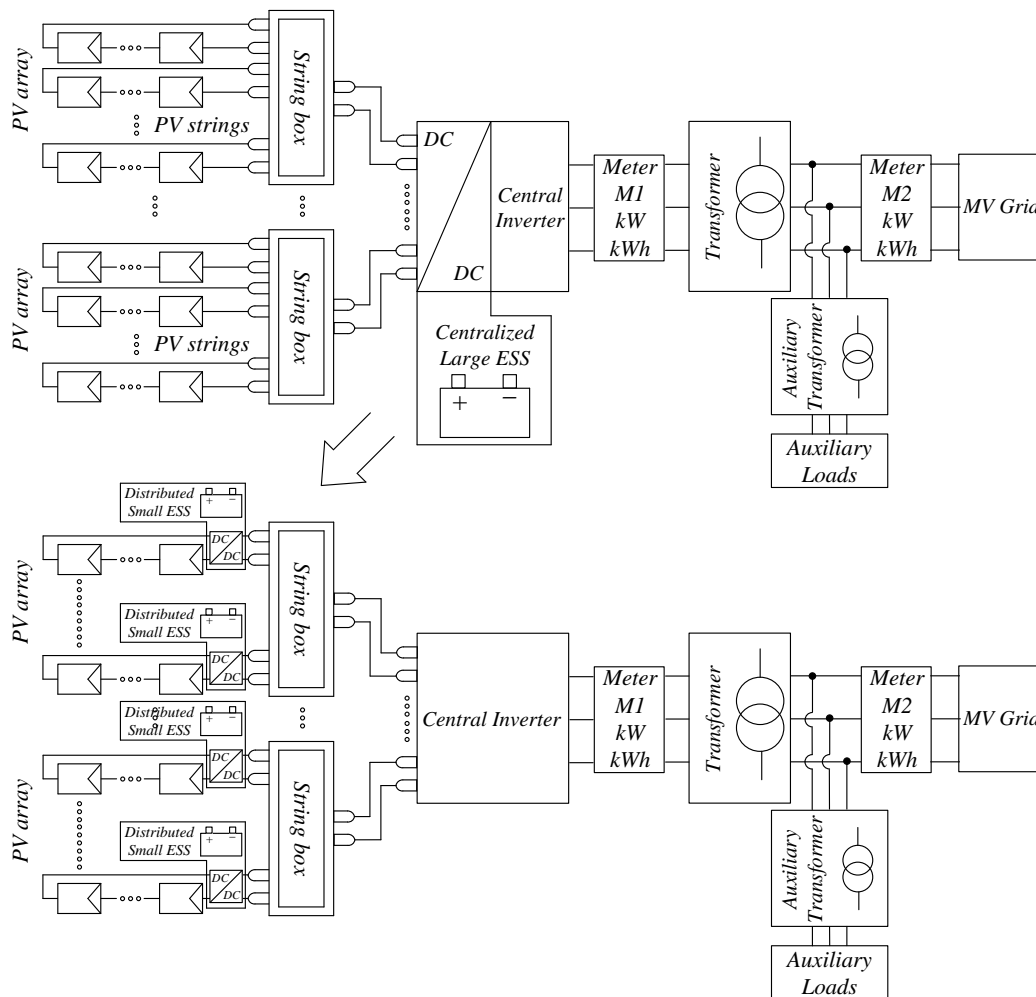


Figure 9. From centralized large ESS to distributed small battery packs

The expected benefits of this innovative approach are [61]:

- in comparison to standard centralized solution, configuration with distributed batteries at string level increases the reliability of the entire storage system;
- in some cases, depending on the actual power and energy requirements, the total number of batteries in operation can be reduced so that losses in batteries, converters and cables decrease;
- a distributed power supply system for loads as lights, trackers, antitheft devices, etc. can be easily realized into the field;
- with respect to centralized solution, sizing of the ESS can be performed with more degrees of freedom;

- battery packs can be used to store the energy produced by the PV arrays for maintenance activities during which the shutdown of string boxes is required.

To benefit from these advantages, a proper energy management strategy supported by suitable models is required. Some novelties presented in this thesis deal with the integration of innovative models for both batteries and PV arrays in order to match the actual PC and EC of the ESS with the power curve of the PV arrays taking into account real operating scenarios occurring in case studies.

Chapter 4 - Power electronics converters in PV plants

4.1 Power converters in PV plants

The exponential growth for the number of new renewable plants in the last years is driven by the increased performance of power electronics converters, able to adapt the electricity generated by the primary source to the utility grid and ESS. Some overviews are in [62]-[64].

Referring to PV plants connected to the utility grid, the core of the conversion system is the DC/AC converter i.e. the inverter. For small PV plants, until 10 kW or little more, inverter is usually single-phase, otherwise it is three-phase. For rated power above about 200 kW, a power transformer is usually placed between the inverters and the grid.

In large PV plants, in addition to the traditional 3-legs 6-devices inverter topology, there are some variants as the multi-stage DC/AC converters and the multi-level inverters. In the first case, the first stage of the converters is realized as the interconnection of one or more DC/DC converters. The input is connected to a PV string or array creating an independent MPPT system with the main purpose to reduce the mismatch effects. The output, usually regulated in constant voltage mode, is connected to the DC-link of the secondary stage that is the DC/AC converter. Some examples are in [14].

Information on multi-level inverters are in [64]. This typology is used to realize MV high power converters with reduced harmonic distortion, reduced EMI filters size and better voltage waveform. The main drawback is the higher number of switch devices.

Recent research activities focuses on the development of High Voltage (HV) inverters, mainly multi-level type, directly connected to the MV grid without using a power transformer. The high system voltage leads to a significant reduction of Joule losses. Moreover, the power transformer is no longer necessary [65].

In large PV plants with a distributed conversion system, there are different possible technical solutions and topologies for the DC/DC converters as well as for the DC/AC ones. See next Sections for more details.

Technical advances in the improvement of traditional converters and the development of new types strictly depend on the novelties in devices, power modules and materials. In particular, alternative materials Silicon Carbide (SiC) and Gallium Nitride (GaN) allow for big advantages like high switching frequencies and losses mitigation, although they are not yet industrially mature [64].

4.2 Distributed conversion systems

4.2.1 Distributed power converters for small PV plants

Distributed power converters in small PV plants represent an established market in solar industry for new constructions and for retrofitting as well. Many tests are carried out in laboratory as well as in small size and medium size PV plants with the purpose to evaluate the benefits of distributed converters and their payback time. Many research papers belong to the literature regarding such topics, for example [66], [67].

The most common devices are DC/DC converters at the cables linking the PV modules or DC/DC converters connected at the string terminals, close to the DC input of the inverter. Examples of products available in the market since several years are in [68], [69].

4.2.2 Distributed power converters for large PV plants

In large PV plants there are several technical solutions and topologies for the DC/DC distributed converters as well as for the DC/AC ones. Anyway, the most common options are string optimizers (at string or array level) or string inverters.

Differently than small plants, for large PV fields information in literature regarding distributed conversion systems is limited to few papers, examples of studies on this topic are [70], [71]. Anyway, in this kind of papers, apart from the description of

converters technology and some simulations, elaborations of results obtained from real plants are mostly missing.

Although the number of plants with distributed converters is continuously growing, a first reason for this lack of information is related to their low number in comparison to large PV fields with traditional central converters. Moreover, data and measurements acquired by plant dataloggers are usually covered by policies on industrial secrets, therefore they are often not available for research purposes. Only the manufacturers provide more technical details on distributed converters but such data comes from laboratory simulations or from small testing facilities instead of real field measurements.

The results of this thesis contribute to increase the knowledge on the actual performance of distributed converters for large PV plants. In fact, the primary data used for elaboration consists of extensive measurements provided by the dataloggers installed in two existing large PV fields, which are the case studies of the thesis. These plants have different solutions for the distribution conversion system.

The first case study is a 300 MW PV plant in Brazil. The power configuration is with central inverters except for a 2.5 MW subfield that is realized using string inverters. This subfield is compared to a 2.5 MW subfield having the same DC configuration but central inverters for the conversion system. The overall 5 MW cluster represents the experimental facility exploited for the performance assessment of the distributed converters.

The second case study is a 2 MW PV plant in Central Italy. A 500 kW subfield was retrofitted in 2018 performing the installation of string optimizers in SiC technology at parallel boxes. The comparison between this experimental subfield and the others (these latter with central inverters) allows the evaluation of the distributed conversion solution.

4.3 Power converters for the integration of ESS in PV plants

In the most cases, the power configuration used to integrate an ESS in a PV plant is the connection of the ESS close to the inverter, at its DC side through a DC/DC converter or at its AC side through a DC/AC converter. In both cases, the ESS is the assembly of several batteries connected each other in order to fulfil the requirements of PC, EC, voltage and so on.

Some papers dealing with power converters for the integration of ESS in PV plants are [63], [72], [73]. From these papers, it emerges that there are several possible topologies. Also the connection configuration can be different: for example, an option is the use of a three-port DC/DC converter, which includes a DC input port for the PV strings, a bidirectional DC input port for the ESS and a DC output port. This could be a preferable solution with respect to the traditional method using two DC/DC converters, one for the PV plant and one for the ESS.

Even if an exhaustive overview on converters for the integration of ESS in PV plants is very difficult, from a literature review it is easy to note that, as for the PV plants, most of the information deals with small or medium size converters. The main reason of this lack of information, aside from policies on industrial secrets, is the low number of large ESS systems connected to existing PV fields because of their cost, technical complexity and issues.

With the purpose to overcome such complexity, the approach followed in this work for the integration of ESS in PV plants is no longer the connection of a large battery pack close to inverters but the installation of several small batteries linked directly into the field at the strings, close to the parallel boxes.

Thanks to this innovative choice, there are significant benefits for the selection of ESS converters. In fact, it is possible to install converters characterized by low rated power, nowadays widely present in the market. Moreover, the reduced size determines other advantages as fast installation procedures, easy compliance to safety requirements and different power configuration options. Regarding the latter point, a common option, especially for retrofitting purpose in existing plants, is the connection of the battery

pack to one or more strings in parallel through an isolated DC/DC converter. Otherwise, the installation of three-ways converters acting as distributed converters for both the PV plant and the ESS could be a cheaper option, particularly for new installations [63].

Chapter 5 - Modelling and simulation of PV plants

5.1 State of the art

Development of accurate models addressed to the simulation of PV systems, from the cell level to the utility-scale plants, is very topical in research but also in several industrial and commercial applications.

Modelling approach depends on the fixed goals and on the size of the analysed systems. For example, a model adopted for the design of the control system of the inverter in a small PV plant is certainly very different with respect to a model used for the forecast of energy production in a utility-scale PV field. The first model, applied for the analysis of short duration events (switching phenomena), shall be very accurate involving a significant computational effort. On the contrary, for the second model, applied for long duration events in a plant having thousands of components, it is necessary to give up to high accuracy in order to limit the complexity getting a reasonable level.

The literature regarding the modelling of PV plants is wide. On the basis of the size of the PV system, it is useful to distinguish the context of some reviews:

- modelling of PV cells: [74], [75];
- modelling of small PV plants for residential use: [76], [77];
- modelling of large PV plants: [78], [79].

In all these cases, the most common modelling approach is based on equivalent circuits.

5.2 Modelling of large PV fields

The selection of modelling approach and simulation platform for large PV plants depends on the specific analysis targets with respect to the requirements in terms of acceptable computational effort. If such target is the yield estimation for a long time period, modelling of power converters is usually neglected. In this case, converters are

replaced by functional blocks which reproduce simply the value of their efficiency [80], [81]. On the contrary, if some specific operating conditions need to be investigated providing details on converters operation and losses, detailed models need to be implemented [82]. In the latter case, simulations are carried out for reproducing short time periods with large accuracy and large computational effort. Under this perspective, in case of energy assessment for a period of some months or years, detailed models cannot be exploited to simulate the behaviour of a PV system having thousands of PV modules and hundreds of distributed converters as for the utility- scale PV fields.

5.2.1 The proposed modelling approach

Some authors tried to overcome the limitations reported in the previous Section by introducing simplified modelling approaches usually known as behavioural models. For example, in [80] a behavioural model for grid-connected photovoltaic inverters simulates the electrical behaviour of commercial inverters in accordance with regulations on power quality. Simulation results show the injected AC current waveform under either power dynamics or grid voltage disturbances. In [83] a non-parametric approach is able to calculate the energy delivered to the grid by six PV fields on an hourly basis in forecast processes using meteorological variables as inputs.

Although the requirements of low computational burden are fulfilled in the behavioural approaches, the actual physical configuration of the PV plant may be completely neglected. In some cases, this represents a relevant drawback. For example, if the performance analysis is addressed to evaluate the losses over time in both DC cables and AC cables, some details about converters topology and their control strategy need to be included so that voltage and current values can be known continuously in both DC side and AC side and then they can be used to calculate losses. Unfortunately, in most real PV plant the monitoring system does not provide data of electrical quantities for each section of the multi-stage conversion system, consequently an accurate estimation of losses is not feasible.

These issues are faced by using a modified behavioural model as the one described in this thesis, in which an integrated state-space average model is used to compute all the electrical quantities in each section of a PV plant thus allowing a simple calculation of losses, voltage drops, etc. The adjective “integrated” refers to the proper merging of the state-space average models developed for each component present in a large PV plant.

In this way, a satisfactory accuracy is obtained while a too large computational effort is avoided. Other advantages of such approach are:

- significant reduction of simulation time;
- the basic model can be easily adapted to different system configurations (e.g. central inverters, string inverters, string optimizers with central inverters, etc.) with minimal modifications;
- state-space representation of each component and of the entire PV system allows a direct implementation of several identification methods well-known in literature. Such methods can be used to fix the parameters value but also to tune the PI regulators in control systems;
- state-space representation allows the implementation of observers. Observers can be very useful to estimate electrical quantities in case of missing data, large modifications in parameters value depending on weather and so on. In other words, it is possible to limit the inaccuracies caused by parameters uncertainty and by wrong or missing measurements;
- technical details about the converters topology and their control system are no longer necessary. Furthermore, in many cases such information is not provided by the converters manufacturer to keep industrial secrets;
- the behavioural model can be effectively integrated in monitoring systems and exploited for forecasting purposes and for fault detection;
- since the state-space representation has a general validity, the proposed model can be implemented in any simulation platform.

The introduced integrated model, developed in MATLAB Simulink environment, has been validated in terms of computational complexity and accuracy. It has been applied to specific case studies as detailed in final Chapters of this thesis.

The basic representation of a utility-scale PV plant, exploitable for modelling purpose, is in Fig. 10. This configuration can be adapted to simulate PV fields with central inverters as well as the ones with string inverters or with power optimizers at module or string level. Moreover, it is easily scalable for the whole PV plant under investigation or for a specific subfield (strings, string boxes, etc.) with minimal modifications.

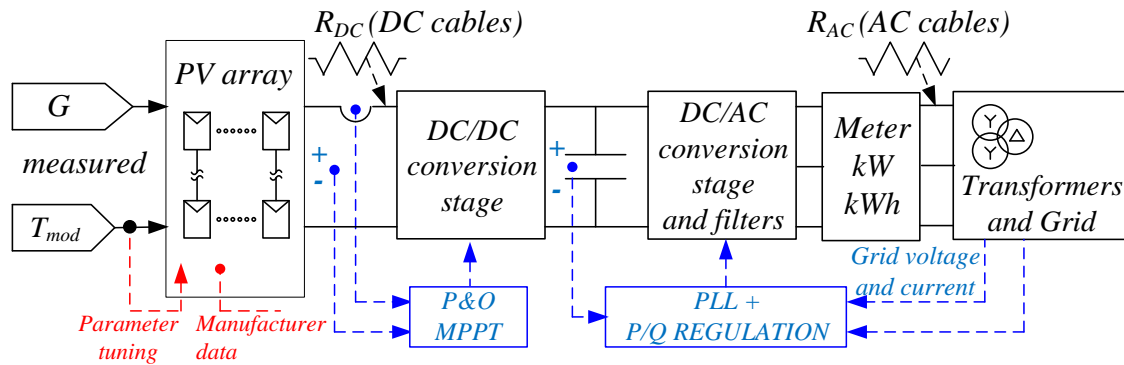


Figure 10. Generic PV plant configuration for modelling purpose

The implementation in a simulation platform can be executed in different ways. In general terms, it is possible to distinguish three main approaches:

- detailed models, meaning that each component (PV array, converters, grid, etc.) is implemented in software environment considering its actual configuration, circuit topology and operation mode. For example, converters are modelled reproducing their detailed topology and switching modulation technique [82];
- models in which the physical models of components are not incorporated [83];
- intermediate models that represent a trade-off between the previous categories [80].

The behavioural model introduced in this work falls into the third category. It is based on a modified state-space averaging method selected with the primary target to

get a simplified representation for the multi-stage conversion system of utility-scale PV fields in case of distributed converters. In fact, in this case there are both DC/DC converters (e.g. first stage of string inverters or power optimizers) and DC/AC converters (grid connected inverters, usually multilevel inverters). The integration of different conversion stages has been obtained thanks to the development of a direct and effective way for the analytical calculation of the DC-link current.

Finally, thanks to the proposed integrated models all the components of the generation and conversion system are mixed into a single state-space average model obtaining a comprehensive representation for the entire PV plant. In other words, the PV plant becomes a single state-space system whose inputs are irradiance and cell temperature and whose outputs are the energy production and the electric quantities exploitable for losses evaluation or for other analysis.

Following Sections and Chapters provide a detailed description of the state-space model built for each component of the PV plant:

- PV arrays;
- conversion system, DC/DC and DC/AC converters;
- filter stage;
- power transformer;
- utility grid;
- ESS.

Then, in Chapter 8 the integration of these models is explained. It is worth noting that, taking into account the primary target to maintain a low computational effort, the ESS model is not directly inserted into the integrated state-space average model of the PV plant but it is linked through the real-time assessment of PC and EC. This choice gives the opportunity to develop, in a separate way, special algorithms for the estimation of the state (SOC and SOH) of the battery pack since this is a very critical point for the proper energy management of the entire system.

5.3 Model for PV modules and PV arrays

The accuracy of the model used for the generation park and in particular for PV arrays model is crucial for the precision of the final integrated model.

The formulation selected in this thesis as basis for modelling of PV modules is in [84], consisting in the well-known single-diode model. Since large temperature variations are expected to take place in real PV plants, a sensitivity analysis has been conducted in order to detect the parameters causing large modifications in the I-V and P-V characteristics. In case of stringent requirements on accuracy level, these temperature-dependent parameters are tuned on-line by means of look-up tables.

A satisfactory accuracy has been obtained taking into account the influence of temperature on short-circuit current and on no-load voltage through the coefficients I_{sc}/T_{mod} and V_{oc}/T_{mod} listed in the datasheet of the PV modules avoiding the use of look-up tables for the benefit of simplicity.

To extend the model of PV modules to PV arrays consisting of N_S modules in series and N_P strings in parallel at the stringboxes, the basic following formulas are [85]:

$$I_{sc,array} = N_P \cdot I_{sc} \quad V_{oc,array} = N_S \cdot V_{oc} \quad R_{s,array} = \frac{N_S}{N_P} \cdot R_s \quad R_{p,array} = \frac{N_S}{N_P} \cdot R_p \quad (4)$$

where R_s is the series resistance and R_p is the parallel resistance in the Equivalent Circuit Model (ECM) [84].

For sake of simplicity, in the following the terms in (4) will be referred to the PV array without using the subscript “array”.

The PV array model is transferred in state-space form:

$$\begin{cases} \dot{x}_p = A_p x_p + B_p u \\ y_p = C_p x_p + D_p u \end{cases} \quad (5)$$

Let us consider the basic equivalent circuit shown in Fig. 11 in which a fictitious resistive load R_{LOAD} is connected to the PV array. Equation (6) is obtained from simple calculations as Kirchhoff Current Law (KCL) and Kirchhoff Voltage Law (KTL):

$$(6)$$

$$\frac{dv_{C_{panel}}}{dt} = \left[-\frac{R_p + R_s + R_{LOAD}}{R_{LOAD} C_{panel} (R_p + R_s)} \right] v_{C_{panel}} + \left[\frac{1}{C_{panel} \left(1 + \frac{R_s}{R_p}\right)} \quad \frac{-1}{C_{panel} \left(1 + \frac{R_s}{R_p}\right)} \right] \begin{bmatrix} i_{ph} \\ i_d \end{bmatrix}$$

Considering $y_p = x_p$ and fixing i_{ph} and i_d as inputs, x_p and u are:

$$x_p = v_{C_{panel}} \quad u = \begin{bmatrix} i_{ph} \\ i_d \end{bmatrix} \quad (7)$$

A_p and B_p become:

$$A_p = \left[-\frac{R_p + R_s + R_{LOAD}}{R_{LOAD} C_{panel} (R_p + R_s)} \right] \quad B_p = \left[\frac{1}{C_{panel} \left(1 + \frac{R_s}{R_p}\right)} \quad \frac{-1}{C_{panel} \left(1 + \frac{R_s}{R_p}\right)} \right] \quad (8)$$

and:

$$C_p = 1 \quad D_p = 0 \quad (9)$$

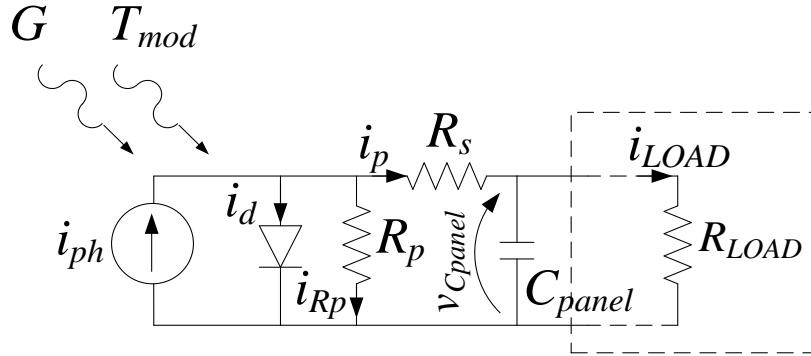


Figure 11. Simplified equivalent circuit used to build the basic state-space representation of PV array

Current i_{ph} is a function of irradiance G and of module temperature T_{mod} as follows:

$$i_{ph} = \left[I_{sc} + K_t (T_{module} - 25) \right] \frac{G}{1000} \quad (10)$$

where K_t is the temperature coefficient calculated as:

$$K_t = \frac{NOCT - 20}{800} \quad (11)$$

The Normal Operating Cell Temperature (NOCT) is usually reported in PV module datasheet. Also the current i_d is a function of irradiance G and of module temperature T_{mod} as described in [84].

Chapter 6 - Modelling and simulation of ESS

6.1 State of the art

Looking at the classification of the possible storage systems [51], [86], ESS based on electrochemical batteries managed by their Battery Management Systems (BMS) play a key role in grid-connected as well as in stand-alone power plants.

An accurate and efficient modelling strategy for the ESS is essential to optimize the management of the PV system as well as to improve the design of electronic and control systems.

Modelling of batteries can be performed in several ways depending on the particular application and on the fixed goal: voltage estimation at a given current rate, SOC estimation, SOH estimation, frequency response or other targets. Each goal involves significant issues due to the large number of variables and environmental conditions affecting the battery behavior. In some cases, this circumstance leads to the development of complex models and algorithms which take into account the actual state of the ESS.

In the field of electrical and electronic engineering, models of battery packs fall into two main categories:

- short time horizon: models for the estimation of voltage and current at battery terminals, typically ECM, see Section 6.2;
- long time horizon: algorithms for the estimation of the actual state of the battery, in particular evaluation of SOC and SOH, see Section 6.3.

Despite of their formal classification, these categories are often mixed together. For example, accurate ECM have some parameters whose value depends on the SOC that is necessary to estimate continuously. Another example is related to some SOC estimation algorithms which incorporate an ECM; in fact, the estimation of voltage terminals is necessary for parameters tuning.

6.2 Equivalent Circuit Modelling

The most common ECM for batteries are presented in [87]-[89]. These papers provide a review of the existing literature. It is easy to note that a fully comprehensive analysis about battery ECM is not feasible due to the large number of possible approaches.

In this thesis, an exhaustive comparison of different ECM for electrochemical ESS is presented using a multi-criteria approach and an extensive experimental validation. This study highlights advantages and limits of the most common circuit models, taking into consideration main applications as well as different technologies in particular VRLA, Li-Ion and Ni-MH batteries.

6.2.1 Main ECM for ESS: features and performance comparison

Table 2 is a list of the main ECM for ESS. The names usually assigned in literature for these ECM and used in this thesis are in Table 3.

Many other variations of ECM can be found in literature, but such modifications usually fall into categories in Tables 2-3.

The simplest circuit used to model the behavior of a real ESS (model A in Table 2) is obtained by the series connection of a constant voltage generator E_0 and a resistor R_i [90], [91]. The generator E_0 represents the no-load voltage referred to the full charge state (SOC=100%). The resistor R_i models the voltage drop due to internal and terminals resistances [28], [92]-[94].

Higher accuracy can be obtained by taking into account the variation of R_i with SOC (model B in Table 2) occurring for most of battery technologies [91], [98]. A popular approach used to calculate the variation of R_i is the equation:

$$R_i(SOC) = \frac{R_{i,SOC=100\%}}{SOC^k} \quad (12)$$

where k is a constant parameter, ranging between 1.05 and 1.30, depending on the actual current rate C_R .

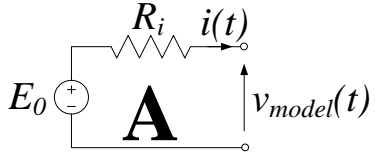
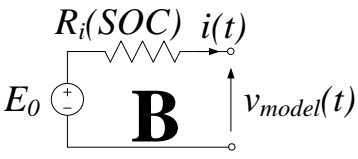
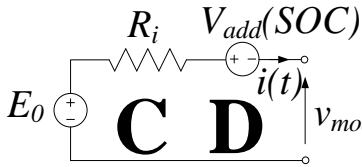
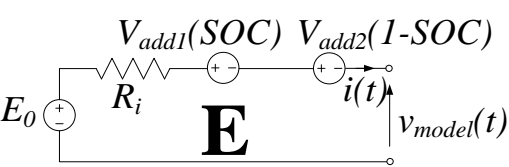
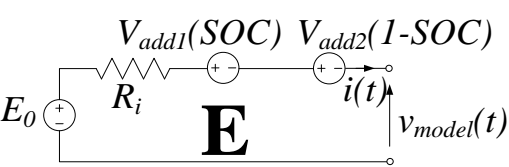
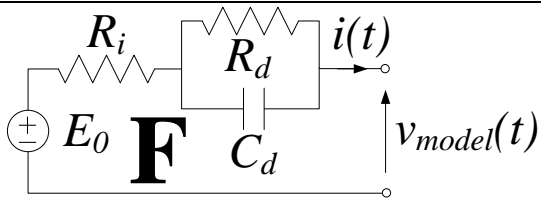
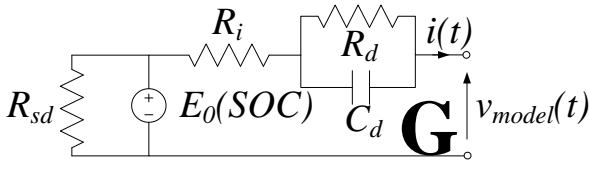
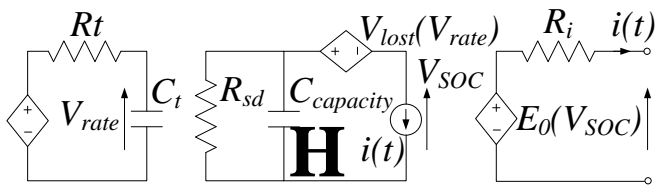
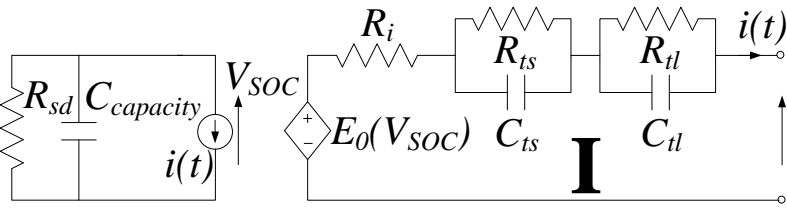
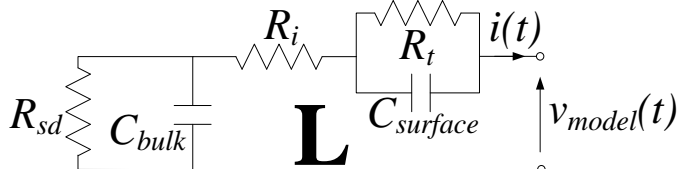
ID	Equivalent circuit
A	
B	
C	
D	
E	
F	
G	
H	
I	
J	See [91], [95], [96]
K	See [91], [97]
L	

Table 2. ECM for battery packs

ID	Name
A	Basic
B	Basic R_{soc}
C	Sheperd
D	Unnewehr
E	Nernst
F	RC
G	Thevenin
H	Runtime
I	Runtime IV
J	Tremblay et al.
K	Jackey et al.
L	Randles

Table 3. Names usually assigned to the ECM in Table 2. Together with ID, such names are used in this thesis to refer to models

Models C, D, E, in Table 2 come from Sheperd, Unnewehr and Nernst stoichiometric formulations. These mathematical models can be represented in the form of ECM placing a V_{add} voltage generator in series with the voltage generator E_0 and the resistor R_i . Voltage V_{add} is a function of the actual SOC.

Another ECM for ESS is the RC linear model (model F in Table 2). The RC network R_d-C_d models the transient behaviour of the ESS during current steps [90], [91], [99]. In some applications the real ESS behaviour complies with several dynamics, therefore the introduction of extra RC networks is required to increase accuracy in voltage estimation [99], [100]. A modified version of the previous model is the Thevenin model (model G in Table 2) [91], [101], [102]. In this case, a functional relation between the no-load voltage E_0 and the actual SOC is introduced. Moreover, an additional resistor R_{sd} is sometimes included in parallel with E_0 generator to model the self-discharge phenomena [102], [103].

In the so-called “runtime models” (model H in Table 2) the electric circuit is divided in two or more sections [23], [91], [98]. Typically, a first section is related to the voltage response depending on the forced current, similarly to the models cited above. A secondary section provides the SOC estimation, evaluated as the voltage on a capacitor $C_{capacity}$ whose capacitance value depends on actual ESS capacity i.e. on SOH.

In 2006 Chen and Rincon-Mora proposed an advanced runtime model capable of

predicting runtime and current-voltage (IV) performance while reducing the inherent complexity (model I in Table 2) [91], [104]. Such model allows to predict runtime operation, steady state and transient response of the battery.

In recent years, the main software houses have developed some battery models to integrate into simulations platforms used in the field of electrical and electronics engineering. An overview of these models is in [91]. In [95], [96] Tremblay et al. proposed an equivalent circuit model (model J in Table 2) derived from [105]. For instance, the function used to describe the charge of lead acid batteries is:

$$f_{lead_acid}(it, i^*, i, Exp) = E_0 - K \cdot \frac{Q_t}{it + 0.1 \cdot Q_t} \cdot i^* - K \cdot \frac{Q_t}{Q_t - it} \cdot it + \\ + Laplace^{-1} \left(\frac{Exp(s)}{Sel(s)} \cdot \frac{1}{s} \right) \quad (13)$$

where it is the extracted capacity, i^* is a function representing the low frequency current dynamics, Exp is a function describing the exponential zone, K is the polarization resistance, Q_t is the maximum battery capacity, $Sel(s)$ has value 1 during charge process. Another ESS model was proposed by Jackey (model K in Table 2) with the purpose to reduce the number of parameters to identify [97]. In such a case, the battery is modeled as a series resistor R_i and a charge-dependent voltage source, whose voltage E is calculated as:

$$E = E_{0, SOC=100\%} \cdot \left[1 - \left(\frac{\alpha \cdot (1-x)}{1 - \beta \cdot (1-x)} \right) \right] \quad (14)$$

where $E_{0, SOC=100\%}$ is the fully-charged battery voltage and x is the ratio of the ampere hours left to the number of ampere hours for which the battery is rated. The constant terms α and β are used to match specific points in the no-load curve $E_0(SOC)$.

The peculiarity of the equivalent circuit models category named as ‘‘Randles models’’ (model L in Table 2) is that some of the circuit parameters are time-varying parameters. In fact, their value depends on the actual battery state (i.e. actual SOC and SOH) as well as on external conditions (such as imposed current rate and temperature). The bulk capacitance C_b represents the main charge store while the voltage across its terminals is an indicator of SOC. SOH deterioration is calculated from the decrease in

the value of C_b capacitance. Kalman Filter (KF) is usually used for parameters tuning [98], [106], [107].

Models peculiarities and information collected from in-depth literature review are presented in Table 4.

Models (*)		Requirements or performance (**)												
Category	ID	1	2	3	4	5	6	7	8	9	10	11	12	13
Basic models	A	+	-	-	-	-	-	-	-	-	-	-	-	-
	B	+	-	-	-	-	-	-	-	-	-	-	-	-
Sheperd, Unnewehr and Nernst	C	+	-	-	-	-	-	-	-	-	-	-	-	-
	D	+	-	-	-	-	-	-	-	-	-	-	-	-
	E	+	-	-	-	-	-	-	-	-	-	-	-	-
RC linear models	F	+	+	-	-	-	-	-	-	-	-	-	-	-
	G	+	+	-	+	+	-	-	-	-	-	-	-	-
Parameter-varying models	H	+	+	-	+	+	-	+	-	-	+	-	-	-
	I	+	+	+	+	+	-	+	+	-	+	-	-	-
	J	+	+	-	-	+	-	+	+	+	-	-	-	-
	K	+	-	-	+	+	-	-	-	-	+	-	-	-
	L	+	+	-	-	+	+	+	+	-	-	+	+	-
Examples of other models in literature	M	+	+	-	-	+	-	+	+	+	+	-	-	+
	N	+	+	-	-	+	-	+	+	+	+	-	-	+
	O	+	+	+	-	+	+	-	-	-	+	-	+	+
	P	+	+	+	-	+	-	-	-	-	+	-	+	+
(*) Model ID, A to H A = Basic [23], [91], [98], [108] B = Basic R_{soc} [23], [98] C = Sheperd [90], [101], [105] D = Unnewehr [90], [101] E = Nernst [90], [101], [109] F = RC [91], [100], [106], [110] G = Thevenin [98], [101]-[103] H = Runtime [91], [98], [111], [112]					(*) Model ID, I to P I = Runtime IV [91], [98], [104] J = Tremblay et al. [91], [95], [96] K = Jackey et al. [91], [97] L = Randles [98], [106], [107] M = CIEMAT [108] N = Monegon [108] O = Impedance [113], [114] P = Third order [115], [116]									
(**) Requirements and performance in modelling physical phenomena + = Requirement fulfilled - = Requirement partially fulfilled or not fulfilled 1 = Voltage estimation during continuous current discharge [90] 2 = Transient behavior, large period pulsed current [100], [103], [110] 3 = Transient behavior, short period pulsed current [100], [103], [110] 4 = Self-discharge 5 = Charge operation modelling [96] 6 = SOC estimation provided by adaptive parameters [106], [107] 7 = Real-time parameters estimation [91], [104], [117] 8 = Real-time IV curve prediction [91], [104], [117] 9 = Exponential operation area [95], [108] 10 = Peukert effect [118] 11 = Memory effect [119] 12 = SOH estimation provided by adaptive parameters [107] 13 = Temperature effect [108], [117]														

Table 4. Models comparison based on main requirements and performance

Main physical phenomena occurring in a real ESS are reported in the same Table and linked to the analyzed models. Obviously, top performing models involve big computational efforts for both parameters identification and model implementation. On the contrary, models featuring a simple circuital structure provide less accurate information on the status of ESS. However, no model is capable to fully match all the listed requirements and performance.

The aforementioned models are compared also in terms of applications and technologies as displayed in Fig. 12. It is worth noting that some models categories show a good versatility given by the capability to track the status of the ESS in different conditions. This fact is confirmed by Fig. 13, in which the models are classified considering the dynamics related to main goals in ESS modelling. On the horizontal axis, for sake of example, the electrochemical phenomena occurring in LA batteries at different dynamics are reported [106].

It can be noted that only few models match a significant number of goals in a large range of dynamics. Simpler models can be effectively exploited only to estimate the voltage waveform in the context of limited dynamics.

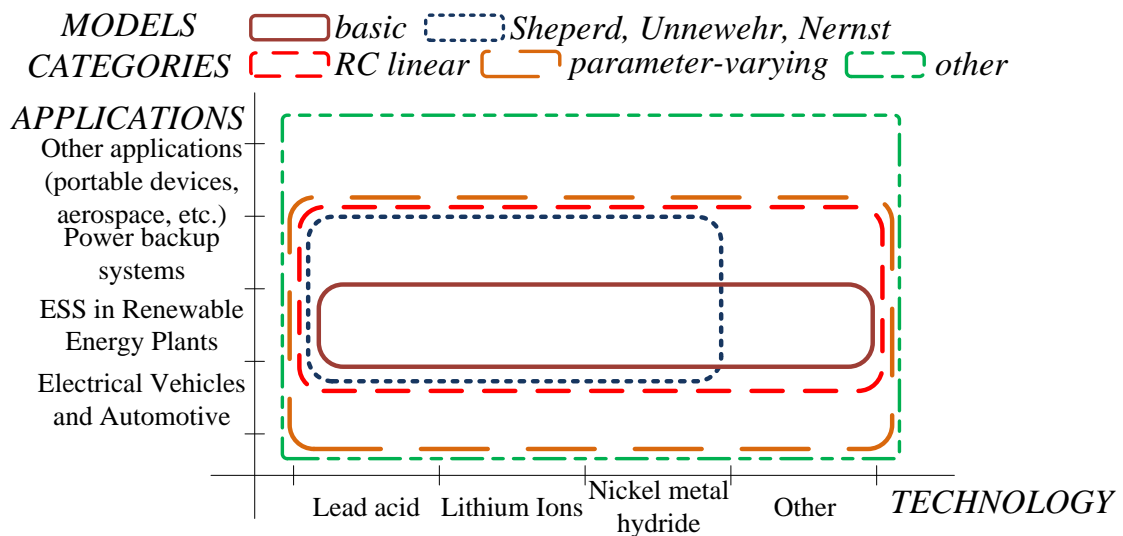


Figure 12. ECM comparative analysis based on applications and technologies

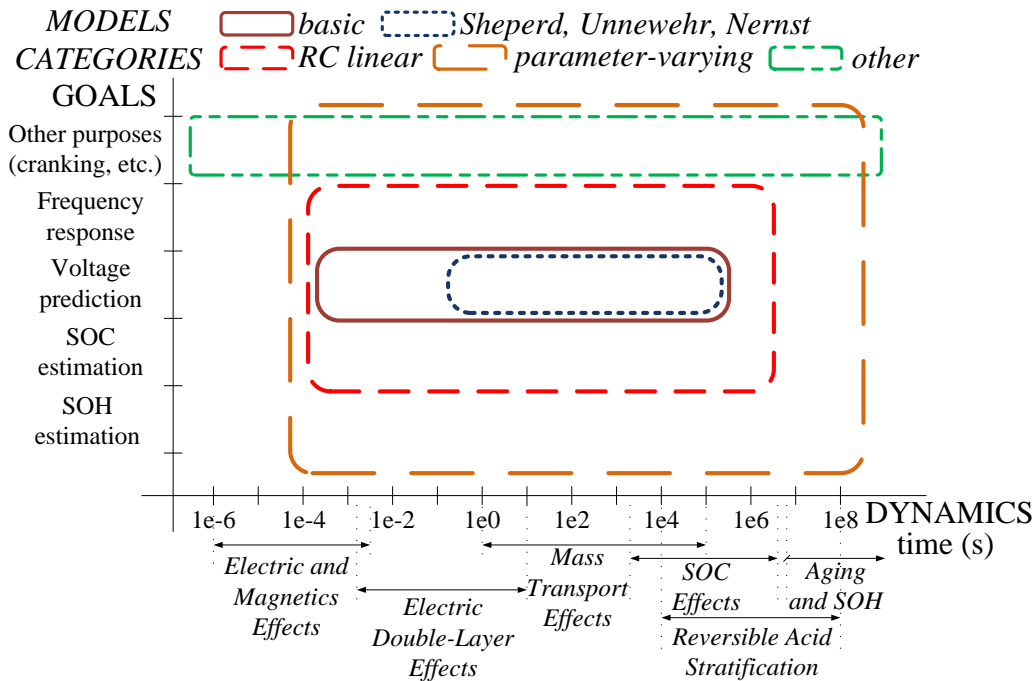


Figure 13. ECM comparative analysis based on modelling goals and dynamics

About the identification of parameters for the ECM of batteries, the method used in this work is adjusted to the one used for the entire PV system, see Section 8.2.

Matching the information coming from the literature review and the results of experimental tests described in Section 9.4, it is possible to state that, in most cases, Thevenin, Runtime and Randles models are the best compromise between performance and complexity.

6.3 SOC and SOH estimation algorithms

SOC and SOH are the main parameters for the evaluation of the actual state of a battery.

SOC is an indicator of the amount of energy available in the battery in comparison to its maximum charge state. SOH is an index of the battery aging in comparison to its native condition, it is basically used to determine the remaining service life of the ESS [23]. For example, a new fully charged battery has 100% SOC and 100% SOH. Then,

during operating cycles, SOC will describe in real-time the percentage of remaining charge while SOH will represent the full charge that the aged battery can hold [90].

A comprehensive classification of SOC and SOH estimation methods is complicated due to the large number of possible approaches described in literature. Some reviews are [120], [121]. The main methods and their characteristics are summarized in Table 5.

Method	SOC SOH	Pros	Cons
Full discharge test (e.g. IEEE Standard)	SOC SOH	Simple, standard	Off-line, recharge necessary, aging effects caused by test
Open Circuit Voltage (OCV) methods	SOC	Simple	Off-line, require long waiting time
Terminal voltage analysis	SOC SOH	Simple, on-line	Inaccuracy if operating conditions differs from rated ones
Internal resistance	SOC SOH	Simple	Inaccuracy, sensitivity to measurement noise
Coulomb Counting Method (CCM)	SOC	Simple, on-line	Integration drift, sensitivity to parameter uncertainty
Genetic algorithms, neural network, fuzzy logic	SOC SOH	Accurate, on-line	Complicated procedures, slow convergence
Two pulse load test	SOC SOH	Simple	Off-line, Inaccuracy if operating point differs from rated one
Real-time model-based estimation methods	SOC SOH	Accurate, on-line	Require on-line identification processes
KF (and KF variants)	SOC SOH	Accurate, on-line	Computational effort, sensitivity to circuit model accuracy and to measurements noise
Hybrid / mixed methods	SOC SOH	Accurate	Sensitive to model accuracy and to measurements noise

Table 5. Features of the main SOC and SOH estimation methods

For the purpose of reaching a satisfactory precision in SOC and SOH estimation while avoiding too large computational resources, the best option is usually represented by real-time model-based algorithms. Basically, these algorithms are built from control system theory and incorporate a ECM of the battery. The error between the measured quantities and the ones provided by the ECM is the key parameter for the working

principle of the algorithm. In fact, as soon as the state estimation, performed by the algorithm, approaches the real state, this error becomes close to zero [122].

6.4 PI-based observer algorithms

One of the real-time model-based algorithms developed in this work belongs to a particular category represented by PI-based observers.

Performing real-time parameters tuning, PI observers reach a good accuracy. Their main advantage is the low complexity and the ease of integration in control systems.

Effective examples of PI-based observers used in ESS state estimation are in [123], [124]. In [123], Thevenin ECM models the battery. This ECM allows for simple implementation but could lead to large errors if operating conditions differ from the rated ones. A single RC network is included to track dynamic behavior implying that ESS can be properly modeled only within a limited frequency range. No information about actual SOH is available.

In [124], the proposed SOC estimation method is a combination of an open-loop current integrator and a PI-based observer. It also uses a drifting current corrector to restrain the influence of the drifting current. Unfortunately, in several cases the implementation of mixed algorithms could be too expensive from a computational point of view. Again, no information about SOH is provided.

The PI observers described in this thesis come from an extensive research activity carried out for years. The result is the creation of innovative algorithms able to overcome the issues found in previous approaches. In particular, in [125] an advanced parameter-varying circuit model, Fig. 14, is inserted into the PI observer in Fig. 15. ECM parameters are tuned in real time by the same observer. The analysis of circuit parameters variation during battery operation leads to simultaneous estimation of SOC and SOH by means of simple formulas. This is also the case in variable working conditions and in presence of disturbance. Moreover, the start-up identification procedure is very simple.

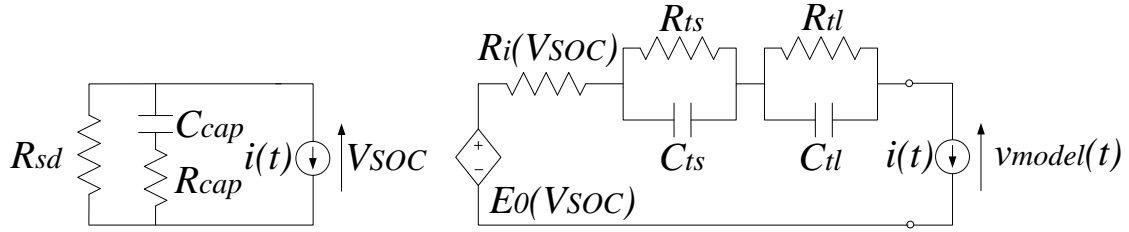


Figure 14. Runtime circuit model for the PI-based observer algorithm in [125]

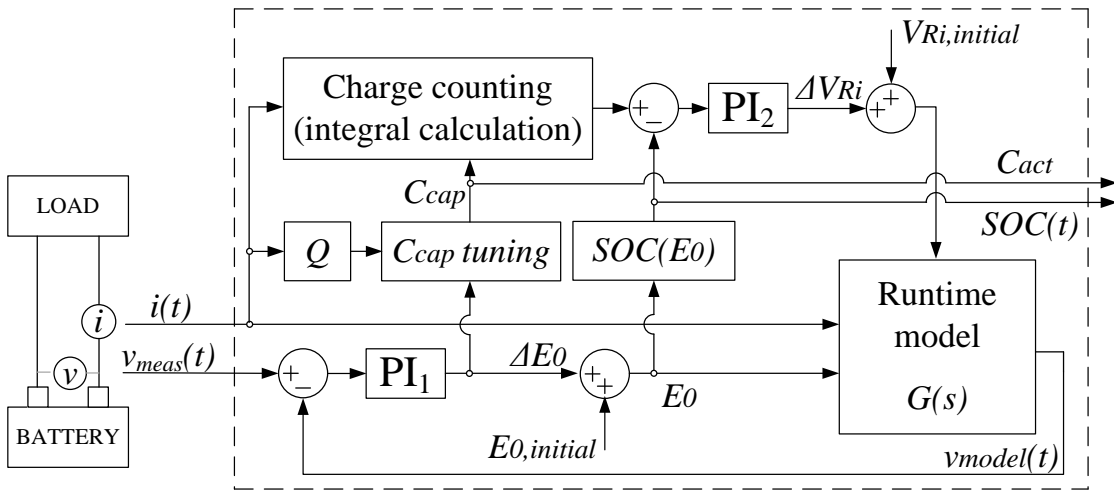


Figure 15. Real-time PI-based observer scheme in [125]

The validation is carried out through comprehensive experimental tests, reported in [125], confirming the adaptability of the algorithm to a wide number of real applications in different operating conditions.

From this initial works, a variant has been created for the scope of this thesis focusing on the limitation of computational effort. This variant is described in Section 6.5.

For the same purpose dealing with complexity reduction, an additional alternative method consisting in a mixed algorithm has been developed. The latter is described in Section 6.6.

6.5 ESS state estimation algorithm 1

The ECM used in this first estimation method is in Fig. 16. The PI-based observer algorithm, shown in Fig. 17, is a modified version of the PI-based observers described in [125], [126]. Basically, the real-time estimation of the observed parameter OCV is used to estimate SOC using the curve $SOC(OCV)$ provided by the battery manufacturer or identified through preliminary tests [126]. To improve this estimation taking into account the relaxation phenomena [127], [128], a prediction function has been integrated.

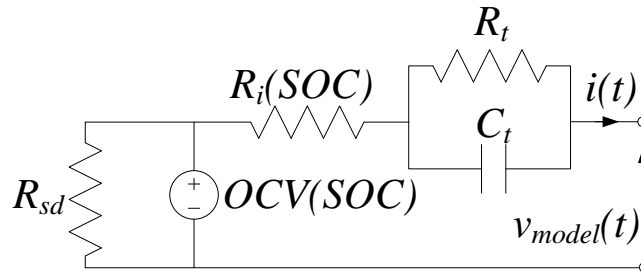


Figure 16. Thevenin ECM being part of the algorithm 1 for ESS state estimation

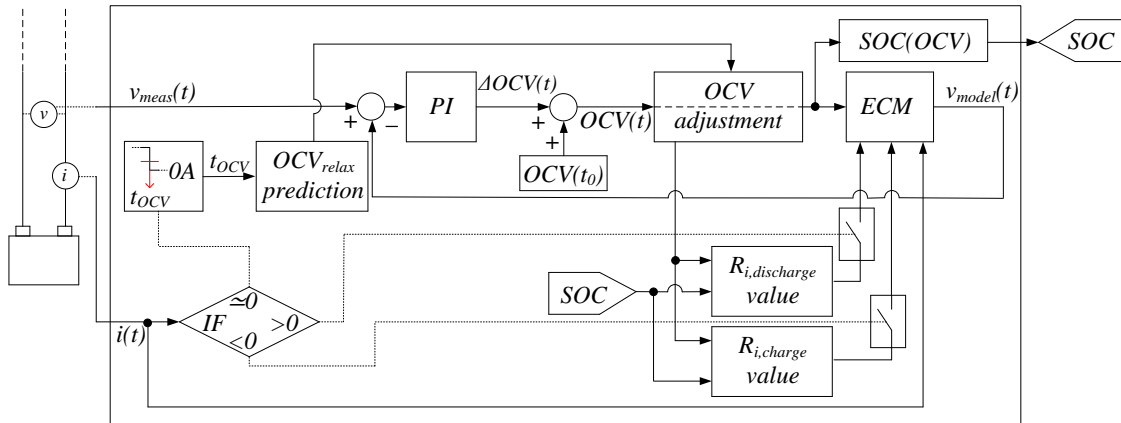


Figure 17. PI-based observer scheme including OCV_{relax} prediction function, algorithm 1 for ESS state estimation

As regards the identification of resistance R_i , that is crucial for the accuracy level of the final estimation, a polynomial approximation of the $R_i(SOC)$ curve is exploited.

Such curve is created from a series of preliminary experimental measurements on the battery under test.

About the relaxation voltage, the related issue is that OCV value becomes an accurate index of SOC only when the battery remains in open circuit conditions (zero current) for a very long time going to an electrochemical equilibrium [129]. On the contrary, just after the removal of a load, the use of OCV value to calculate the SOC from the $SOC(OCV)$ curve determines an error in estimation. Unfortunately, the simple idea to wait long resting time to get OCV_{relax} in order to reduce such error is not feasible in many real applications.

In the proposed algorithm, the need for a long rest time is overcome by creating a polynomial prediction function which calculates the expected relaxation voltage from the OCV_{10s} . The latter quantity is the OCV recorded 10 seconds after the time instant in which the current becomes zero (i.e. 10 seconds after the end of the previous charging or discharging process). To create the polynomial prediction function, preliminary experimental tests are required, see Section 9.5.

From Fig. 17, one question that arises is how to integrate practically the PI-based observer with the OCV_{relax} polynomial prediction function taking into account the delay of 10 s necessary to measure the OCV_{10s} . To do this, the approach is essentially based on the Boolean logic. Looking at a generic current curve i_{meas} measured during a discharge, as the one represented in Fig. 18, value 1 is assigned to the high current state and value 0 to the null one. The same assignment is also made for the time-shifted current curve i_{meas_d10s} .

Considering the logical values corresponding to the current states for each instant, the Boolean operator OR is applied to the current waveforms. Then, through the NOT Boolean operator, the OCV_{relax} prediction trigger is obtained as shown in Fig. 18. This last waveform determines the activation of the voltage relaxation prediction function within the estimation algorithm. In particular, the trigger is active (state 1) starting from 10 s after the current becomes zero and until the current reappears. On the contrary, during the charging or discharging processes and up to 10 s from their end, the PI-based observer is active (state 0).

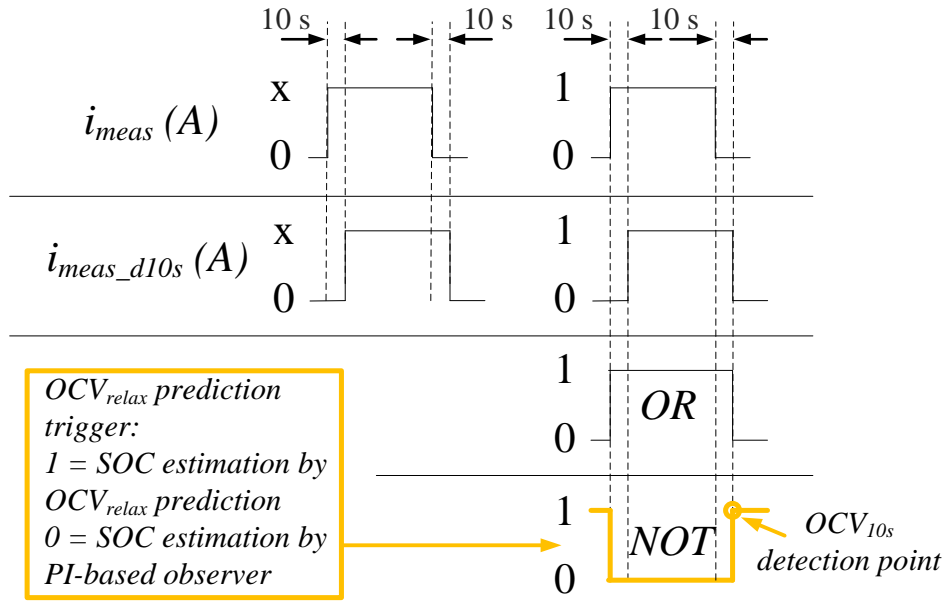


Figure 18. Identification of the OCV_{10s} detection point for the implementation of algorithm 1

In such a way, the relaxation voltage prediction function is thus activated (calculated) exactly 10 s after the end of the last charge or discharge. The OCV_{relax} value now obtained, calculated from the prediction function, is the updated and corrected value of the relaxation voltage exploitable for the calculation of SOC.

The function deriving from the polynomial approximation of the $OCV(SOC)$ curve is implemented in look-up tables present into the algorithm (" OCV_{relax} prediction" block in Fig. 17).

It is important to pay attention to the switching phases in which the PI-based observer and the prediction function become active respectively. In this regard, reset logic has been adopted for the integral component.

About the evaluation of SOH, it is calculated according to [125] thanks to the estimation of SOC provided by the PI observer and to the charge exchange calculated by equation (15) occurring during a charge or a discharge process:

$$Q_{[t_1, t_2]} = \int_{t_1}^{t_2} i(t) \quad (15)$$

Polynomial approximations for the $R_i(SOC)$ curve and for OCV_{relax} prediction function should be identified for each battery under test. In case of more batteries belonging to the same production batch, identification could be carried out for one battery and extended to the others.

In Section 9.5, focused on experimental validation, readers can find more details about the implementation of the algorithm and of its relaxation voltage prediction function.

6.6 ESS state estimation algorithm 2

This second algorithm was developed following the main target to estimate SOH. Anyway, the estimation of SOC is practically concomitant.

The idea is to investigate the opportunity to merge two basic approaches in order to create a mixed algorithm with a large versatility, exploitable for the main electrochemical technologies as VRLA, Li-Ion and Ni-MH. The merged basic approaches are CCM and parameter-varying ECM. The motivation of this matching is highlighted in Table 6.

Basic methods	Main advantages [130]-[132]	Main disadvantages [130]-[132]	Expectations from merging
CCM	Simple Real-time Low complexity Low computational effort	Inaccuracies in case of high current rate Integration drift Sensitivity to parameter uncertainty	Good accuracy in SOH estimation Low complexity Acceptable computational effort Automatic parameter tuning in case of varying operating conditions
Parameter-varying ECM	Accuracy Integration of estimation algorithms Real-time parameter tuning	Requires advanced estimation algorithms High computational effort	

Table 6. Basic methods combined in the mixed algorithm i.e. the method 2 for ESS state estimation

About the CCM method, which is the first component of the mixed algorithm, its basic formulation is the well-known formula:

$$SOC(t_1) = SOC(t_0) - \frac{1}{C_{act}} \int_{t_0}^{t_1} i_{meas}(t) dt \quad (16)$$

In this formula, i_{meas} is the measured current and C_{act} is the actual capacity. The ratio between C_{act} and the rated capacity C_n is the SOH:

$$SOH = \frac{C_{act}}{C_n} \quad (17)$$

Performing simple calculations and considering a finite time interval $[t_0, t_1]$, C_{act} can be calculated as a function of the SOC variation and of the total charge Q due to a charging or to a discharging process, equation (18). An efficiency index η is usually added to take into account temperature, current rate, measurement errors, Peukert effect, dissipative phenomena during charge and so on [133], [134].

$$C_{act} = \frac{\int_{t_0}^{t_1} i_{meas}(t) dt}{SOC(t_0) - SOC(t_1)} = \frac{Q_{[t_0, t_1]}}{\Delta SOC_{[t_0, t_1]}} \rightarrow C_{act} = \frac{Q_{[t_0, t_1]}}{\Delta SOC_{[t_0, t_1]}} \eta(t) \quad (18)$$

It is worth noting that, in this case, the estimation of SOC at time instants t_0 and t_1 cannot be longer performed using formula (16) but it is necessary to exploit other methods. In particular, a good accuracy can be obtained using the no-load curve SOC(OCV) [130]. Value of OCV should be always referred to the electrochemical relaxation state (OCV_{relax}) but the long waiting time that is required to reach such state represents an obstacle in real applications.

Similarly to the state estimation method 1 presented in the previous Sections, a prediction function for the OCV_{relax} can be integrated in method 2 as an additional feature to improve the final accuracy of the results. In particular, the present algorithm exploits the OCV_{10s} in case of fast dynamics as for the method 1, otherwise the value of $OCV_{quasi-relax}$ is used. This latter parameter is the OCV measured in quasi-relaxation state meaning that the electric transient effects, occurring at the end of charging or discharging process, is considered as finished despite the electrochemical phenomena are not completely concluded. The inaccuracy caused by this approximation can be neglected in most cases.

The implementation of CCM formulation is not able to provide a stable SOH estimation. For the sake of example, Fig. 19 shows the SOH values obtained for a 51.2 V 40 Ah LiFePO₄ battery pack during discharge processes at different SOC values and current rates. The results are not consistent. In fact, the differences in terms of SOH estimations are too large. Finally, the CCM is a very simple approach requiring a low computational effort, but it is necessary to integrate another method to obtain a satisfactory accuracy in SOH estimation.

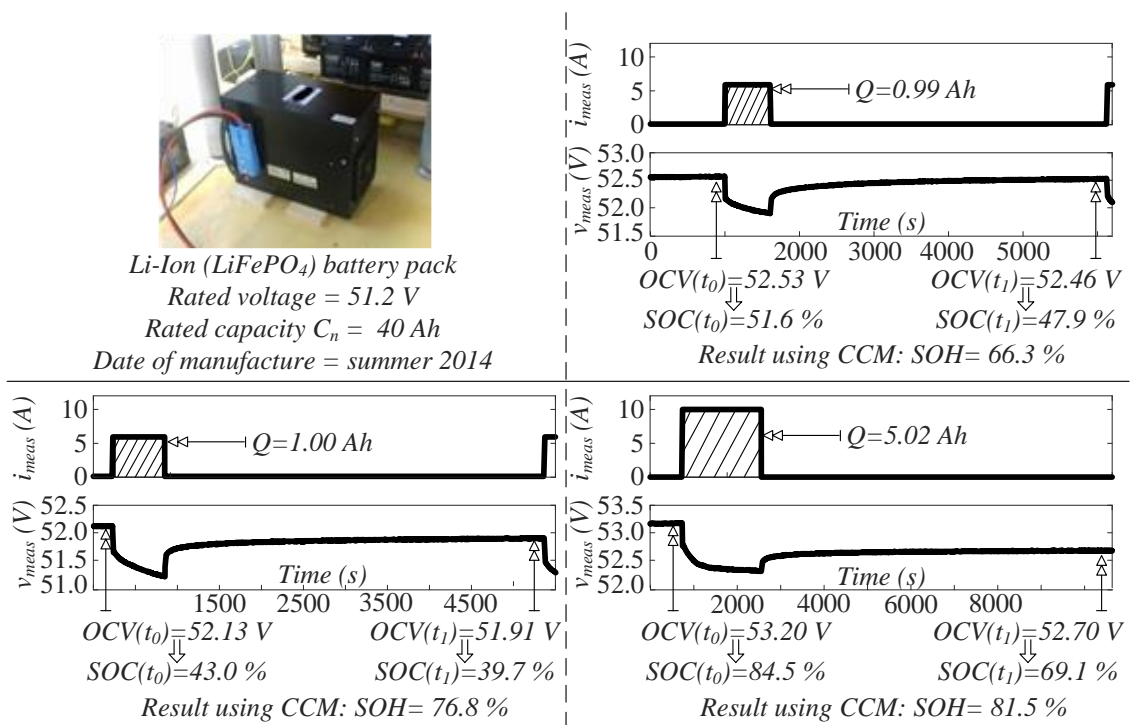


Figure 19. Estimation of SOH for a Li-Ion battery pack through the implementation of CCM in different discharging operations. The $OCV_{quasi-relax}$ (in quasi-relaxation state) is used to calculate the SOC on the basis of no-load curve $SOC(OCV)$

About the second component belonging to the mixed algorithm, ECM is the parameter-varying Randles topology shown in Fig. 20.

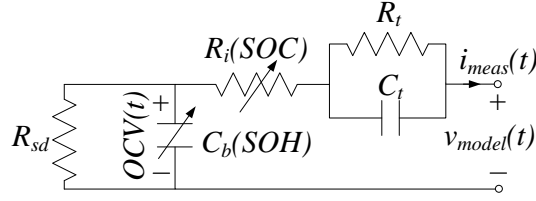


Figure 20. The parameter-varying Randles ECM included in the proposed mixed algorithm

The resistance R_i is function of SOC, this relationship is described through a polynomial function. On the contrary, the influence of current rate is usually neglected [135], [136]. Parameters in the RC branch R_t and C_t are used to model the transient phenomena, typically their value is assumed to be constant over time [132], [135]. The large resistance R_{sd} is introduced to take into account self-discharge phenomena. The capacitance C_b (measured in F) is proportional to the actual capacity C_{act} by means of formula (19):

$$C_b = \frac{C_{act} \cdot 3600}{OCV_{max} - OCV_{min}} = \frac{SOH \cdot C_n \cdot 3600}{OCV_{max} - OCV_{min}} \quad (19)$$

where the voltages OCV_{max} and OCV_{min} correspond to SOC = 100% and SOC = 0%, respectively.

The voltage across C_b is the OCV . Real-time tuning of ECM parameters, based on the comparison between v_{meas} and v_{model} , allows to reach a precise estimation of C_b so that C_{act} and SOH can be estimated. Unfortunately, if a big accuracy is required, such tuning implies the implementation of estimation algorithms having a significant complexity [130].

The CCM and ECM approaches are finally mixed into a unified algorithm in order to benefit from their advantages while compensating their drawbacks. In particular, the ECM approach improves the accuracy of CCM while CCM reduces the overall computational effort related to ECM. The flow chart in Fig. 21 shows such mixed algorithm. Tuning of the efficiency index η is executed by reversing formula (18) belonging to CCM but using data provided by ECM from time to time.

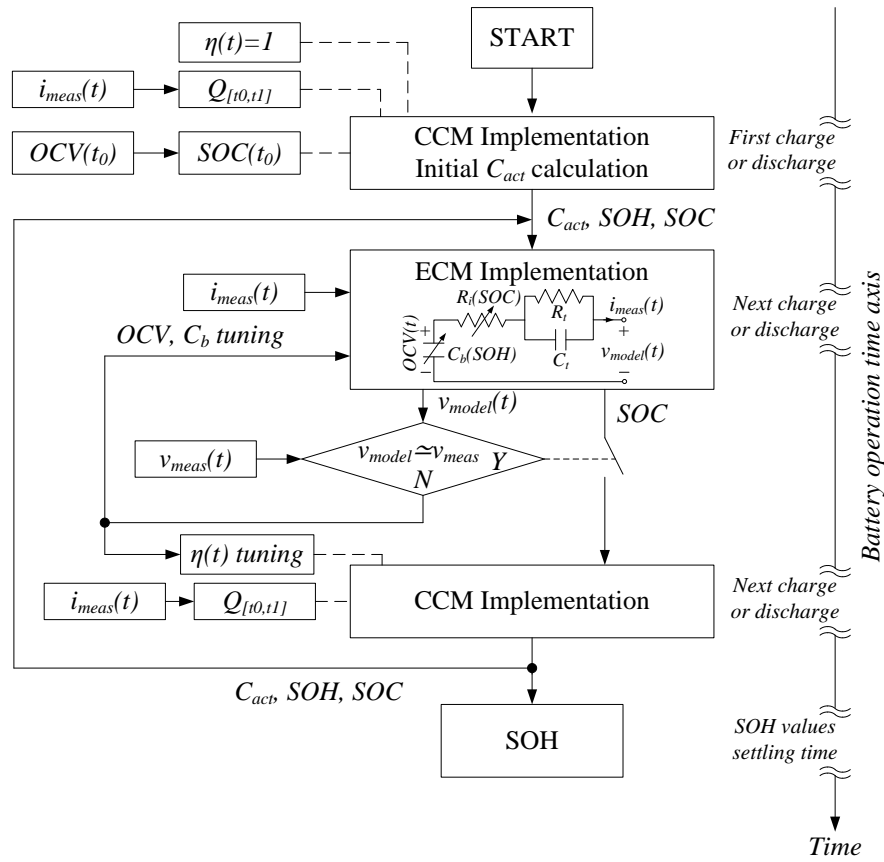


Figure 21. Flow chart of the proposed mixed algorithm i.e. algorithm 2 for ESS state estimation

In Section 9.6 focused on experimental validation, readers can find more details about the implementation of the algorithm.

6.7 Calculation of PC and EC

Parameters PC and EC are fundamental for the scope of this thesis. In fact, they represent the link between models of the ESS and of the PV plant.

PC is the power level tolerable by the battery during a charge or a discharge for a given time horizon Δt specified from time to time for the particular application and working cycle. The value of PC depends mainly on SOC, SOH and current rate. It is usually referred to specific limits of SOC (SOC_{max} and SOC_{min}) and of terminal voltage ($v_{bt,min}$ and $v_{bt,max}$).

The product between PC and Δt is the EC i.e. the energy that can continuously flow in the ESS for the assigned time interval Δt without overcoming the fixed SOC and voltage thresholds.

The accuracy in PC calculation is proportional to accuracy in SOC and SOH estimation. The formulation used here for the calculation of PC comes from [24], but it is adapted to the context of this work. Basic formulas are:

$$\text{Charge: } i_{bt,ch,PC} = \frac{SOC - SOC_{max}}{\eta_{ch} \cdot \Delta t} \cdot SOH \cdot C_{act} \Rightarrow PC_{bt,ch} = v_{bt,max} \cdot i_{bt,ch,PC} \quad (20)$$

$$\text{Discharge: } i_{bt,ds,PC} = \frac{SOC - SOC_{min}}{\Delta t} \cdot SOH \cdot C_{act} \Rightarrow PC_{bt,ds} = v_{bt,min} \cdot i_{bt,ds,PC} \quad (21)$$

where the subscripts *max* and *min* refer to the thresholds fixed for SOC and voltage. In charge process the Coulomb efficiency factor η_{ch} depends on the actual current level [133], [134]. This factor is usually neglected for the discharge process.

With special reference to the maximum charging current for ESS with lead acid batteries, in some cases the PC formulation can be too optimistic with respect to the thresholds fixed by the battery manufacturer. More generally, the analysis regarding the assessment of PC and EC during charge process needs to be matched with the recommendations of the battery manufacturers.

In Section 9.7 focused on validation, readers find experimental example of calculation for PC and EC.

Chapter 7 - Modelling of converters, transformers and utility grid

7.1 Power converters models

In literature, power converters models in PV applications are designed in different ways. In case of stringent requirements about the computational effort for energy assessment in long-term time horizon as for this work, the common modelling approach for DC/DC converters and for their control system is the state-space averaging method. Some examples are in [137]-[139]. On the contrary, grid connected inverters are usually modeled using relationships derived from energy balances [80], [139], [140] or from equivalent circuits [94]. In the latter case, the electrical quantities are sometimes expressed in form of phasors [89], [141].

This Section refers to a specific multi-stage topology represented in Fig. 22. This topology has been chosen as basic configuration for a multi-stage conversion system in order to better explain the novelty of this work.

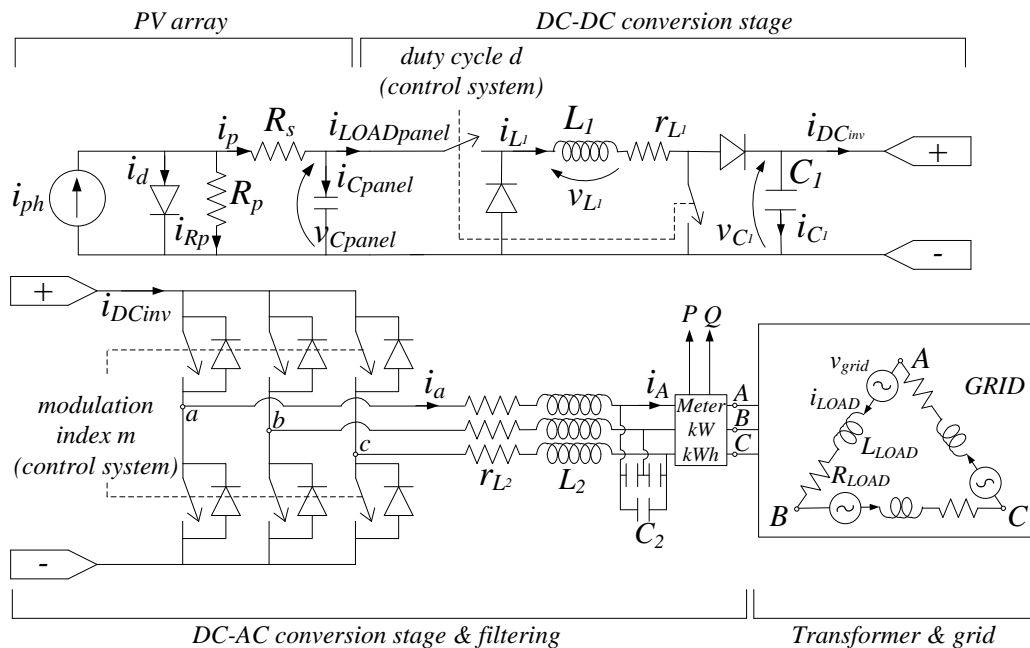


Figure 22. Block diagram of a grid-connected PV system with multi-stage conversion system

Focusing on DC/DC converter and supposing the same be a single block with a fictitious voltage source v_{in} and a fictitious load R as in Fig. 23, its state-space average form can be obtained as in [137].

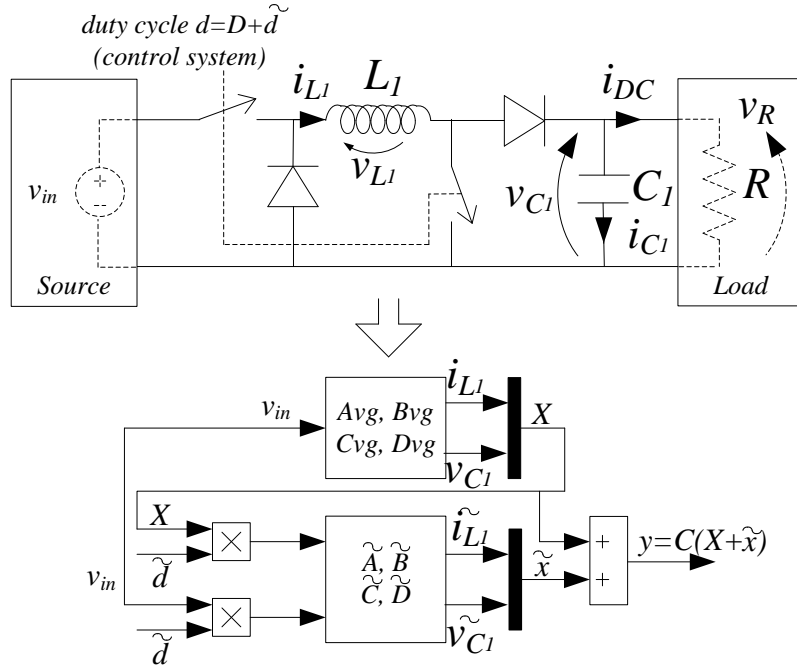


Figure 23. DC/DC converter basic topology and its state-space form including duty cycle variation

The variation of duty cycle d due to the implementation of the MPPT control strategy can be obtained as a perturbation \tilde{d} [138] superimposed to the steady-state duty cycle D , starting from a basic state-space average model:

$$\begin{cases} \dot{X} = \bar{A}_{DC} X + \bar{B}_{DC} u \\ Y = \bar{C}_{DC} X + \bar{D}_{DC} u \end{cases} \quad (22)$$

where:

$$\bar{A}_{DC} = A_{DC_{ON}} d + A_{DC_{OFF}} (1-d) \quad (23)$$

$$\begin{aligned}
A_{DC_{ON}} &= \begin{bmatrix} 0 & 0 \\ 0 & -\frac{1}{RC_1} \end{bmatrix} & A_{DC_{OFF}} &= \begin{bmatrix} 0 & -\frac{1}{L_1} \\ \frac{1}{C_1} & -\frac{1}{RC_1} \end{bmatrix} \\
\bar{B}_{DC} = B_{DC_{ON}} d + B_{DC_{OFF}} (1-d) & & B_{DC_{ON}} &= \begin{bmatrix} \frac{1}{L_1} \\ 0 \end{bmatrix} & B_{DC_{OFF}} &= \begin{bmatrix} 0 \\ 0 \end{bmatrix}
\end{aligned} \tag{24}$$

$$\bar{C}_{DC} = C_{DC_{ON}} = C_{DC_{OFF}} = \begin{bmatrix} 1 & 0 \\ 0 & 1 \end{bmatrix} \quad \bar{D}_{DC} \quad \text{null} \tag{25}$$

The extension of this state-space system, in presence of \tilde{d} , is:

$$\begin{cases} \tilde{\dot{x}} = \bar{A}_{DC} \tilde{x} + \left[(A_{DC_{ON}} - A_{DC_{OFF}}) (B_{DC_{ON}} - B_{DC_{OFF}}) \right] \begin{bmatrix} X \tilde{d} \\ v_{in} \tilde{d} \end{bmatrix} \\ \tilde{y} = \bar{C}_{DC} \tilde{x} + \left[(C_{DC_{ON}} - C_{DC_{OFF}}) X \right] \tilde{d} = \bar{C}_{DC} \tilde{x} \end{cases} \tag{26}$$

where:

$$u = U = v_{in} \quad y = Y + \tilde{y} \quad x = X + \tilde{x} \quad d = D + \tilde{d} \quad x = \begin{bmatrix} i_{L1} \\ v_{C1} \end{bmatrix} \tag{27}$$

In this way, a simple state-space average system is built to model the behavior of any DC/DC converter topology and the variation of duty cycle \tilde{d} forced by the MPPT strategy.

About the inverter and filtering stage in Fig. 24, for the sake of clarity the load is here assumed to be three-phase inductive-resistive in delta connection without grid sources.

The basic modelling approach is described in [141] exploiting a generalized state-space averaging method based on Fortescue symmetrical components and on Fourier transform. The state-space form is obtained from Kirchhoff laws:

$$\left\{ \begin{array}{l} \frac{d}{dt} \begin{bmatrix} i_{ab} \\ i_{bc} \\ i_{ca} \end{bmatrix} = -\frac{r_{L_2}}{L_2} \begin{bmatrix} i_{ab} \\ i_{bc} \\ i_{ca} \end{bmatrix} - \frac{1}{3L_2} \begin{bmatrix} v_{AB} \\ v_{BC} \\ v_{CA} \end{bmatrix} + \frac{\sqrt{3}m}{6L_2} \begin{bmatrix} v_{DC} \cos\left(\omega t - \varphi_a + \frac{\pi}{6}\right) \\ v_{DC} \cos\left(\omega t - \varphi_b + \frac{\pi}{6}\right) \\ v_{DC} \cos\left(\omega t - \varphi_c + \frac{\pi}{6}\right) \end{bmatrix} \\ \\ \frac{d}{dt} \begin{bmatrix} v_{AB} \\ v_{BC} \\ v_{CA} \end{bmatrix} = \frac{1}{C_2} \begin{bmatrix} i_{ab} \\ i_{bc} \\ i_{ca} \end{bmatrix} - \frac{1}{C_2} \begin{bmatrix} i_{LOAD_{AB}} \\ i_{LOAD_{BC}} \\ i_{LOAD_{CA}} \end{bmatrix} \\ \\ \frac{d}{dt} \begin{bmatrix} i_{LOAD_{AB}} \\ i_{LOAD_{BC}} \\ i_{LOAD_{CA}} \end{bmatrix} = -\frac{R_{LOAD}}{L_{LOAD}} \begin{bmatrix} i_{LOAD_{AB}} \\ i_{LOAD_{BC}} \\ i_{LOAD_{CA}} \end{bmatrix} + \frac{1}{L_{LOAD}} \begin{bmatrix} v_{AB} \\ v_{BC} \\ v_{CA} \end{bmatrix} \end{array} \right. \quad (28)$$

where m is the modulation index while i_{ab} , i_{bc} and i_{ca} are “virtual” line currents. The latter are calculated using common star-delta transformation equations and exploited to carry out the theoretical analysis described in this Section.

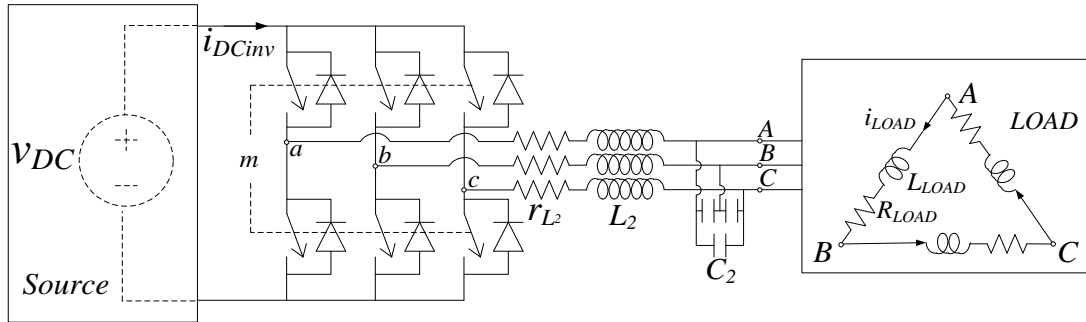


Figure 24. Grid connected inverter and AC filtering stage, basic topology

The AC currents and voltages are represented by the sum of their Fortescue symmetrical components as follows:

$$\begin{cases}
i_{ab} = (i_{ab})_{-1} e^{-j\omega t} + (i_{ab})_0 + (i_{ab})_1 e^{j\omega t} \\
i_{bc} = (i_{bc})_{-1} e^{-j\omega t} + (i_{bc})_0 + (i_{bc})_1 e^{j\omega t} \\
i_{ca} = (i_{ca})_{-1} e^{-j\omega t} + (i_{ca})_0 + (i_{ca})_1 e^{j\omega t} \\
v_{AB} = (v_{AB})_{-1} e^{-j\omega t} + (v_{AB})_0 + (v_{AB})_1 e^{j\omega t} \\
v_{BC} = (v_{BC})_{-1} e^{-j\omega t} + (v_{BC})_0 + (v_{BC})_1 e^{j\omega t} \\
v_{CA} = (v_{CA})_{-1} e^{-j\omega t} + (v_{CA})_0 + (v_{CA})_1 e^{j\omega t} \\
i_{LOAD_{AB}} = (i_{LOAD_{AB}})_{-1} e^{-j\omega t} + (i_{LOAD_{AB}})_0 + (i_{LOAD_{AB}})_1 e^{j\omega t} \\
i_{LOAD_{BC}} = (i_{LOAD_{BC}})_{-1} e^{-j\omega t} + (i_{LOAD_{BC}})_0 + (i_{LOAD_{BC}})_1 e^{j\omega t} \\
i_{LOAD_{CA}} = (i_{LOAD_{CA}})_{-1} e^{-j\omega t} + (i_{LOAD_{CA}})_0 + (i_{LOAD_{CA}})_1 e^{j\omega t}
\end{cases} \quad (29)$$

Neglecting the presence of the other components as a first approximation, the state variables are the real and imaginary parts of the direct component of each term:

$$\begin{cases}
(i_{ab})_1 = x_1 + jx_2 \\
(i_{bc})_1 = x_3 + jx_4 \\
(i_{ca})_1 = x_5 + jx_6 \\
(v_{AB})_1 = x_7 + jx_8 \\
(v_{BC})_1 = x_9 + jx_{10} \\
(v_{CA})_1 = x_{11} + jx_{12} \\
(i_{LOAD_{AB}})_1 = x_{13} + jx_{14} \\
(i_{LOAD_{BC}})_1 = x_{15} + jx_{16} \\
(i_{LOAD_{CA}})_1 = x_{17} + jx_{18}
\end{cases} \quad (30)$$

Anyway, the other components can be easily included as described in [141]. The AC currents and voltages become:

$$\begin{cases} i_{ab} = 2x_1 \cos \omega t - 2x_2 \sin \omega t \\ i_{bc} = 2x_3 \cos \omega t - 2x_4 \sin \omega t \\ i_{ca} = 2x_5 \cos \omega t - 2x_6 \sin \omega t \\ v_{AB} = 2x_7 \cos \omega t - 2x_8 \sin \omega t \\ v_{BC} = 2x_9 \cos \omega t - 2x_{10} \sin \omega t \\ v_{CA} = 2x_{11} \cos \omega t - 2x_{12} \sin \omega t \\ i_{LOAD_{AB}} = 2x_{13} \cos \omega t - 2x_{14} \sin \omega t \\ i_{LOAD_{BC}} = 2x_{15} \cos \omega t - 2x_{16} \sin \omega t \\ i_{LOAD_{CA}} = 2x_{17} \cos \omega t - 2x_{18} \sin \omega t \end{cases} \quad (31)$$

Starting from these relationships, the state-space equations of the DC/AC converter, for which (x_1, \dots, x_{18}) are the state variables, can be integrated in the model of the entire PV plant.

7.1.1. DC-link current calculation

From the description of the conversion stages, the proper matching of their modelling approaches becomes a necessity to obtain a comprehensive representation for the entire PV system. The key parameter to get this matching is the DC-link current $i_{DC_{inv}}$.

In literature, the average or Root Mean Square (RMS) value of this current is usually calculated from power balances [142] or from integral calculation [142], [143]. In some cases the latter method is applied by means of a reduced-order Fourier transform. One of the main drawbacks of these methods is the computational effort related to data storage in integrals.

In this work, a direct way has been developed to calculate the average value of the DC-link current as a linear function of the AC current components. To explain this significant achievement, the starting point is this formula:

$$\begin{aligned} i_{DC_{inv}} &= s_a i_a + s_b i_b + s_c i_c = s_a i_{ab} - s_a i_{ca} + s_b i_{bc} - s_b i_{ab} + s_c i_{ca} - s_c i_{bc} = \\ &= (s_a - s_b) i_{ab} + (s_b - s_c) i_{bc} + (s_c - s_a) i_{ca} \end{aligned} \quad (32)$$

where s is a function representing the Pulse Width Modulation (PWM) modulation signals:

$$s_a = \frac{m}{2} \cos(\omega t - \varphi_a) + \frac{1}{2} \quad s_b = \frac{m}{2} \cos(\omega t - \varphi_b) + \frac{1}{2} \quad s_c = \frac{m}{2} \cos(\omega t - \varphi_c) + \frac{1}{2} \quad (33)$$

Using prosthaphaeresis formulas to calculate the differences $(s_a - s_b)$, $(s_b - s_c)$ and $(s_c - s_a)$, and focusing on the zero-sequence component of DC-link current, the initial relationship becomes:

$$i_{DC_{inv}} = (i_{DC_{inv}})_0 = \frac{\sqrt{3}m}{2} \left[\left(i_{ab} \cos\left(\omega t - \varphi_a + \frac{\pi}{6}\right) \right)_0 + \left(i_{bc} \cos\left(\omega t - \varphi_b + \frac{\pi}{6}\right) \right)_0 + \left(i_{ca} \cos\left(\omega t - \varphi_c + \frac{\pi}{6}\right) \right)_0 \right] \quad (34)$$

The first term into square parenthesis is rewritten as:

$$\left(i_{ab} \cos\left(\omega t - \varphi_a + \frac{\pi}{6}\right) \right)_0 = (i_{ab})_1 \left(\cos\left(\omega t - \varphi_a + \frac{\pi}{6}\right) \right)_{-1} + (i_{ab})_0 \left(\cos\left(\omega t - \varphi_a + \frac{\pi}{6}\right) \right)_0 + (i_{ab})_{-1} \left(\cos\left(\omega t - \varphi_a + \frac{\pi}{6}\right) \right)_1 \quad (35)$$

thanks to the following Fourier transform property:

$$(Y(t)Z(t))_0 = (Z(t))_1 (Y(t))_{-1} + (Z(t))_0 (Y(t))_0 + (Z(t))_{-1} (Y(t))_1 \quad (36)$$

In equation (35), the second term on the right is null. On the contrary, using Euler formulas the other terms can be calculated:

$$\left(i_{ab} \cos\left(\omega t - \varphi_a + \frac{\pi}{6}\right) \right)_0 = (i_{ab})_1 \left(\cos\left(\omega t - \varphi_a + \frac{\pi}{6}\right) \right)_{-1} + (i_{ab})_{-1} \left(\cos\left(\omega t - \varphi_a + \frac{\pi}{6}\right) \right)_1 = (x_1 + jx_2) \frac{1}{2} e^{j\left(\varphi_a - \frac{\pi}{6}\right)} + (x_1 - jx_2) \frac{1}{2} e^{-j\left(\varphi_a - \frac{\pi}{6}\right)} \quad (37)$$

that is rewritten as follows:

$$\begin{aligned} \left(i_{ab} \cos\left(\omega t - \varphi_a + \frac{\pi}{6}\right) \right)_0 &= (x_1 + jx_2) \frac{1}{2} e^{j\left(\varphi_a - \frac{\pi}{6}\right)} + (x_1 - jx_2) \frac{1}{2} e^{-j\left(\varphi_a - \frac{\pi}{6}\right)} = \\ &= \frac{1}{2} \left\{ (x_1 + jx_2) \left[\cos\left(\omega t - \varphi_a + \frac{\pi}{6}\right) + j \sin\left(\omega t - \varphi_a + \frac{\pi}{6}\right) \right] \right\} + \\ &+ \frac{1}{2} \left\{ (x_1 - jx_2) \left[\cos\left(\omega t - \varphi_a + \frac{\pi}{6}\right) - j \sin\left(\omega t - \varphi_a + \frac{\pi}{6}\right) \right] \right\} \end{aligned} \quad (38)$$

so that:

$$\left(i_{ab} \cos\left(\omega t - \varphi_a + \frac{\pi}{6}\right) \right)_0 = x_1 \cos\left(\varphi_a - \frac{\pi}{6}\right) - x_2 \sin\left(\varphi_a - \frac{\pi}{6}\right) \quad (39)$$

Repeating the same elaboration for the other zero-sequence components in (34), the final algebraic formula that links the DC-link current to the AC current components is:

$$\begin{aligned} i_{DC_{mv}} = (i_{DC_{mv}})_0 = \frac{\sqrt{3}m}{2} & \left[x_1 \cos\left(\varphi_a - \frac{\pi}{6}\right) - x_2 \sin\left(\varphi_a - \frac{\pi}{6}\right) + \right. \\ & \left. + x_3 \cos\left(\varphi_b - \frac{\pi}{6}\right) - x_4 \sin\left(\varphi_b - \frac{\pi}{6}\right) + x_5 \cos\left(\varphi_c - \frac{\pi}{6}\right) - x_6 \sin\left(\varphi_c - \frac{\pi}{6}\right) \right] \end{aligned} \quad (40)$$

This is a straightforward way to calculate the average DC-link current from the direct-sequence components of the AC currents, the latter being state variables in this study. In other words, no any data storage is required to calculate integral terms in the common formulation of DC-link current, obtaining a significant simplification without decreasing the accuracy level.

7.2 Transformers and grid models

The implementation of a detailed equivalent circuit for the LV/MV transformer as well as the creation of a distributed parameters model for the AC grid cannot be executed for computational effort reasons. Anyway, a satisfactory accuracy is reached with a minimum order model as the one shown in Fig. 22, using simplified versions of the models described in [144].

It is important to point out that the values of load resistors, load inductances and grid voltage sources are calculated referring to the primary side of the transformer i.e. to the LV side connected to the AC filter stage.

Chapter 8 – Integration of PV plant and ESS models

8.1 PV plant model

Integration of models built for each component of the PV system in Fig. 22 leads to a comprehensive state-space representation for the entire plant or, similarly, for a specific subfield. In this way, power and energy values at the meter are calculated from irradiance and cell temperature data by simply running such integrated state-space average model.

In such integrated model, the RMS value of phase-to-phase grid voltage V_{grid} is considered as an input. Alternatively, it could be assigned as a constant term into matrices. The control variables d and m are set by the control system described in the following Section.

The general state-space representation of the whole PV system in Fig. 22 is:

$$\begin{cases} \dot{x} = \bar{A}x + \bar{B}u \\ y = \bar{C}x + \bar{D}u \end{cases} \quad (41)$$

where:

$$x = \begin{bmatrix} v_{C_{panel}} \\ i_{L_1} \\ v_{C_1} \\ x_1 \\ \dots \\ \dots \\ x_{18} \end{bmatrix} \quad u = \begin{bmatrix} i_{ph} \\ i_d \\ V_{grid} \end{bmatrix} \quad y = \begin{bmatrix} x_1 \\ \dots \\ \dots \\ x_{12} \end{bmatrix} \quad (42)$$

$y = x$ or

Matrix \bar{A} is:

$$\bar{A} = A_{ON}d + A_{OFF}(1-d) \quad (43)$$

with:

$$A_{ON} = \begin{bmatrix} A_{ON_{1,1}} & \dots & A_{ON_{1,21}} \\ \dots & \dots & \dots \\ A_{ON_{21,1}} & \dots & A_{ON_{21,21}} \end{bmatrix} \quad A_{OFF} = \begin{bmatrix} A_{OFF_{1,1}} & \dots & A_{OFF_{1,21}} \\ \dots & \dots & \dots \\ A_{OFF_{21,1}} & \dots & A_{OFF_{21,21}} \end{bmatrix} \quad (44)$$

Non-zero elements in matrix A_{ON} are listed here:

$$A_{ON_{1,1}} = -\frac{1}{C_{panel}(R_s + R_p)} \quad A_{ON_{1,2}} = -\frac{1}{C_{panel}} \quad A_{ON_{2,1}} = \frac{1}{L_1} \quad A_{ON_{2,2}} = -\frac{r_{L_1}}{L_1} \quad (45)$$

$$A_{ON_{3,4}} = -\frac{\sqrt{3}m}{2C_1} \cos\left(\varphi_a - \frac{\pi}{6}\right) \quad A_{ON_{3,5}} = \frac{\sqrt{3}m}{2C_1} \sin\left(\varphi_a - \frac{\pi}{6}\right) \quad (46)$$

$$A_{ON_{3,6}} = -\frac{\sqrt{3}m}{2C_1} \cos\left(\varphi_b - \frac{\pi}{6}\right) \quad A_{ON_{3,7}} = \frac{\sqrt{3}m}{2C_1} \sin\left(\varphi_b - \frac{\pi}{6}\right) \quad (47)$$

$$A_{ON_{3,8}} = -\frac{\sqrt{3}m}{2C_1} \cos\left(\varphi_c - \frac{\pi}{6}\right) \quad A_{ON_{3,9}} = \frac{\sqrt{3}m}{2C_1} \sin\left(\varphi_c - \frac{\pi}{6}\right) \quad (48)$$

$$A_{ON_{4,3}} = \frac{\sqrt{3}m}{12L_2} \cos\left(\varphi_a - \frac{\pi}{6}\right) \quad A_{ON_{5,3}} = -\frac{\sqrt{3}m}{12L_2} \sin\left(\varphi_a - \frac{\pi}{6}\right) \quad (49)$$

$$A_{ON_{6,3}} = \frac{\sqrt{3}m}{12L_2} \cos\left(\varphi_b - \frac{\pi}{6}\right) \quad A_{ON_{7,3}} = -\frac{\sqrt{3}m}{12L_2} \sin\left(\varphi_b - \frac{\pi}{6}\right) \quad (50)$$

$$A_{ON_{8,3}} = \frac{\sqrt{3}m}{12L_2} \cos\left(\varphi_c - \frac{\pi}{6}\right) \quad A_{ON_{9,3}} = -\frac{\sqrt{3}m}{12L_2} \sin\left(\varphi_c - \frac{\pi}{6}\right) \quad (51)$$

and:

$$A_{ON_{4,4}} = A_{ON_{5,5}} = A_{ON_{6,6}} = A_{ON_{7,7}} = A_{ON_{8,8}} = A_{ON_{9,9}} = -\frac{r_{L_2}}{L_2} \quad (52)$$

$$A_{ON_{4,10}} = A_{ON_{5,11}} = A_{ON_{6,12}} = A_{ON_{7,13}} = A_{ON_{8,14}} = A_{ON_{9,15}} = -\frac{1}{3L_2} \quad (53)$$

$$\begin{aligned} A_{ON_{5,4}} &= A_{ON_{7,6}} = A_{ON_{9,8}} = A_{ON_{11,10}} = A_{ON_{13,12}} = \\ &= A_{ON_{15,14}} = A_{ON_{17,16}} = A_{ON_{19,18}} = A_{ON_{21,20}} = -\omega \end{aligned} \quad (54)$$

$$\begin{aligned} A_{ON_{4,5}} &= A_{ON_{6,7}} = A_{ON_{8,9}} = A_{ON_{10,11}} = A_{ON_{12,13}} = \\ &= A_{ON_{14,15}} = A_{ON_{16,17}} = A_{ON_{18,19}} = A_{ON_{20,21}} = \omega \end{aligned}$$

$$A_{ON_{10,4}} = A_{ON_{11,5}} = A_{ON_{12,6}} = A_{ON_{13,7}} = A_{ON_{14,8}} = A_{ON_{15,9}} = \frac{1}{C_2} \quad (55)$$

$$A_{ON_{10,16}} = A_{ON_{11,17}} = A_{ON_{12,18}} = A_{ON_{13,19}} = A_{ON_{14,20}} = A_{ON_{15,21}} = -\frac{1}{C_2} \quad (56)$$

$$A_{ON_{16,10}} = A_{ON_{17,11}} = A_{ON_{18,12}} = A_{ON_{19,13}} = A_{ON_{20,14}} = A_{ON_{21,15}} = \frac{1}{L_{LOAD}} \quad (57)$$

$$A_{ON_{16,16}} = A_{ON_{17,17}} = A_{ON_{18,18}} = A_{ON_{19,19}} = A_{ON_{20,20}} = A_{ON_{21,21}} = -\frac{R_{LOAD}}{L_{LOAD}} \quad (58)$$

The elements in A_{OFF} whose expression differs from the corresponding A_{ON} terms are:

$$A_{OFF_{1,2}} = A_{OFF_{2,1}} = 0 \quad A_{OFF_{2,3}} = -\frac{1}{L_1} \quad A_{OFF_{3,2}} = \frac{1}{C_1} \quad (59)$$

Matrix \bar{B} is:

$$\bar{B} = B_{ON}d + B_{OFF}(1-d) \quad (60)$$

with:

$$B_{ON} = \begin{bmatrix} B_{ON_{1,1}} & B_{ON_{1,2}} & B_{ON_{1,3}} \\ \dots & \dots & \dots \\ B_{ON_{21,1}} & B_{ON_{21,2}} & B_{ON_{21,3}} \end{bmatrix} \quad B_{OFF} = B_{ON} \quad (61)$$

whose non-zero elements are:

$$B_{ON_{1,1}} = \frac{1}{C_{panel} \left(1 + \frac{R_s}{R_p}\right)} \quad B_{ON_{1,2}} = -\frac{1}{C_{panel} \left(1 + \frac{R_s}{R_p}\right)} \quad (62)$$

$$B_{ON_{16,3}} = -\frac{\sqrt{2}}{L_{LOAD}} \cos(\varphi_{grida}) \quad B_{ON_{17,3}} = \frac{\sqrt{2}}{L_{LOAD}} \sin(\varphi_{grida}) \quad (63)$$

$$B_{ON_{18,3}} = -\frac{\sqrt{2}}{L_{LOAD}} \cos(\varphi_{gridb}) \quad B_{ON_{19,3}} = \frac{\sqrt{2}}{L_{LOAD}} \sin(\varphi_{gridb}) \quad (64)$$

$$B_{ON_{20,3}} = -\frac{\sqrt{2}}{L_{LOAD}} \cos(\varphi_{gridc}) \quad B_{ON_{21,3}} = \frac{\sqrt{2}}{L_{LOAD}} \sin(\varphi_{gridc}) \quad (65)$$

Each state variable can be extracted as output of the system through a proper assignment of matrix \bar{C} . Alternatively, the latter is set as an identity matrix.

The calculation of the energy produced by the PV plant is easy to perform from simple formulas with variables from x_1 to x_{12} i.e. by the AC voltage and current components. Matrix \bar{D} is null.

The values of DC and AC cables resistance, useful to calculate the distribution losses and to compare the same in case of different plant configurations, can be added to the resistive elements included in state-space matrices or inserted in the form of new resistive elements.

8.1.1 Control system

The DC/DC converter is controlled in P&O MPPT mode [32]. The control system of the grid connected inverter is implemented in qd reference frame using a common PLL subsystem to regulate active and reactive power. The DC-link voltage is fixed controlling the d -axis current [33].

Time sampling of quantities in control system can be set larger in comparison to the time step used for PV plant simulation e.g. 10x or more, in order to allow a fast computational time.

With reference to the case studies discussed in this work, the design of the control system needs to take into account additional constraints, in particular the maximum power internal threshold of each converter, the power limitation strategy related to the IGBT stack temperature and the power limit fixed by Power Plant Controller (PPC). This latter is a variable threshold fixed by the local utility company for safety or operating reasons.

8.2 Parameters identification

PV array parameters are assigned exploiting data listed in PV modules datasheet and considering the number N_S of modules per string and the number N_P of strings per string box. On the contrary, some parameters in ECM e.g. R_s and R_p need to be identified. A suitable identification method, used in this work, is in [84]. In running model, a satisfactory accuracy is obtained taking into account the influence of temperature on short-circuit current and on no-load voltage through the coefficients I_{sc}/T_{mod} and V_{oc}/T_{mod} listed in datasheet of PV modules avoiding the use of look-up tables for the benefit of simplicity.

About the converters, detailed information on topology, components and control system are usually not available due to industrial secrets policies. Anyway, the modelling approach described in this work allows to overcome this lack of information

giving the opportunity to identify an equivalent behavioral model in a simple but effective way. To perform such identification, one of the many possible methods in literature dealing with the identification of systems in the form of state-space function can be used.

In this work, the identification process is carried out using data collected by monitoring system and applying a constrained minimums formulation characterized by high flexibility and adaptability to different identification processes. The target is to minimize the deviation between model output and real data [145]. In general terms, let $y_{meas}(k)$ be a given electrical variable measured by the PV plant datalogger for a given time period in the form of a timeseries with N time samples:

$$Y_{meas} = \begin{bmatrix} y_{meas}(1) \\ y_{meas}(2) \\ \dots \\ y_{meas}(k) \\ \dots \\ y_{meas}(N) \end{bmatrix} \quad (66)$$

The corresponding quantity provided by the model is $y_{model}(k)$. Each $y_{model}(k)$ sample can be expressed as the linear composition of the p_n parameters (to be identified) and of the terms h_{ki} , the latter representing the relations between $y_{model}(k)$ and each p_i parameter for a given system input:

$$y_{model}(k) = h_{k1}p_1 + h_{k2}p_2 + \dots + h_{kn}p_n \quad (67)$$

which is, for N time samples:

$$\begin{bmatrix} y_{model}(1) \\ y_{model}(2) \\ \dots \\ y_{model}(k) \\ \dots \\ y_{model}(N) \end{bmatrix} = \begin{bmatrix} h_{11} & h_{12} & \dots & h_{1n} \\ h_{21} & h_{22} & \dots & h_{2n} \\ \dots & \dots & \dots & \dots \\ h_{k1} & h_{k2} & \dots & h_{kn} \\ \dots & \dots & \dots & \dots \\ h_{N1} & h_{N2} & \dots & h_{Nn} \end{bmatrix} \begin{bmatrix} p_1 \\ p_2 \\ \dots \\ p_n \end{bmatrix} \quad (68)$$

or:

$$[Y_{model}] = [H][P] \quad (69)$$

The implementation of the constrained minimums formulation provides the

optimal set of parameters reducing the deviation between the value of the measured variable and the one provided by the model:

$$P \cong \left([H]^T [H] \right)^{-1} [H]^T [Y_{meas}] \quad (70)$$

The identification of parameters for the ECM of a battery pack can be performed in several ways. Some examples are in [4], [99]. Taking into account the integrated modelling strategy of this work, for which the battery model shall combine with the PV plant model, the constrained minimums formulation is used also for the identification of the battery ECM. In this case, input data is typically the forced current $i(t)$ as well as the corresponding voltage $v_{meas}(t)$ measured at ESS terminals during preliminary experimental tests carried out at different current rates C_R .

8.3 Merging models using PC and EC

The parameters PC and EC are fundamental for the scope of this thesis. In fact, they represent the link between the models of the ESS and of the PV plant, as schematically represented in Fig. 25.

The justification of this approach deals with limitation of complexity. In fact, the separation of PV plant model and ESS estimation algorithm is useful to keep a low computational effort. At the same time, link based on actual values of PC and EC allows a suitable integration of the models for the optimal energy management of the entire system.

For the sake of example, exploiting the weather forecast services, the introduced PV plant model is able to predict the expected power curve for a certain time horizon as an entire specific day. If a maintenance activity on more PV arrays is scheduled for the same day, one can assess the capability of the distributed ESS to store the energy produced during the shutdown. From this information, it is possible to reshape the works. For instance the technicians could perform the maintenance only for the PV arrays whose ESS is able to store all the produced energy while postponing the works for the rest of PV arrays connected to ESS having a low SOC. In such a way, the energy losses caused by maintenance shutdown are virtually reduced to zero.

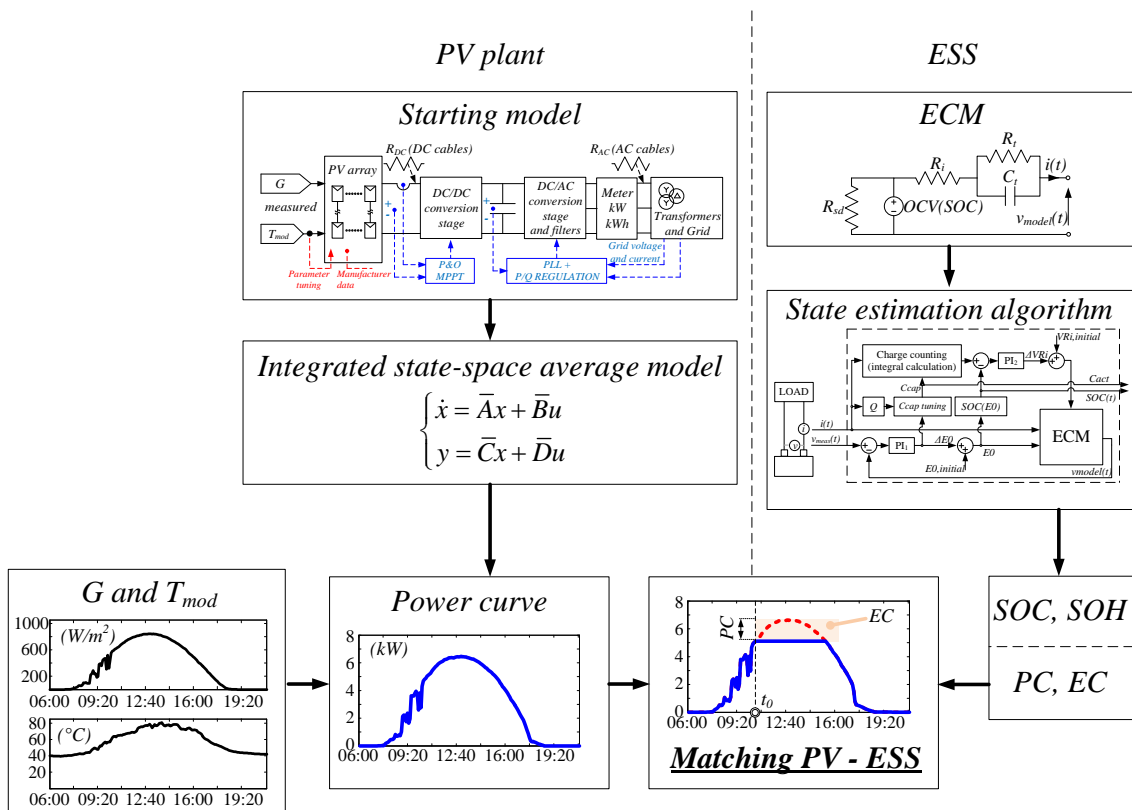


Figure 25. Schematic representation of the matching between ESS and PV plant models

The same freedom degrees could be exploited by PPC to decide the battery packs to be charged or discharged on the basis of energy time shift service, dynamic power thresholds fixed by the utility company and so on.

It is obvious that, in case of maintenance on one or more PV modules, no energy can be saved during shutdown of the specific string.

In Chapter 11 there are some numerical examples referred to a real case study.

Chapter 9 - Models validation

Validation of models for PV plants and for ESS has been carried out through extensive experimental tests, described in following Sections.

9.1 Experimental tests for validation of PV modules modelling

Validation of models for PV plants has been done performing two different test sessions. Such validation is addressed to the core component of the system that is the PV module. In fact, the precision of its model, described in Section 5.3, has a big impact on the accuracy of the plant model and on the correctness of the final result. In both the test sessions, target is to verify the effectiveness of the developed models through the comparison with data acquired for different PV modules.

The first session has been performed in University of Catania (UNICT) laboratory. PV modules of different size and typology are emulated by a programmable DC power supply. The test bench is shown in Fig. 26.

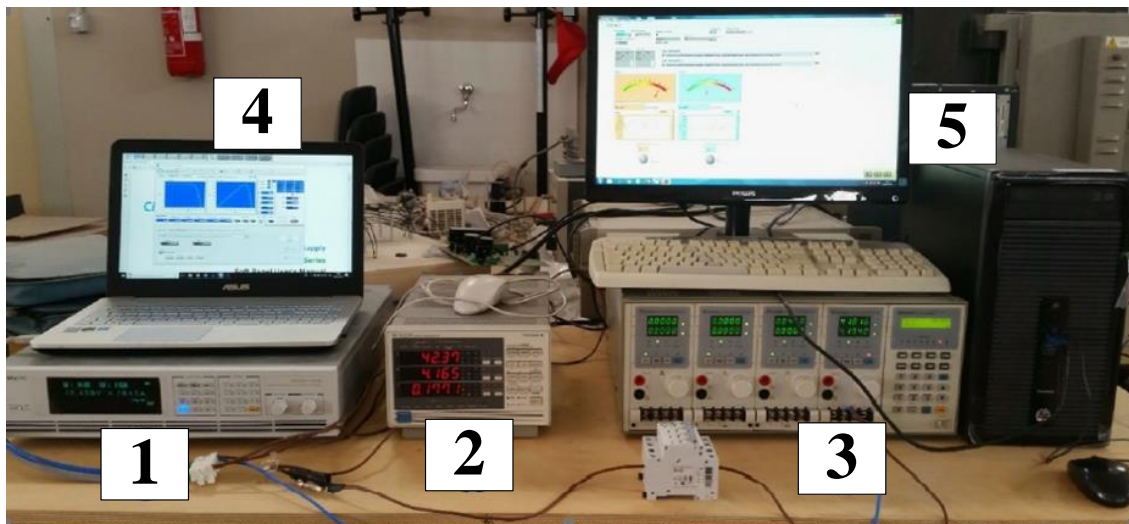


Figure 26. PV modules model validation, first session: UNICT laboratory test bench. Legend: 1. programmable DC power supply / PV emulator, 2. power analyzer, 3. DC electronic load, 4. PC with emulator software, 5. PC / LabVIEW

The DC power supply is controlled by PC via USB in order to emulate the I-V curve of different types of PV modules. Fig. 27 shows the graphic interface of the power supply software.

The power analyzer is a digital wattmeter, used for the measurement of power, voltage and current. The interface with PC is via GPIB, data is acquired using LabVIEW. Fig. 28 shows the front panel. The operation modes set for the electronic load are Constant Current (CC), Constant Power (CP) and Constant Resistance (CR). These controls are used to modify the working point of modules from time to time.



Figure 27. PV modules model validation, first session: emulation of a PV module through the DC power supply software

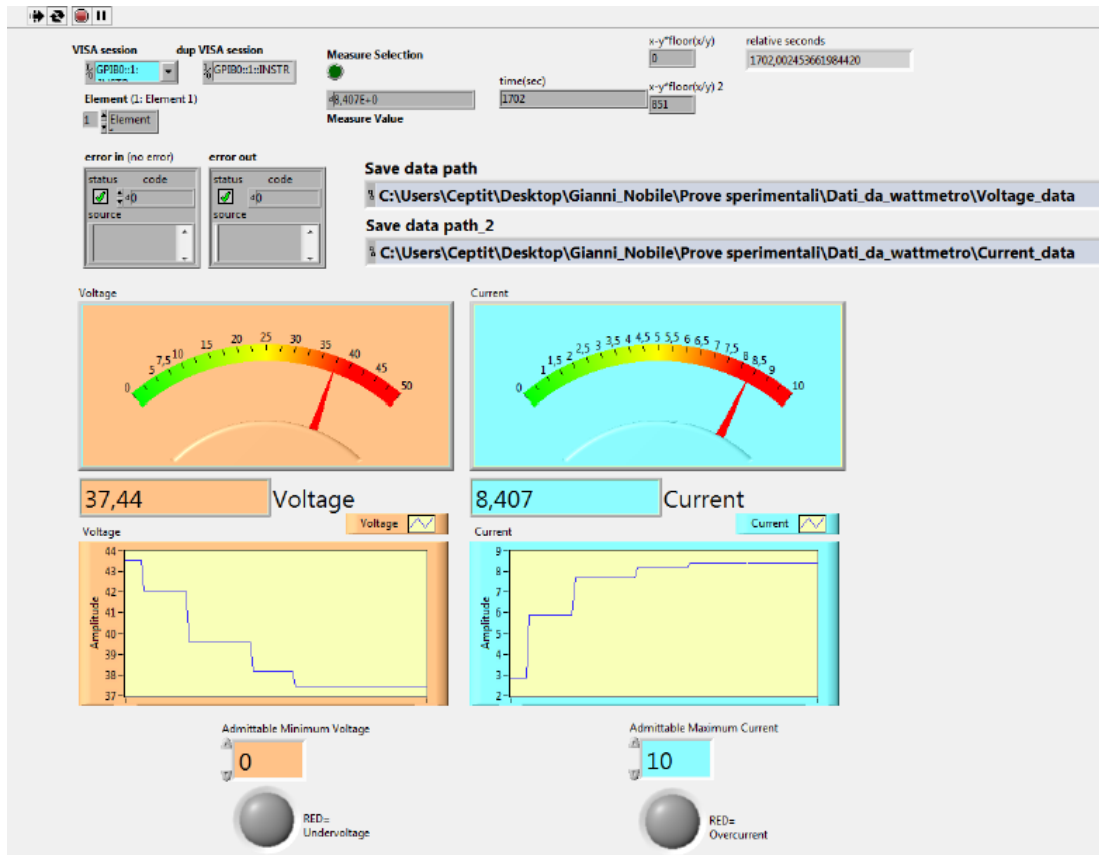


Figure 28. PV modules model validation, first session: LabVIEW front panel

The second test session concerns the measurement acquired for real PV modules in the Enel Green Power (EGP) laboratory of Catania. Test bench includes a pulsed light emitter, three irradiance sensors, an electronic load and a PC with the management software and Graphical User Interface (GUI).

Some pictures of the test bench are in Fig. 29.

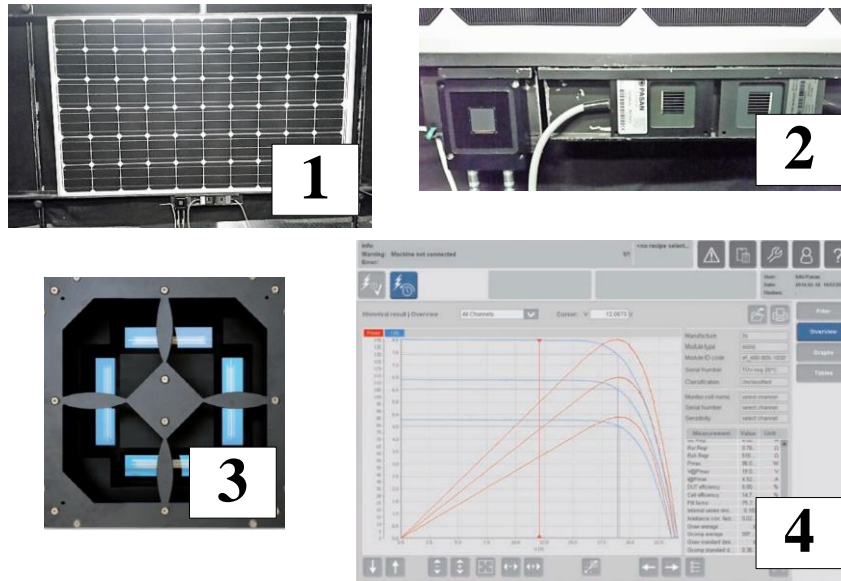


Figure 29. PV modules model validation, second session: pictures of the test bench. Legend: 1. PV module under test, 2. irradiance sensors, 3. pulsed light emitter, 4. GUI, plot of results

Tests in both sessions are carried out for a wide range of irradiance and module temperature values, in order to verify the accuracy of the models built for the PV modules.

For the sake of brevity, here is reported only an example of the comparison between the model and the real module, the latter being a Solar World SW 255 whose technical specifications are in Table 7. This module was one of those tested in the second measurement session.

Manufacturer datasheet	
P_{mod} (W)	255
V_{oc} (V)	38.0
I_{sc} (A)	8.88
V_{MPP} (V)	30.9
I_{MPP} (A)	8.32
$NOCT$ ($^{\circ}C$)	46
P_{mod}/T_{mod} ($\%/^{\circ}C$)	-0.41
V_{oc}/T_{mod} ($\%/^{\circ}C$)	-0.31
I_{sc}/T_{mod} ($\%/^{\circ}C$)	+0.051
Cells	Poly
Number of cells	60

Table 7. Technical specifications of the Solar World SW 255 PV module

Table 8 reports some measurements acquired during the second test session forcing an irradiance level in a narrow range around 1000 W/m².

Measured data									
Test	G (W/m ²)	V_{oc} (V)	I_{sc} (A)	P_{mod} (W)	V_{MPP} (V)	I_{MPP} (A)	FF (%)	η_{mod} (%)	T_{mod} (°C)
1	999.6	37.59	9.00	253.6	30.10	8.42	0.749	0.151	23.84
2	1001.1	37.60	9.00	253.5	30.11	8.42	0.750	0.151	23.84
3	1002.2	37.61	9.00	253.7	30.12	8.42	0.750	0.151	23.75
4	1001.5	37.62	8.99	253.7	30.14	8.42	0.750	0.151	23.75
5	1002.6	37.63	9.00	253.9	30.14	8.43	0.750	0.151	23.75
6	1001.9	37.64	8.99	254.0	30.17	8.42	0.750	0.151	23.75
7	1003.2	37.65	8.99	254.1	30.17	8.42	0.750	0.152	23.75
8	1004.3	37.66	8.99	254.0	30.18	8.42	0.750	0.152	23.75
9	1003.6	37.66	9.00	254.3	30.18	8.43	0.750	0.152	23.75
10	1003.5	37.67	9.00	254.5	30.19	8.43	0.750	0.152	23.75
Avg	1002.3	37.63	9.00	253.9	30.15	8.42	0.750	0.151	23.77
Maximum deviation ΔP_{mod} , measurement error distribution calculation (W)				± 7.0					

Table 8. Example of measurements acquired during the second test session in case of irradiance fixed in a narrow range around 1000 W/m²

A preliminary identification process through the technique described in Section 8.2 leads to the estimation of resistance parameters of the single-diode equivalent circuit, Table 9.

R_s (Ω)	0.16
R_p (Ω)	236.00

Table 9. Preliminary identification of the resistance parameters in single-diode model for the PV module under test

The average values of measurements acquired for the main parameters at different irradiance levels, listed in Table 10, are compared to the ones provided by the model, Table 11. This latter Table reports also the percentage deviation of the model with respect to real data. It emerges that the model accuracy is satisfactory in comparison to the uncertainty ΔP_{mod} related to the measurement procedure performed in this second test session. As expected, the error caused by model becomes larger in case of low irradiance.

Measured data (average values)				
G (W/m ²)	V_{oc} (V)	I_{sc} (A)	P_{mod} (W)	ΔP_{mod} (W)
1000	37.63	9.00	253.9	± 7.0
800	37.34	7.19	204.8	± 5.8
700	37.18	6.31	180.1	± 4.5
400	36.24	3.61	102.5	± 9.1

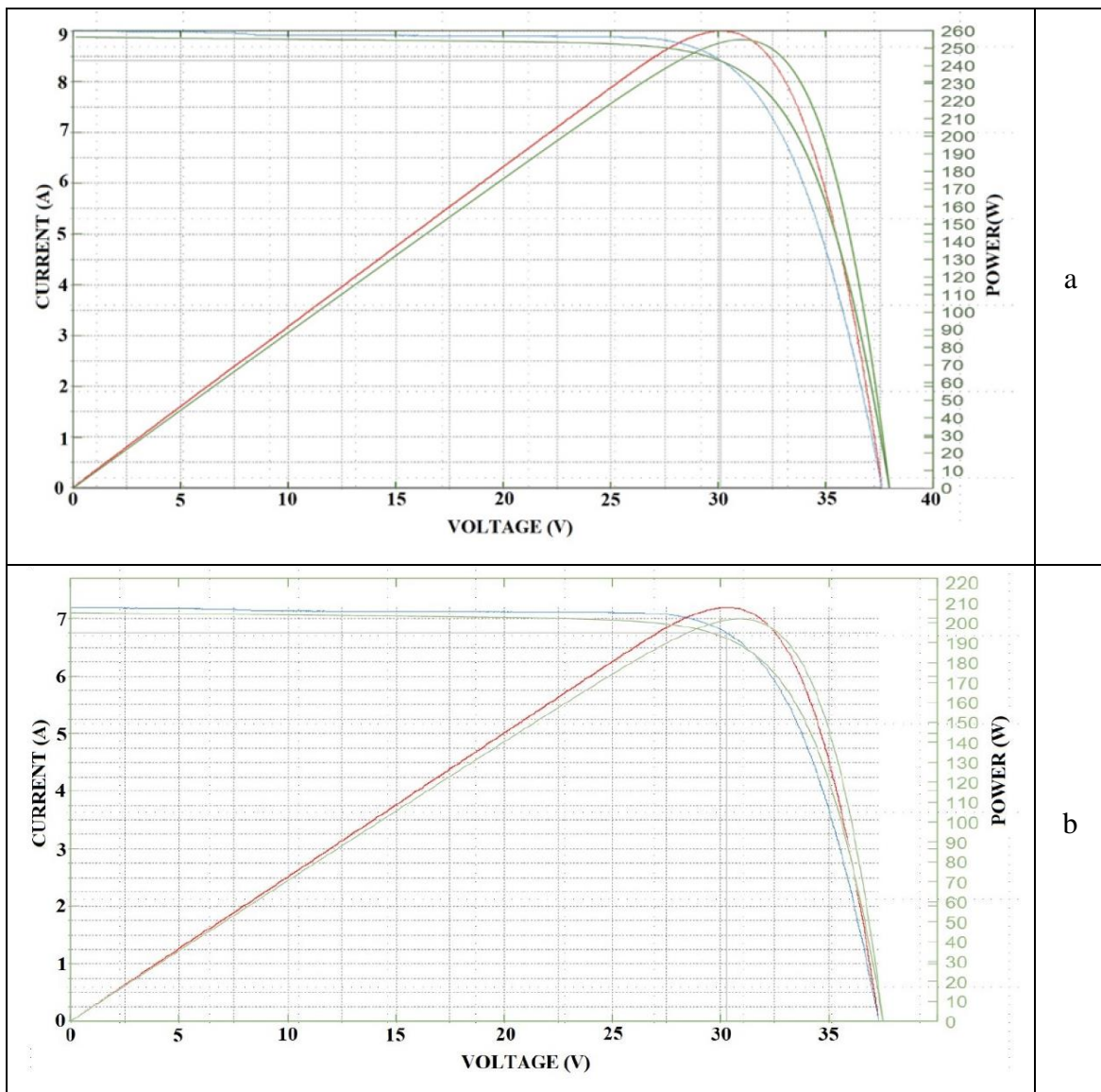
Table 10. Average value and maximum deviation in measured power for the Solar World SW 255 PV module

Model data				Model vs measured data Absolute difference		
G (W/m ²)	V_{oc} (V)	I_{sc} (A)	P_{mod} (W)	εV_{oc} (V)	εI_{sc} (A)	εP_{mod} (W)
1000	37.96	8,87	254.9	+0.33	-0.13	+1.0
800	37.50	7.10	201.9	+0.16	-0.09	-2.9
700	37.23	6.21	175.4	+0.05	-0.10	-4.7
400	36.07	3.55	96.3	-0.17	-0.06	-6.2

Table 11. Parameters values provided by the model

Data in Tables 10-11 are used to superimpose the plot of measured I-V curve with the plot of the same curve obtained in simulation. Graphical comparisons, for different irradiance level, are in Fig. 30, confirming that the model well matches real data.

Repeating similar calculations for different module temperatures and taking into account the temperature-dependent parameters listed in the manufacturer datasheet (P_{mod}/T_{mod} , V_{oc}/T_{mod} and I_{sc}/T_{mod}), the result is a deviation around 3 % or rather larger than the error experienced for different irradiance values. More generally, the error caused by model becomes significant in case of irradiance and temperature far from Standard Test Conditions (STC).



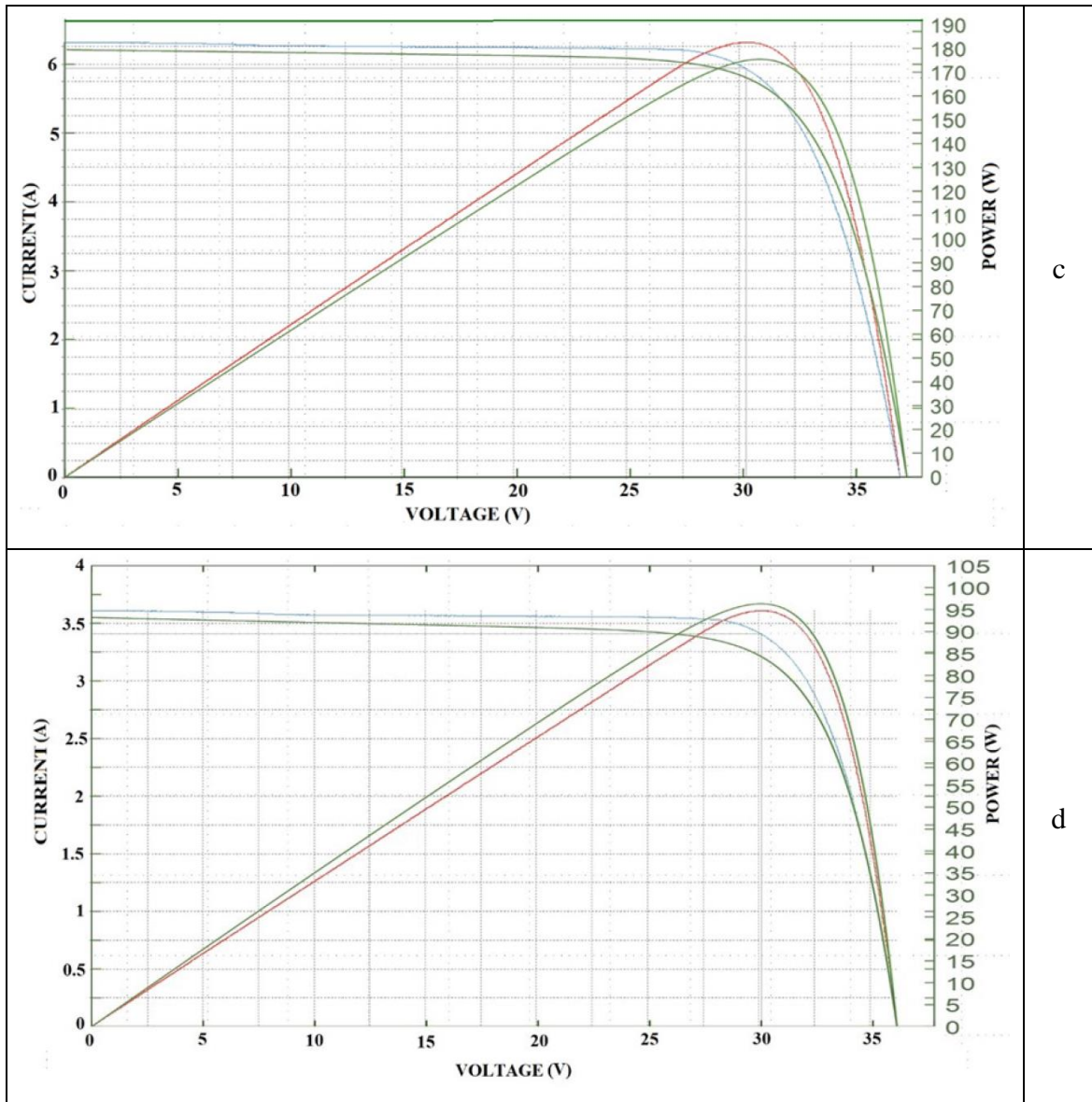


Figure 30. Simulation vs measured data for the Solar World SW 255 PV module under test. Charts created automatically by the monitoring system during the second test session. Green curves: I-V and P-V characteristics from simulation, blue curves: measured I-V characteristics, red curves: measured P-V characteristics. Legend: a. $G = 1000 \text{ W/m}^2$, $T_{mod} = 25^\circ\text{C}$, b. $G = 800 \text{ W/m}^2$, $T_{mod} = 25^\circ\text{C}$, c. $G = 700 \text{ W/m}^2$, $T_{mod} = 25^\circ\text{C}$, d. $G = 400 \text{ W/m}^2$, $T_{mod} = 25^\circ\text{C}$

The same analysis was extended to several types of PV modules, including the ones in case studies, following the purpose to set the optimal parameter tuning from time to time.

9.2 Validation of PV plant integrated model

The integrated model for large PV plants, introduced in this work, has been implemented in MATLAB Simulink environment. In the following Sections the proposed approach, based on the state-space average technique, is compared to detailed models in which high-frequency switching and related phenomena are taken into account. The validation process involves both accuracy and complexity performances.

9.2.1 Model running

For the purpose to show some simulations, the reference PV system considered in this Section is a PV array composed by two strings in parallel. Each string is the series connection of 30 PV modules whose datasheet is in Table 12 together with other technical information of the conversion system. Such array type is the basic generation unit linked to a single MPPT channel of string inverters in case study 1, more details are in Chapter 10. The model described in Chapter 8, schematically shown in Fig. 22, is adapted in simulation for PV array size.

PV module			
P_{mod} (W)	315	$NOCT$ ($^{\circ}C$)	45±2
V_{oc} (V)	46.2	P_{mod}/T_{mod} ($\%/^{\circ}C$)	-0.40
I_{sc} (A)	9.01	V_{oc}/T_{mod} ($\%/^{\circ}C$)	-0.30
V_{MPP} (V)	37.2	I_{sc}/T_{mod} ($\%/^{\circ}C$)	+0.06
I_{MPP} (A)	8.48	Cells, number	Poly, 72
String		Array	
N_S	30	N_P	2
P_{str} (kW)	9.45	P_{array} (kW)	18.90
String inverter			
Rated AC power (kVA)	60 (up to 66)	MPPT input DC voltage range	600 ÷ 1450
AC voltage output (V)	800	MPPT channels per inverter	4
AC frequency output (Hz)	50 / 60	Maximum efficiency (%)	99.0

Table 12. Technical specifications of main power components for simulation of PV array

For the sake of example, Fig. 31 and Fig. 32 show the time plots of the main electric quantities of the PV array in two simulated operating scenarios.

In both the operating scenarios, the state-space average model is implemented in a straightforward way exploiting formulas in Section 8.1 while for the detailed model all the components (PV modules, converters, filters, etc.) are placed into the simulation platform using their physical description.

Fig. 31 depicts the waveforms of main electric quantities obtained in case of 1000 W/m^2 as irradiance and of 25° C as module temperature (STC). Values of parameters used to implement this simulation are in Table 13. The integrated state-space average model well matches the detailed model in both DC and AC side. Control system is able to force a null reactive power while the active power at the power meter reaches around 18.5 kW that is close to the PV array STC rated power with a slight difference caused by power losses in DC and AC side.

In Fig. 32 the irradiance is 800 W/m^2 and the module temperature is 45° C . Values of the main parameters used in this simulation are listed in Table 14. At time 0.1 s , control system forces a variation in reactive power that is, for example, requested by the grid. Also in this case the integrated state-space average model is compliant to the detailed model.

Finally, the integrated state-space average approach is able to provide the average values of all the electric quantities in every operating conditions.

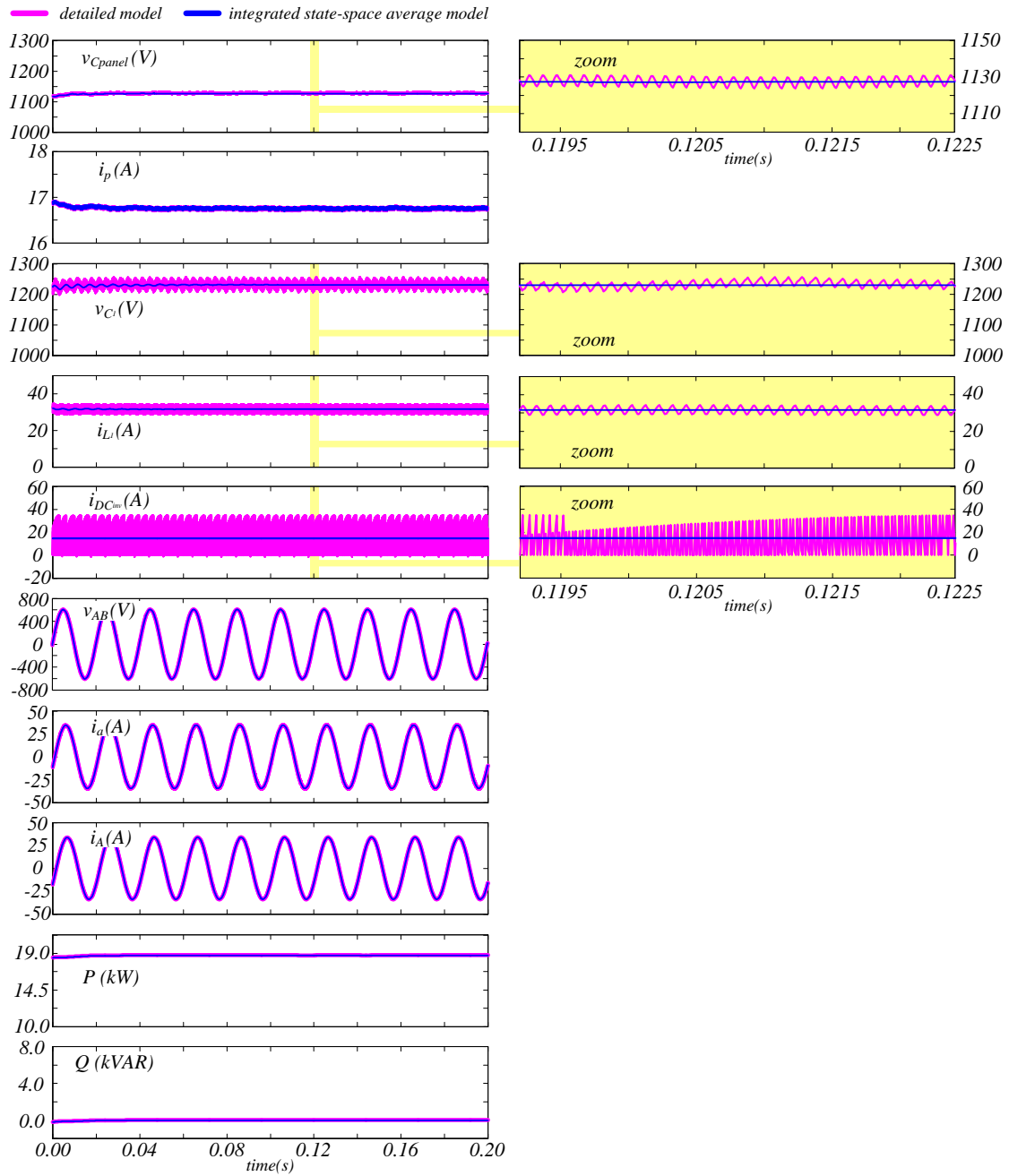


Figure 31. Simulation of a 18.9 kW PV array. PV system topology is represented in Fig. 22, technical data of components in Table 13. Irradiance is 1000 W/m^2 , module temperature is 25°C . Comparison between detailed model and integrated state-space average model

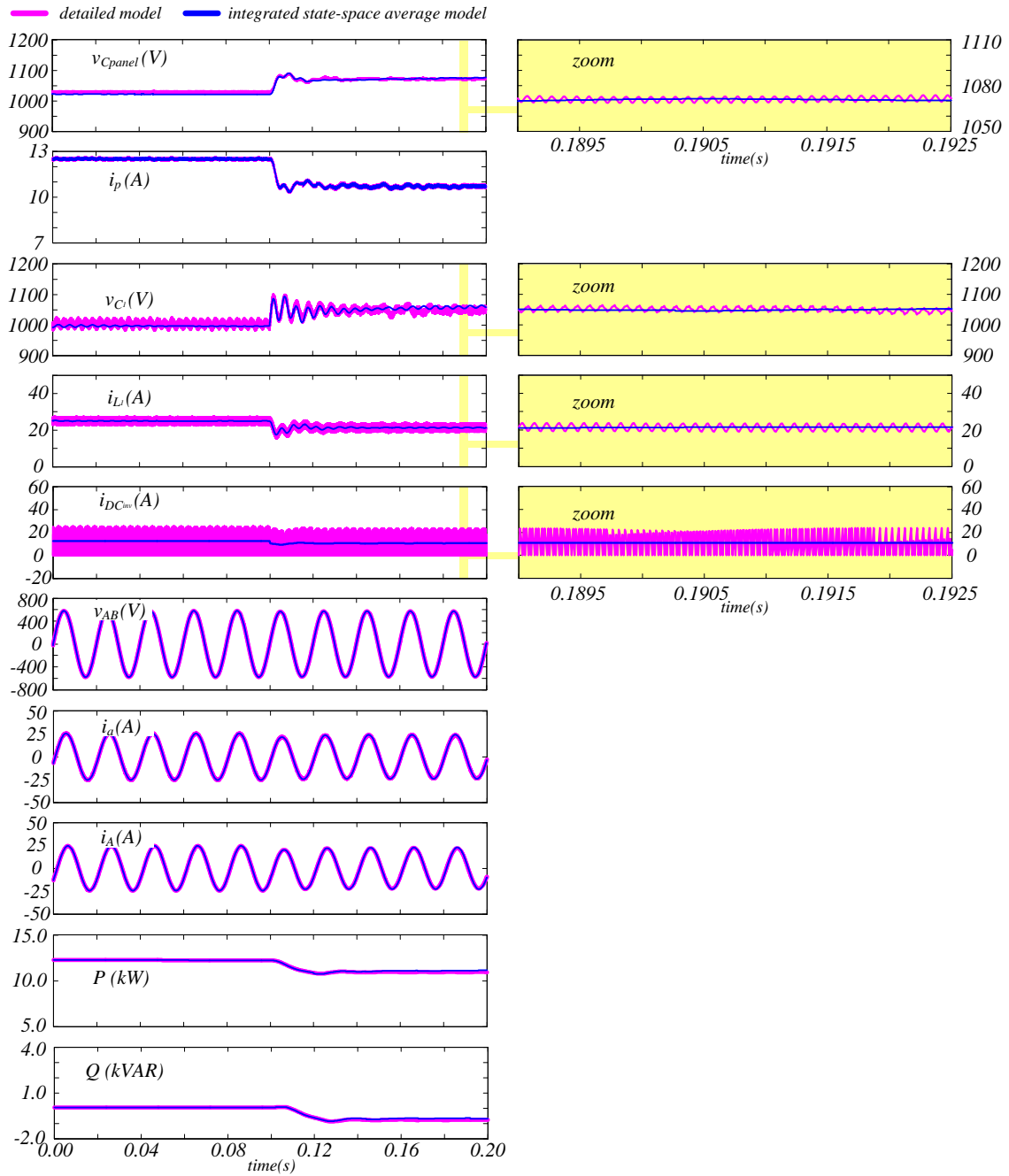


Figure 32. Simulation of a 18.9 kW PV array. PV system configuration is represented in Fig. 22, technical data of components in Table 14. Irradiance is 800 W/m^2 , module temperature is 45° C . At time 0.1 s the control system forces non null reactive power. Comparison between detailed model and integrated state-space average model

PV module	see Table 12		T_s (s) *	$1 \cdot 10^{-6}$
N_S	30		t_{end} (s) *	0.2
N_P	2		$G(t_0)$ (W/m ²)	1000
R_s (Ω)	$0.2 N_S/N_P$		$T_{mod}(t_0)$ ($^{\circ}$ C)	25
R_p (Ω)	$300 N_S/N_P$		$f_{s,DCDC}$ (kHz) **	10
C_{panel} (μ F)	110		$f_{s,inv}$ (kHz) ***	20
L_1 (mH)	10		f_n (Hz) ****	50
r_{L1} (Ω)	0.5		$\varphi_a(t_0)$ (rad)	$2\pi/15$
C_1 (μ F)	25		$\varphi_{grida}(t_0)$ (rad)	0
L_2 (mH)	34		$V_{DC-link}$ (V) *****	700
r_{L2} (Ω)	0.2		V_{gridLV} (V)	400
C_2 (μ F)	0.22		V_{gridHV} (kV)	34.5
R_{LOAD} (Ω)	5		$d(t_0)$	0.53
L_{LOAD} (mH)	223		$m(t_0)$	0.75
(*) T_s : simulation time step, t_{end} : simulation final time (**) DC/DC converter switching frequency (***) Inverter switching frequency (****) Grid frequency (*****) Rated DC-link voltage				

Table 13. Parameters list for the simulation shown in Fig. 31

PV module	see Table 12		T_s (s) *	$1 \cdot 10^{-6}$
N_S	30		t_{end} (s) *	0.2
N_P	2		$G(t_0)$ (W/m ²)	800
R_s (Ω)	$0.2 N_S/N_P$		$T_{mod}(t_0)$ ($^{\circ}$ C)	45
R_p (Ω)	$300 N_S/N_P$		$f_{s,DCDC}$ (kHz) **	10
C_{panel} (μ F)	110		$f_{s,inv}$ (kHz) ***	20
L_1 (mH)	10		f_n (Hz) ****	50
r_{L1} (Ω)	0.5		$\varphi_a(t_0)$ (rad)	$2\pi/23$
C_1 (μ F)	25		$\varphi_{grida}(t_0)$ (rad)	0
L_2 (mH)	34		$V_{DC-link}$ (V) *****	700
r_{L2} (Ω)	0.2		V_{gridLV} (V)	400
C_2 (μ F)	0.22		V_{gridHV} (kV)	34.5
R_{LOAD} (Ω)	5		$d(t_0)$	0.5
L_{LOAD} (mH)	223		$m(t_0)$	0.75
(*) T_s : Simulation time step, t_{end} : Simulation final time (**) DC/DC converter switching frequency (***) Inverter switching frequency (****) Grid frequency (*****) Rated DC-link voltage				

Table 14. Parameters list for the simulation shown in Fig. 32

9.2.2 Execution time performance

Referring to the same PV system described in the previous Section, the advantages of the proposed approach in terms of computational effort have been evaluated performing a comparison with detailed model on the basis of the execution time of simulation. This comparison takes into account two different cases:

- case A: the same simulation sample time is assigned to the state-space average model and to the detailed model. In such a case, the selected step size is $1 \cdot 10^{-6}$ s, established referring to dynamic features of the detailed model at value.
- case B: a larger simulation sample time equal to $2 \cdot 10^{-5}$ s is assigned to the state-space average model since high-frequency switching and related phenomena are neglected. About the detailed model, the step size needs to be set equal to the previous case otherwise it cannot work properly.

For both A and B cases, four different working scenarios have been simulated. To get a large statistical database, each scenario run 1000 times using two different processors named computer 1 and computer 2.

The evaluation of the execution time exploits stopwatch functions in MATLAB Simulink environment. The relative difference in execution time between the state-space average model and the detailed model is calculated by applying this formula:

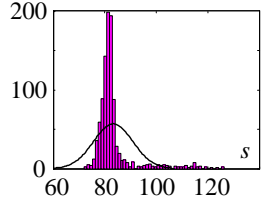
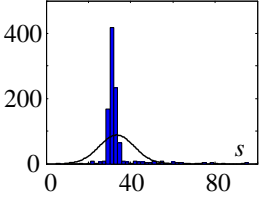
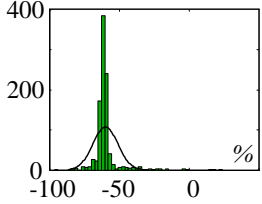
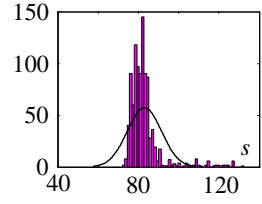
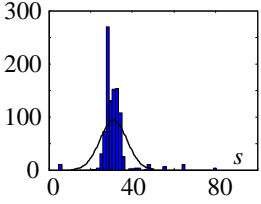
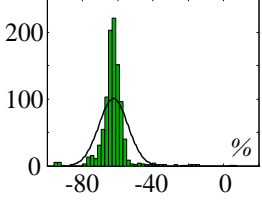
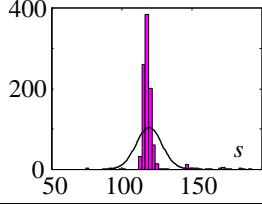
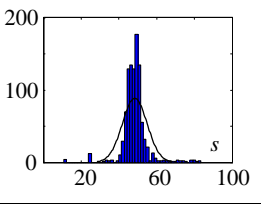
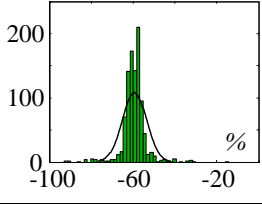
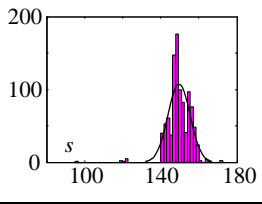
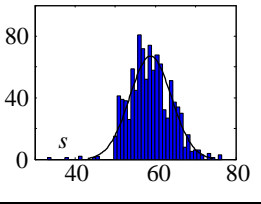
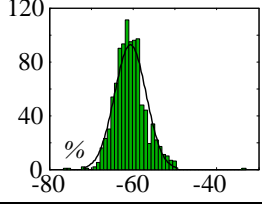
$$\Delta t_{\%} = \frac{t_{issa} - t_{det}}{t_{det}} 100 \quad (71)$$

where t_{issa} is the execution time for the simulation of the integrated state-space average model while t_{det} is the execution time of the detailed model.

Tables 15-18 summarize the results coming from the analysis of execution time performance using a statistical approach based on mean value and standard deviation.

As expected, the novel behavioural model ensures a significant reduction in computational time for both the processors. In case A, the integrated state-space average model is about 3 times faster in comparison to the detailed model. In case B this performance in computational speed rises to 25 times.

Computer 1, hardware: Intel Core i3-4005U CPU@1.70 GHz (4 CPUs), RAM 4096 MB, HD SSD 240 GB read speeds up to 545 MB/s, 64 bit

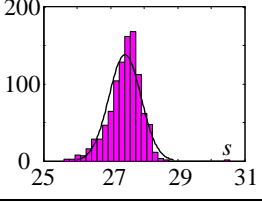
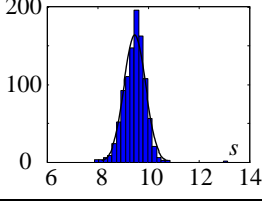
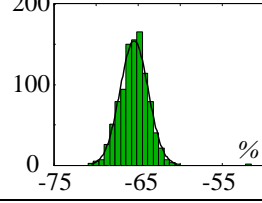
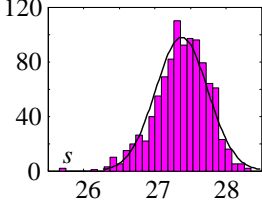
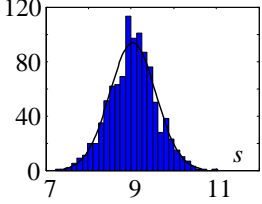
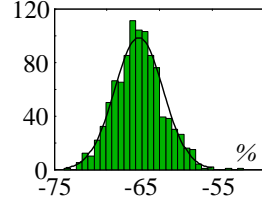
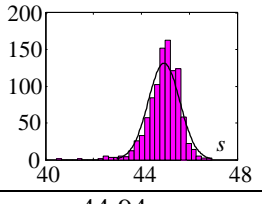
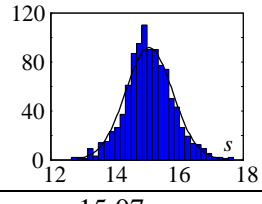
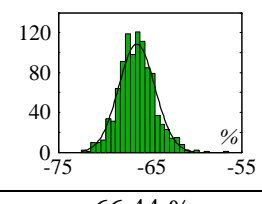
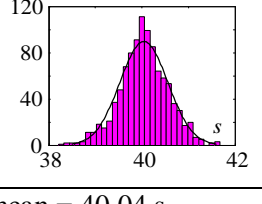
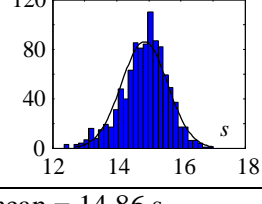
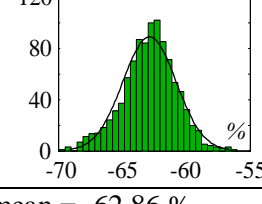
	t_{det}	t_{issa}	$\Delta t\%$
Scenario 1			
	mean = 83.28 s std dev = 7.62 s	mean = 33.40 s std dev = 8.25 s	mean = -59.82 % std dev = 8.92 %
Scenario 2			
	mean = 83.01 s std dev = 8.41 s	mean = 31.01 s std dev = 6.46 s	mean = -62.35 % std dev = 8.20 %
Scenario 3			
	mean = 119.61 s std dev = 9.13 s	mean = 48.38 s std dev = 6.55 s	mean = -59.37 % std dev = 7.79 %
Scenario 4			
	mean = 149.57 s std dev = 8.79 s	mean = 58.79 s std dev = 5.66 s	mean = -60.64 % std dev = 7.75 %

All the scenarios: simulation of the PV system described in Section 9.2.1, fixed time step is $1 \cdot 10^{-6}$ s. Scenario 1 and 2: simulation time 0.0 to 0.3 s. Scenario 3 and 4: simulation time 0.0 to 0.5 s.

Scenario 1: 1000 W/m^2 , 25° C - Scenario 2: 800 W/m^2 , 45° C , non-zero reactive power is forced after 0.1 s - Scenario 3: irradiance increases from 800 W/m^2 to 950 W/m^2 , module temperature increases from 40° C to 55° C - Scenario 4: irradiance decreases from 1000 W/m^2 to 850 W/m^2 , module temperature decreases from 55° C to 40° C

Table 15. Execution time performance evaluation, case A (simulation time step is $1 \cdot 10^{-6}$ s for state-space average model and for detailed model), computer 1

Computer 2, hardware: Intel Core i7-8700K CPU@3.70 GHz (12 CPUs), RAM 32768 MB, HD SSD 250 GB read speeds up to 540 MB/s, 64 bit

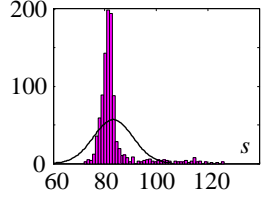
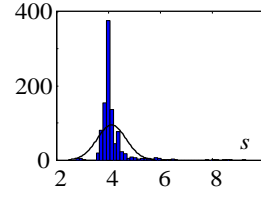
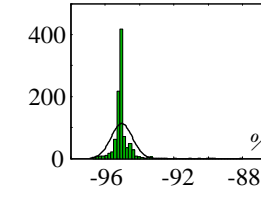
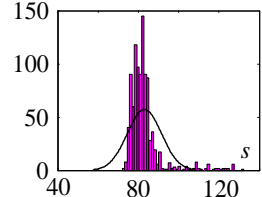
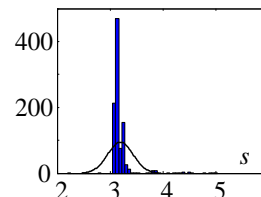
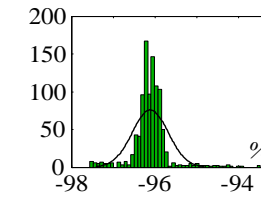
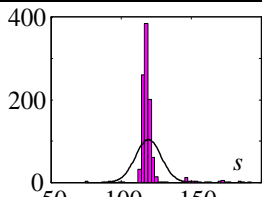
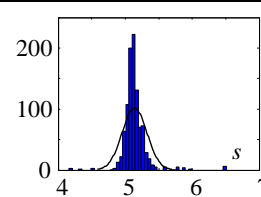
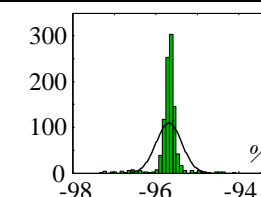
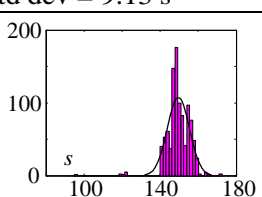
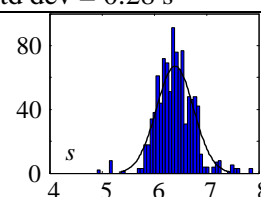
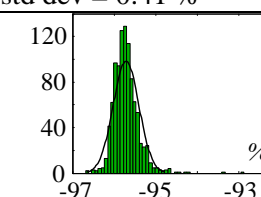
	t_{det}	t_{issa}	$\Delta t\%$
Scenario 1			
	mean = 27.43 s std dev = 0.48 s	mean = 9.47 s std dev = 0.43 s	mean = -65.47 % std dev = 1.67 %
Scenario 2			
	mean = 27.38 s std dev = 0.37 s	mean = 9.04 s std dev = 0.54 s	mean = -66.96 % std dev = 2.30 %
Scenario 3			
	mean = 44.94 s std dev = 0.66 s	mean = 15.07 s std dev = 0.73 s	mean = -66.44 % std dev = 1.97 %
Scenario 4			
	mean = 40.04 s std dev = 0.52 s	mean = 14.86 s std dev = 0.72 s	mean = -62.86 % std dev = 2.09 %

All the scenarios: simulation of the PV system described in Section 9.2.1, fixed time step is $1 \cdot 10^{-6}$ s. Scenario 1 and 2: simulation time 0.0 to 0.3 s. Scenario 3 and 4: simulation time 0.0 to 0.5 s.

Scenario 1: 1000 W/m^2 , 25° C - Scenario 2: 800 W/m^2 , 45° C , non-zero reactive power is forced after 0.1 s - Scenario 3: irradiance increases from 800 W/m^2 to 950 W/m^2 , module temperature increases from 40° C to 55° C - Scenario 4: irradiance decreases from 1000 W/m^2 to 850 W/m^2 , module temperature decreases from 55° C to 40° C

Table 16. Execution time performance evaluation, case A (simulation time step is $1 \cdot 10^{-6}$ s for state-space average model and for detailed model), computer 2

Computer 1, hardware: Intel Core i3-4005U CPU@1.70 GHz (4 CPUs), RAM 4096 MB, HD SSD 240 GB read speeds up to 545 MB/s, 64 bit

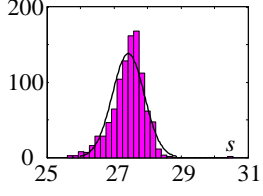
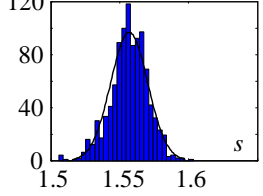
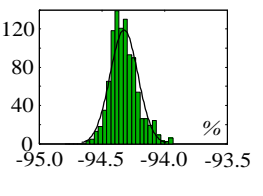
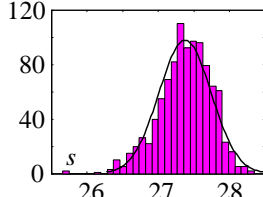
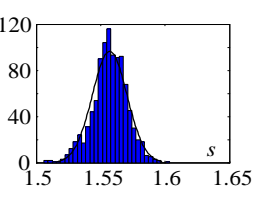
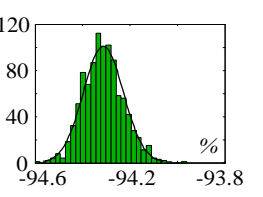
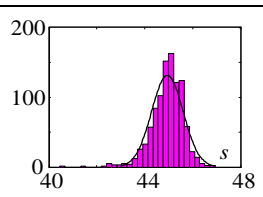
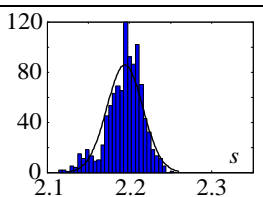
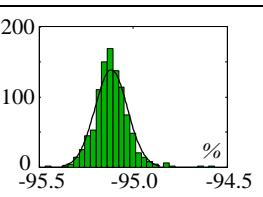
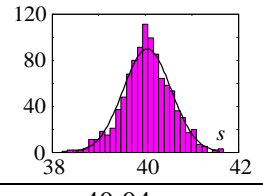
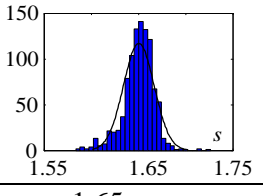
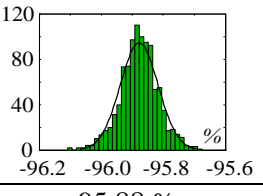
	t_{det}	t_{issa}	$\Delta t\%$
Scenario 1			
	mean = 83.28 s std dev = 7.62 s	mean = 4.13 s std dev = 0.55 s	mean = -95.03 % std dev = 0.62 %
Scenario 2			
	mean = 83.01 s std dev = 8.41 s	mean = 3.20 s std dev = 0.25 s	mean = -96.12 % std dev = 0.43 %
Scenario 3			
	mean = 119.61 s std dev = 9.13 s	mean = 5.14 s std dev = 0.28 s	mean = -95.7 % std dev = 0.41 %
Scenario 4			
	mean = 149.57 s std dev = 8.79 s	mean = 6.40 s std dev = 0.35 s	mean = -95.8 % std dev = 0.41 %

All the scenarios: simulation of the PV system described in Section 9.2.1, fixed time step is $2 \cdot 10^{-5}$ s. Scenario 1 and 2: simulation time 0.0 to 0.3 s. Scenario 3 and 4: simulation time 0.0 to 0.5 s.

Scenario 1: 1000 W/m^2 , 25° C - Scenario 2: 800 W/m^2 , 45° C , non-zero reactive power is forced after 0.1 s - Scenario 3: irradiance increases from 800 W/m^2 to 950 W/m^2 , module temperature increases from 40° C to 55° C - Scenario 4: irradiance decreases from 1000 W/m^2 to 850 W/m^2 , module temperature decreases from 55° C to 40° C

Table 17. Execution time performance evaluation, case B (simulation time step is $2 \cdot 10^{-5}$ s for state-space average model, $1 \cdot 10^{-6}$ s for detailed model), computer 1

Computer 2, hardware: Intel Core i7-8700K CPU@3.70 GHz (12 CPUs), RAM 32768 MB, HD SSD 250 GB read speeds up to 540 MB/s, 64 bit

	t_{det}	t_{issa}	$\Delta t\%$
Scenario 1			
	mean = 27.43 s std dev = 0.48 s	mean = 1.55 s std dev = 0.03 s	mean = -94.33 % std dev = 0.15 %
Scenario 2			
	mean = 27.38 s std dev = 0.37 s	mean = 1.56 s std dev = 0.01 s	mean = -94.31 % std dev = 0.08 %
Scenario 3			
	mean = 44.94 s std dev = 0.66 s	mean = 2.19 s std dev = 0.02 s	mean = -95.12 % std dev = 0.09 %
Scenario 4			
	mean = 40.04 s std dev = 0.52 s	mean = 1.65 s std dev = 0.02 s	mean = -95.88 % std dev = 0.08 %

All the scenarios: simulation of the PV system described in Section 9.2.1, fixed time step is $2 \cdot 10^{-5}$ s. Scenario 1 and 2: simulation time 0.0 to 0.3 s. Scenario 3 and 4: simulation time 0.0 to 0.5 s.

Scenario 1: 1000 W/m^2 , 25° C - Scenario 2: 800 W/m^2 , 45° C , non-zero reactive power is forced after 0.1 s - Scenario 3: irradiance increases from 800 W/m^2 to 950 W/m^2 , module temperature increases from 40° C to 55° C - Scenario 4: irradiance decreases from 1000 W/m^2 to 850 W/m^2 , module temperature decreases from 55° C to 40° C

Table 18. Execution time performance evaluation, case B (simulation time step is $2 \cdot 10^{-5}$ s for state-space average model, $1 \cdot 10^{-6}$ s for detailed model), computer 2

9.2.3 Accuracy evaluation

To assess the accuracy of the model proposed for large PV plants, the best way is to compare its output in the form of power curves and daily energy with the measurements registered by the power meter in real plants as the ones being the case studies of this work.

Irradiance and module temperature timeseries, acquired by the monitoring system in the PV plants become the input of the integrated state-space average model together with the RMS value of the phase-to-phase grid voltage.

For the sake of example, data coming from the dataloggers of the PV plant in case study 1 (see Chapter 10 for more details) are here exploited to assess the accuracy of the model. The experimental subfield in case study 1 is composed by 4 subfields, total power is 2.5 MW. Power configuration of 2 subfields is with central inverters, the other 2 subfields have string inverters, grouped in a cabin using AC parallel switchboards named QPCA. Table 19 lists the main technical data of the experimental subfield.

PV module		Central inverter	
P_{mod} (W)	315	Rated AC power (kVA)	1025
V_{oc} (V)	46.2	AC output (V, Hz)	400±10%, 50/60
I_{sc} (A)	9.01	MPPT input DC voltage range (V)	675-1320
V_{MPP} (V)	37.2	Maximum Efficiency (%)	98.9
I_{MPP} (V)	8.48	MPPTs per power converter	1
$NOCT$ (°C)	45±2	String inverter	
P_{mod}/T_{mod} (%/°C)	-0.40	Rated AC power (kVA)	60 (up to 66)
V_{oc}/T_{mod} (%/°C)	-0.30	AC output (V, Hz)	800, 50/60
I_{sc}/T_{mod} (%/°C)	+0.06	MPPT input DC voltage range (V)	600-1450
Cells	Poly	Maximum Efficiency (%)	99.0
Number of cells	72	MPPTs per power converter	4

Table 19. Main technical specifications of the experimental subfield in case study 1, used for the assessment of model accuracy

Figs. 33-36 show the operation of the considered PV subfields during some days. Power curve provided by the integrated state-space average model is superimposed to the measured one. During these days no any unavailability, data missing or external

constraints occur so that the comparison is consistent.

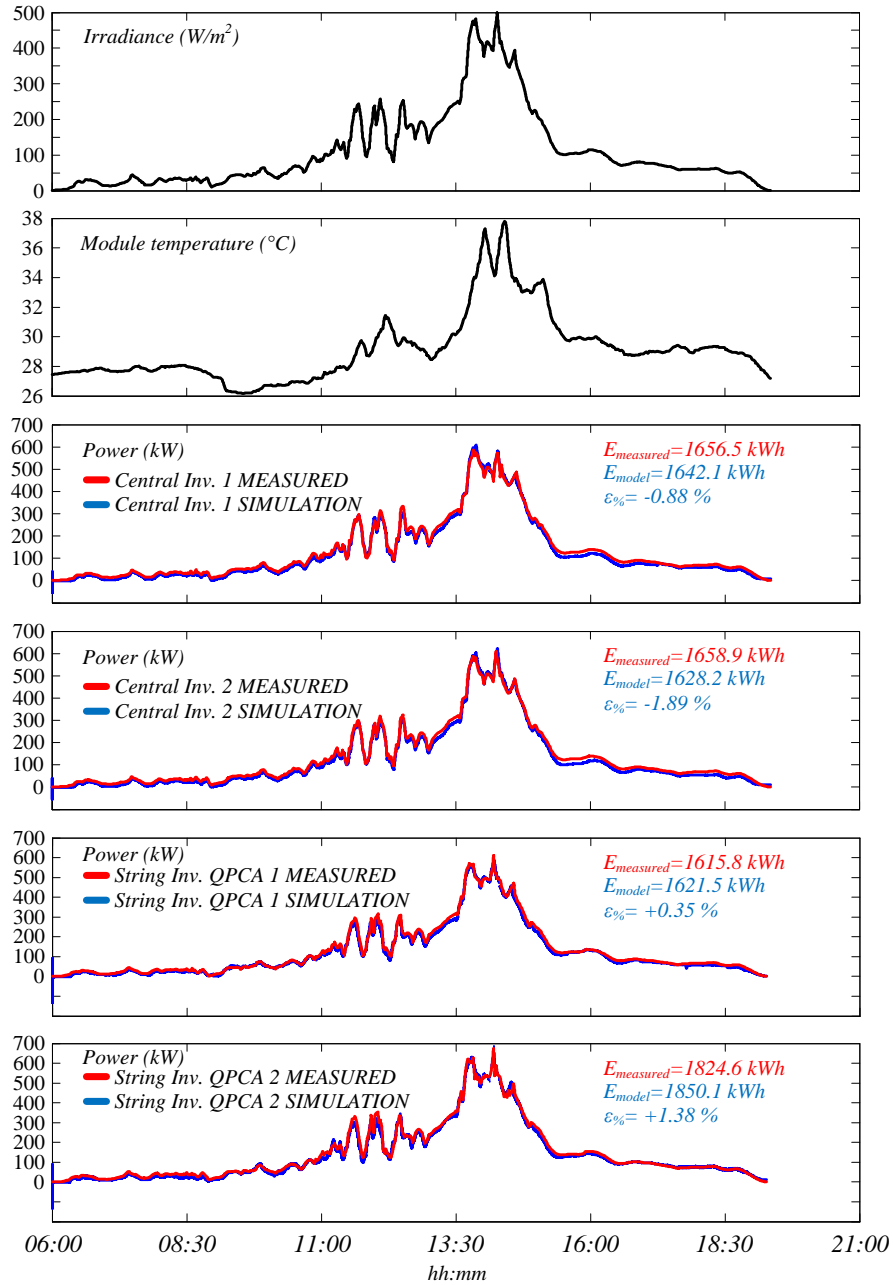


Figure 33. Example of daily power curves measured in the experimental subfield of case study 1. Proposed model output (simulation) vs measured data. Calculation of percentage relative error

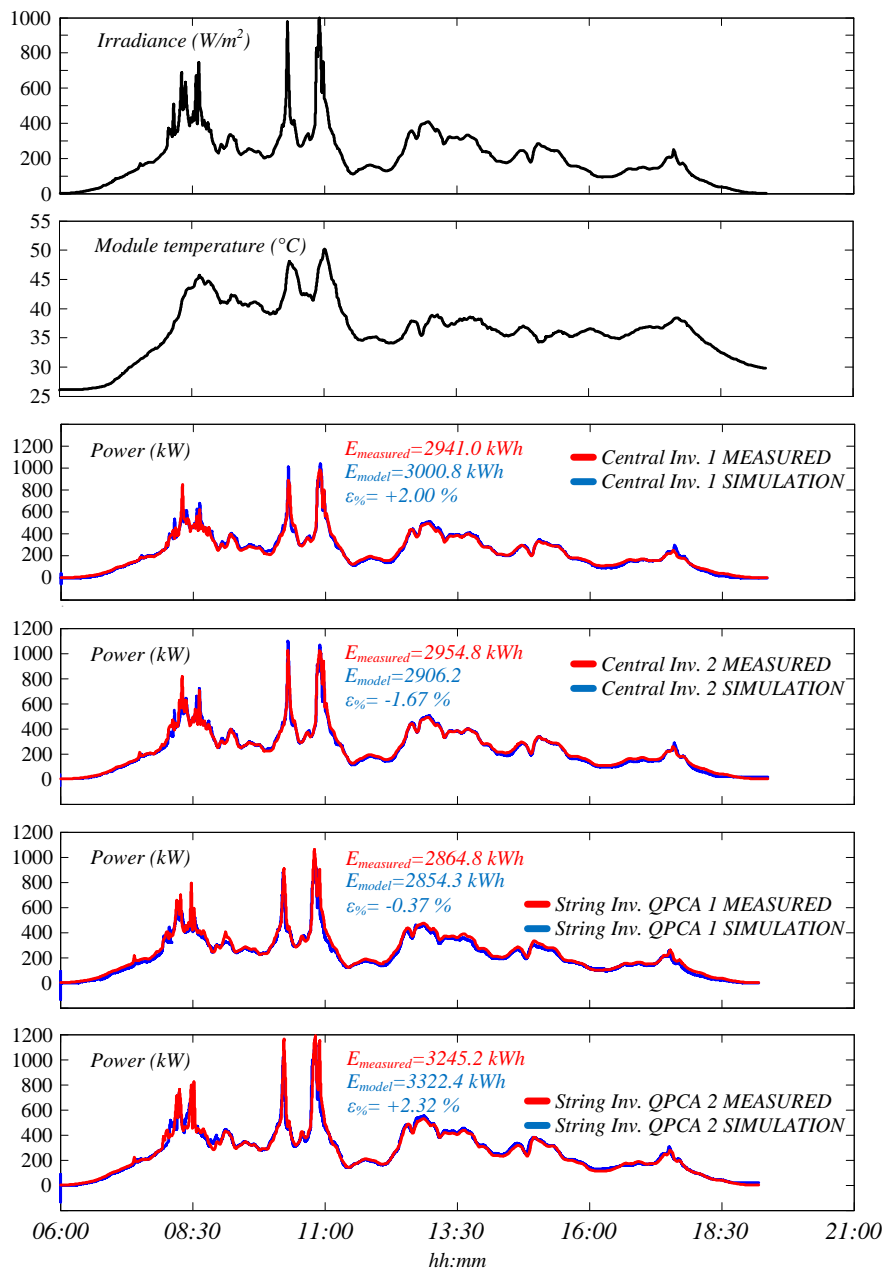


Figure 34. Another example of daily power curves measured in the experimental subfield of case study 1. Proposed model output (simulation) vs measured data. Calculation of percentage relative error

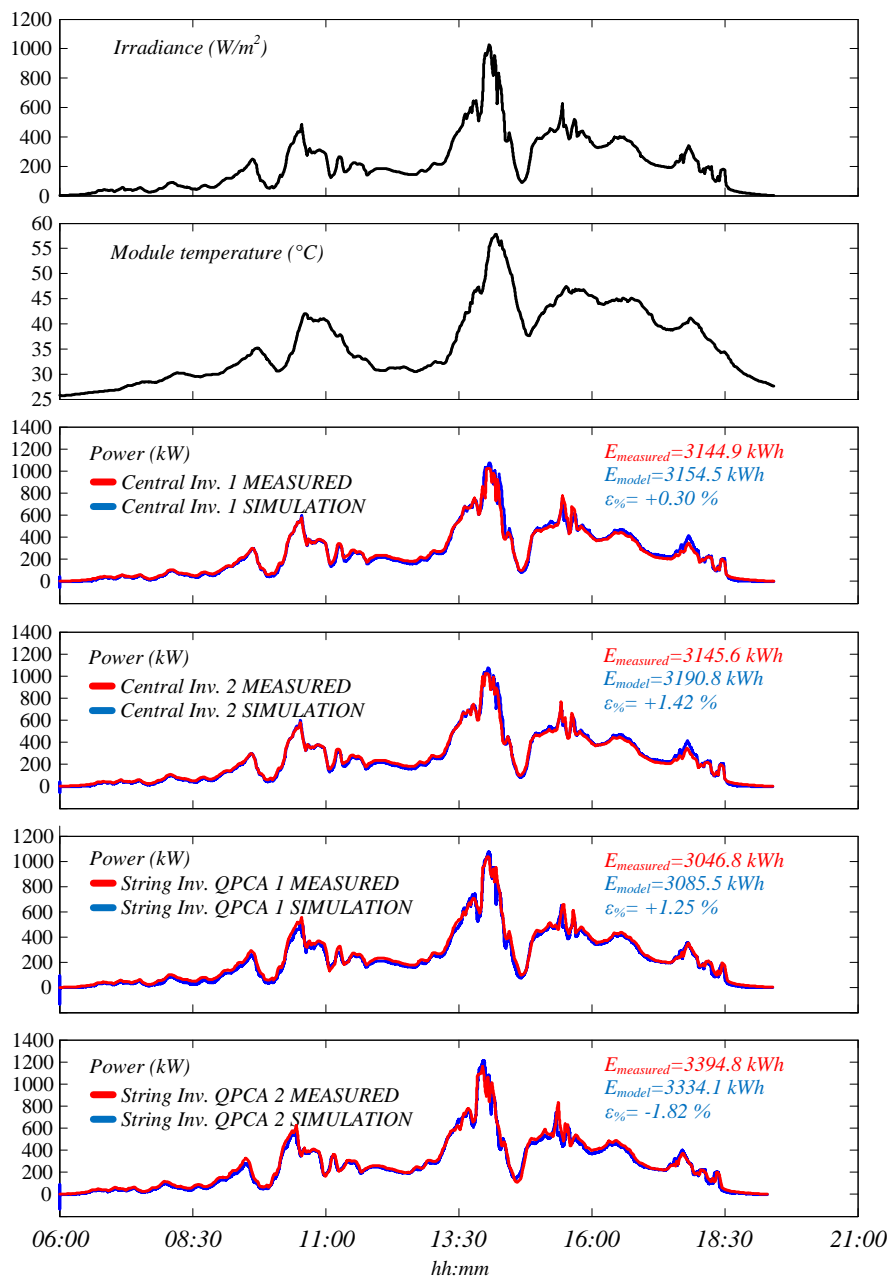


Figure 35. Another example of daily power curves measured in the experimental subfield of case study 1. Proposed model output (simulation) vs measured data. Calculation of percentage relative error

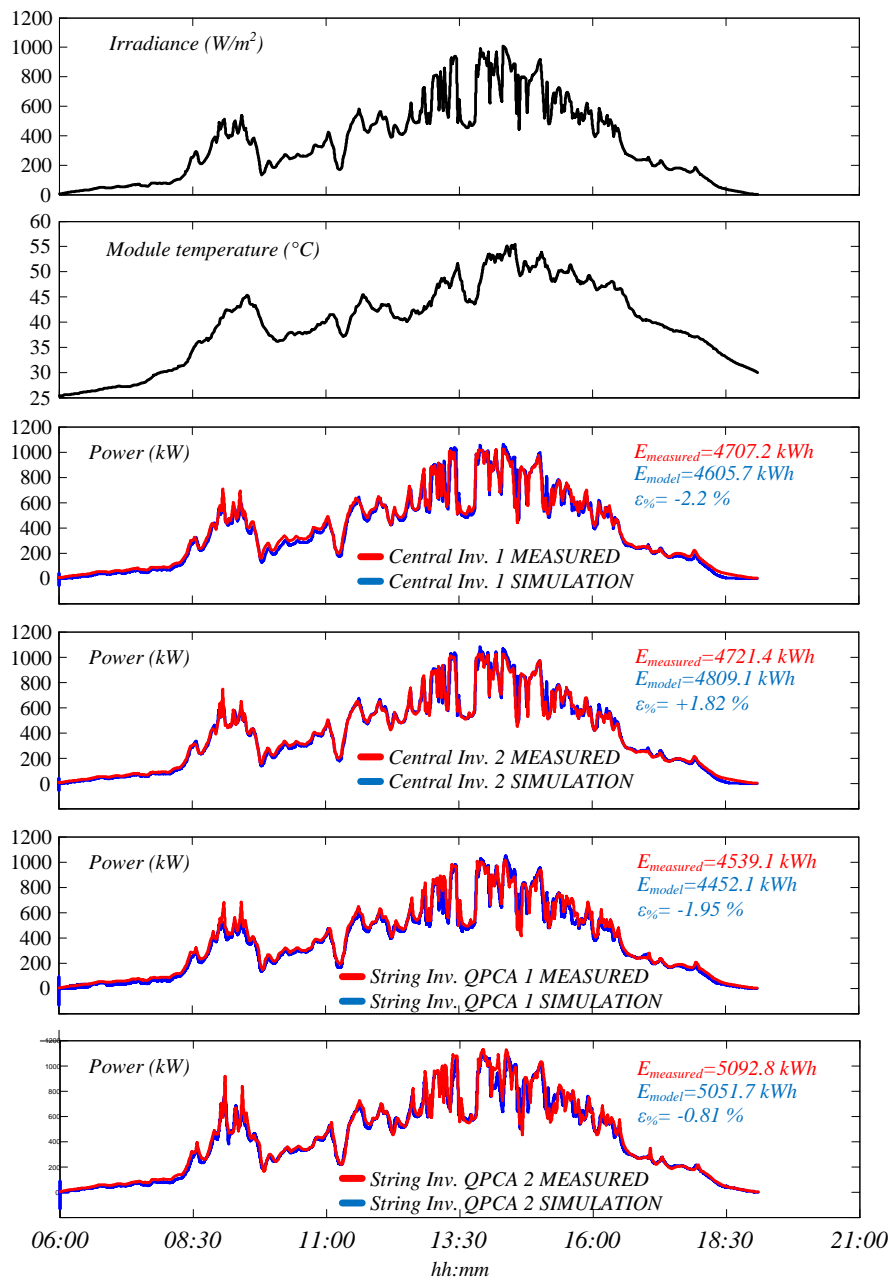


Figure 36. Another example of daily power curves measured in the experimental subfield of case study 1. Proposed model output (simulation) vs measured data. Calculation of percentage relative error

For each day, the calculation of the percentage relative error for the daily energy is pointed out:

$$\varepsilon_{\%} = \frac{E_{model} - E_{measured}}{E_{measured}} 100 \quad (72)$$

The maximum error caused by the model is around 2.2 ÷ 2.7% on a daily basis. This can be considered an accuracy index for the model also for those cases in which such model is exploited to simulate the plant behaviour in presence of missing data, PPC limitation, etc.

9.3 Experimental setup for battery testing

This and the following Sections describe the experimental tests carried out to validate the ESS models and algorithms introduced in this thesis.

Fig. 37 shows the workbench at the UNICT laboratory.

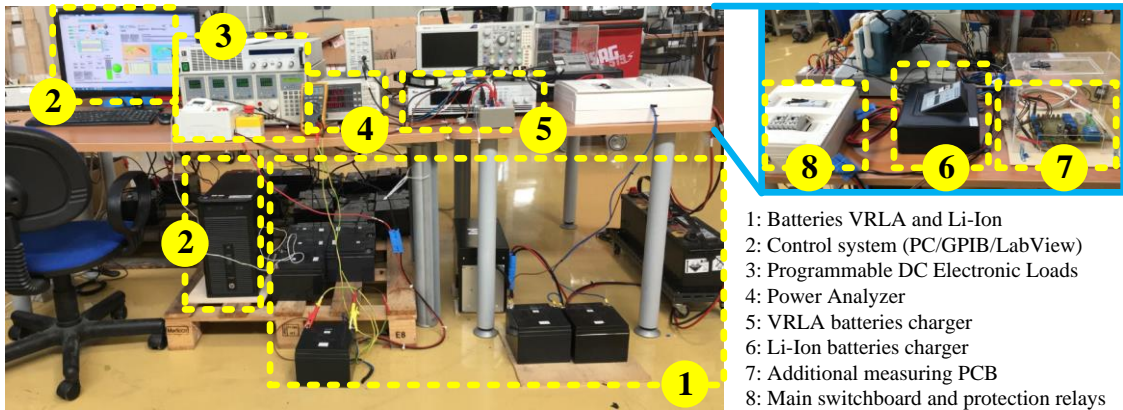


Figure 37. UNICT laboratory test bench for the experimental validation of ESS models and algorithms

9.3.1 Batteries under test

The typologies of batteries under test and the main technical data are shown in Tables 20-22.


Type	Technology	Picture	Main data
1	AGM VRLA LA battery		12 V, 27 Ah

Table 20. Battery under test type 1


Type	Technology	Picture	Main data
2	AGM VRLA LA battery		12 V, 7.2 Ah

Table 21. Battery under test type 2


Type	Technology	Picture	Main data
3	Li-ion LiFePO ₄ battery pack		51.2 V, 40 Ah

Table 22. Battery under test type 3

Some of the batteries belonging to these typologies were used in the past for laboratory tests regarding automotive applications in UNICT laboratories. In particular, they operated for about 2- 3 years as storage system in Multi-Drives test facilities [146], [147]. For this reason, some of the batteries used in experimental tests are aged batteries.

Several preliminary measurements have been performed for each type of ESS in order to compensate the voltage drop occurring at DC cables that connect the batteries to the electronic equipment.

9.4 ECM performance assessment and comparison

This Section deals with the experimental tests addressed to the performance assessment of ECM and on comparison of the main topologies presented in Section 6.2.1. The target of the experimental tests is the selection of the suitable ECM for its integration in the developed algorithms for the estimation of battery SOC and SOH.

9.4.1 Experimental comparison between ECMs

The comparison between the ECM as regards the accuracy is done by forcing charge or discharge processes for the batteries under test. For each current profile and for each battery, the voltage provided by models is compared to the measured voltage obtaining an error value that is an index of accuracy.

For the sake of example, the tests described here refers to a VRLA battery pack created by the interconnection of 8 batteries type 1 in Table 20. The connection scheme is in Fig. 38. Rated voltage of the battery pack under test is 24 V, capacity is 108 Ah.

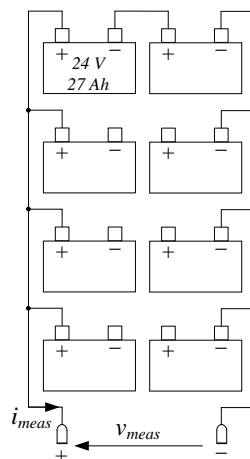
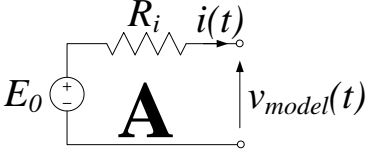
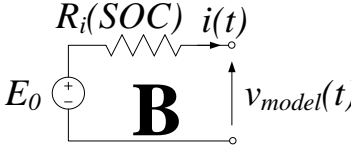
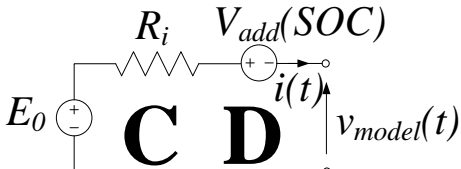
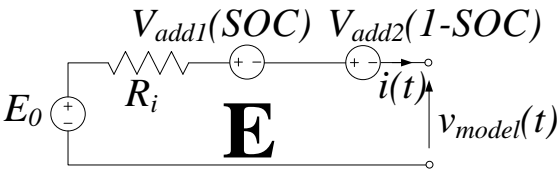
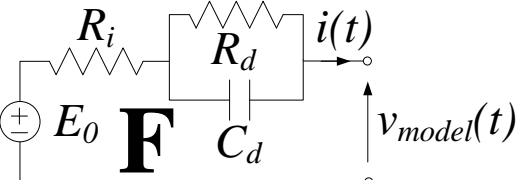


Figure 38. Electrical scheme of the 24 V 108 Ah VRLA battery pack under test

Technical details about the experimental test bench are in [145].

Considering the ECMs listed in Table 2, Table 23 reports the parameters assigned to each model. Identified values come from the implementation of the constrained minimums formulation described in Section 8.2.

ID	Parameters	Equivalent circuit
A	$E_0=25.355$ V $R_i=0.191$ Ω	
B	$E_0=25.274$ V $R_{i,SOC=100\%}=0.0165$ Ω $k=1.05$	
C	$E_0=25.517$ V $R_i=0.193$ Ω $\mu_s=4.806$	
D	$E_0=22.955$ V $R_i=0.215$ Ω $\mu_u=0.041$	
E	$E_0=25.832$ V $R_i=0.213$ Ω $\mu_1=1.176$ $\mu_2=0.281$	
F	$E_0=25.355$ V $R_i=0.181$ Ω $R_d=0.009$ Ω $C_d=5247$ F	
G	$E_0(SOC)$ datasheet $R_i=0.187$ Ω $R_d=0.010$ Ω $C_d=5071$ F $R_{sd}=100000$ Ω	

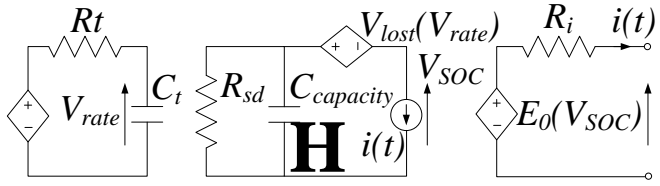
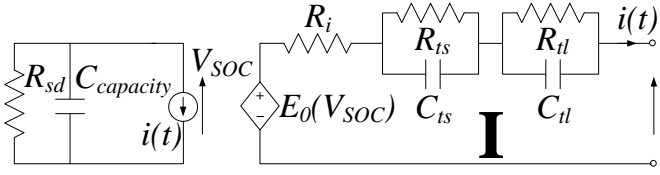
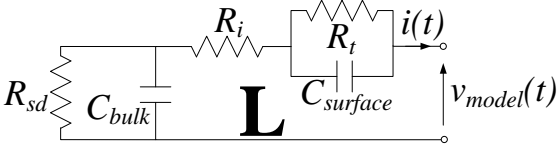
H	$E_0(V_{SOC})$ datasheet $R_t=0.197 \Omega$ $R_r=0.018 \Omega$ $C_r=951 \text{ F}$ $R_{sd}=100000 \Omega$ $C_{capacity}=388800 \text{ F}$	
I	$E_0(V_{SOC})$ datasheet $R_t=0.1973 \Omega$ $R_{ts}=0.018 \Omega$ $C_{ts}=5555 \text{ F}$ $R_{tl}=0.005 \Omega$ $C_{tl}=20000 \text{ F}$ $R_{sd}=100000 \Omega$ $C_{capacity}=388800 \text{ F}$	
J	Parameters in (13) calculated as in [91], [95], [96] from battery datasheet	See [91], [95], [96]
K	Parameters in (14) calculated as in [91], [97] from battery datasheet	See [91], [97]
L	$R_t=0.187 \Omega$ $R_r=0.010 \Omega$ $C_{surface}=5071 \text{ F}$ $R_{sd}=100000 \Omega$ $C_b=388800 \text{ F}$	

Table 23. ECM parameters for the 24 V 108 Ah VRLA battery pack under test

The experimental data have been acquired at different initial SOC values (ranging from 10 to 100 % with steps of 10%) and different currents (ranging from -5 to 20 A with steps of 1 A). Method applied to each model requiring a continuous evaluation of SOC is CCM [23].

The relation $E_0(\text{SOC})$ has been implemented from curve provided by the manufacturer. It is a quasi-straight line linking the extreme points ($E_0=22.8 \text{ V}$; SOC = 2 %) - ($E_0=26.4 \text{ V}$; SOC = 100 %) in the plane (E_0 ; SOC).

Figs. 39-41 show the voltage waveform provided by each model in comparison to

real data acquired for three different operating scenarios (environmental temperature is maintained around 20°C). The percentage relative error is also reported. In such a way, it is possible to highlight the differences between models.

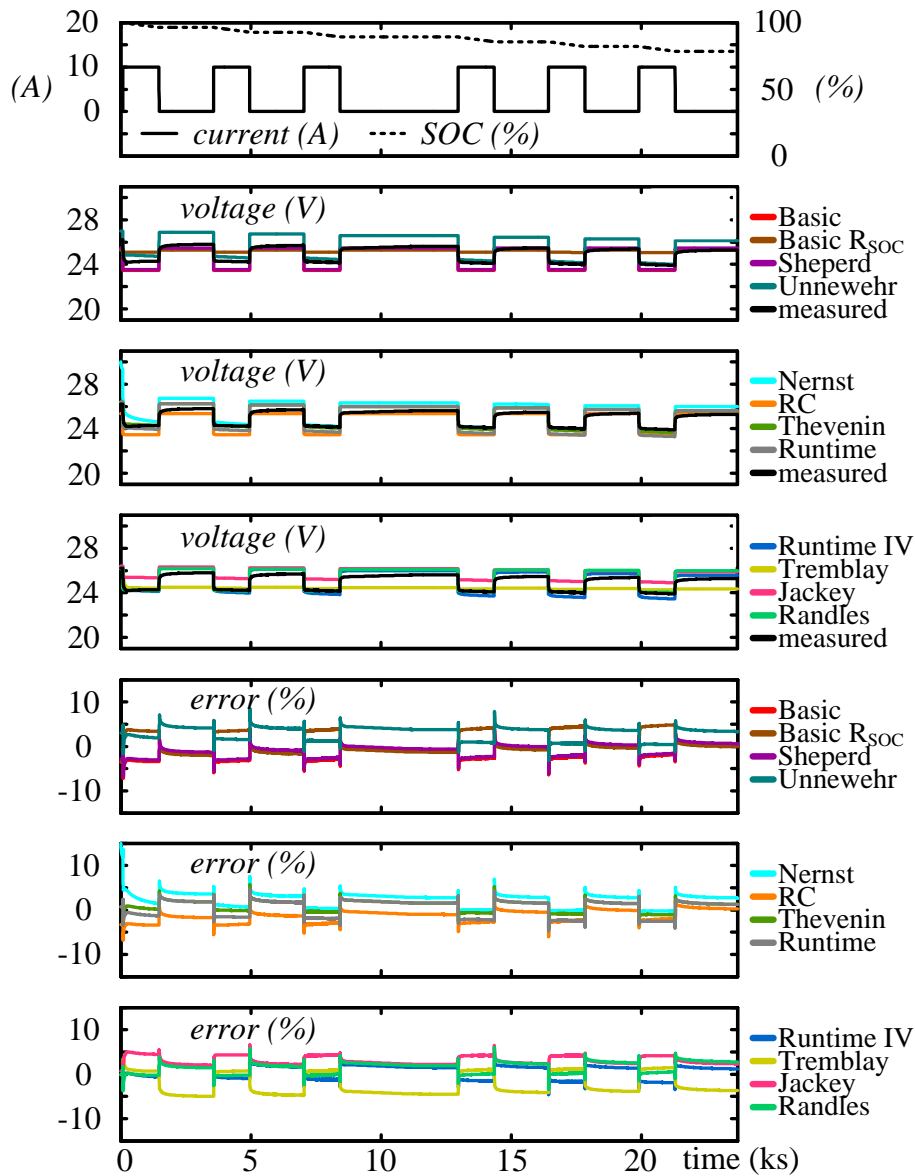


Figure 39. Test performed by forcing discharge operation for the 24 V 108 Ah VRLA battery pack under test. Comparison between voltage waveform provided by ECM and measured voltage. The relative error is also represented

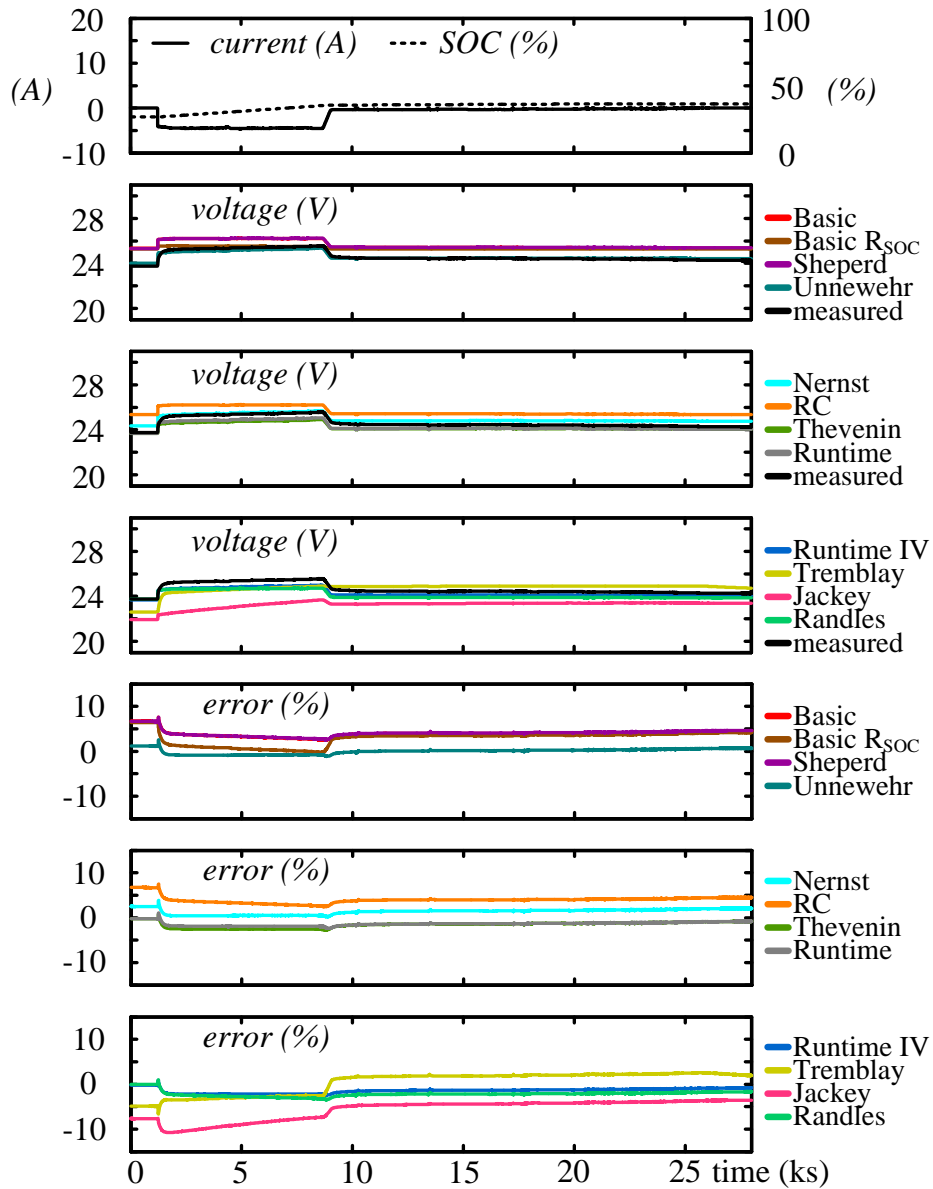


Figure 40. Test performed by forcing charge operation for the 24 V 108 Ah VRLA battery pack under test. Comparison between voltage waveform provided by ECM and measured voltage. The relative error is also represented

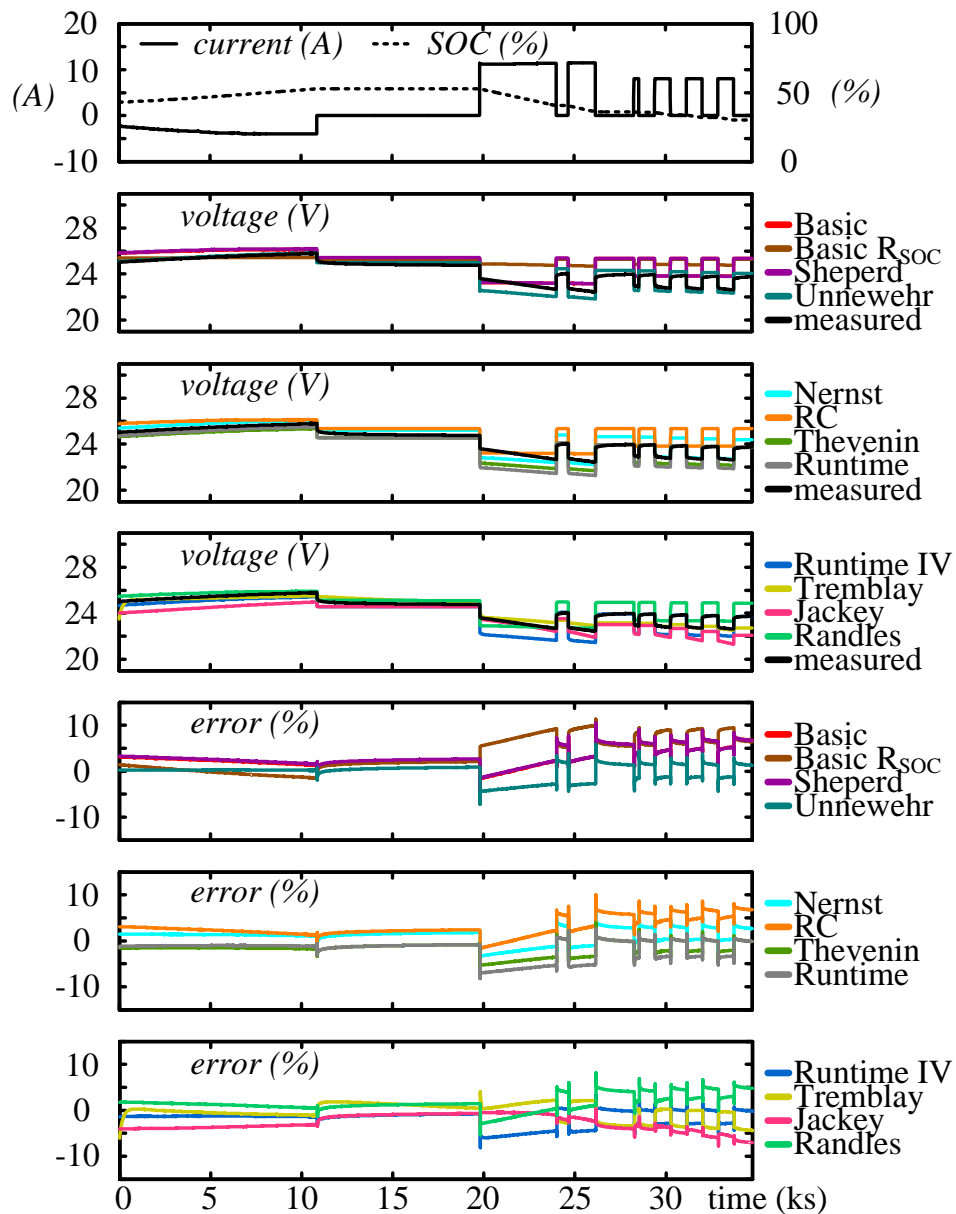


Figure 41. Test performed by forcing charge and discharge operation (CC and CP control) for the 24 V 108 Ah VRLA battery pack under test. Comparison between voltage waveform provided by ECM and measured voltage. The relative error is also represented

During the tests the battery pack, from an initial SOC value, is discharged (or charged) by forcing a given current. Time horizon ranges from a minimum of 2 hours to a maximum of 10 hours.

In order to consider a large range for current rates (considering both charge and discharge operations) and for SOC values, a set of 250 experimental tests at various

load conditions was scheduled. Couples of values assigned to current $i(t)$ and SOC cover the entire operating range for which the ESS is rated. Referring to accuracy in voltage estimation carried out by the ECMs, for each test the mean relative error has been calculated obtaining the 3D plots shown in Fig. 42. This mean value of the error for a time interval consisting of N_{time} samples $k=[1:N_{time}]$ is given by:

$$error_{mean} = \frac{\sum_{k=1}^N error_k}{N_{time}} \quad (73)$$

where $error_k$ is the percentage deviation between model voltage and measured voltage.

Starting from data displayed in Fig. 42, Figs. 43-44 show the mean error trend for different SOC values at a given current, while Figs. 45-46 show the mean error trend for different current rates at a given SOC value.

Looking at the results coming from described tests, it is confirmed that the more complicated models allow better accuracy with a reduced error. However, each model implies large variation in error waveform.

The mean error in voltage estimation provided by circuit models is strongly affected by the actual ESS state. In particular, a strong dependence on the SOC value can be recognized. Large deviations occur at low SOC values, Figs. 41, 43 and 44.

On the contrary, looking at Figs. 41, 45 and 46, the influence of current variations on voltage estimation is clearly more limited.

Models specifically designed for software platforms and exploitable for several applications, such as Tremblay and Jackey models, involve large inaccuracies in some specific working points. In other words, a large adaptability causes significant inaccuracies in many cases, Figs. 39 and 42.

Charge operation modelling typically implies a strong degradation in accuracy level due to complicated phenomena to model, Figs. 40 and 42.

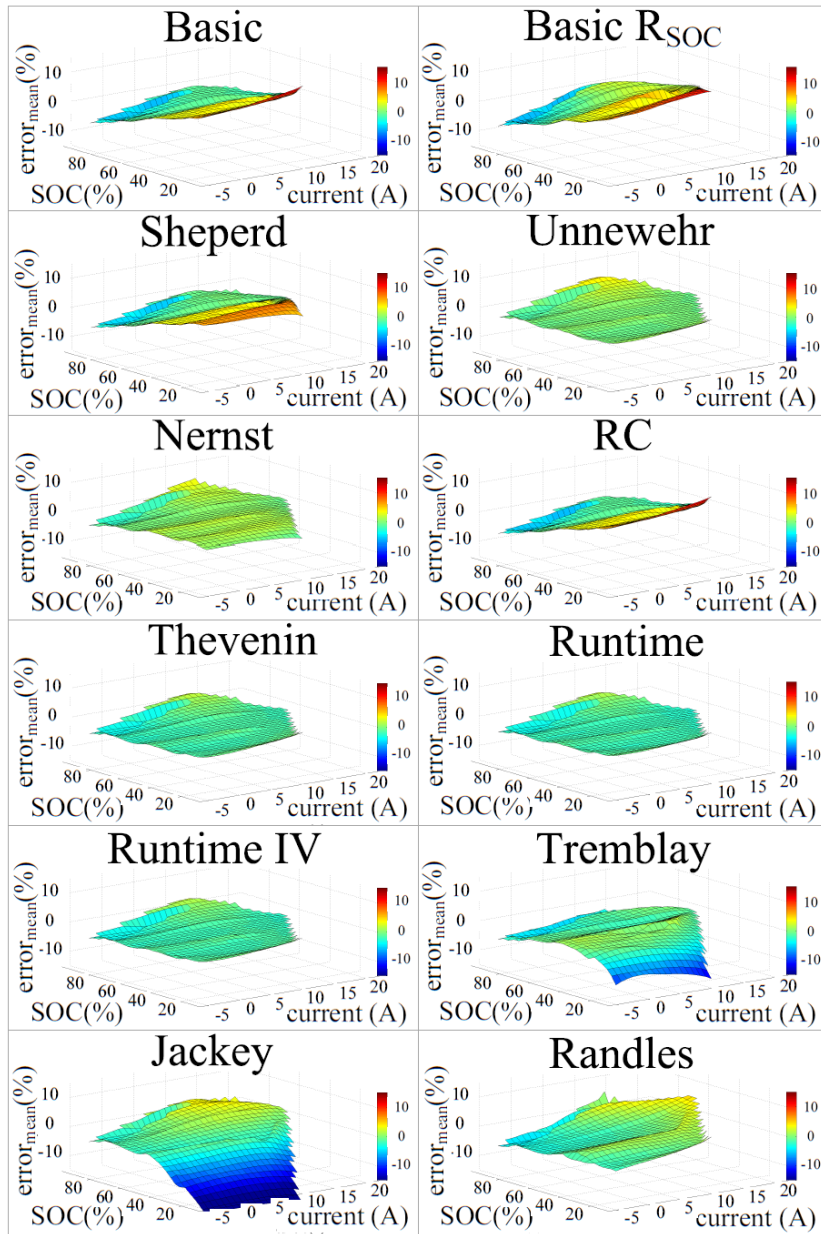


Figure 42. 3D plots of the mean relative error related to the voltage estimation carried out by each ESS equivalent circuit model, for different current rates and SOC values.

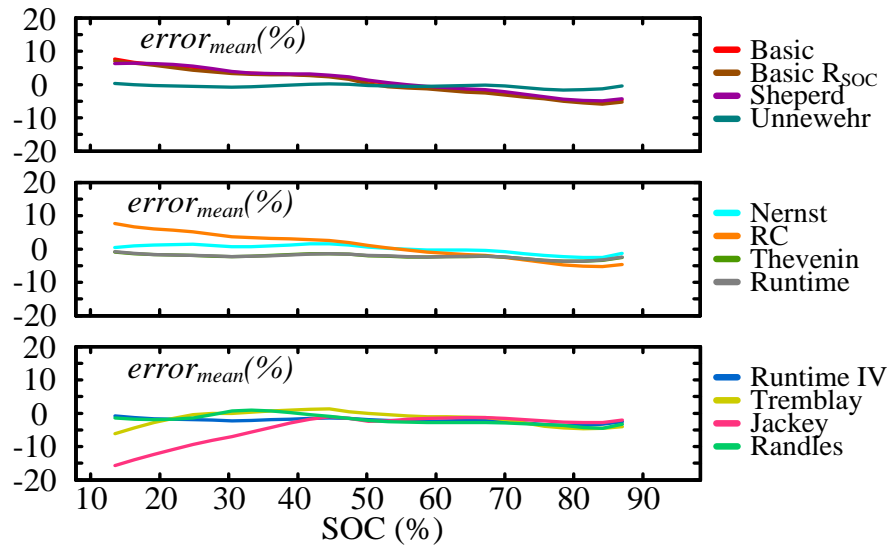


Figure 43. Mean relative error vs SOC. Selected current in 3D plots is -2 A

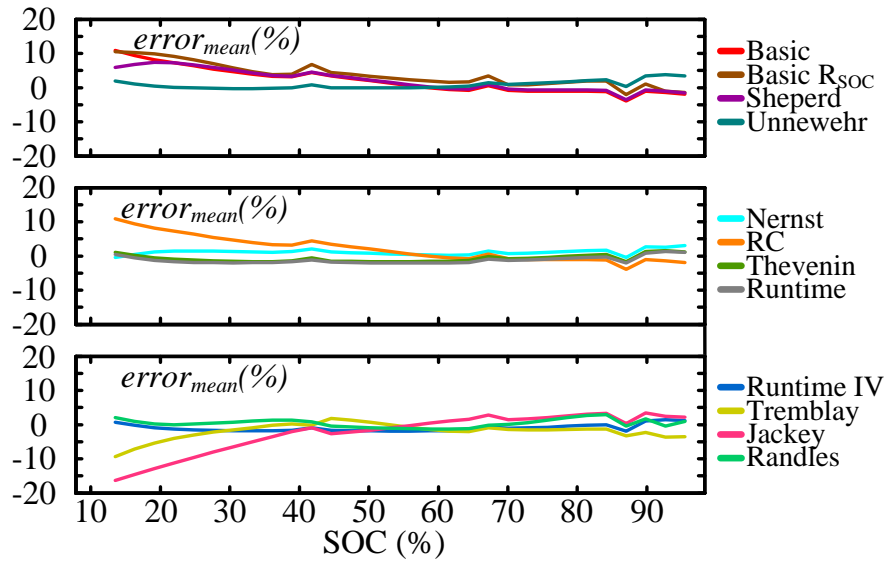


Figure 44. Mean relative error vs SOC. Selected current in 3D plots is 10 A

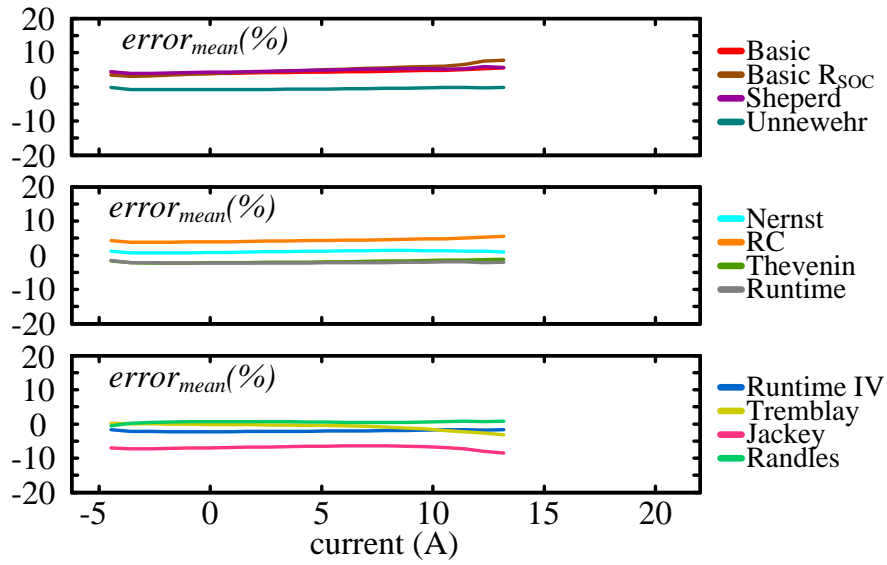


Figure 45. Mean relative error vs SOC. Selected SOC in 3D plots is 30 %

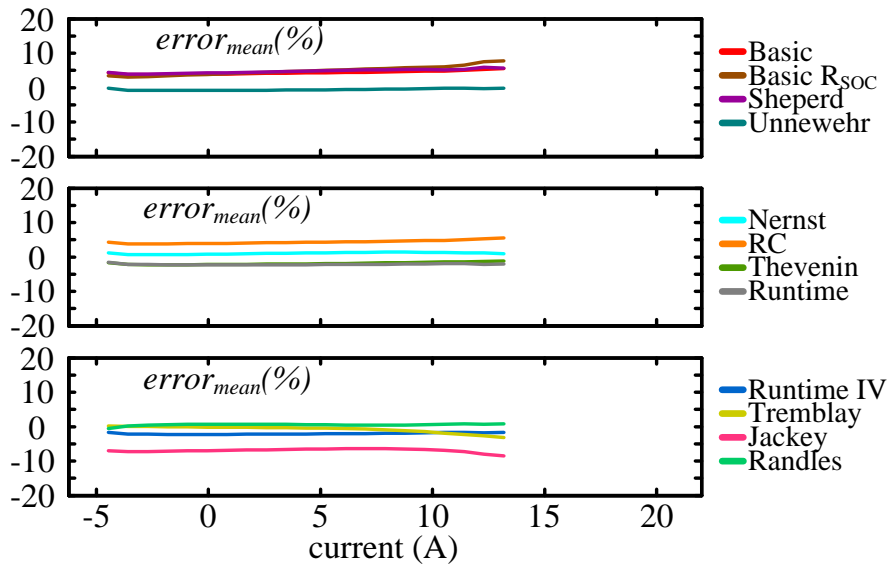


Figure 46. Mean relative error vs SOC. Selected SOC in 3D plots is 80 %

9.4.2 Sensitivity to parameters uncertainty

Collected experimental data allows to carry out additional information about the sensitivity of each model to parameters uncertainty [145]. Let us consider the working cycle represented in Fig. 39, which includes charging, CC and CP discharging phases.

Referring to voltage estimation, for each ESS circuit model the mean error $error_{mean,o}$ is calculated by equation (73) for the selected scenario, considering the optimal set of parameters $[x_1, \dots, x_n]$ identified by means of equation (70). This error value is compared to the mean error $error_{mean,p}$ occurring in case of perturbed values assigned to a single parameter $x_i=x_{i,p}$ or rather in case of parameter uncertainty:

$$error_{mean,p} = error_{mean}|_{x_i=x_{i,p}} \quad (74)$$

For each model, the sensitivity to the selected parameter uncertainty is calculated by assigning $x_{i,p}=1.1 x_{i,o}$:

$$sens|_{x_{i,p}=1.1 \cdot x_{i,o}} = \frac{error_{mean,p} - error_{mean,o}}{error_{mean,o}} \cdot \frac{x_{i,o}}{x_{i,p} - x_{i,o}}|_{x_{i,p}=1.1 \cdot x_{i,o}} \quad (75)$$

Sensitivity to uncertainty $x_{i,p}=0.9 x_{i,o}$ is calculated in the same way.

Fig. 47 shows a comparison between ECMs based on sensitivity to uncertainty of the main parameters. For each parameter x_i , a perturbed value $x_{i,p}=1.1 x_{i,o}$ is assigned to the circuit model. Fig. 48 refers to the case $x_{i,p}=0.9 x_{i,o}$.

From Figs. 47 and 48, it emerges that a large sensitivity is usually related to the uncertainty on the no-load voltage value E_0 . This statement can be reported for each model except for the Randles one since it does not include the E_0 parameter.

It is also clear that the sensitivity related to parameters representing the dynamic behavior of the ESS (e.g. R_t and C_t in Runtime model) can be often neglected.

Referring to parameters representing the actual battery capacity (e.g. $C_{capacity}$ in the Runtime IV model), sensitivity values are not so large. Such sensitivity could be much larger if a longer time horizon is considered, for example if SOH is taken into account.

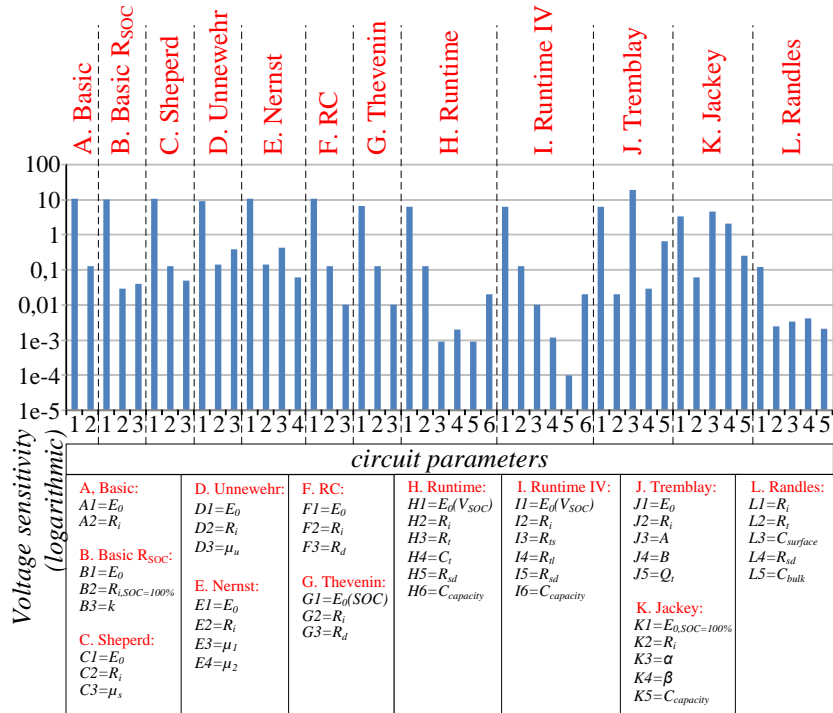


Figure 47. ECM comparison based on voltage estimation error sensitivity to parameters uncertainty, perturbation of parameters is $x_{i,p}=1.1 x_{i,o}$

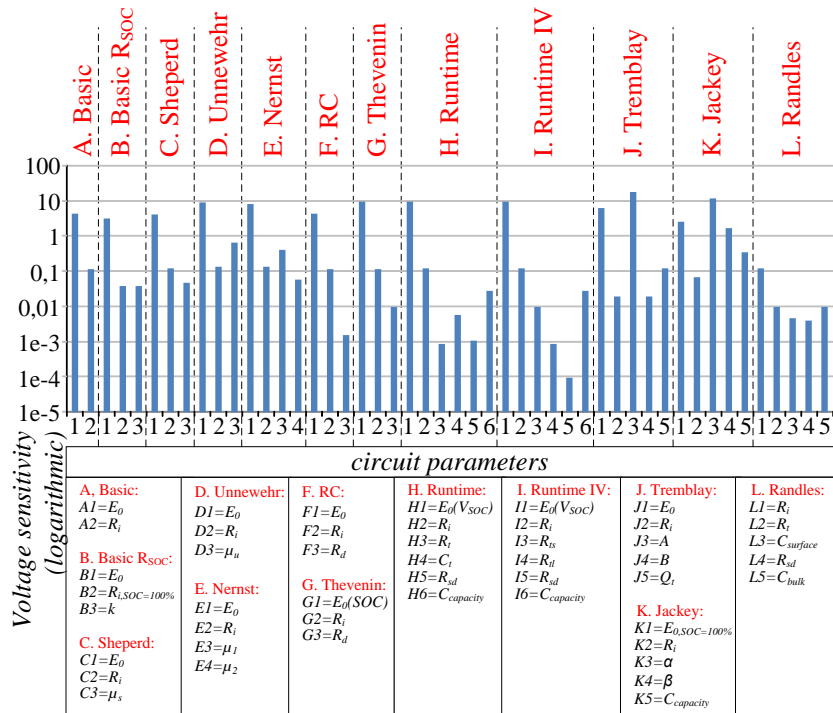


Figure 48. Circuit models comparison based on voltage estimation error sensitivity to parameters uncertainty, perturbation of parameters is $x_{i,p}=0.9 x_{i,o}$

9.4.3 Selection of the ECM for this work

In previous Sections, a comparison on main ECMs available in literature for ESS modelling has been presented. An extensive comparative investigation including several experimental tests has been performed based on suitable criteria related to accuracy requirements. Moreover, the sensitivity to parameters uncertainty has been investigated for each model.

On the basis of this results and including the information reported in Section 6.2.1, some conclusions can be reported as follows.

Simpler models ensure fast implementation but their precision in modelling the real behavior is typically not satisfactory. Their implementation is a suitable option in few cases, for example when accuracy is not a priority as well as when the analysis is focused on a restricted operating area. On the contrary, the more complicated models lead to a satisfactory accuracy in most cases. However, their complexity can be sometimes an obstacle due to the amount of training data required for parameter identification.

Because of large dynamics range that can occur in ESS operation, the accurate tracking of transient phenomena requires at least the presence of one series RC branch in ECM.

The inclusion of other specific physical phenomena such as temperature effect, memory effect, etc. requires particular circuit topologies with time-varying parameters whose values depend on the environmental and operating conditions.

From the assessment of sensitivity to parameters uncertainty, it has been recognized that a large sensitivity is related to uncertainty on the no-load voltage E_0 .

A graphical recap of the results coming from the ECM performance assessment is in the radar charts of Fig. 49.

Matching the information coming from the literature review and the experimental data it is possible to state that, in most cases, Thevenin, Runtime and Randles models represent the best compromise between performance and complexity. These results

9.5 Tests for validation of ESS state estimation algorithm 1

This Section described the experimental tests for the validation of ESS state estimation algorithm 1 described in Section 6.5.

The experimental test bench is the one described in Section 9.3. Batteries under test belong to the typologies shown in Tables 20-22.

The approximation of $R_i(SOC)$ curve used in algorithm 1 is in the form of 2nd or 3rd order polynomial functions implemented by means of the look-up tables " $R_{i,discharge}$ value" and " $R_{i,charge}$ value" shown in Fig. 17.

Figs. 50-52 show the $R_i(SOC)$ curve obtained from experimental tests on three batteries type 1. Note that, depending on the specific battery under test, fitting could require a third order polynomial approximation.

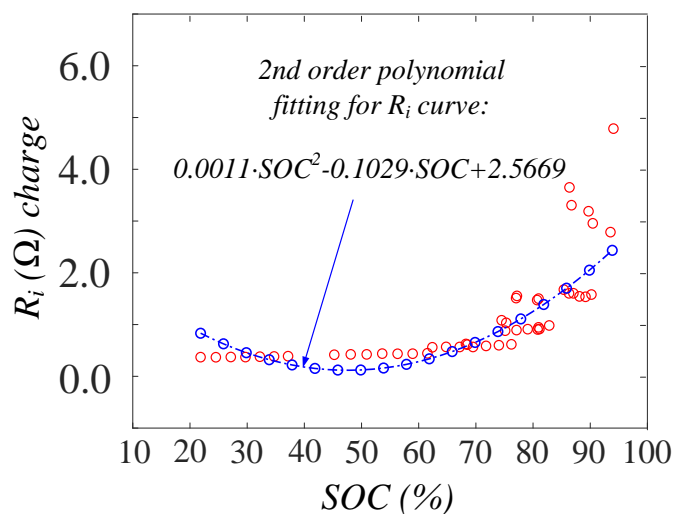


Figure 50. Variation of R_i with SOC during a charge process, battery type 1

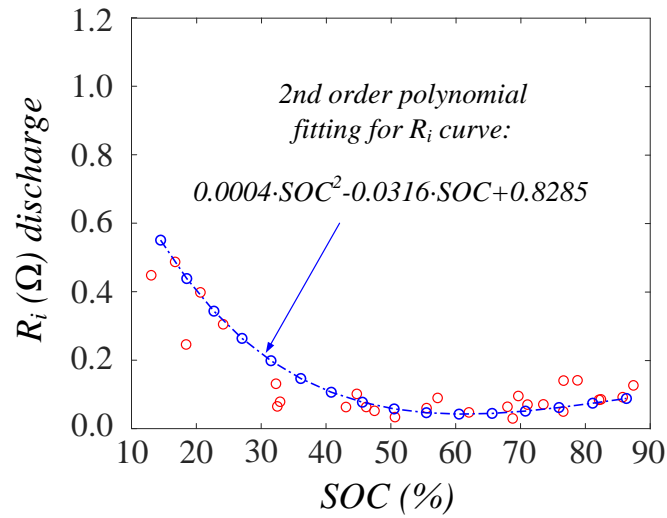


Figure 51. Variation of R_i with SOC during a discharge process, another battery type 1

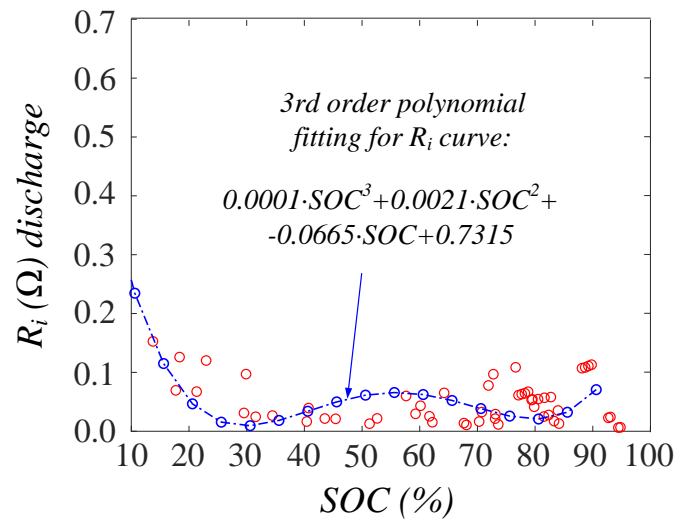


Figure 52. Variation of R_i with SOC during a discharge process, another battery type 1

As regard the relaxation voltage, that is crucial for the implementation of estimation algorithm 1, the relaxation behavior of batteries has been recorded by performing preliminary laboratory tests at different SOC and forcing several charging and discharging processes.

Hence, in order to build a relaxation voltage prediction function, *OCV* was measured at different time intervals (10 s, 20 s, 30 s, 40 s, 50 s, 60 s, 1000 s) just after

the current becomes zero, creating a fitting curve for each of these cases. Likewise, the OCV value after 12 h has been recorded and considered as OCV_{relax} . Example curves obtained for charging and discharging processes of some batteries are shown in Fig. 53 and 54.

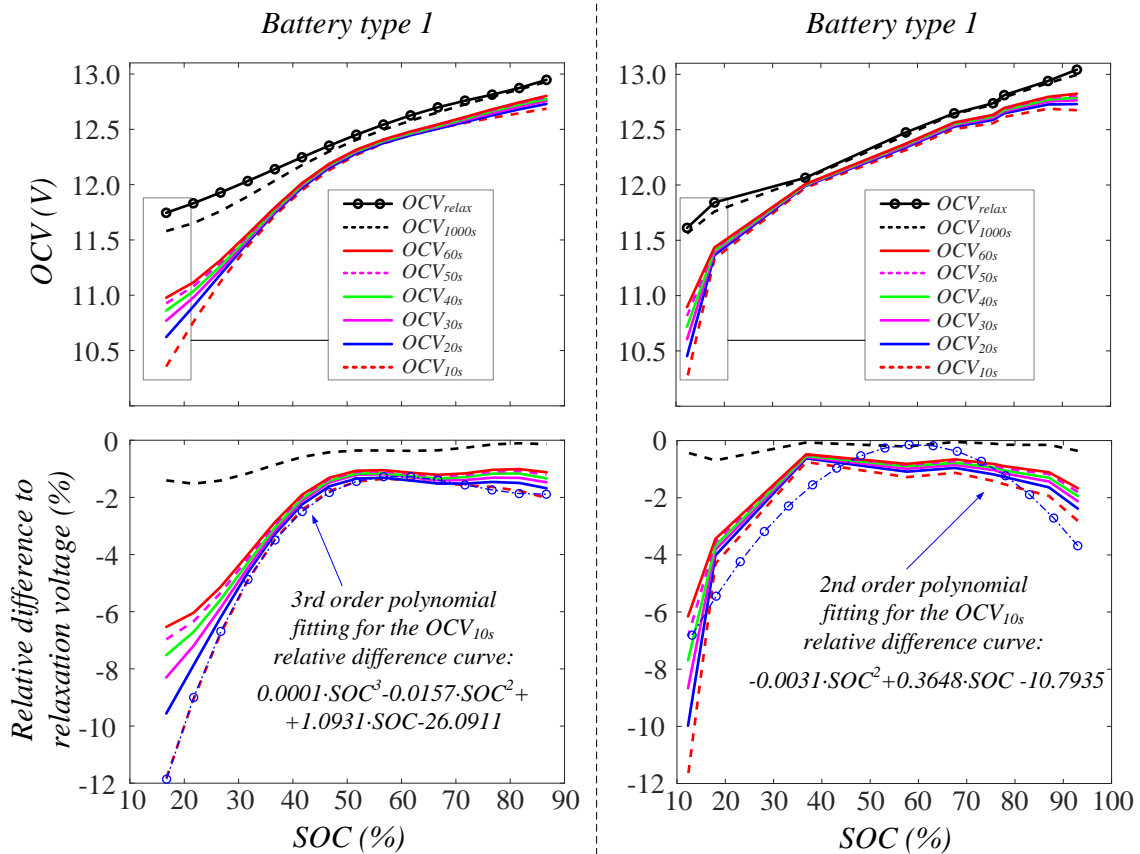


Figure 53. Comparison between the OCV_{relax} curve after a discharge and the measured one at different time intervals. The polynomial fitting curve for the OCV_{10s} terminal voltage is also shown. Charts are related to two batteries type 1

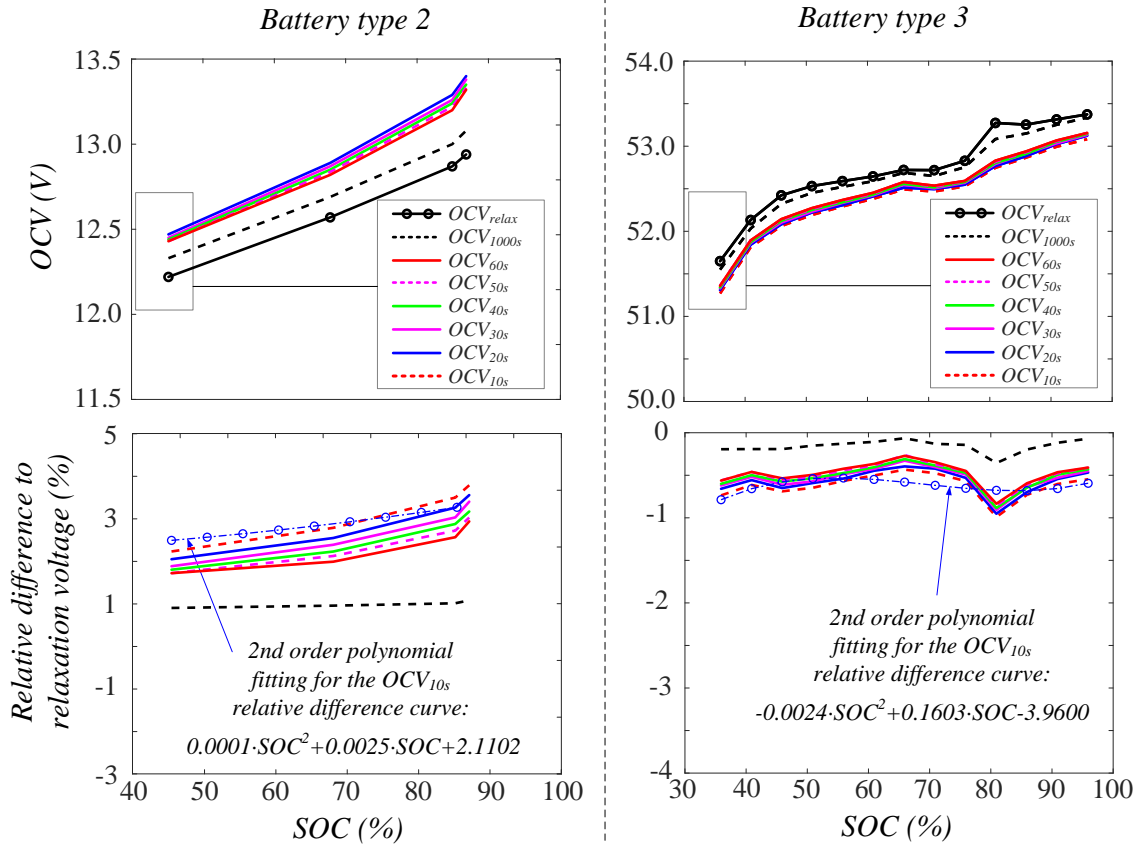


Figure 54. Left: Battery belonging to typology 1, comparison between the OCV_{relax} curve after a charge and the measured one at different time intervals. Right: Battery belonging to typology 3, comparison between the OCV_{relax} curve after a discharge and the measured one at different time intervals. The polynomial fitting curve for the OCV_{10s} terminal voltage is also shown for both batteries

The relative error Δ_{10s} committed considering the OCV_{10s} in place of the OCV_{relax} , is calculated through (76) for each SOC value reached during experimental tests. It was experimentally found that Δ_{10s} is 2% on average.

$$\Delta_{10s} = \frac{OCV_{10s} - OCV_{relax}}{OCV_{relax}} \quad (76)$$

The interval time 10 s was chosen to test the proposed algorithm as it is the minor interval among the selected. It allows to obtain a fast estimation even for high dynamic applications.

As shown in Fig. 53 and 54, the Δ_{10s} curve has been approximated with a polynomial function. Then, this function is used to estimate the OCV_{relax} using the OCV_{10s} by means of (77) that is the reverse equation of (76).

$$OCV_{relax} = \frac{OCV_{10s}}{1 + \Delta_{10s}} \quad (77)$$

The effect of current rate on relaxation process has been neglected. This assumption is fine for the applications considered in this thesis because high dynamic performance is not required so that current rate is usually very low.

About the practical implementation of the algorithm 1, Fig. 55 shows an experimental scenario as example of implementation of the Boolean logic described in Section 6.5. Such logic is used to integrate the PI-based observer with the OCV_{10s} polynomial prediction function.

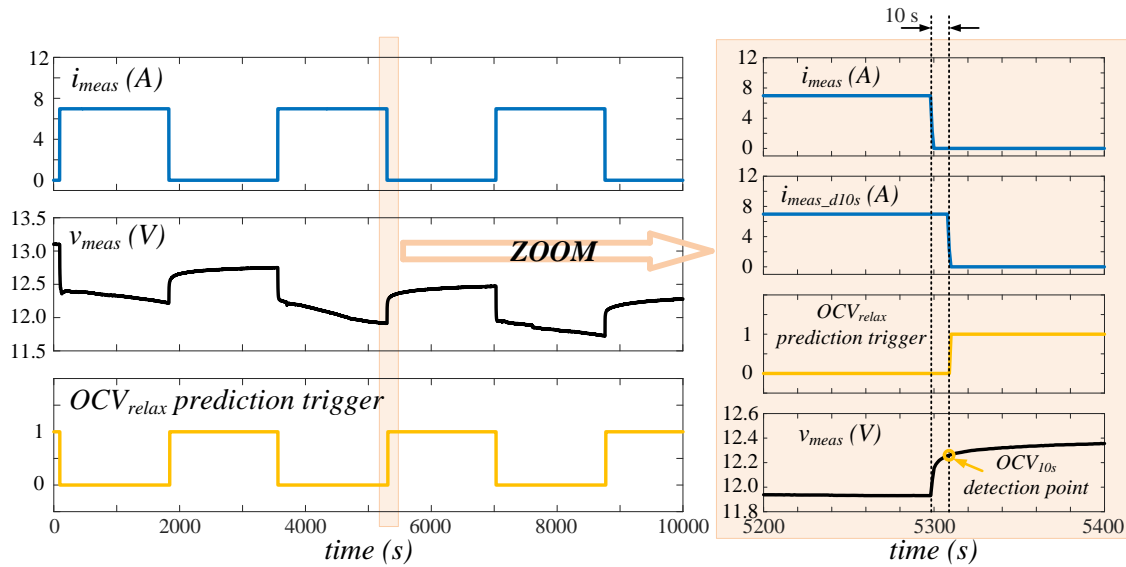


Figure 55. Experimental test example. Implementation of the Boolean logic for the identification of the OCV_{10s} value

Fig. 56, related to a discharging process, shows the result of the algorithm 1 in terms of SOC estimation. It is highlighted how the obtained SOC curve is aligned with the one traced by applying CCM.

Finally, an accurate estimation of SOC with a low computational load is obtained. Moreover, the proposed method does not suffer from the well-known issues occurring in the implementation of CCM.

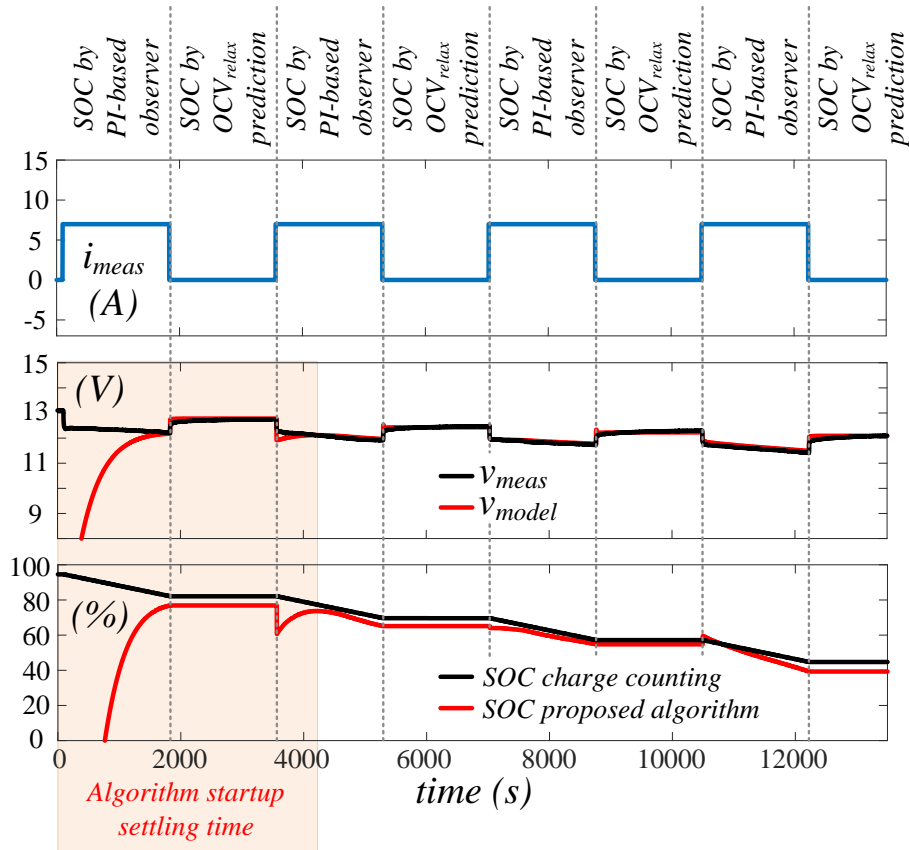


Figure 56. Example of experimental test on a battery type 1. Estimation algorithm 1 provides an estimation of SOC that is very close to the SOC curve calculated by the popular CCM. The proposed method does not suffer from the well-known issues occurring in the implementation of the CCM

A brief recap on the main characteristics of the ESS state estimation algorithm 1 is here:

- the real-time algorithm 1 includes a PI-based observer and a voltage relaxation prediction function. The latter is added under the consideration that the SOC of the battery can be reliably deduced from relaxation voltage;

- this special prediction function is designed from extensive experimental tests addressed to link the relaxation voltage to the terminal voltage measured just after the completion of a charging or a discharging process;
- in this way, it is possible to estimate the SOC in a fast way avoiding long waiting time;
- the prediction function is effectively exploited to periodically correct the SOC tracking provided by the PI-based observer.

9.6 Tests for validation of ESS state estimation algorithm 2

This Section describes an example of the experimental tests carried out for the validation of ESS state estimation algorithm 2 described in Section 6.6.

The experimental test bench is the one described in Section 9.3. Batteries under test belong to typologies shown in Tables 20-22.

Fig. 57 shows an experimental test in which a battery type 1, manufactured in 2016 but rarely used, is discharged using a square wave current. The mixed algorithm is implemented following the steps shown by the flow chart in Fig. 21. From the implementation of CCM and ECM continuously used in sequence, the SOH estimation process leads to a final value of $78 \% \pm 2 \%$, see Table 24.

A brief recap on the main characteristics of ESS state estimation algorithm 2 is here:

- two basic estimation methods are combined into a mixed algorithm with the purpose of estimating the SOH of battery packs with a good accuracy while limiting the computational effort
- experimental validation is carried out for other battery packs having different size and electrochemical technology
- as for the algorithm 1, a prediction function for the relaxation voltage could be integrated in the form of an additional feature for fast dynamic applications

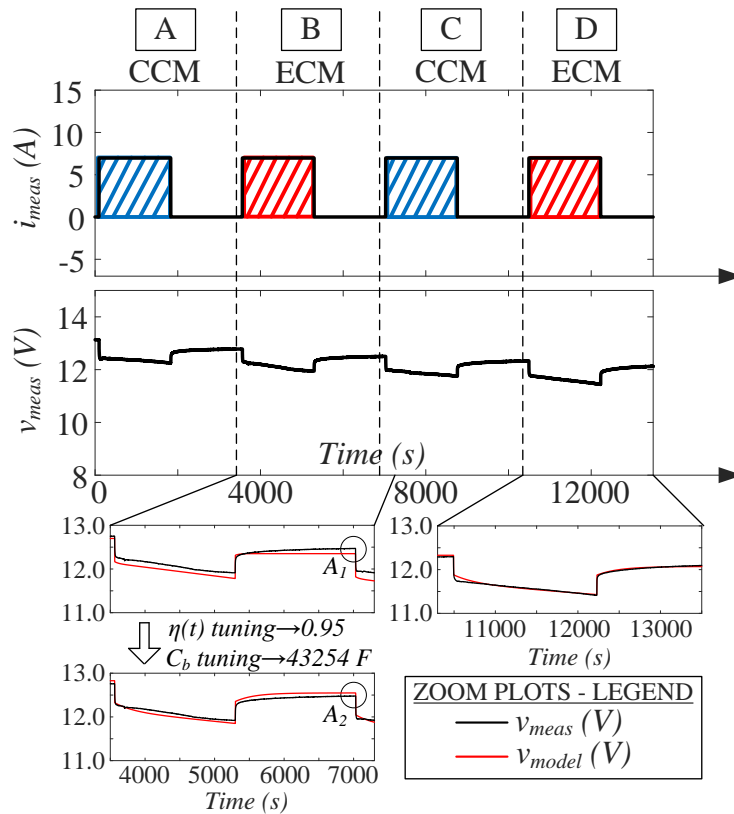


Figure 57. Implementation of the proposed algorithm for a battery type 1. Numerical results for each time period (A to D) are reported in Table 24. Circle areas A1 and A2 in period B: the proper tuning of parameters improves the accuracy of ECM in quasi-relaxation state. If such tuning is not performed, difference between v_{model} and v_{meas} will increase over time, as evident in A1, leading to significant errors in terms of SOH estimation

→ → → → → → → → → → → →			
A	B	C	D
CCM	ECM	CCM	ECM
$Q = 3.37 \text{ Ah}$ $\text{SOC}(t_0) = 94.3 \%$ $\text{SOC}(t_1) = 75.0 \%$ $\eta(t) = 1$ $\text{SOH} = 64.6 \%$	$\eta(t) = 0.95$ $\text{SOC}(t_1) = 64.0 \%$ $\text{SOH} = 80.1 \%$	$Q = 3.36 \text{ Ah}$ $\text{SOC}(t_0) = 64.0 \%$ $\text{SOC}(t_1) = 48.7 \%$ $\eta(t) = 0.95$ $\text{SOH} = 77.1 \%$	$\eta(t) = 0.95$ $\text{SOC}(t_1) = 36.6 \%$ $\text{SOH} = 78.4 \%$
A	B	C	D

Table 24. Numerical data for time periods in Fig. 57

9.7 Experimental assessment of PC and EC

To better explain the importance of the quantities PC and EC and the calculation methodology described in Section 6.7, this Section shows some experimental examples.

The experimental test bench is the one introduced in Section 9.3. The power electronics converters, used to force the charge and discharge operation of batteries, are described in [126]. The ESS state estimation technique, described in the same paper, is the algorithm 1 with minimal changes related to the specific application. Such changes are not relevant for the present analysis.

The experimental tests refer to a VRLA battery pack created by the interconnection of 8 batteries belonging to typology 1 in Table 20. The connection scheme is in Fig. 38. Rated voltage of the battery pack under test is 24 V, rated capacity is 108 Ah.

Fig. 58 shows forced current, measured and estimated voltage and SOC during a discharge sequence. Working temperature is 20°C. SOC estimation, provided by algorithm 1, is compared to SOC calculated via CCM. The estimated value of SOH is 93 %.

The PC assessment, performed as described in Section 6.7, is shown in Figs. 59-60 for the time instants $t_{0,a}$ and $t_{0,b}$ in Fig. 58. PC is calculated for different time horizons Δt .

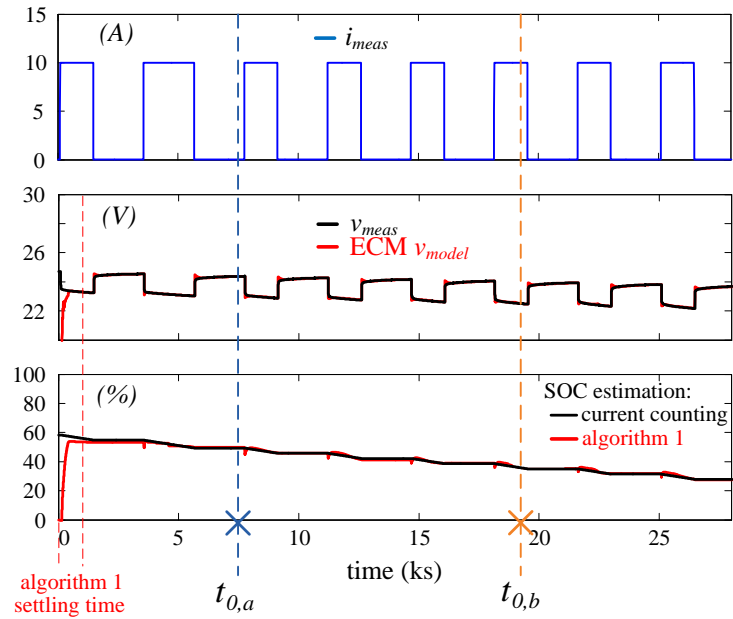


Figure 58. Experimental test performed by forcing discharge operation on a 24 V 108 Ah VRLA battery pack. SOC estimation, provided by the algorithm 1, is superimposed to the SOC calculated via CCM. Estimated SOH is 93%

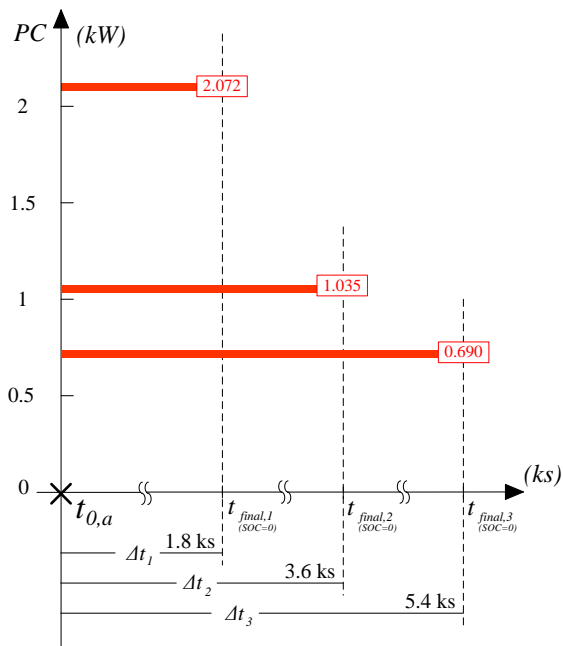


Figure 59. Power capability prediction during discharge. Initial time instant $t_{0,a}$ is pointed out in Fig. 58 (zero current state)

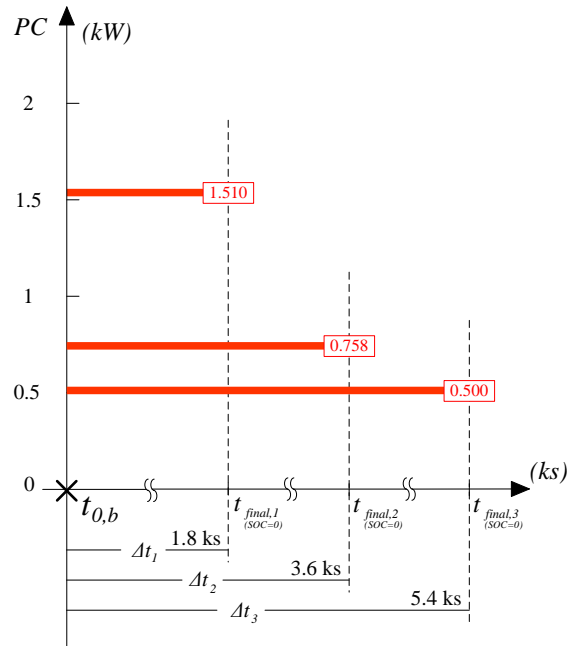


Figure 60. Power capability prediction during discharge. Initial time instant $t_{0,b}$ is pointed out in Fig. 58 (non-zero current state)

Fig. 61 shows a charging sequence. PC graph is in Fig. 62 for the time instants $t_{0,c}$. PC is again calculated for different time horizons Δt .

Here are some brief observations coming from these experimental results:

- the real-time estimation of SOC and SOH, made possible by the introduced estimation algorithms, allows for a fast and easy calculation of PC and EC that can be evaluated at any time;
- as expected, PC decreases as Δt increases;
- EC can be immediately calculated as the product between PC and Δt .

It is worth noting that in the examples shown above, at a given time instant ($t_{0,a}$, $t_{0,b}$ or $t_{0,c}$) the value of EC keeps constant for different Δt values. This is due to the simplified calculation of PC considered in this work following the primary target to maintain a low complexity at the expense of accuracy. Anyhow, a better accuracy is easily obtained by introducing efficiency factors in formulas (20) and (21) in order to take into account Peukert effect, thermal losses and so on.

In following Sections, the calculation of PC and EC is carried out taking into account the reduction of actual battery capacity at high current rates. This is the main phenomenon affecting the PC.

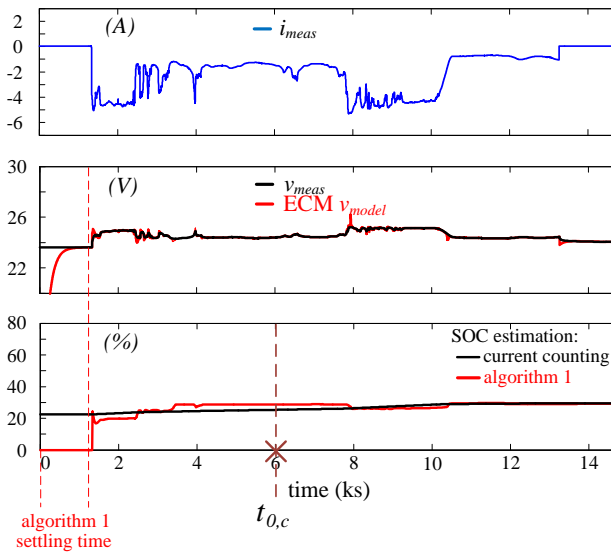


Figure 61. Experimental test performed by forcing charge operation for a 24 V 108 Ah VRLA battery pack. SOC estimation, provided by the algorithm 1, is superimposed to the SOC calculated via CCM. Estimated SOH is 93%

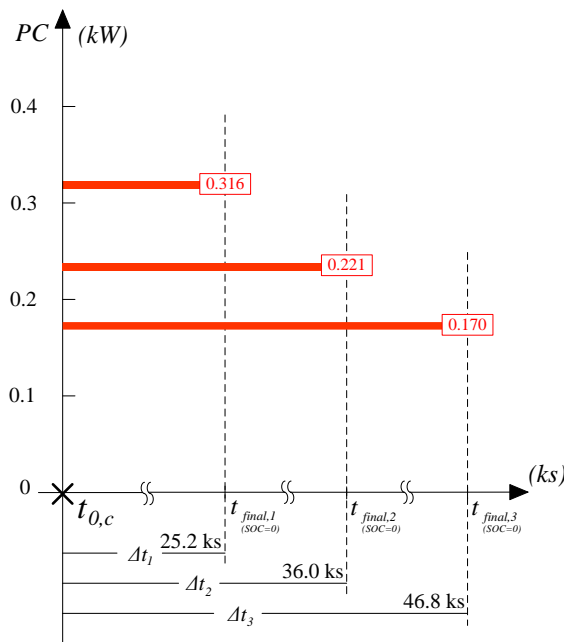


Figure 62. Power capability prediction during charge. Initial time instant $t_{0,c}$ is pointed out in Fig. 61 (non-zero current state)

Chapter 10 - Case study 1, PV plant in Brazil

The case study 1 of this work is a 300 MW PV plant in Brazil. Two pictures are in Fig. 63. The PV field is connected to the 34.5 kV 60 Hz utility grid through power transformers. Each transformer is connected to a 2.5 MW subfield. PV modules are mounted on a horizontal single-axis tracking system.



Figure 63. Pictures of the 300 MW PV plant in Brazil representing the case study 1 of this work

A 5 MW (DC rated power) cluster was realized for testing purpose with the objective to compare the performance of distributed converters vs central inverters. The total AC nominal power is 4.1 MW. Power configurations of the two subfields under test, being part of the experimental cluster, are in Figs. 64-65. Table 25, that is a copy of Table 19, summarizes technical data for the main power components.

The number of PV modules connected to each conversion system is exactly the same. In fact, the DC rated power is 2570.4 kW for both the subfields. In such a way, the comparison is consistent. PV strings are composed by 30 PV modules in series. The rated power of PV modules is 315 W.

In the 2.5 MW subfield with central converters, Fig. 64, there are two inverters whose rated power is 1025 kVA, fan cooled, mounted into an electric cabin. Each inverter has a modular structure, in fact it is internally assembled by the connection of 10 sub-inverters i.e. 10 IGBT stacks. The AC power can reach about 1045 kVA in case of unity power factor. The power transformer has double low voltage windings, each one powered by a central inverter.

Each central inverter receives 6 lines from 6 string boxes. 5 string boxes have 24 strings in parallel, 1 string box has 16 PV strings in parallel. Here is a resume for the

central inverters subfield:

- central inverter 1: 1 inverter, 1 MPPT, rated DC power = 1285.2 kW, rated AC power = 1025 kW, DC/AC ratio = 125.40 %
- central inverter 2: 1 inverter, 1 MPPT, rated DC power = 1285.2 kW, rated AC power = 1025 kW, DC/AC ratio = 125.40 %
- central inverter 1 + central inverter 2: 2 MPPTs, rated DC power = 2570.4 kW, rated AC power = 2050 kW

In the 2.5 MW subfield with distributed converters, Fig. 65, each string inverter has a rated power of 60 kVA but can reach 66 kW in case of unity power factor and ambient temperature below 30° C. String converters, mounted in the field without using cabinets and without fan cooling, are grouped in a cabin close to the transformers using AC parallel switchboards named QPCA. The power transformer has double low voltage windings, each one powered by a QPCA.

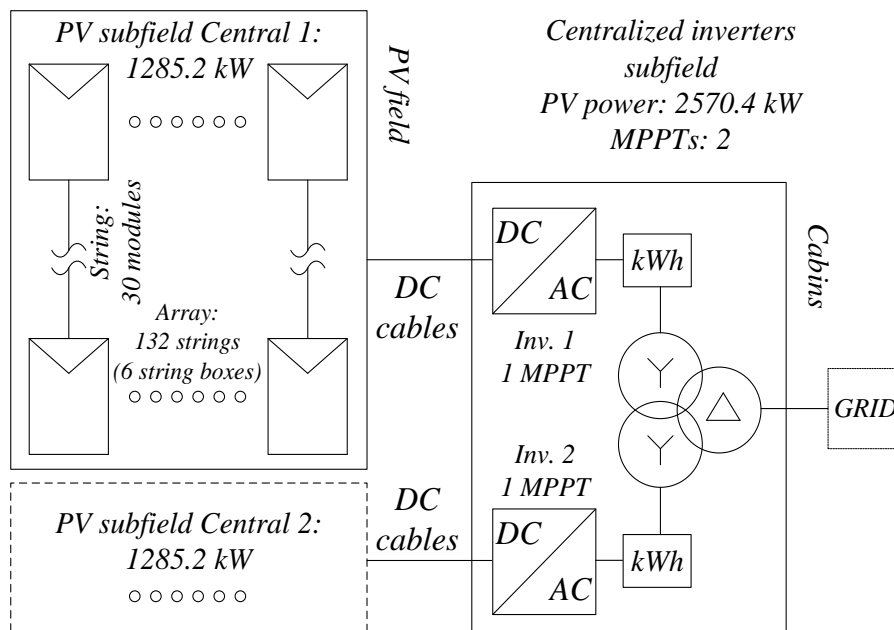


Figure 64. Power system configuration of the 2.5 MW subfield with central inverters

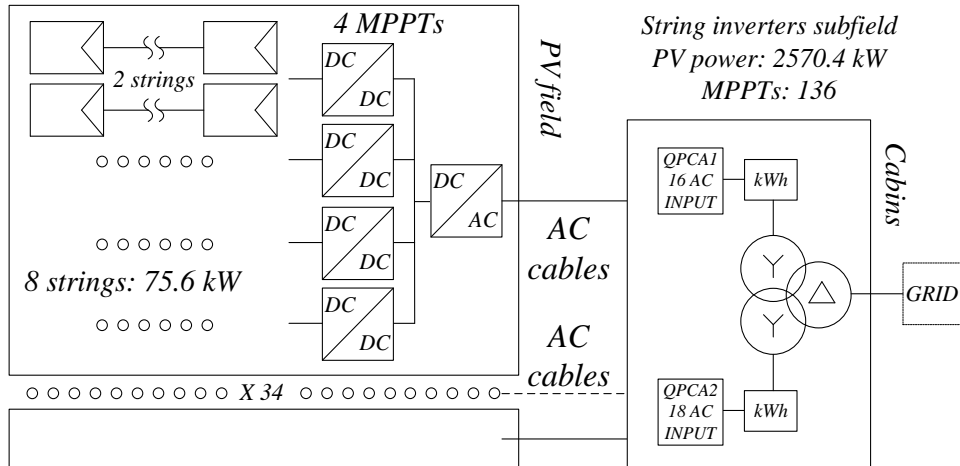


Figure 65. Power system configuration of the 2.5 MW subfield with string inverters

PV module		Central inverter	
P_{mod} (W)	315	Rated AC power (kVA)	1025
V_{oc} (V)	46.2	AC output (V, Hz)	400±10%, 50/60
I_{sc} (A)	9.01	MPPT input DC voltage range (V)	675-1320
V_{MPP} (V)	37.2	Maximum Efficiency (%)	98.9
I_{MPP} (V)	8.48	MPPTs per power converter	1
$NOCT$ (°C)	45±2	String inverter	
P_{mod}/T_{mod} (%/°C)	-0.40	Rated AC power (kVA)	60 (up to 66)
V_{oc}/T_{mod} (%/°C)	-0.30	AC output (V, Hz)	800, 50/60
I_{sc}/T_{mod} (%/°C)	+0.06	MPPT input DC voltage range (V)	600-1450
Cells	Poly	Maximum Efficiency (%)	99.0
Number of cells	72	MPPTs per power converter	4

Table 25. Main technical specifications of the experimental subfield in case study 1

Each string inverter receives 8 strings for a DC power of 75.6 kW. At the AC side, QPCA 1 groups 16 inverters, QPCA 2 groups 18 inverters. Here is a resume for the string inverters subfield:

- QPCA 1: 16 inverters, 64 MPPTs, rated DC power = 1209.6 kW, rated AC power = 960 kW, DC/AC ratio = 126.00 %
- QPCA 2: 18 inverters, 72 MPPTs, rated DC power = 1360.8 kW, rated AC power = 1080 kW, DC/AC ratio = 126.00 %
- QPCA 1 + QPCA 2: 136 MPPTs, rated DC power = 2570.4 kW, rated AC power = 2040 kW

The monitoring system of the PV plant consists of global irradiance sensors mounted on trackers, ambient temperature sensors, module temperature sensors placed on the rear side of some PV modules, inverter temperature sensors, power analyzers and power meters. Energy of central inverters is measured by an energy counter connected to voltage and current sensors placed at the AC side of the inverters. In subfields with string inverters, a meter provides the measure of AC energy. In DC side, string monitoring is embedded in each converter.

The accuracy of data provided by the monitoring system can be assumed to be in the range from 2 to 3 %.

The main criterion selected for the performance comparison described in this Chapter is basically the average gain obtained by using string inverters in terms of produced energy with respect to central inverters. The following Sections provide detailed information also on:

- implementation of the integrated model developed for large PV plant to support data elaboration in case of missing or wrong measurements;
- mismatch losses assessment;
- behaviour of converters at high ambient temperatures;
- study on 1500 V_{DC} PV systems.

10.1 Criteria for performance assessment

This Section reports general information regarding the analysis for the performance assessment of distributed converters in case study 1. Details about the specific criteria taken into account for the comparison with central inverters are in following Sections.

During design process, the installation of distributed converters in the PV plant of case study 1 was considered interesting from execution, production and operation point of view. Generally, the three parameters of the cost-benefit analysis taken into account during the design activities of a PV plant are:

- the expected yield. Distributed converters should ensure higher production due to mismatch reduction, higher dynamic efficiency, lower impact of inverter failures;
- Capital Expenditure (CAPEX) in terms of both converters and BOP estimation of costs;
- Operating Expense (OPEX) related to lower labor costs during maintenance and simpler fault detection.

The main advantage of string inverters is the expected increase in energy yield with limited impacts on the CAPEX of the plant. From this point of view, the performance analysis described for case study provides useful numerical information regarding the actual increase in energy production obtained thanks to distributed converters of case study 1. On the contrary, the evaluation of CAPEX and OPEX is out of the scope of this work.

The analysis carried out for case study 1 is based on data acquired by dataloggers of the PV plant in the period from December 2017 to October 2019. Flow chart in Fig. 66 is a schematical representation of the elaboration process of such data. Data processing and post-processing is performed using Matlab scripts, some examples are in Appendix 1.

The integrated state-space average model introduced in this work is used to replace wrong or missing data coming from dataloggers. In such a way, a large database is available for the post-processing analysis also in case of frequent unavailability cases.

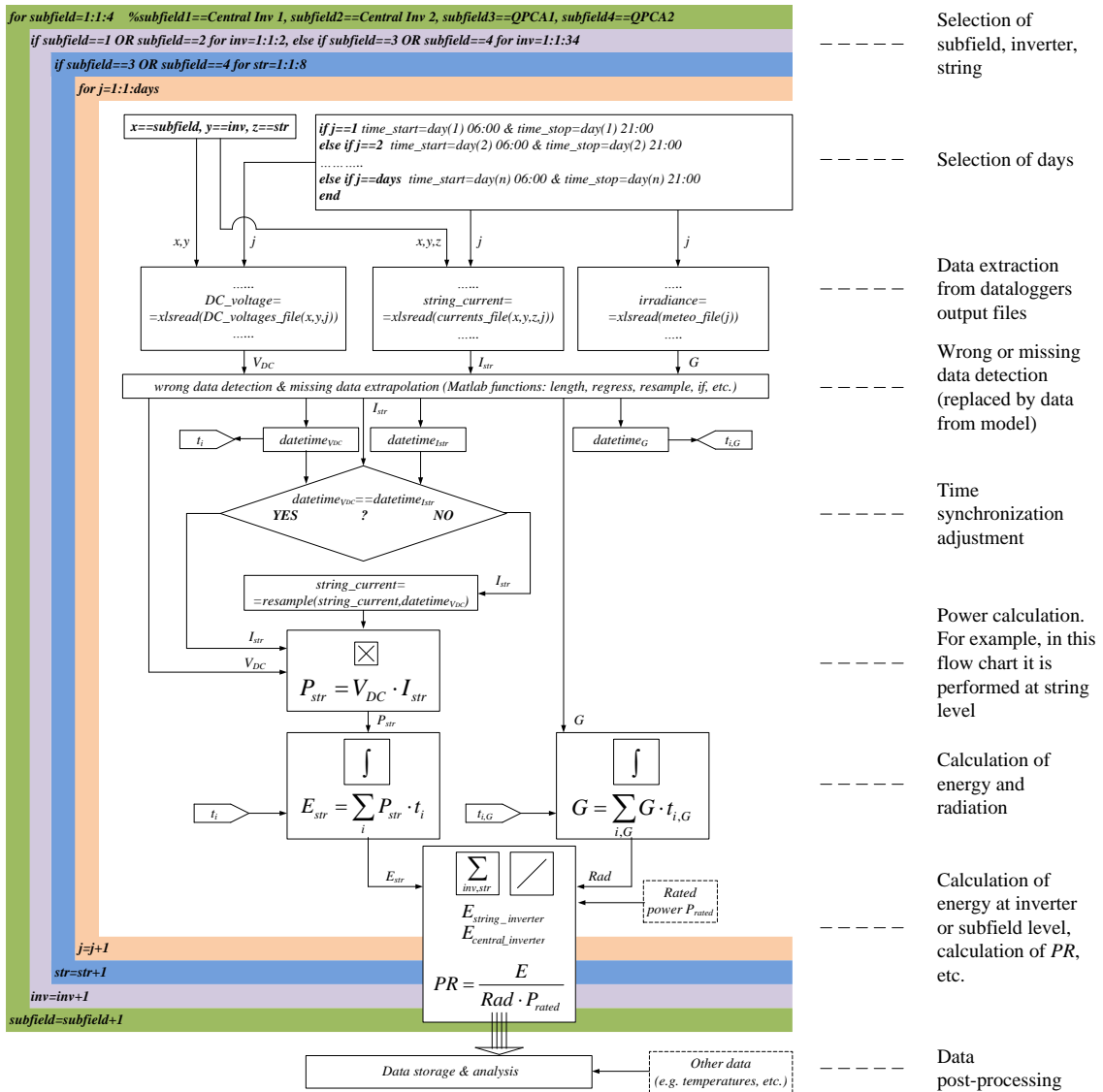


Figure 66. Data processing of measurements provided by plant dataloggers in case study 1

10.1.1 Relevance of the PV plant model

Referring to case study 1, the usefulness of the modelling approach presented in this work can be highlighted with some examples.

In Fig. 67 the power measured at the meter of the string inverters group QPCA 1 is compared to the power curve obtained in simulation for the same subfield (rated DC power is 1209.6 kW). In the selected day, a power limitation occurs. Such limitation is

due to the activation of the maximum power threshold fixed for the inverters. The graph shows that, thanks to the simulation, the theoretical extra-energy is estimated with a good accuracy.

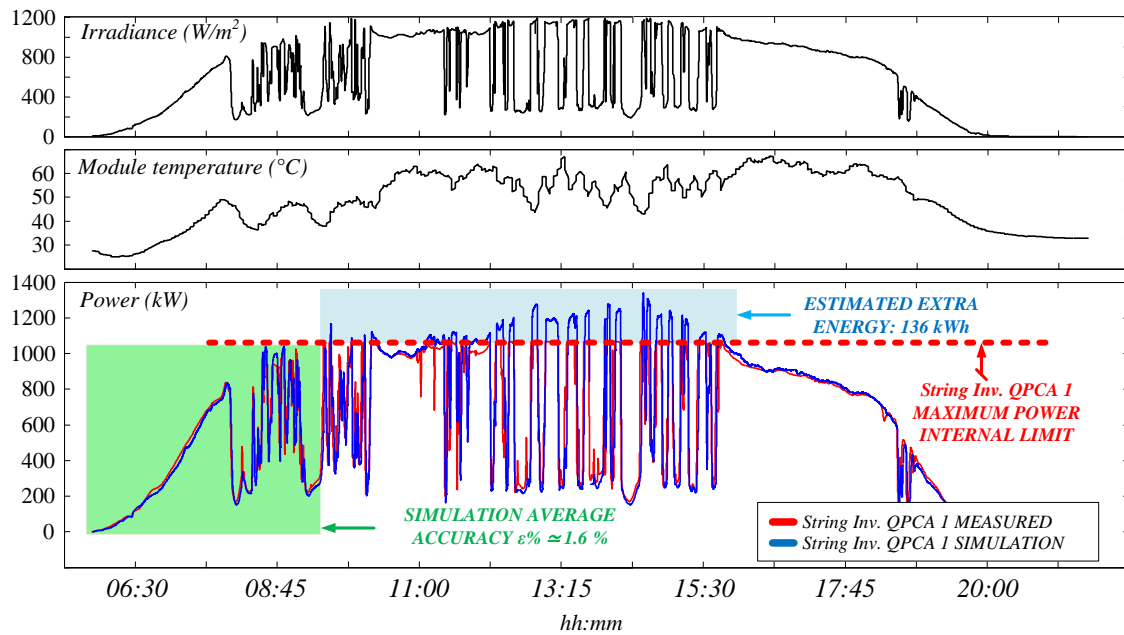


Figure 67. Proposed model output vs measured data for QPCA 1 during a selected day. The integrated state-space average model is able to estimate the theoretical extra energy produced in absence of inverter maximum power threshold.

In Fig. 68 the model is applied to estimate the energy lost in the subfield of central inverter 1 caused by a fault in the power supply system of solar trackers. Also in this case, the model is capable to overcome wrong data due to the abnormal operation.

These examples point out how the introduced model can represent a very useful tool to track the behaviour of the PV plant in normal operation as well as in case of missing data, PPC limitation due to grid capability, etc.

About the assessment of execution time performance related to modelling approach, see Section 9.2.2.

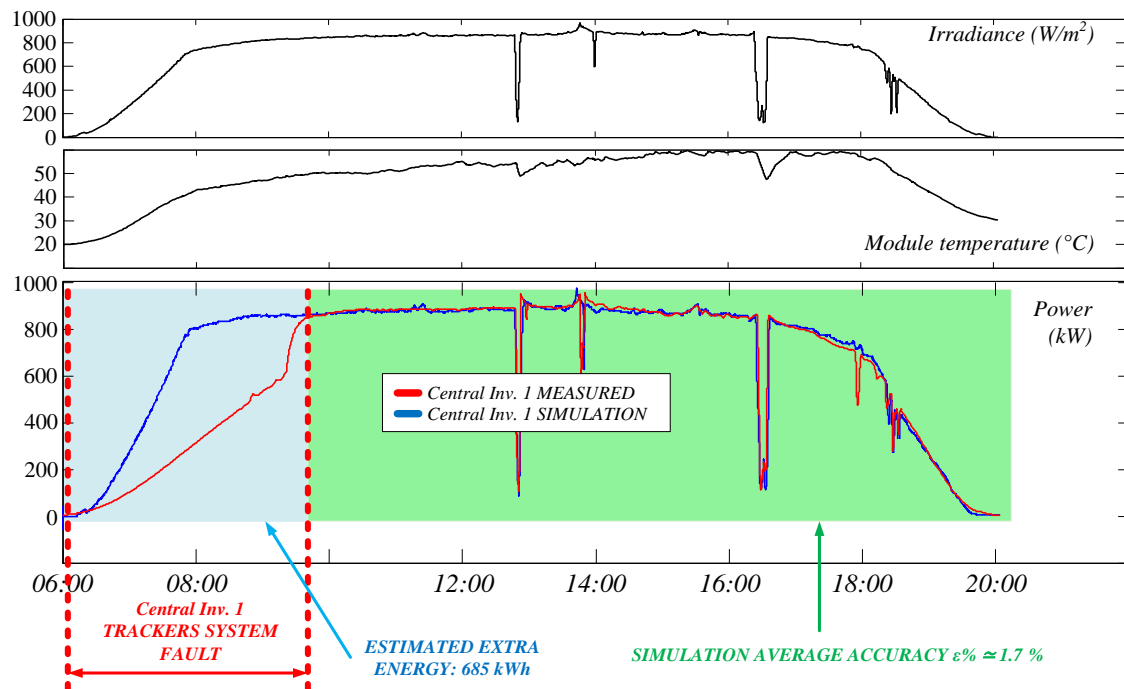


Figure 68. Proposed model output vs measured data of central inverter 1 subfield in a selected day during which a fault occurs in the power supply of solar trackers. The integrated state-space average model is able to estimate the theoretical energy that could be produced in absence of such fault.

10.2 Mismatch losses assessment

This Section focuses on mismatch calculation at string and array level for case study 1. As mentioned in Section 2.2.3, there is no a sole criterion for determining mismatch. The criteria chosen in this thesis derive from [45], [48], but they were modified and adapted for case study 1.

The result coming from the application of such criteria is the estimation of actual mismatch occurring in the plant during normal operation as consequence of various factors such as variable aging, uneven dirt between panels belonging to the same tracking structure, faulty trackers, etc.

The proposed integrated model, applied for the experimental PV subfields, supports the analysis of data with a satisfactory level of accuracy, whose value is close to precision level of measurement devices. Furthermore, the use of a state-space average technique limits the overall computational load.

10.2.1 Mismatch evaluation criteria

The rated power of strings and arrays is the basis for comparison in each criterion. In some math symbols of this Section and of the next one, the subscript “*rated*” is added to distinguish the rated values of power and the instantaneous ones.

The rated power of a PV array is calculated through (78):

$$P_{array,rated} = P_{mod,rated} \cdot N_S \cdot N_P \quad (78)$$

where $P_{mod,rated}$ is the rated power of a single PV module in STC conditions (315 W in the case study), N_S is the number of modules in series for each string (equal to 30 in case study), N_P is the number of strings in parallel.

The parameter N_P is 1 if the calculation refers to the rated power of a single string:

$$P_{str,rated} = P_{mod,rated} \cdot N_S \quad (79)$$

Otherwise, if the calculation refers to the input of a single DC/DC converter of the string inverter, N_P is 2:

$$P_{invDCinput,rated} = P_{mod,rated} \cdot N_S \cdot 2 \quad (80)$$

Lastly, if the calculation refers to the total DC power at the DC side of the string inverter, i.e. $P_{array,rated}$, N_P is 8.

It is worth noting that, for calculation purposes, starting from the theoretical STC conditions, in this work the $P_{mod,rated}$ is recalculated from time to time on the basis of actual irradiance and cell temperature measured in operating conditions. To calculate the $P_{mod,rated}$ in operating conditions different than STC, model described in 5.3 has been effectively applied. The rated power quantities used for strings and arrays are listed in Table 26.

The criteria selected for mismatch evaluation are summarized in Tables 27-31. Note that the first four criteria refer to the instantaneous power while the last refers to daily energy.

$P_{str,rated1}$	String rated power ($N_S=30, N_P=1$), calculated on the basis of: - maximum level of irradiance measured at a certain instant of time in the selected day G_{max} - cell temperature measured in the same time instant $T_{cell}@G_{max}$
$P_{str,rated2}$	String rated power ($N_S=30, N_P=1$), calculated on the basis of: - irradiance value in the range from 900 to 1100 W/m ² measured at a certain instant of time in the selected day $G_{\approx 1.000}$ - cell temperature measured in the same time instant $T_{cell}@G_{\approx 1.000}$
$P_{array,rated}$	As for $P_{str,rated2}$ but referred to arrays at the DC side input of string inverter ($N_S=30, N_P=8$)

Table 26. Rated power quantities for strings and arrays

Criterion 1	
Approach:	Mismatch calculation at string level for each string. The measured peak power is compared with $P_{str,rated1}$ in the selected day
Formula:	$M_{str,1} = \left \frac{(P_{str,max} - P_{str,rated1})}{P_{str,rated1}} \right \cdot 100$
Symbols:	$M_{str,1}$ Mismatch at string level calculated under this criterion
	$P_{str,max}$ Peak power of the string power
	$P_{str,rated1}$ Calculated as shown in Table 26

Table 27. Criterion 1 formulation

Criterion 2	
Approach:	Mismatch calculation at string level for each string. The measured instantaneous string power is compared with $P_{str,rated2}$ measured in the same time instant during the selected day
Formula:	$M_{str,2} = \left \frac{(P_{str,2} - P_{str,rated2})}{P_{str,rated2}} \right \cdot 100$
Symbols:	$M_{str,2}$ Mismatch at string level calculated under this criterion
	$P_{str,2}$ Instantaneous string power measured in the PV plant in the same time instant considered for $P_{str,rated2}$ calculation
	$P_{str,rated2}$ Calculated as shown in Table 26

Table 28. Criterion 2 formulation

Criterion 3		
Approach:	Mismatch calculation at DC array level (DC side input of inverter) for each inverter. The measured instantaneous array power is compared with $P_{array, rated}$ measured in the same time instant during the selected day	
Formula:	$M_{array,1} = \left \frac{(P_{array,1} - P_{array, rated})}{P_{array, rated}} \right \cdot 100$	
Symbols:	$M_{array,1}$	Mismatch at DC array level calculated under this criterion
	$P_{array,1}$	Instantaneous array power measured in the PV plant in the same time instant considered for $P_{array, rated}$ calculation
	$P_{array, rated}$	Calculated as shown in Table 26

Table 29. Criterion 3 formulation

Criterion 4		
Approach:	Mismatch calculation at DC array level (DC side input of inverter) for each inverter. The instantaneous array power, obtained as a product between the minimum voltage of the string connected in parallel and the minimum string current [45], is compared with $P_{array, rated}$ measured in the same time instant during the selected day	
Formula:	$M_{array,2} = \left \frac{(P_{array,2} - P_{array, rated})}{P_{array, rated}} \right \cdot 100$	
Symbols:	$M_{array,2}$	Mismatch at DC array level calculated under this criterion
	$P_{array,2}$	Instantaneous array power, obtained as a product between the minimum voltage of the string connected in parallel and the minimum string current, in the same time instant considered for $P_{array, rated}$ calculation
	$P_{array, rated}$	Calculated as shown in Table 26

Table 30. Criterion 4 formulation

Criterion 5		
Approach:	Energy-based mismatch calculation at DC array level (DC side input of inverter) obtained by comparing the average daily energy produced by 8 strings and the maximum daily energy between those of each string	
Formula:	$M_{array,3} = \left \frac{(E_{array,avg} - E_{str,max})}{E_{str,max}} \right \cdot 100$	
Symbols:	$M_{array,3}$	Energy-based mismatch at DC array level calculated under this criterion
	$E_{array,avg}$	Average daily energy produced by the 8 strings connected to the DC side of inverter
	$E_{str,max}$	Maximum daily energy between those produced by each string

Table 31. Criterion 5 formulation

10.2.2 Mismatch assessment results

Figs. 69-73 show the main results obtained by applying the criteria described above using data coming from the plant datalogger for one year, from November 2018 to October 2019.

In order to perform a statistical analysis of results, the mean value and the standard deviation of mismatch have been calculated and reported in the same charts.

In case of unavailability of electrical data such as voltages and string currents, the model introduced in this work has been exploited.

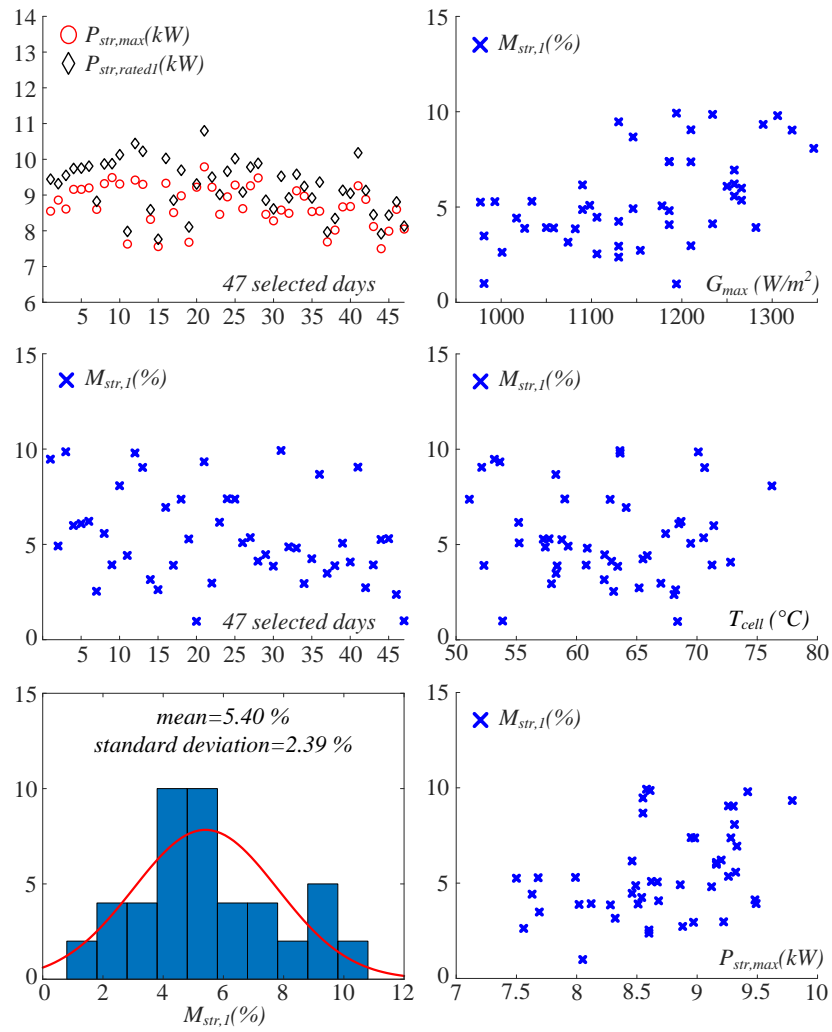


Figure 69. Criterion 1 results, database: 47 days selected in the reference period

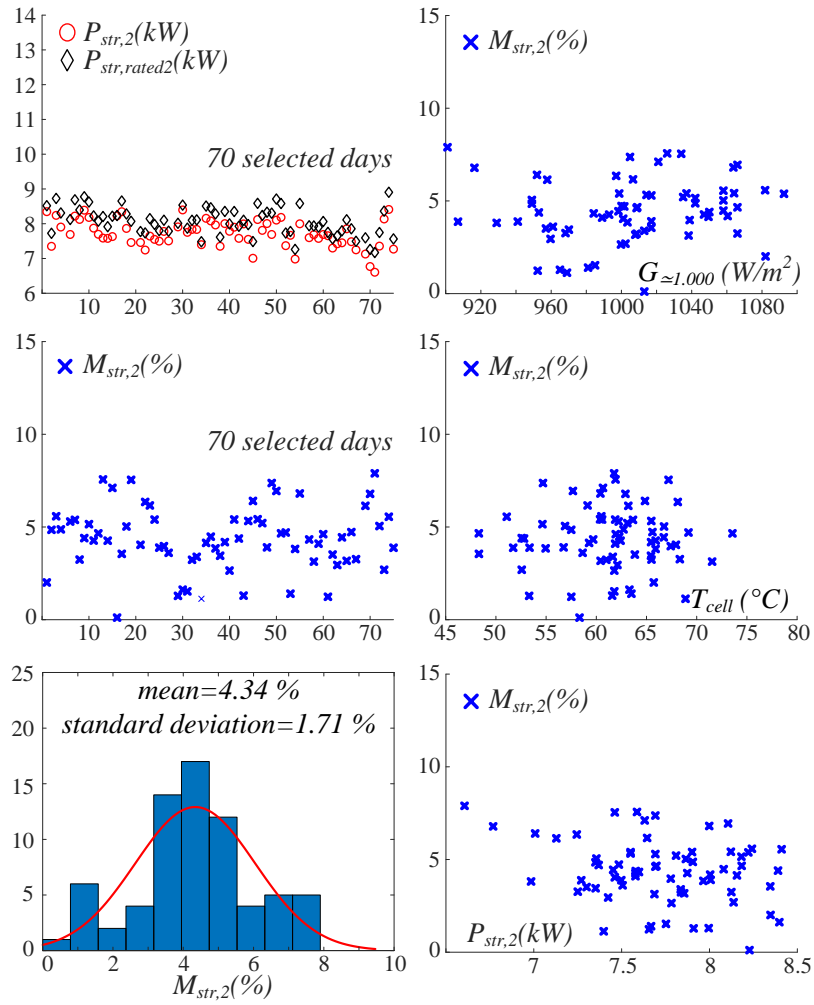


Figure 70. Criterion 2 results, database: 70 days selected in the reference period

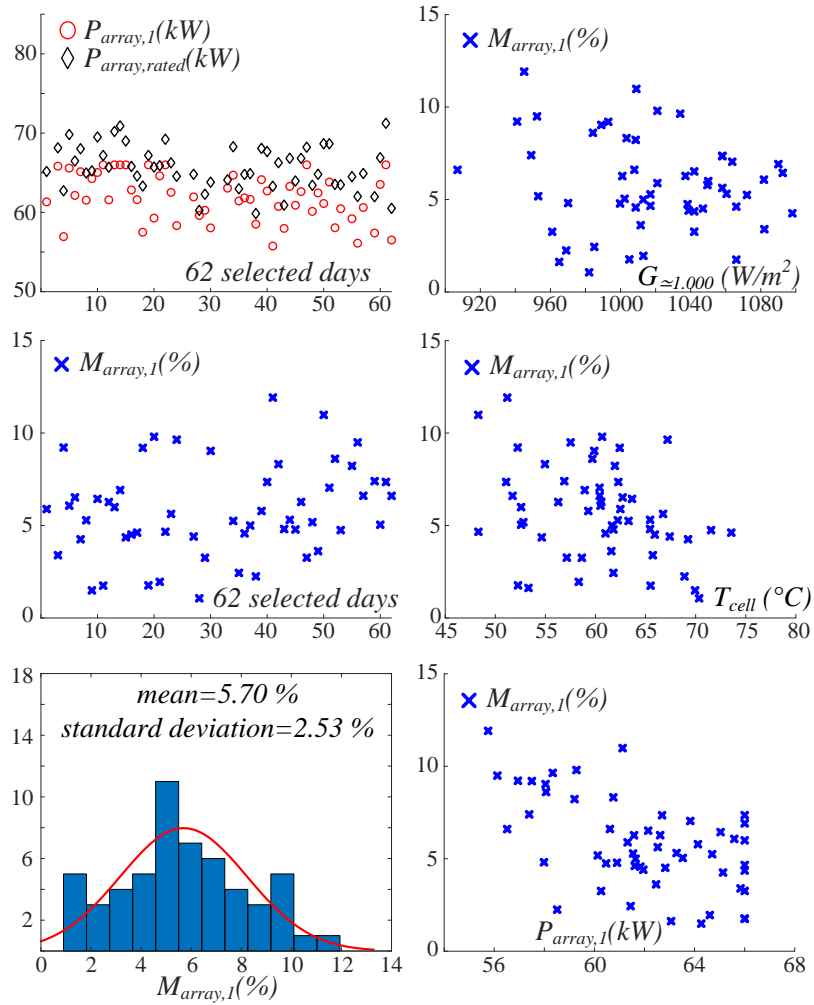


Figure 71. Criterion 3 results, database: 62 days selected in the reference period

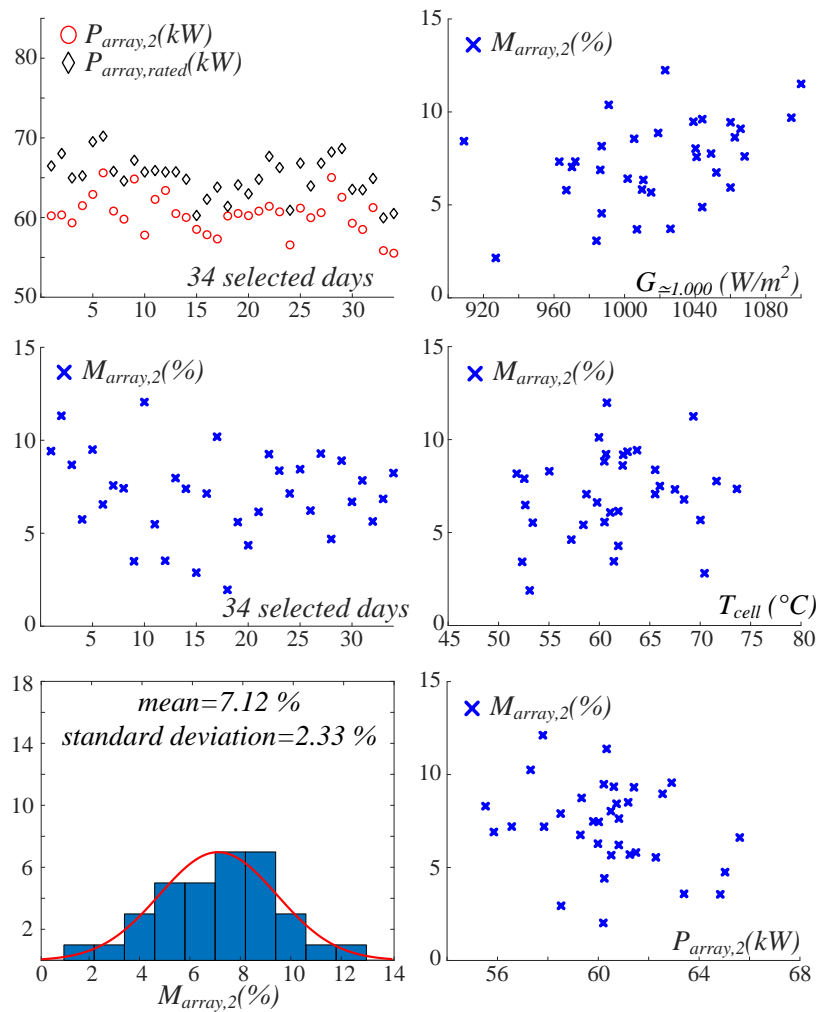


Figure 72. Criterion 4 results, database: 34 days selected in the reference period

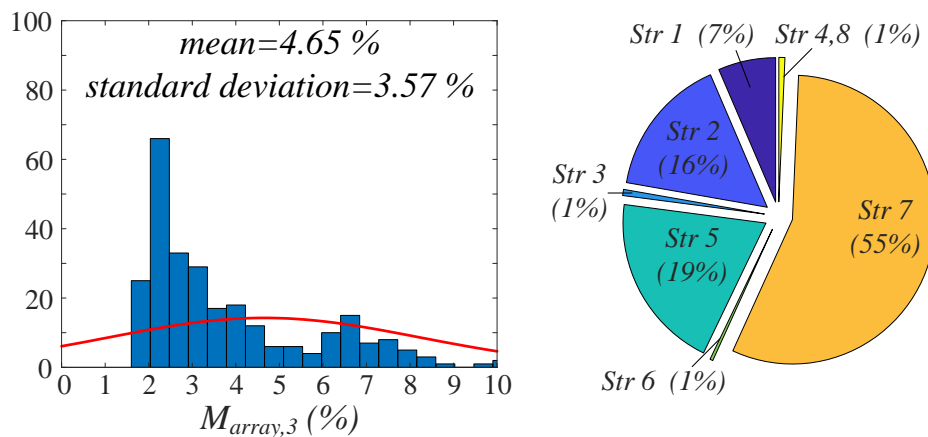


Figure 73. Criterion 5 results, database: 200 days selected in the reference period. Pie chart shows the distribution of worst strings in the selected array for the same period

The accurate analysis of the graphical results leads to the following points:

- the mismatch percentages, calculated under different criteria, are quite consistent since they increase as the considered PV subfield size increases. In the case study, the mismatch is around 4 - 5 % for strings and around 6 % for arrays;
- as expected, the maximum mismatch percentage is reached in Fig. 72 with criterion 4 because it represents the worst case in which the instantaneous array power is calculated as the product between the lower DC voltage and the lower string current. In other words, it is the higher limit for array mismatch in the case study;
- generally, the impact of irradiance and of cell temperature on mismatch level is not significant. Anyway, looking at Figs. 69-70, it is clear that higher mismatch effects are measured if the analysis is carried out using the maximum irradiance instead of the standard 1000 W/m²;
- in Fig. 71, $P_{array,1}$ shows a saturation limit at 66 kW. This is the maximum instantaneous power that the string inverter can manage for a limited time period in presence of high irradiance and low cell temperature;
- looking at the pie chart in Fig. 73, the worst string in the selected array is the string no. 7 for the most part of the selected days. Similar situations can be recognized for the rest of the arrays in the experimental subfield. This is due to the particular layout of modules and strings mounted on the trackers. In fact, some strings are mounted on the east side of the tracker, other strings are mounted on the west side while the rest of strings are mounted on both sides. This layout has a beneficial impact on mounting and cabling works but causes the increase of mismatch at array level;
- the mismatch percentages obtained in this work are similar to those reported in other papers dealing with large PV plants [42], [45], [148], [149];
- the standard deviation is about 2 - 3 % for each criterion. This value is acceptable because it is close to the typical accuracy of devices mounted in PV plants for the measurement of electrical data, irradiance, temperature and other quantities.

- thanks to the described integrated state-space average model, applied in case of missing or wrong data, the sum of measured data and data provided from model form a significant database that is sufficient to get consistent results.

Finally, the results obtained in terms of mismatch percentage calculated under different criteria are quite consistent leading to a clear evaluation of mismatch effects in the case study.

10.2.3 Investigating the causes of mismatch

This Section provides some information on the causes of mismatch in the case study.

A first simple reason is the fault of one or more solar tracker. For example, Fig. 74 shows the waveforms of voltage, current and power for the 8 strings belonging to an array connected to a string inverter during a certain day. The underperformance of string no. 7 is evident especially in the initial and final part of the day. This fact suggests that the tracker is blocked in horizontal or quasi-horizontal position.

In the chart representing the voltages, curves for string 1 and 2 are superimposed. The same is for 3 and 4 and for the rest of couples. This fact is related to the specific power configuration of the string inverters, see Fig. 65. An independent MPPT is forced for each couple of strings connected to inverters so that the voltage is the same for the two strings forming the couple.

The energy produced by the strings in this example is in Table 32. With respect to the mean value of daily energy produced by the other strings, the underperformance of string no. 7 is about 27 %.

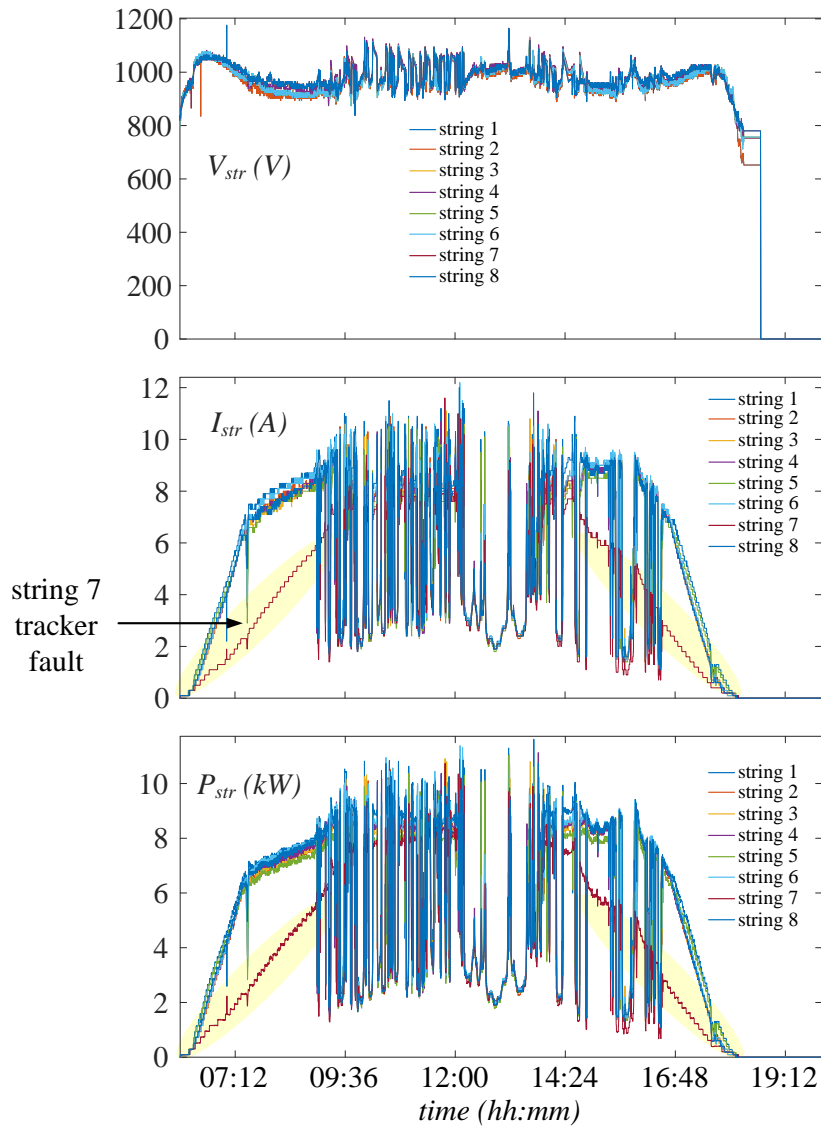


Figure 74. Graph of the electrical quantities for an array in the string inverter subfield. A tracker fault occurs in string no. 7

	String 1	String 2	String 3	String 4	String 5	String 6	String 7	String 8
Energy (kWh)	65.3	62.8	62.6	62.6	61.5	64.3	46.3	63.9

Table 32. Daily energy produced by strings in an array of the string inverter subfield. The underperformance of string no. 7, due to the tracker fault, is about 27 %

Except for the cases in which the fault of a tracker occurs, the energy mismatch between strings in the subfield with distributed converters keeps around 4 - 5 % as

calculated in the previous Section. This “inherent” mismatch is the average value for the subfield. Anyway, in some cases, there are additional percentages related to:

- differences between modules performance;
- presence of a damaged or dirty PV module in a string;
- DC side cabling configuration (mainly differences in voltage drops among strings connected to the same inverter);
- slight misalignment of solar trackers (minor or temporary position control issues).

Non-uniform aging effects cannot cause a significant increase of mismatch level because the PV plant is in operation for only three years.

Considering more days, it is interesting to observe that the “worst” string in many string inverters is almost always the same string. For example, the cells highlighted in red in Table 33 refer to the worst string of a string inverter for the months February and March 2018. In this case, string no. 5 is almost always the worst one, the reason deals with plant layout. Generally, it is important to evaluate the impact of DC cabling configuration that means to investigate the effect of voltage drops on each string because of the different distances between each string and its string inverter.

Considering the information reported in project documentation and calculating the voltage drop in the worst case (farther string, distance 150 - 200 mt to inverter), such maximum voltage drop is around 10 V leading to a power loss of about $0.7 \div 1.0$ % in such worst case.

This percentage could appear significant, but:

- it is referred to the worst case, limited to few particular situations;
- the relative differences in terms of distance of the strings belonging to the same inverter are smaller, leading to a small difference in voltage drop.

Although the DC cabling configuration is not the main responsible of mismatch, its contribution cannot be neglected in large plants as for the case study.

Date	Daily energy production (kWh)							
	String 1	String 2	String 3	String 4	String 5	String 6	String 7	String 8
20/02/2018	45,3	38,3	44,4	38,9	37,0	44,7	38,7	45,2
21/02/2018	44,3	43,0	42,5	43,5	41,4	43,7	43,5	42,9
22/02/2018	54,0	46,4	51,9	47,4	44,8	52,7	52,1	53,0
23/02/2018	47,8	37,4	47,1	38,2	36,4	47,2	46,6	47,8
26/02/2018	45,6	43,4	43,5	44,8	38,1	44,2	43,9	44,6
27/02/2018	64,8	63,1	62,0	65,1	45,9	63,5	62,8	63,5
28/02/2018	50,4	48,1	48,8	43,2	41,4	49,2	48,8	49,0
01/03/2018	35,8	34,4	34,5	27,0	31,7	35,0	34,9	35,7
02/03/2018	60,1	57,8	57,1	55,8	43,8	58,2	57,6	58,9
03/03/2018	63,2	60,7	60,4	62,3	50,0	61,4	61,2	61,6
04/03/2018	56,6	53,7	54,7	45,6	43,8	55,1	54,5	54,9
05/03/2018	65,3	61,2	61,0	58,5	55,9	62,8	60,5	63,3
06/03/2018	83,4	78,7	78,1	82,5	78,4	79,6	78,8	82,1
08/03/2018	77,8	73,5	72,8	77,1	73,1	74,1	73,5	76,6
09/03/2018	39,0	37,7	38,1	36,5	34,9	36,2	36,0	36,6
10/03/2018	54,8	52,4	52,2	44,4	42,7	45,0	44,5	44,7
11/03/2018	31,0	29,5	29,6	28,0	27,2	28,2	28,2	28,2
12/03/2018	41,2	39,6	39,5	36,1	35,1	35,9	35,4	36,1
13/03/2018	16,1	15,4	15,4	15,7	16,5	17,2	17,0	17,2
14/03/2018	65,7	63,8	63,0	65,4	50,2	52,3	51,8	52,8
15/03/2018	53,1	51,9	51,4	52,6	42,7	45,1	44,7	44,8
16/03/2018	81,2	78,5	78,5	80,8	70,0	73,0	72,0	73,5
17/03/2018	68,5	66,6	66,6	68,9	64,9	67,4	67,3	68,6
18/03/2018	49,9	47,7	47,7	49,5	46,5	48,6	48,3	49,4

Table 33. Daily energy produced by strings in an array of the string inverter subfield. For each day, the worst string is highlighted in red

10.3 Performance assessment

Performance assessment for distributed converters in case study 1, focused on energy production, has been carried out for the years from 2017 to 2019. This time interval includes the post-commissioning period from December 2017 to September 2018 that is quite large to detect variations due to seasonality.

In case of faults, unavailability or wrong measurements, the model introduced in this work has been used to replace missing data. Anyway, according to IEC 61724, days with very large issues in measured data were removed from the analysis in order to

avoid any false results.

For the sake of example, Table 34 reports the main fault events registered from January to September 2018. The same Table shows the percentage of days with normal operating conditions for each subfield. Although a detailed reliability analysis is out of the scope of this work, it is possible to observe that unavailabilities are quite frequent and can be recognized in central inverter subfield as well as in the distributed converter subfield. Obviously, due to the different sizes, the effect of a fault in a central inverter causes bigger energy losses in comparison to a fault in a string inverter.

Month	Central inverters subfield		String inverters subfield	
	Full availability days	Fault events	Full availability days	Fault events
January	30 ÷ 50 %	Central Inv. 1: 1/10 module KO; Central Inv. 2: 2/10 modules KO	≥ 50 %	No fault events
February	≥ 50 %	Central Inv. 2: 1/10 module KO	≥ 50 %	Missing measurements; String Inv. 11.1: string 2 KO
March	≤ 30 %	Central Inv. 2: 2/10 modules KO	30 ÷ 50 %	Missing measurements; String Inv. 11.1: string 2 KO
April	≤ 30 %	Central Inv. 1: 1/10 missing measurements; Central Inv. 2: 2/10 modules KO	≥ 50%	String Inv. 4.3: string 7 KO
May	≤ 30 %	Central Inv. 1: 1/10 module KO; Central Inv. 2: 2/10 modules KO	≤ 30 %	8 String Inv. KO
June	≥ 50 %	Solar trackers faults	≤ 30 %	All String Inv. KO
July	30 ÷ 50 %	Solar trackers faults	≤ 30 %	24 String Inv. KO; Solar trackers faults
August	≤ 30 %	Solar trackers faults	≤ 30 %	Missing measurements; 3 String Inv. KO; Solar trackers faults
September	≤ 30 %	Solar trackers faults	≤ 30 %	3 String Inv. KO; Solar trackers faults

Table 34. Period from January to September 2018: main fault and unavailability events in the subfields under investigation

10.3.1 Temperature effects and overload ability

According to manufacturer datasheet, the string inverter has a rated power of 60 kVA but can reach 66 kW in case of unity power factor and ambient temperature below 30° C. With the purpose to verify this declaration, several short time intervals have been analyzed in order to detect the presence of power derating related to high temperatures in absence of other power limitations. From this data analysis, it emerges that power derating is not evident in case of temperatures above 30°C.

Fig. 75 shows the AC peak power measured for the string inverters connected to QPCA 1 and QPCA 2 for about 1 month during winter 2018, with respect to ambient and module temperature. It is clear that string inverters reach their maximum power 66 kW in any cases despite of temperature level, except for cloudy or rainy days characterized by low irradiance. Such maximum power is the internal threshold fixed by the control system of inverters while power derating effects do not take place.

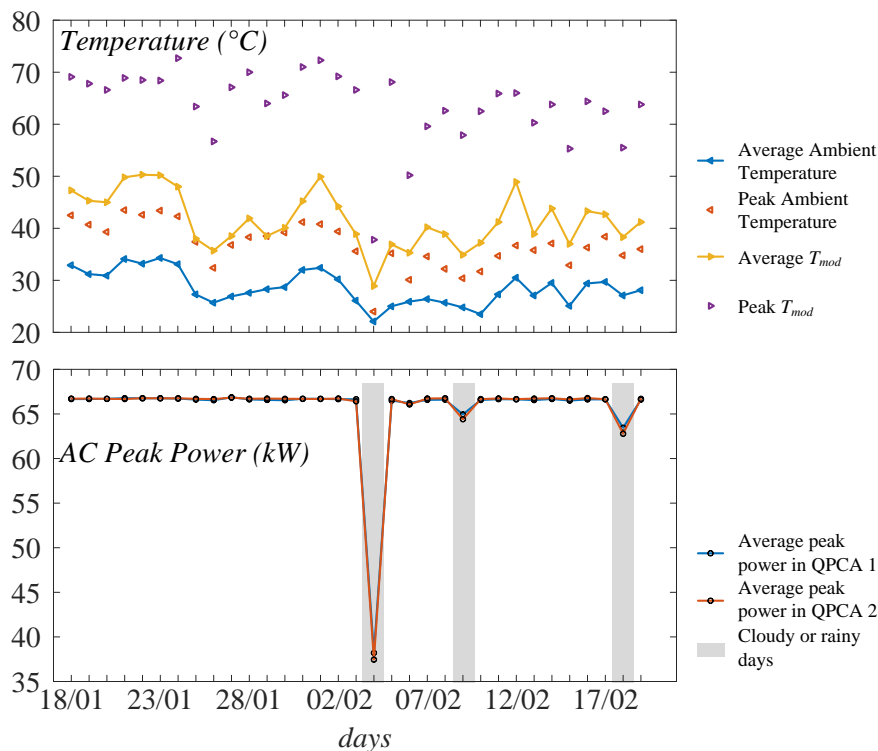


Figure 75. Period from 18th January to 19th February 2018: string inverters AC peak power, ambient and module temperature

As a consequence of this temperature behaviour, an additional advantage of string inverters is a significant overload ability. In fact, the string inverters are able to exceed the rated value of 60 kW until about 66 kW in case of clear sky conditions in a wide temperature range if power factor is 1.

As a result, in case of high irradiance, the string inverters have the opportunity to manage extra energy over their rated limit. On the contrary, when the central inverters reach their maximum power threshold there is no any opportunity to manage extra energy. Moreover, due to the large size of central inverters, in case of high temperatures the heat dissipation is sometimes problematic causing the necessity to adopt power derating procedures.

An example showing the overload ability of string inverters is in Fig. 76. It is clear that central inverters cut part of the energy produced by modules causing an underperformance.

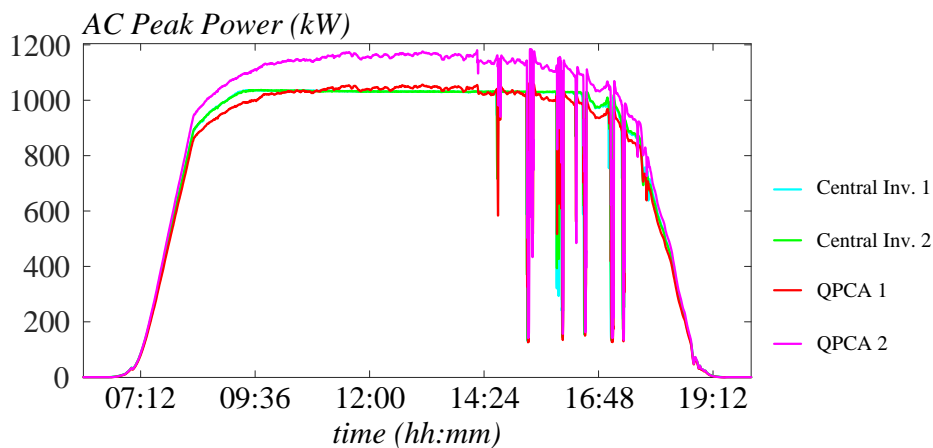


Figure 76. Sunny day in winter 2018: power plots of central inverters, QPCA 1 and QPCA 2. In the central part of the day (high irradiance) the energy flow in string inverters is not limited while the central inverters work at maximum power threshold

To better explain what reported before, frequency histograms in Fig. 77, referred to another sunny day in winter 2018, reports the time (in minutes) associated to each power value measured for both central and string inverters:

- central inverter 1 is at maximum AC power (1025 kW) for about 95 minutes;

- central inverter 2 is at maximum AC power (1025 kW) for about 80 minutes. It also experiences a reduced maximum AC power (923 kW) caused by an internal fault for other 75 minutes;
- QPCAs (string inverters subfield) are at maximum AC power (2266 kW) for about 45 minutes.

In other words, central inverters work in limitation state for a much more time with respect to string inverters.

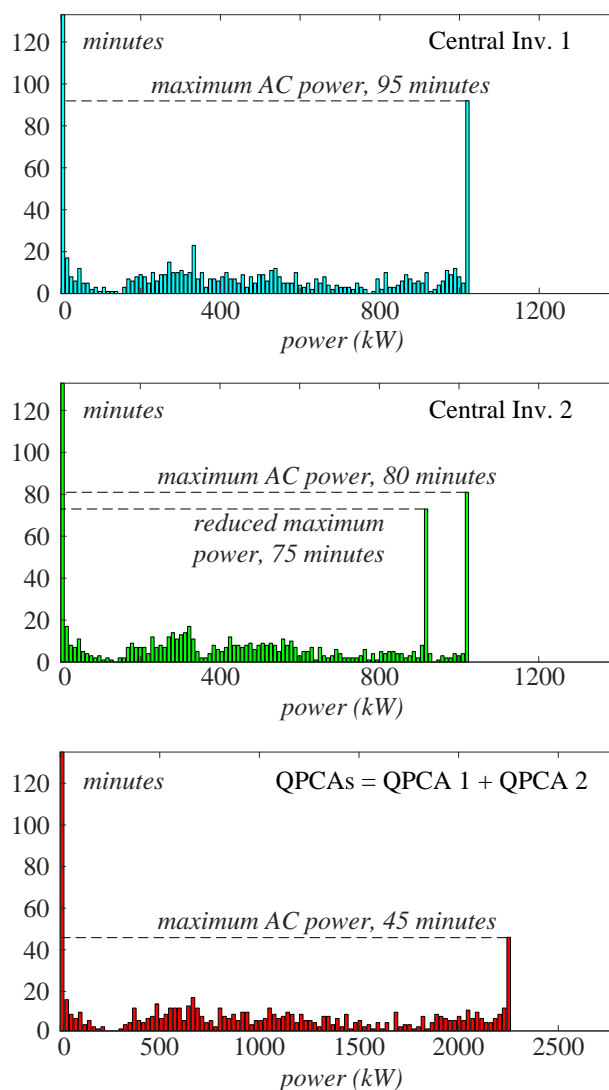


Figure 77. Sunny day in winter 2018: frequency hystogram for the instantaneous power of central inverters and QPCAs

10.3.2 Energy yield

Focusing on energy yield, performance comparison of central and string inverters described in this Section exploits data belonging to the post-commissioning period (5 months long) from December 2017 to April 2018 i.e. during summer and autumn in Brazil.

The basic formula used to evaluate the gain obtained by string converters G_{string_inv} is:

$$G_{string_inv} = \frac{\frac{E_{string_inv}}{P_{string_inv}} - \frac{E_{central_inv}}{P_{central_inv}}}{\frac{E_{central_inv}}{P_{central_inv}}} \cdot 100 \quad (81)$$

where E_{string_inv} is the daily energy produced by the string inverters (or by a QPCA), $E_{central_inv}$ is the daily energy produced by the central inverters (or by a single inverter), P is the DC rated power of each subfield. Such comparison criterion is equivalent to the comparison between the Performance Ratio (PR) values.

To better clarify the comparison criterion, Fig. 78 shows the energy produced in subfields with central and in subfields with string inverters measured during a cloudy day, in absence of power derating, unavailability, PPC limitation or other constraints. In this specific case, the gain of string inverters subfield in comparison to centralized inverters is around +1.5%, calculated by formula (81).

This calculation was repeated for all the days within the considered period. In case of issues caused by wrong data, PPC limitation, partial unavailability, etc. occurring for one or more converters, the integrated state-space average model presented in this work was used to replace data coming from the monitoring system of the real PV plant.

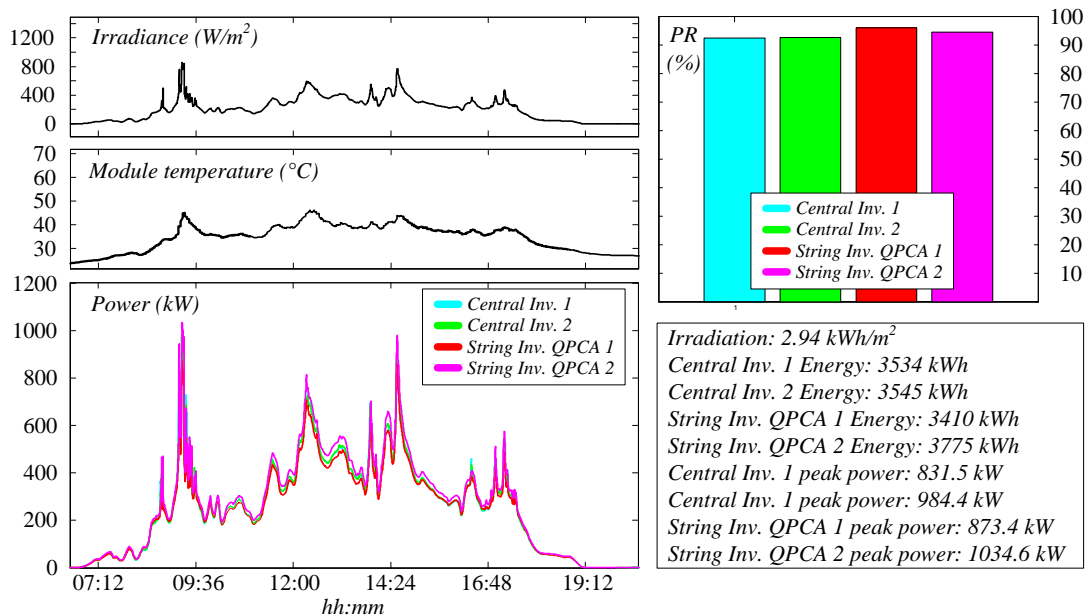


Figure 78. Comparison between central and string inverters in the experimental subfield based on daily energy during a cloudy day

Considering the days during which no any limitation related to inverter peak power thresholds occur, the aggregate results are reported in Fig. 79 through distribution charts including a normal density function fitting curve. The average gain obtained by the string converters in this case is around + 2.1 % in terms of daily production, with a standard deviation about 1.4 %.

Finally, in absence of peak power limitations forced by inverters control system, the average gain of distributed converters vs central inverters is about 2.2 %.

Repeating the same analysis including days with high power levels cut by the inverters (in the central part of these days), the average gain of distributed converters vs central inverters goes up to 3.2 %. The justification is related to the technical reasons described in the previous Section.

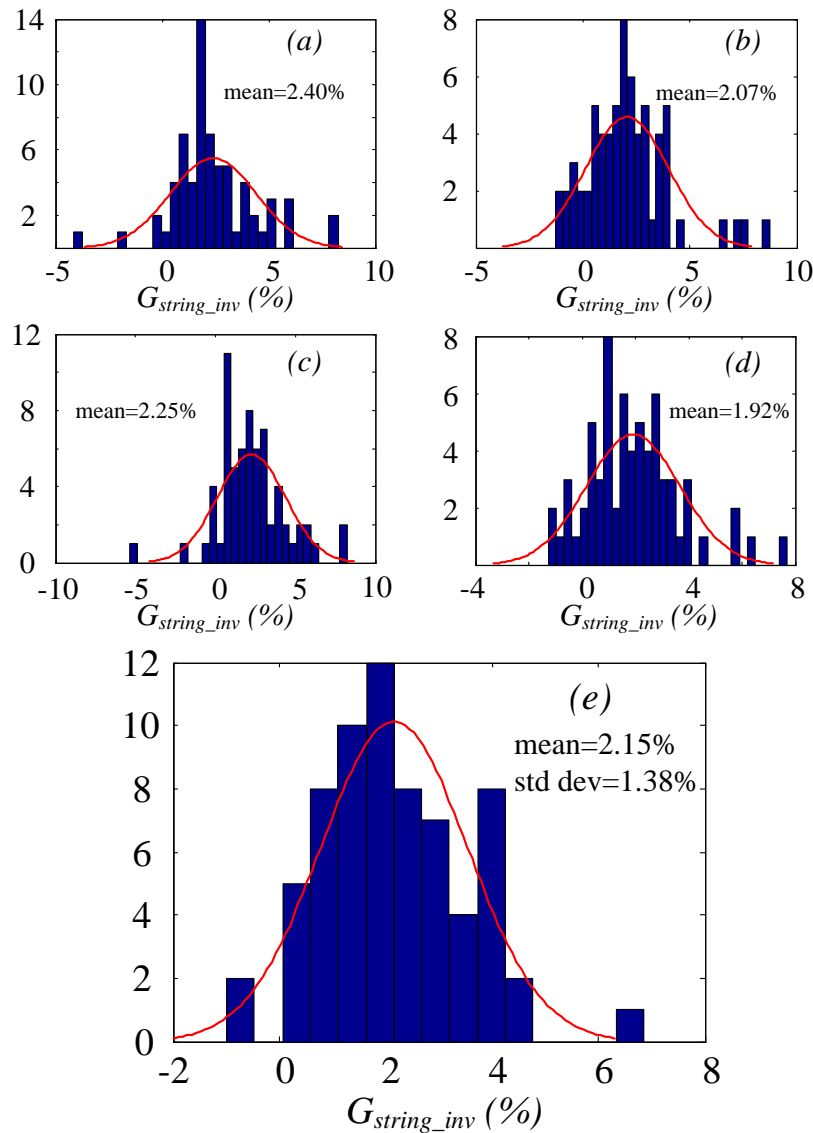


Figure 79. Results obtained considering the days during which no any limitation related to inverter peak power thresholds occur. String inverters gain distribution charts and normal density fitting functions: (a) QPCA 1 vs central inverter 1, (b) QPCA 1 vs central inverter 2, (c) QPCA 2 vs central inverter 1, (d) QPCA 2 vs central inverter 2, (e) string inverters subfield (QPCA 1 + QPCA 2) vs central inverters subfield (central 1 + central 2). The integrated state-space average model has been used to replace data coming from the monitoring system of the PV plant in case of data issues, unavailability or external constraints

Performing other post-processing elaborations, an attempt to provide a rough estimation of the main factors contributing to the total energy gain has been made by considering:

- mismatch recovery;

- self-consumption;
- overload ability;
- dynamic efficiency.

The results of this analysis, including days with some cases of limitations related to inverter peak power thresholds, are in Table 35 and in Fig. 80.

Gain component	String inverter vs central inverter
total gain	+ 3.2%
mismatch recovery + dynamic efficiency	+ 1.9%
reduction in self-consumption (manufacturer datasheets)	+ 0.3 %
overload ability	+ 1.0 %

Table 35. Rough estimation of the main factors contributing to energy gain obtained by string inverters, including the days during which some cases of limitations related to inverter peak power thresholds occur

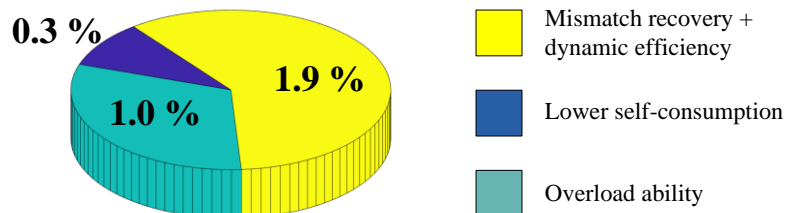


Figure 80. Plot of the energy gain components, including the days during which some cases of limitations related to inverter peak power thresholds occur

Obviously, the contribution of each component can vary from time to time, depending on the operating conditions as irradiance, temperature, frequency of power limitation events and so on. For example, the dynamic efficiency has a greater impact in case of rapidly variable irradiance conditions (clouds partial coverage) as well as the overload ability has a greater impact in sunny clear sky days.

10.4 Technical note on 1500 V_{DC} PV systems

The string inverter in case study 1 has a maximum input voltage equal to 1500 V_{DC}. This means that, in this case study, the generation system headed by a string inverter is a 1500 V_{DC} electrical system.

The analysis performed in this work can be useful for the design of new large PV plants because the current trend in PV market is the realization of generation systems having a rated voltage ≥ 1500 V_{DC}. Under this perspective, in this Section a brief overview regarding this topic is reported. Readers can also refer to [150]-[153].

The main novelties related to the realization of ≥ 1500 V_{DC} PV plants are:

- the number of PV modules in a string increases of about 50%. This leads to a reduction on the number of wires but, at the same time, to an increase in their total length in a range from 8% to 16%. New topology concepts and the exploitation of PV modules with higher rated power will mitigate the effects of longer DC cables;
- faster and easier installation on the jobsite translates to lower labor costs;
- thanks to the increased operational voltage, the reduction in the number of equipments for the DC subsystem is expected to be around 33% (fuses, switchgears, circuit breakers, etc.);
- ability of the inverters to operate at higher power without having to increase the amount of current they must handle. This translates into higher power inverters and fewer number of inverters required for a given installation;
- the raise in DC voltage (1500 V_{DC} or more) implies the utilization of multi-level inverters, described above in Section 4.1. Typically, the 1500 V_{DC} inverters allow a DC-link voltage variation of 35% compared to 20% for the traditional 1000 V_{DC} inverter. This is a relevant advantage concerning irradiation and temperature variations during operation. Several leading manufacturers currently offer high power high voltage PV inverters with maximum input voltage reaching 1500 V_{DC} (or more in some particular cases);

- in turn, this influences the PV module market encouraging the manufacturers to offer the new generation of 1500 V_{DC} PV panels with suitable insulation resistance and leakage current performance;
- the new power level of the inverters will influence also the AC side of the PV field connected to a single inverter. In particular, it will lower the investment for medium voltage switchgears and equipments within high power plants. In other words, a high voltage inverter produces some collateral advantages also for the AC subsystem;
- the total reduction in PV system cost per watt is expected to be from 3% to 5%.

A numerical comparison between 1000 V_{DC} and 1500 V_{DC} inverters, referred to commercial systems, is in [155]. Table 36 summarizes the contents of such comparison. From the value of ratio for each analysed parameter, the advantages of 1500 V_{DC} inverter are clear.

	1667 kW 1000 V _{DC} inverter	2300 kW 1500 V _{DC} inverter	ratio
Maximum input DC voltage (V)	1000	1500	1.5
MPPT voltage range (V)	605 ÷ 950 ΔV = 345	800 ÷ 1300 ΔV = 500	1.45
Minimum MPPT voltage (V)	605	800	1.32
Current per kW at minimum MPPT voltage (A/kW)	1.65	1.25	0.76
Current per kW at maximum MPPT voltage (A/kW)	1.05	0.77	0.73
Ohmic losses at the DC side, average value (%)	-	-	0.55
Output power (kW)	1667	2300	1.44
Power density of inverter (kW/m ³)	126.82	174.97	1.38

Table 36. Comparison between 1000 V_{DC} and 1500 V_{DC} inverters, database derives from [154]

About the regulation, there is a lack of standards with regards to the electrical installations over 1500 V_{DC}.

The actual regulations in most countries (e.g. CEI 11-27 in Italy) do not permit to perform electrical activities during which the technicians work directly on the active parts in MV. Therefore, many maintenance activities on PV components (for example

the scheduled maintenance of a string box) could become illegal in high voltage PV systems.

Generally, passing over 1500 V_{DC} all the following components at the DC side of a PV plant should be designed and certified for MV level:

- PV modules;
- solar cables;
- connectors: solar cables connectors and string boxes connectors;
- string boxes;
- manual (or automatic) switches in string boxes;
- protection devices in string boxes (e.g. fuses);
- DC cables from string boxes to inverters;
- DC/DC converters and their power devices;
- DC/AC converters and their power device.

For some of these components, the present regulations are already extended to higher voltage level. For example, for solar cables (usually unipolar with insulation class II), voltage levels higher than 1500 V_{DC} are allowed by:

- IEC 60502 Power cables with extruded insulation and their accessories for rated voltages from 1 kV (insulation voltage 1,2 kV) up to 30 kV (insulation voltage 36 kV);

while in other few cases, it is pointed out the maximum voltage limit as in:

- EN 50618 Electric cables for photovoltaic systems (up to 1800 V);
- UL 4703 Standard for photovoltaic wire (up to 2000 V).

On the contrary, for power converters used in PV plants, the main standards are limited to LV thresholds below 1500 V_{DC}:

- IEC 62109-1 Safety of power converters for use in photovoltaic power systems - Part 1: General requirements;
- IEC 60364-7 Low voltage electrical installations - Requirements for special installations or locations - Solar photovoltaic (PV);
- IEC 60947 Low-voltage switchgear and controlgear.

Only some standards dealing with the safety issues for inverters are still applicable over 1500 V_{DC}:

- IEC 62109-2 Safety of power converters for use in photovoltaic power systems – Part 2: Particular requirements for inverters;
- IEC 62477-2 Safety requirements for power electronic converter systems and equipment - Part 2: Power electronic converters from 1000 V_{AC} or 1500 V_{DC} up to 36 kV_{AC} or 54 kV_{DC}.

The lack of standards and regulations for most of the components in ≥ 1500 V_{DC} PV plant needs to be filled in the next years in order to drive the development of high voltage installations and obtain their benefits.

Chapter 11 - Case study 2, PV plant in Central Italy

The ground-mounted 2 MW PV field in Central Italy, shown in Fig. 81, represents the case study 2 of this work.



Figure 81. Pictures of the ground-mounted 2 MW PV plant in Central Italy representing the case study 2 of this work

The PV plant is in operation since 2011. It is divided in 4 subfields. The rated power of each subfield is about 500 kW. There is a central inverter for each subfield. There are two 1250 kVA transformers with double low voltage windings, each one powered by a central inverter.

The rated power of PV modules is 235 W with the exception of some strings whose modules have a rated power of 230 W or 240 W.

PV modules are affected by non-uniform aging degradation causing relevant mismatch phenomena between strings. Because of these phenomena and of local shadowing effects depending on the particular morphology of the terrain, significant differences between the subfields in terms of energy production were experienced over the years.

In particular, since 2011 subfield 4 registered the worst performance. Therefore, with the aim of improve its energy production, string power optimizers realized with

SiC devices have been installed in August 2018. Some pictures of such installation are in Fig. 82. Technical specifications of the main component of PV plant, including distributed converters, are in Table 37.



Figure 82. Pictures regarding the assembly of string optimizers. Left: cabling modification at the string box. Right: string optimizers mounted on the back side of the string box

PV modules (poly, 60 cells)	
P_{mod}	235 W (230 or 240 in some strings)
V_{oc}	36.65 V (235 W module)
I_{sc}	8.59 A (235 W module)
V_{MPP}	28.70 V (235 W module)
I_{MPP}	8.19 A (235 W module)
P_{mod}/T_{mod} , V_{oc}/T_{mod} , I_{sc}/T_{mod}	-0.43%/°C, -0.35%/°C, +0.03%/°C
Strings and String boxes	
Modules in a string	20
Number of power inputs	16
Monitoring channels for string current	8 (the measured current is the sum of two strings)
String power optimizers	
Rated power	10 kW
Power inputs	1 PV array = 2 strings
Maximum Efficiency	99.5 %
Power Devices Technology	SiC
Central inverters	
Number of inverters	4
Rated AC power	500 kVA
AC voltage, frequency	400 V, 50/60 Hz
MPPT DC voltage range	450 to 820 V
Maximum Efficiency	98.6 %

Table 37. Main technical specifications of the experimental subfield in case study 2

Fig. 83 shows the original configuration for all the subfields. This configuration has been kept for subfield 1, 2 and 3. Fig. 84 shows the configuration for the experimental subfield 4, where the string optimizers were mounted in August 2018. As a consequence of this retrofit activity, the control system of the central inverter 4 was modified disabling the original MPPT control while regulating the DC-link voltage value in a narrow range around 730 V.

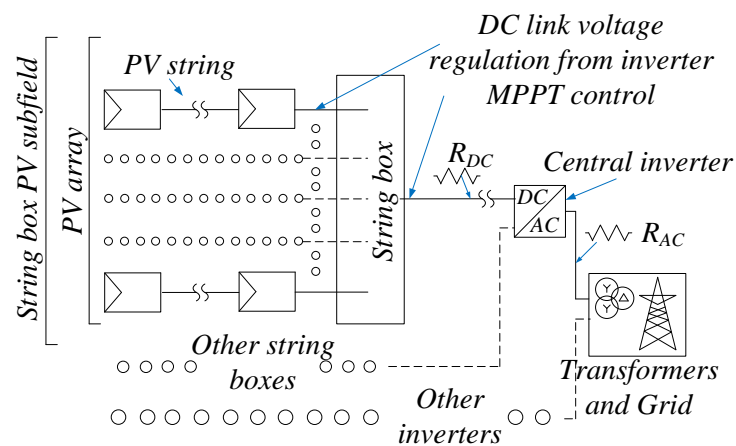


Figure 83. Single line diagram of the subfields whose layout maintained the original configuration

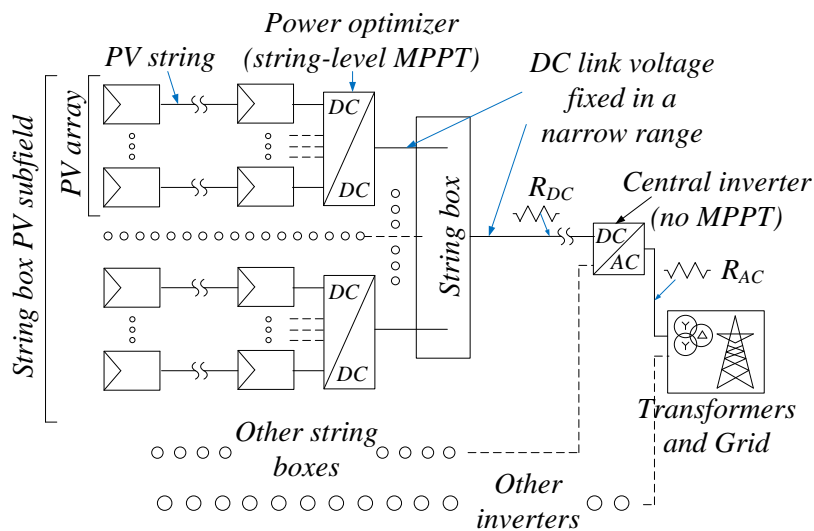


Figure 84. Single line diagram of the experimental subfield with power optimizers mounted at string level in August 2018

Several sensors and meters, characterized by a total accuracy in the range from 2.0 % to 3.0 %, form the monitoring system of the PV plant and of its subfields.

It worth noting that, in this specific PV plant, the number of strings connected to a single monitoring channel (at the string boxes and at the string optimizers) is 2. Therefore, the “string” in the monitoring system is a set of two strings. We could name the latters as “sub-strings”.

If the sub-strings of a certain couple are composed by PV modules having different rated power (e.g. 230 W for the first sub-string and 235 W for the second one), it has been considered a fictitious average rated power for the string. It is the case for the cells coloured in orange in Tables 38-41. The power configuration of subfield 4 remained unchanged after the installation of string optimizers.

	Inverter 1 – SB 1 – Strings								Inverter 1 – SB 2 – Strings							
	1	2	3	4	5	6	7	8	1	2	3	4	5	6	7	8
P_{mod}	235	235	235	235	235	235	235	235	235	235	232.5	235	235	235	235	235
N_S	20	20	20	20	20	20	20	20	20	20	20	20	20	20	20	20
Sub-strings	2	2	2	2	2	2	2	2	2	2	2	2	2	2	2	2
P_{str}	9.4	9.4	9.4	9.4	9.4	9.4	9.4	9.4	9.4	9.4	9.3	9.4	9.4	9.4	9.4	9.4
	Inverter 1 – SB 3 – Strings								Inverter 1 – SB 4 – Strings							
	1	2	3	4	5	6	7	8	1	2	3	4	5	6	7	8
P_{mod}	230	230	230	230	230	230	230	232.5	235	235	235	235	235	235	235	235
N_S	20	20	20	20	20	20	20	20	20	20	20	20	20	20	20	20
Sub-strings	2	2	2	2	2	2	2	2	2	2	2	2	2	2	2	2
P_{str}	9.2	9.2	9.2	9.2	9.2	9.2	9.2	9.3	9.4	9.4	9.4	9.4	9.4	9.4	9.4	9.4
	Inverter 1 – SB 5 – Strings								Inverter 1 – SB 6 – Strings							
	1	2	3	4	5	6	7	8	1	2	3	4	5	6	7	8
P_{mod}	235	235	235	235	235	235	235	235	235	235	235	235	235	235	235	235
N_S	20	20	20	20	20	20	20	20	20	20	20	20	20	20	20	20
Sub-strings	2	2	2	2	2	2	2	2	2	2	2	2	2	2	2	2
P_{str}	9.4	9.4	9.4	9.4	9.4	9.4	9.4	9.4	9.4	9.4	9.4	9.4	9.4	9.4	9.4	9.4
	Inverter 1 – SB 7 – Strings						Inverter 1 – SB 8 – Strings									
	1	2	3	4	5	6	1	2	3	4	5	6				
P_{mod}	235	235	235	235	235	235	235	235	235	235	235	235				
N_S	20	20	20	20	20	20	20	20	20	20	20	20				
Sub-strings	2	2	2	2	2	2	2	2	2	2	2	2				
P_{str}	9.4	9.4	9.4	9.4	9.4	9.4	9.4	9.4	9.4	9.4	9.4	9.4				

Table 38. Power configuration of strings in subfield 1

	Inverter 2 – SB 1 – Strings								Inverter 2 – SB 2 – Strings							
	1	2	3	4	5	6	7	8	1	2	3	4	5	6	7	8
P_{mod}	235	235	235	235	235	235	235	235	235	235	235	235	235	235	235	235
N_S	20	20	20	20	20	20	20	20	20	20	20	20	20	20	20	20
Sub-strings	2	2	2	2	2	2	2	2	2	2	2	2	2	2	2	2
P_{str}	9.4	9.4	9.4	9.4	9.4	9.4	9.4	9.4	9.4	9.4	9.4	9.4	9.4	9.4	9.4	9.4
	Inverter 2 – SB 3 – Strings								Inverter 2 – SB 4 – Strings							
	1	2	3	4	5	6	7	8	1	2	3	4	5	6	7	8
P_{mod}	235	235	235	235	235	235	235	235	235	235	235	235	235	235	235	235
N_S	20	20	20	20	20	20	20	20	20	20	20	20	20	20	20	20
Sub-strings	2	2	2	2	2	2	2	2	2	2	2	2	2	2	2	2
P_{str}	9.4	9.4	9.4	9.4	9.4	9.4	9.4	9.4	9.4	9.4	9.4	9.4	9.4	9.4	9.4	9.4
	Inverter 2 – SB 5 – Strings								Inverter 2 – SB 6 – Strings							
	1	2	3	4	5	6	7	8	1	2	3	4	5	6	7	8
P_{mod}	235	235	235	235	235	235	235	235	235	235	235	235	235	235	235	235
N_S	20	20	20	20	20	20	20	20	20	20	20	20	20	20	20	20
Sub-strings	2	2	2	2	2	2	2	2	2	2	2	2	2	2	2	2
P_{str}	9.4	9.4	9.4	9.4	9.4	9.4	9.4	9.4	9.4	9.4	9.4	9.4	9.4	9.4	9.4	9.4
	Inverter 2 – SB 7 – Strings								Inverter 2 – SB 8 – Strings							
	1	2	3	4	5	6	7	8	1	2	3	4	5	6	7	8
P_{mod}	235	235	235	232.5	230	230	230	230	230	230	230	230	230	230	230	230
N_S	20	20	20	20	20	20	20	20	20	20	20	20	20	20	20	20
Sub-strings	2	2	2	2	2	2	2	2	2	2	2	2	2	2	2	2
P_{str}	9.4	9.4	9.4	9.3	9.2	9.2	9.2	9.2	9.2	9.2	9.2	9.2	9.2	9.2	9.2	9.2

Table 39. Power configuration of strings in subfield 2

	Inverter 3 – SB 1 – Strings								Inverter 3 – SB 2 – Strings							
	1	2	3	4	5	6	7	8	1	2	3	4	5	6	7	8
P_{mod}	235	235	235	235	235	235	235	235	235	235	235	235	235	235	235	235
N_S	20	20	20	20	20	20	20	20	20	20	20	20	20	20	20	20
Sub-strings	2	2	2	2	2	2	2	2	2	2	2	2	2	2	2	2
P_{str}	9.4	9.4	9.4	9.4	9.4	9.4	9.4	9.4	9.4	9.4	9.4	9.4	9.4	9.4	9.4	9.4
	Inverter 3 – SB 3 – Strings								Inverter 3 – SB 4 – Strings							
	1	2	3	4	5	6	7	8	1	2	3	4	5	6	7	8
P_{mod}	230	230	230	230	230	230	230	230	230	232.5	235	235	230	230	230	230
N_S	20	20	20	20	20	20	20	20	20	20	20	20	20	20	20	20
Sub-strings	2	2	2	2	2	2	2	2	2	2	2	2	2	2	2	2
P_{str}	9.2	9.2	9.2	9.2	9.2	9.2	9.2	9.2	9.2	9.3	9.4	9.4	9.2	9.2	9.2	9.2
	Inverter 3 – SB 5 – Strings								Inverter 3 – SB 6 – Strings							
	1	2	3	4	5	6	7	8	1	2	3	4	5	6	7	8
P_{mod}	230	230	230	235	240	240	240	235	230	230	240	240	230	240	240	240
N_S	20	20	20	20	20	20	20	20	20	20	20	20	20	20	20	20
Sub-strings	2	2	2	2	2	2	2	2	2	2	2	2	1	2	2	2
P_{str}	9.2	9.2	9.2	9.4	9.6	9.6	9.6	9.4	9.2	9.2	9.6	9.6	4.6	9.6	9.6	9.6
	Inverter 3 – SB 7 – Strings								Inverter 3 – SB 8 – Strings							
	1	2	3	4	5	6	7	8	1	2	3	4	5	6	7	8
P_{mod}	230	230	230	230	235	235	235	235	235	235	235	235	235	235	235	235
N_S	20	20	20	20	20	20	20	20	20	20	20	20	20	20	20	20
Sub-strings	2	2	2	2	2	2	2	2	2	2	2	2	2	2	2	2
P_{str}	9.2	9.2	9.2	9.2	9.4	9.4	9.4	9.4	9.4	9.4	9.4	9.4	9.4	9.4	9.4	9.4

Table 40. Power configuration of strings in subfield 3

	Inverter 4 – SB 1 – Strings								Inverter 4 – SB 2 – Strings							
	1	2	3	4	5	6	7	8	1	2	3	4	5	6	7	8
P_{mod}	235	235	235	235	235	235	235	235	235	235	235	235	235	235	235	235
N_S	20	20	20	20	20	20	20	20	20	20	20	20	20	20	20	20
Sub-strings	2	2	2	2	2	2	2	2	2	2	2	2	2	2	2	2
P_{str}	9.4	9.4	9.4	9.4	9.4	9.4	9.4	9.4	9.4	9.4	9.4	9.4	9.4	9.4	9.4	9.4
	Inverter 4 – SB 3 – Strings								Inverter 4 – SB 4 – Strings							
	1	2	3	4	5	6	7	8	1	2	3	4	5	6	7	8
P_{mod}	235	235	235	235	235	235	235	235	235	235	235	235	235	235	235	235
N_S	20	20	20	20	20	20	20	20	20	20	20	20	20	20	20	20
Sub-strings	2	2	2	2	2	2	2	2	2	2	2	2	2	2	2	2
P_{str}	9.4	9.4	9.4	9.4	9.4	9.4	9.4	9.4	9.4	9.4	9.4	9.4	9.4	9.4	9.4	9.4
	Inverter 4 – SB 5 – Strings								Inverter 4 – SB 6 – Strings							
	1	2	3	4	5	6	7	8	1	2	3	4	5	6	7	8
P_{mod}	235	235	235	240	235	235	240	240	240	240	240	240	240	240	240	240
N_S	20	20	20	20	20	20	20	20	20	20	20	20	20	20	20	20
Sub-strings	2	2	2	2	2	2	2	2	2	2	2	2	2	2	2	2
P_{str}	9.4	9.4	9.4	9.6	9.4	9.4	9.6	9.6	9.6	9.6	9.6	9.6	9.6	9.6	9.6	9.6
	Inverter 4 – SB 7 – Strings						Inverter 4 – SB 8 – Strings									
	1	2	3	4	5	6	1	2	3	4	5	6				
P_{mod}	240	237.5	240	240	237.5	235	235	235	235	235	235	235				
N_S	20	20	20	20	20	20	20	20	20	20	20	20				
Sub-strings	2	2	2	2	2	2	2	2	2	2	2	2				
P_{str}	9.6	9.5	9.6	9.6	9.5	9.4	9.4	9.4	9.4	9.4	9.4	9.4				

Table 41. Power configuration of strings in subfield 4

11.1 Criteria for performance assessment

As for the case study 1, in case study 2 a multi-criteria approach has been applied to evaluate the performance of distributed converters. This Section reports general information about such performance assessment.

The main comparison criterion is the difference between the subfield 4 and the others subfields in terms of energy production. At the same time, it is possible to compare the performance of subfield 4 for the period preceding the retrofitting and for the period following the same. Moreover, similar studies can be performed at string or at array level. Details about the specific criteria taken into account for the comparison between string optimizers and central inverters are in following Sections.

The analysis carried out for case study 2 is based on data acquired by the dataloggers of the PV plant in the period from February 2018 to February 2019. Flow chart in Fig. 66, introduced in the context of case study 1, is valid also for case study 2 but with some modifications, see Fig. 85. Data processing and post-processing is performed using Matlab scripts, see Appendix 2 for some examples.

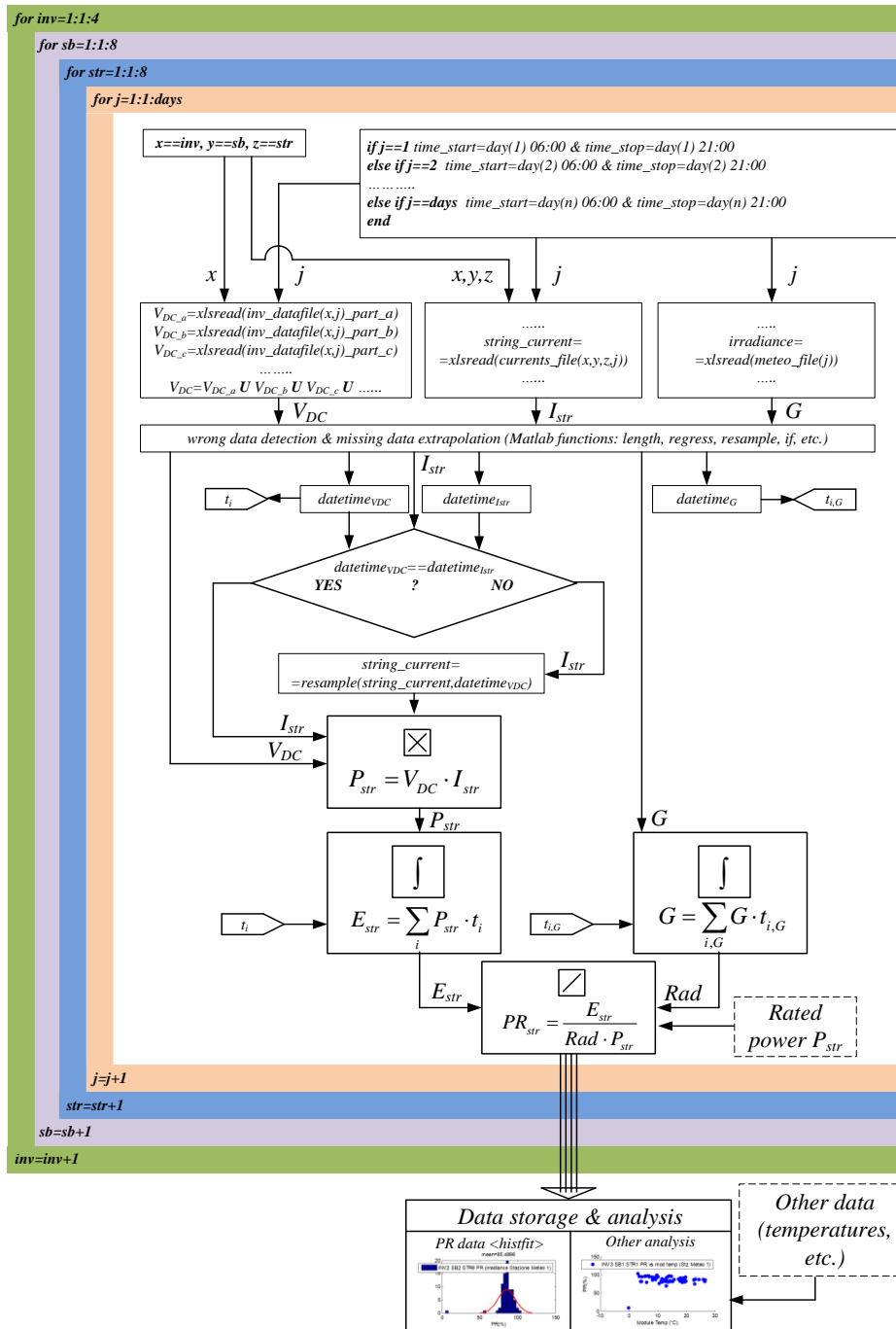


Figure 85. Data processing of measurements provided by plant dataloggers in case study 2

Fig. 86 shows the timeline of the data exploited in the present analysis. Days in yellow refer to unavailabilities, faults, issues in monitoring system, etc. causing wrong

or missing data. The integrated state-space average model introduced in this work is used in many cases to replace such data. Anyway, according to IEC 61724, the days with very large issues in measured data, were removed from the analysis in order to avoid any false results.

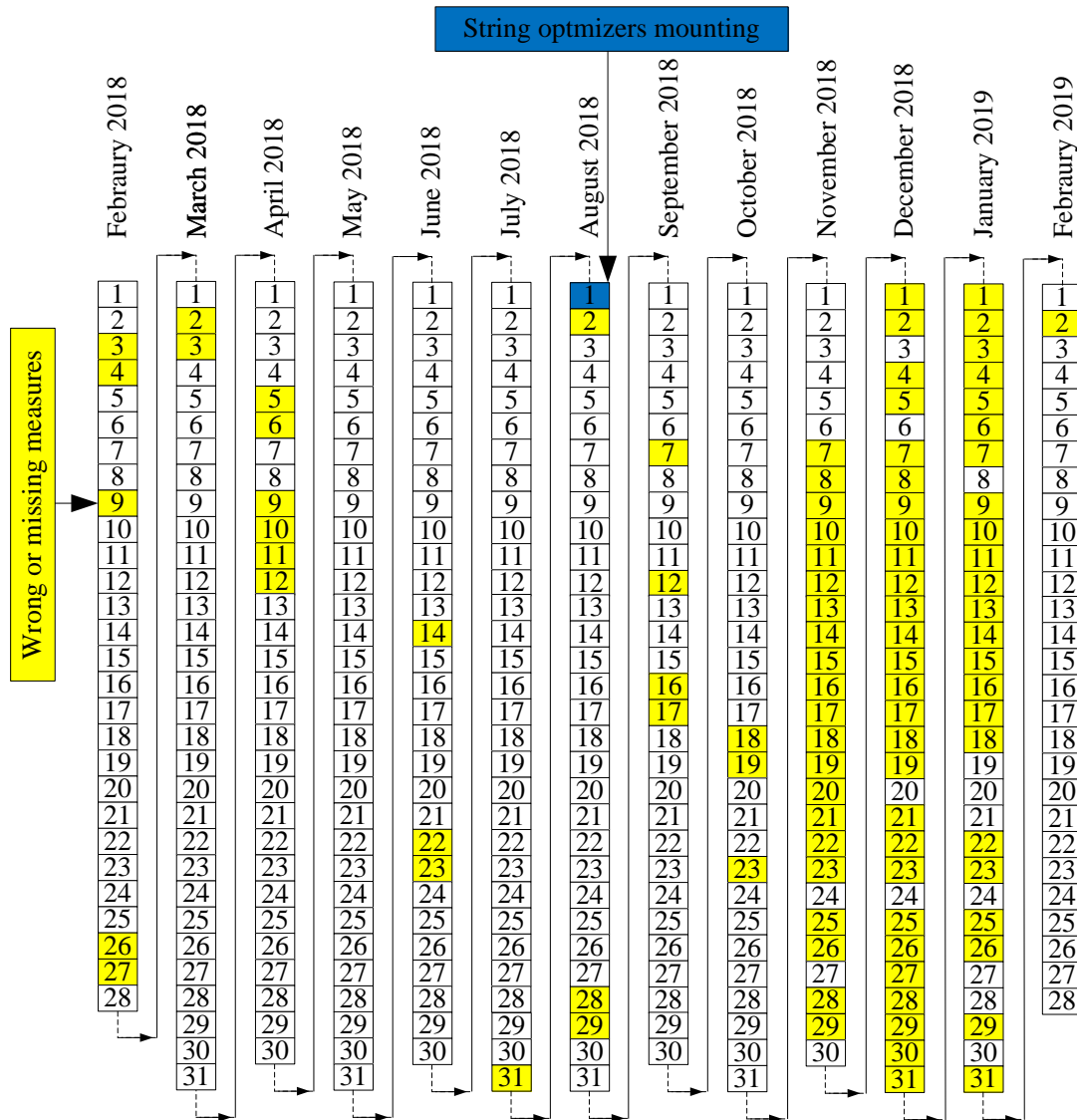


Figure 86. Timeline of data exploited in case study 2. Days in yellow refer to unavailabilities, faults, issues in monitoring system, etc. causing wrong or missing data

A list of the main cases of unavailability occurring in the period under consideration is in Table 42.

PV Component	Date	Unavailability
Inverter 1, SB 1, String 2	1 Feb to 31 Jul 2018	1 sub-string KO = 1/2 string KO
Inverter 1, SB 7, String 1	1 Feb to 31 Jul 2018	2 sub-strings KO = 1 string KO
Inverter 2, SB 1, String 1	1 Feb 2018 to 3 Feb 2019	1 sub-string KO = 1/2 string KO
Inverter 2, SB 2, String 3	1 Feb to 31 Jul 2018	1 sub-string KO = 1/2 string KO
Inverter 3, SB 1, String 7	1 Feb to 31 Jul 2018	1 sub-string KO = 1/2 string KO
Inverter 3, SB 5, String 7	1 Feb to 31 Jul 2018	1 sub-string KO = 1/2 string KO
Inverter 3, SB 8, String 3	1 Feb to 31 Jul 2018	1 sub-string KO = 1/2 string KO
Inverter 4, SB 2, String 8	1 Feb to 31 Jul 2018	1 sub-string KO = 1/2 string KO
Inverter 4, SB 6	12 Apr to 31 Jul 2018	Fault at SB level
Inverter 4, SB 1, String 1	7 Sep 2018 to 3 Feb 2019	2 sub-strings KO = 1 string KO
Inverter 4, SB 8, String 5	7 Sep to 11 Dec 2018	2 sub-strings KO = 1 string KO
Inverter 4, SB 2, String 2	7 Sep to 19 Dec 2018	2 sub-strings KO = 1 string KO
Inverter 1, SB 1, String 6	25 Jan to 3 Feb 2019	1 sub-string KO = 1/2 string KO
Inverter 2, SB 2, String 1	22 Dec 2018 to 3 Feb 2019	1 sub-string KO = 1/2 string KO
Inverter 4, SB 8	12 Dec to 19 Dec 2018	Fault at SB level

Table 42. List of the main cases of unavailability in the period under consideration

11.1.1 Relevance of the PV plant model

The usefulness of the model addressed to large PV plant, introduced in this work, can be highlighted with an example.

Fig. 87 shows the power curve of a PV array in the experimental subfield measured during a sunny day in the autumn 2018. The power waveform provided by the behavioral model is superimposed to the measured one. From 10:40 to 12:00 a maintenance shutdown occurs. Thanks to the model, the theoretical energy during this shutdown is estimated with a good accuracy. The relative error in the pink area, that is about 1.8 %, is calculated from:

$$\varepsilon_{\%} = \frac{E_{model} - E_{measured}}{E_{measured}} 100 \quad (82)$$

To establish an average reference value for the accuracy of the proposed modelling approach, the power curve provided by the model is compared to the one measured in the field during several days in 2018 and 2019. The accuracy level

calculated by (82) is in the range from 1.5 % to 3.0 % that is fully acceptable in comparison to the typical accuracy of standard power meters and sensors.

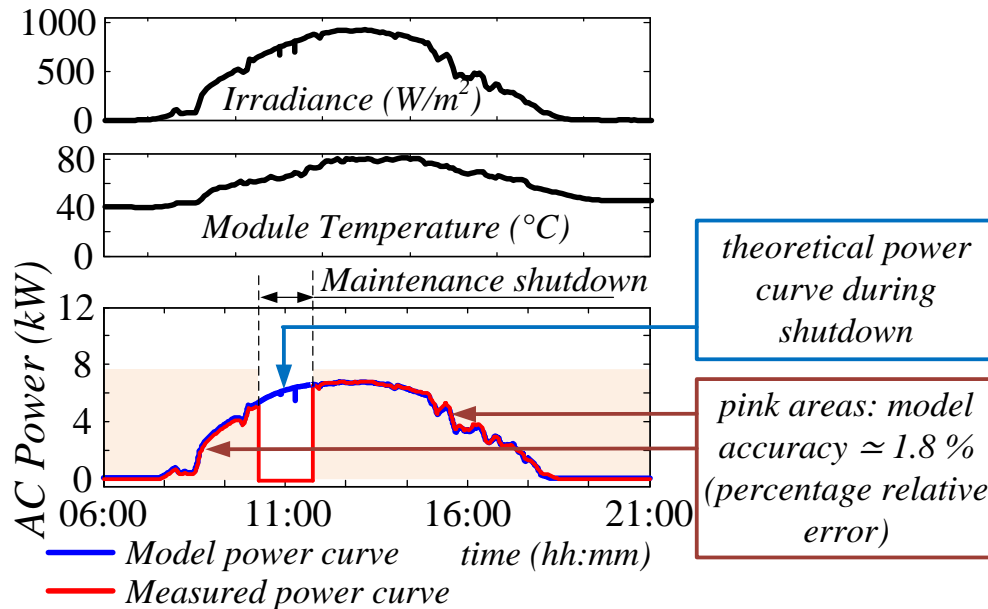


Figure 87. Comparison between measured power and power curve provided by model during a sunny day in autumn 2018. The behavioral model is used to trace the theoretical power curve during a maintenance shutdown

11.1.2 Execution time performance

Performing a procedure similar to that described in Section 9.2.2, the computational complexity of the behavioral model has been tested for case study 2. The execution time is the basic parameter for the comparison of the integrated state-space average model with a detailed model, as in Section 9.2.2.

Two different cases are considered:

- Case A: the same simulation step size $1 \cdot 10^{-6}$ s is assigned to the state-space average model and to the detailed one
- Case B: a larger sample time, equal to $2 \cdot 10^{-5}$ s, is assigned to the state-space average model. The step size of the detailed model is equal to the previous case otherwise such model cannot run properly

For both cases, two different operating scenarios have been implemented and run 1000 times to get a large statistical database. The relative difference in execution times

is summarized in Table 43. As expected, the behavioral model ensures a significant reduction in computational effort.

	Case A, execution time	Case B, execution time
Scenario 1	Detailed model: mean=72.2 s, std=3.0 s	Detailed model: mean=72.2 s, std=3.0 s
	Proposed model: mean=27.7 s, std=4.8 s	Proposed model: mean=3.5 s, std=0.2 s
	Relative difference: mean= -61.6 % std= 6.6 %	Relative difference: mean= -95.1 % std= 0.3 %
Scenario 2	Detailed model: mean=72.1 s, std=0.8 s	Detailed model: mean=72.1 s, std=0.8 s
	Proposed model: mean=30.0 s, std=1.5 s	Proposed model: mean=3.5 s, std=0.1 s
	Relative difference: mean= -62.6 % std= 2.2 %	Relative difference: mean= -95.1 % std= 0.1 %

Table 43. Execution time performance evaluation for case study 2, state-space average model vs detailed model. Simulation end time instant: 0.3 s. Scenario 1: 1000 W/m², 25° C. Scenario 2: 800 W/m², 45° C, non-zero reactive power is forced after 0.1 s. Computer hardware: Intel Core i3-4005U CPU@1.70 GHz (4 CPUs), RAM 4096 MB, HD SSD 240 GB read speeds up to 545 MB/s, 64 bit.

11.2 Performance assessment

11.2.1 DC cables voltage drops

In the experimental subfield, a direct measurement of the current in the cables that connect the optimizers to the DC-link of the central inverter is not available. The integrated state-space average model described in this work is able to calculate the average DC-link current (flowing in DC cables) in a straightforward way as a linear function of the symmetrical components of the AC currents, see Section 7.1.1. In such a way, it is possible to evaluate in a direct way the actual voltage drop and Joule losses for each DC cable.

In Figs. 83-84, these DC cables are represented by their resistance R_{DC} . On the basis of the real power configuration, for each line R_{DC} is the sum of 2 resistances, related to:

- DC line from the string box to an intermediate parallel switchboard named DCHV;
- DC line from the switchboard DCHV to the inverter.

Fig. 88 reports an aerial photo with an example of calculation for R_{DC} . Table 44 lists the values of resistance for each DC line in the PV plant.

Exploiting data acquired during a sunny day in winter 2019, Fig. 89 reports the time graph of voltage drop calculated for two DC lines, one belonging to the experimental subfield and the other belonging to another subfield. Thanks to the higher DC voltage value, the voltage drops as well as the Joule losses are lower in the experimental subfield in comparison to the other subfields. However, in the PV plant under investigation such effects can be sometimes neglected thanks because of the short lengths of DC cables and of their large cross sections.

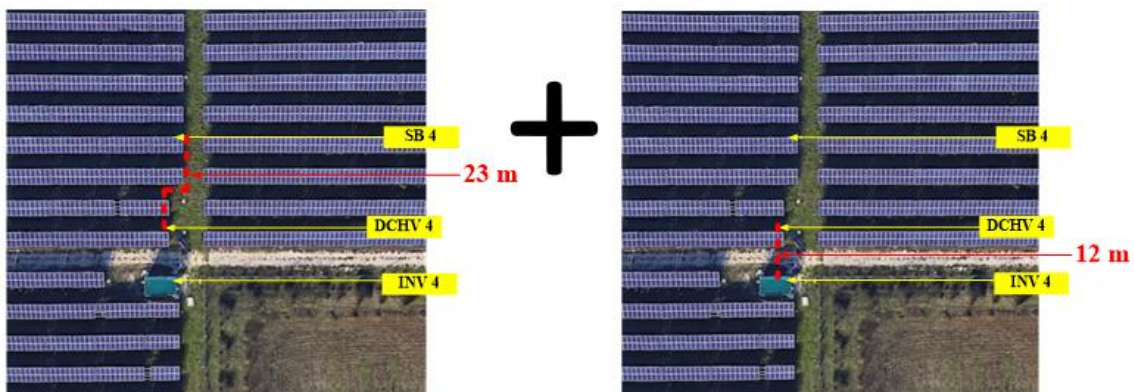


Figure 88. Example of calculation for R_{DC} . Left: first part of the DC line, cable cross section 120 mm^2 , resistance per kilometre $0.16 \text{ } \Omega/\text{km}$, resistance $0.0037 \text{ } \Omega$. Right: second part of the DC line, cable cross section 240 mm^2 , resistance per kilometre $0.080 \text{ } \Omega/\text{km}$, resistance $0.0010 \text{ } \Omega$

	SB to DCHV		DCHV to inverter	
	Distance (m)	Resistance (Ω)	Distance (m)	Resistance (Ω)
Subfield Inverter 1	13.0	0.00208	13.0	0.00104
	1.5	0.00024	13.0	0.00104
	13.0	0.00208	13.0	0.00104
	26.0	0.00416	13.0	0.00104
	39.0	0.00624	13.0	0.00104
	55.0	0.00880	13.0	0.00104
	72.0	0.01152	13.0	0.00104
	81.0	0.01296	13.0	0.00104
Subfield Inverter 2	31.0	0.00496	20.0	0.00160
	23.0	0.00368	20.0	0.00160
	38.0	0.00608	20.0	0.00160
	20.0	0.00320	20.0	0.00160
	1.5	0.00024	20.0	0.00160
	20.0	0.00320	20.0	0.00160
	26.0	0.00416	20.0	0.00160
	62.0	0.00992	20.0	0.00160
Subfield Inverter 3	1.5	0.00024	25.0	0.00200
	14.0	0.00224	25.0	0.00200
	27.0	0.00432	25.0	0.00200
	40.0	0.00640	25.0	0.00200
	53.0	0.00848	25.0	0.00200
	73.0	0.01168	25.0	0.00200
	66.0	0.01056	25.0	0.00200
	88.0	0.01408	25.0	0.00200
Subfield Inverter 4	28.0	0.00448	12.0	0.00096
	1.5	0.00024	12.0	0.00096
	7.0	0.00112	12.0	0.00096
	23.0	0.00368	12.0	0.00096
	38.0	0.00608	12.0	0.00096
	50.0	0.00800	12.0	0.00096
	57.0	0.00912	12.0	0.00096
	72.0	0.01152	12.0	0.00096

Table 44. Values of resistance for each DC line in the PV plant.

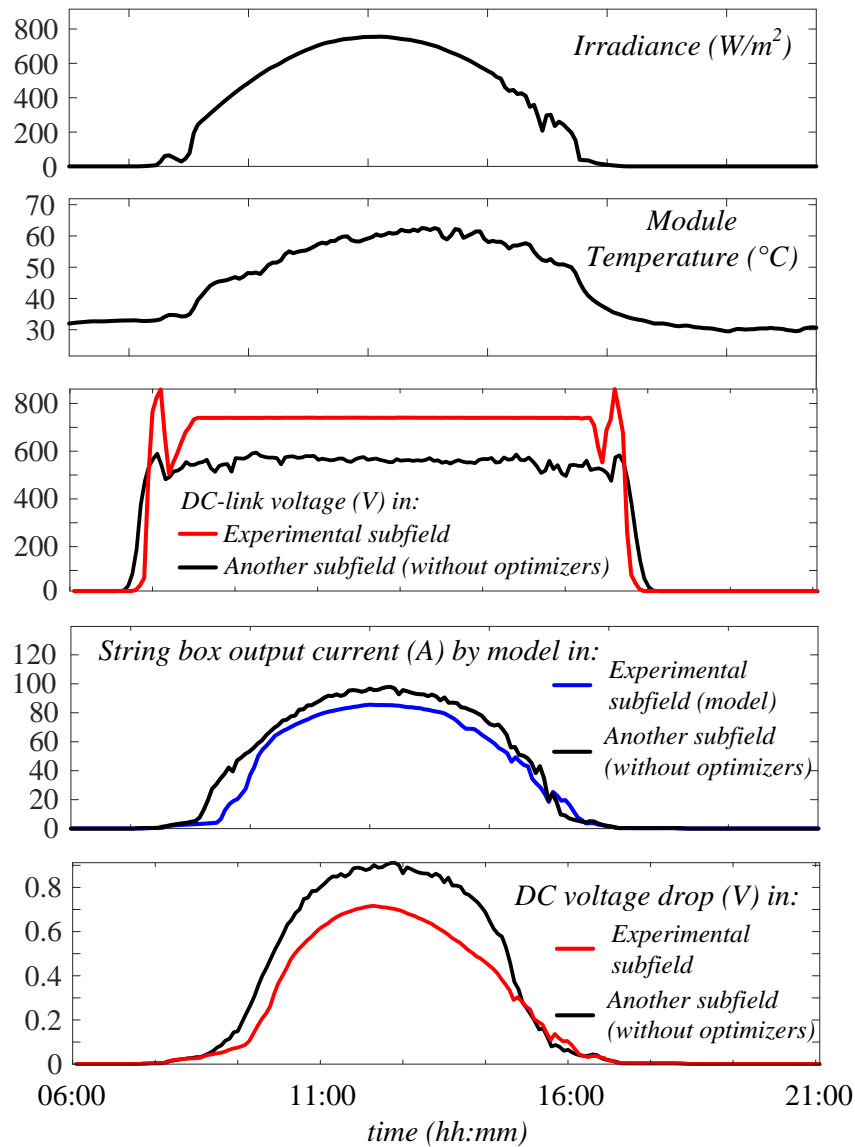


Figure 89. Calculation of voltage drop during a sunny day in winter 2019. Comparison between the experimental subfield and another subfield with the original configuration

11.2.2 Analysis 1: Inverter EOH from strings data

In this first analysis, the DC energy of each string is calculated by integrating the DC active power. The latter is the product between DC-link voltage (considering DC voltage drop) and string current measured at the output of string optimizer. The DC energy at the inverter DC_Energy_{invx} is the sum of the DC energy of the connected

strings. x is the subfield number (1, 2, 3 or 4). For each day, the Equivalent Operating Hours (EOH) of each inverter is calculated as:

$$EOH_{invx} = \frac{DC_Energy_{invx}}{rated_power_{invx,actual}} \cdot 100 \quad (83)$$

where the denominator is the actual value of the sum of PV modules power calculated by excluding the unavailable power.

For each day, the value EOH_{inv4} , calculated for the experimental subfield, is compared to EOH_{inv2} , EOH_{inv3} and EOH_{inv1} :

$$\Delta EOH_{inv4-1} = \frac{EOH_{inv4} - EOH_{inv1}}{EOH_{inv1}} \cdot 100 \quad (84)$$

$$\Delta EOH_{inv4-2} = \frac{EOH_{inv4} - EOH_{inv2}}{EOH_{inv2}} \cdot 100 \quad (85)$$

$$\Delta EOH_{inv4-3} = \frac{EOH_{inv4} - EOH_{inv3}}{EOH_{inv3}} \cdot 100 \quad (86)$$

The values of these percentage differences for the periods “before distributed converters” bDC and “after distributed converters” aDC, are reported in Table 45. The comparison of these values leads to the assessment of the average gain related to the installation of string optimizers that, under the present criterion, is + 1.96 %. A discussion on this result is in Section 11.2.7.

	bDC	aDC	Average gain
ΔEOH_{inv4-1}	- 2.19 %	- 0.05 %	+ 1.96 %
ΔEOH_{inv4-2}	- 2.59 %	- 1.48 %	
ΔEOH_{inv4-3}	- 2.36 %	+ 0.28 %	

Table 45. Results of analysis 1

11.2.3 Analysis 2: Inverter EOH from counters

In this second analysis, data is provided by counters place outside the inverters. The AC active energy data measured by such counters AC_Energy_{invx} is in the form of 1/4 hour energy.

The EOH of each inverter is calculated as:

$$EOH_{invx} = \frac{AC_Energy_{invx}}{rated_power_{invx,actual}} 100 \quad (87)$$

where the denominator is the actual value of the sum of PV modules power calculated by excluding the unavailable power.

For each day, the value EOH_{inv4} calculated for the experimental subfield is compared to EOH_{inv2} , EOH_{inv3} and EOH_{inv4} as reported for the analysis 1 in Section 11.2.2.

The values of the percentage differences in (84)-(86) for the periods “before string optimizers” bDC and “after string optimizers” aDC, are reported in Table 46 in relation to the present criterion. The comparison of these values leads to the assessment of the average gain related to the installation of string optimizers that, under the present criterion, is - 1.56 % i.e. negative. A discussion on this result is in Section 11.2.7.

	bDC	aDC	Average gain
ΔEOH_{inv4-1}	- 0.77 %	- 2.12 %	- 1.56 %
ΔEOH_{inv4-2}	- 0.53 %	- 2.85 %	
ΔEOH_{inv4-3}	- 0.68 %	- 1.68 %	

Table 46. Results of analysis 2

11.2.4 Analysis 3: Inverter EOH from monitoring system AC data

In this third analysis, data source is the AC power measurement provided by dataloggers. The AC active energy data AC_Energy_{invx} is calculated by integrating the AC active power data.

The EOH of each inverter is calculated in the same way described in for analysis 2 in Section 11.2.3.

For each day, the value EOH_{inv4} , calculated for the experimental subfield, is compared to EOH_{inv2} , EOH_{inv3} and EOH_{inv4} as reported for the analysis 1 in Section 11.2.2.

The values of the percentage differences in (84)-(86) for the periods “before string optimizers” bDC and “after string optimizers” aDC, are reported in Table 47 for the present criterion. The comparison of these values leads to the assessment of the average gain related to the installation of string optimizers that, under the present criterion, is - 2.34 % i.e. negative. A discussion on this result is in Section 11.2.7.

	bDC	aDC	Average gain
ΔEOH_{inv4-1}	- 1.50 %	- 3.62 %	- 2.34 %
ΔEOH_{inv4-2}	- 0.03 %	- 2.88 %	
ΔEOH_{inv4-3}	- 1.08 %	- 3.13 %	

Table 47. Results of analysis 3

11.2.5 Analysis 4: Daily PR of PV arrays in experimental subfield

Fig. 90 shows the distribution plots of the daily PR for some PV strings connected at the input of the DC/DC optimizers in the experimental subfield for the time periods bDC (February 2018 to July 2018) and aDC (August 2018 to February 2019). Vertical axis for charts are adapted on the basis of available data.

The daily PR of each PV string is calculated using formula:

$$PR_{str} = \frac{E_{str}}{P_{str} \cdot Rad} \quad (88)$$

where P_{str} is the rated power of the string (sum of the rated power of 2 sub-strings), Rad is the daily solar radiation, E_{str} is the daily energy calculated from the power curve of the selected string. This power is calculated using the current value at the optimizer output and the DC-link voltage, taking into account the voltage drop on DC cables.

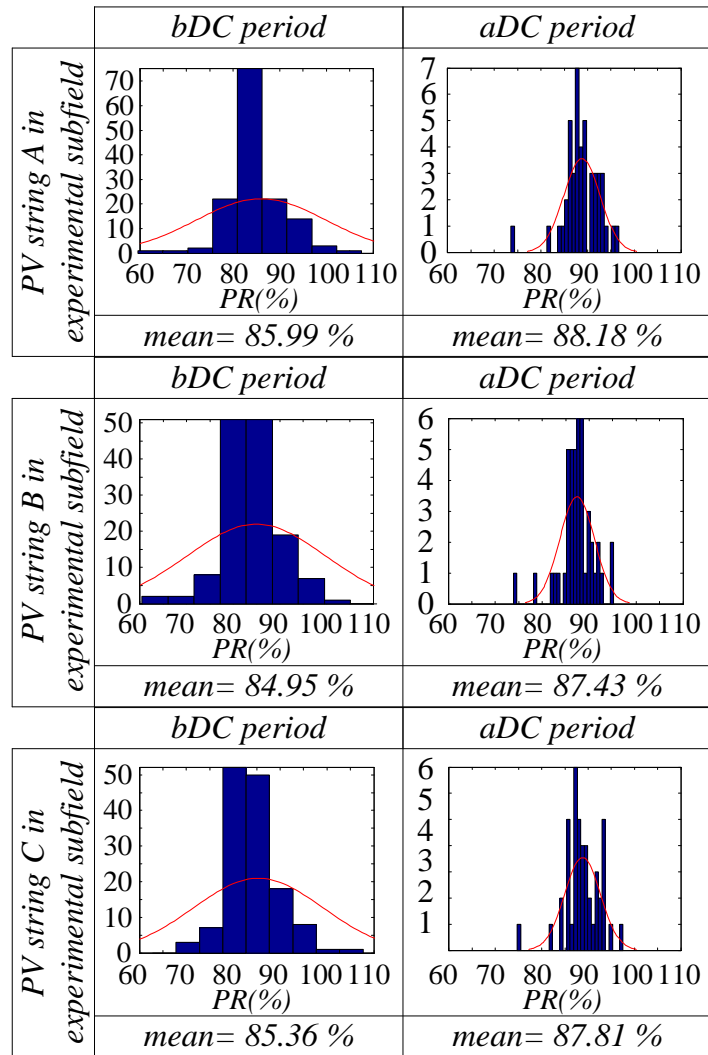


Figure 90. Distribution plots of the daily PR in some strings of the experimental subfield for periods bDC and aDC

From the examples in Fig. 90, the benefit of distributed converters is evident. Charts of PR for all the strings in the experimental subfield for the periods bDC and aDC are in Appendix 3.

Repeating the calculation in (88) for all the PV strings in the experimental subfield and comparing bDC and aDC periods, the aggregate result in Fig. 91 shows that, under the present criterion, the average benefit obtained in terms of PR is about 2%.

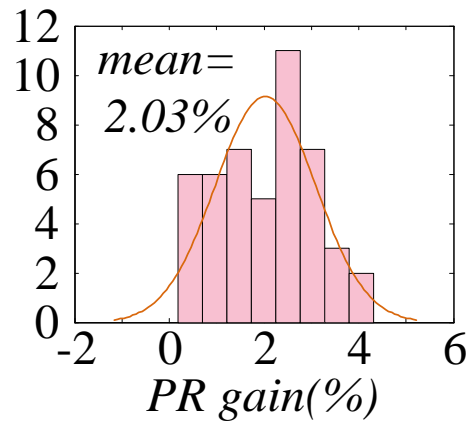


Figure 91. Distribution plot of the PR gain in all the arrays of the experimental subfield, time period February 2018 to February 2019

11.2.6 Central inverter operation

It is useful to investigate the behaviour of the central inverter whose control system was modified removing the original MPPT control and fixing the DC-link voltage in a narrow range around 730 V.

This investigation is justified by the following evidences:

- looking at gain calculation process using strings data (DC side, analysis 1 and 4), the installation of string optimizers gives a benefit around 2 %;
- looking at inverter data (AC side, analysis 2 and 3), the installation of string optimizers causes a loss around 2 % or more.

In other words, the results of the analysis seem not consistent each other.

It is necessary to check the behaviour of the inverter in the experimental subfield. For the sake of example, Fig. 92 shows the main electrical quantities acquired by the datalogger of the inverter 4 in the experimental subfield during two days belonging to the bDC and aDC period.

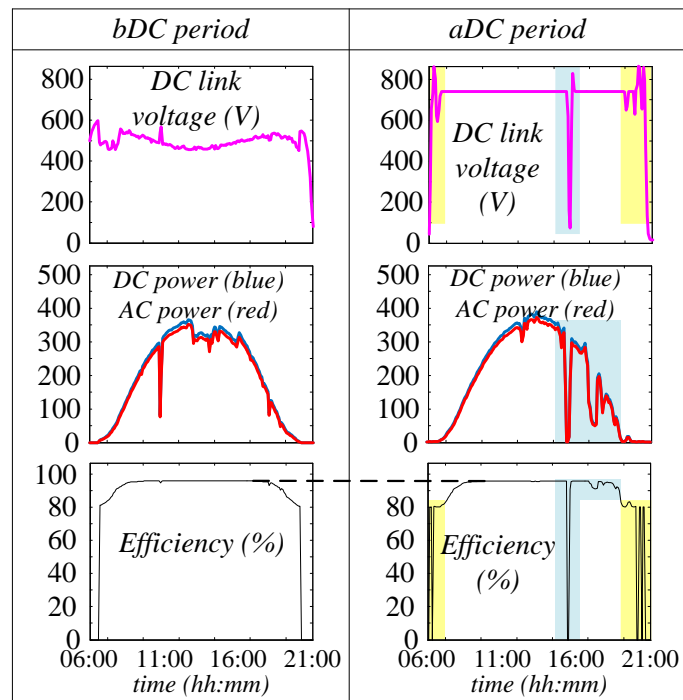


Figure 92. Main electrical quantities acquired by the datalogger of the central inverter in the experimental subfield during two days close to the installation date of string optimizers

It emerges that:

- the maximum efficiency in the aDC period is equal to the one measured in the bDC period (dashed line);
- in the aDC period, during sunrise and sunset the DC-link voltage exhibits large fluctuations (yellow areas);
- the same phenomenon occurs in case of fast power variations (cyan areas) causing temporary significant decrease in efficiency level.

Finally, the modification of the control strategy in central inverter implies bad effects on its operation in case of large power fluctuations, leading to a reduction of the energy gain measured at the AC side in variable weather conditions.

11.2.7 Conclusions on performance assessment

The performance evaluation of distributed converters in case study 2 leads to the determination of average benefit whose value is about 2 % measured at the DC side of the PV plant under analysis.

Unfortunately, this benefit worsens at the AC side causing negative effects that would make the installation of string optimizers not convenient. The situation originates from the inverter, whose control system was modified during the mounting of distributed converters. Further investigations in collaboration with the inverter manufacturer are needed to clarify the technical reasons of this behavior.

At the same time, exploiting data coming from similar retrofits in other large PV plants, it was verified that this kind of problems is recurrent only for a few specific inverter brands as the one in case study 2 while it does not occur for the most part of cases.

11.3 Integration of ESS in case study 2

This Section refers to the verification of the proposed approach regarding the matching between the PV plant model and the ESS state estimation algorithm. Such novel approach is described in Section 8.3.

The examples in following Section deal with such matching. The analysis is carried out with some examples using real data acquired during 2018 in the PV plant representing the case study 2.

The reference scheme is in Fig. 93.

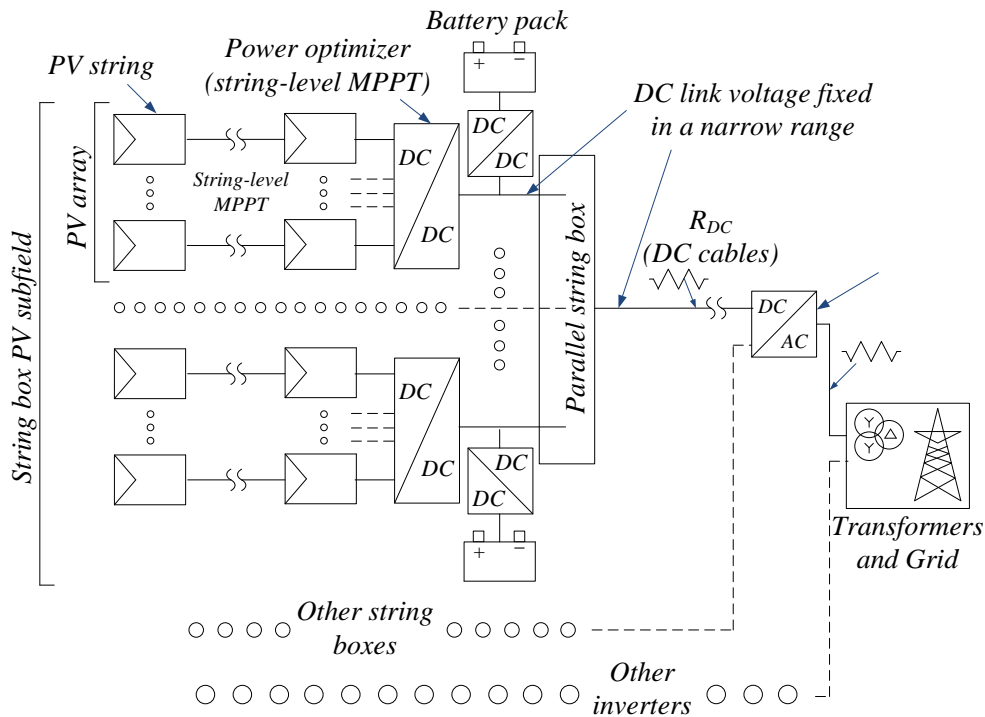


Figure 93. Single line diagram for the case study 2 with the integration of distributed ESS

11.3.1 Scenario 1

Fig. 94 shows the main electric quantities for the PV array no. 1 of a string box in the experimental subfield 4 as well as for its ESS (ESS 1) during a cloudy day in autumn 2018. The ESS is a 48 V 200 Ah LA battery pack. A scheduled maintenance activity was performed at 10 AM with the purpose to check the insulation level of the DC cable that links the string box to the central inverter. During this work activity, all the PV arrays connected to that string box were disconnected for about 2 hours causing a significant production loss.

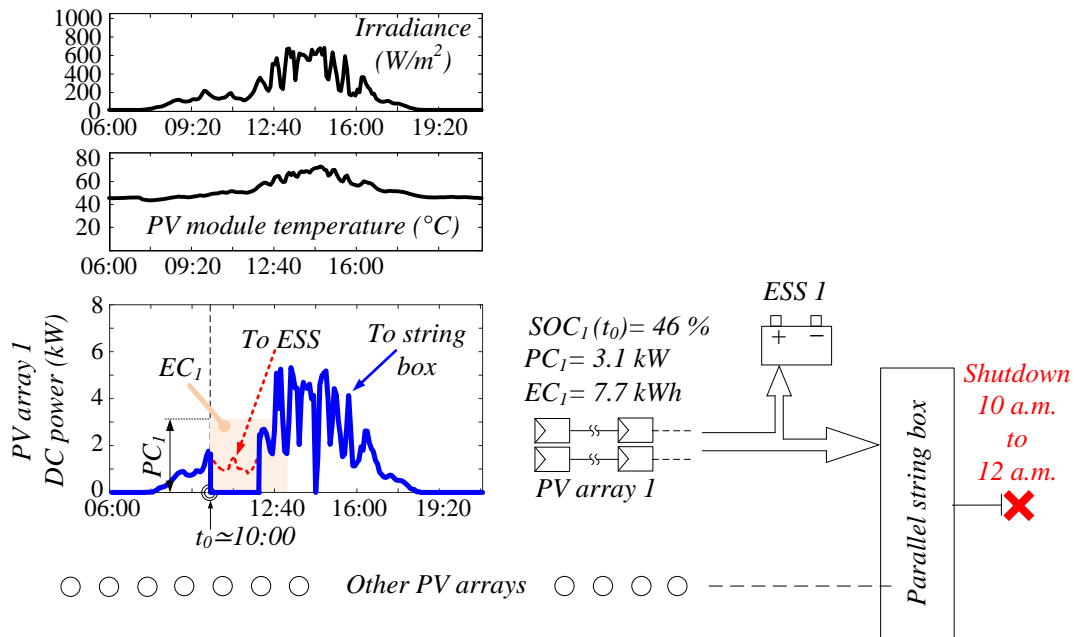


Figure 94. Example of operating scenario: the ESS is used to store the energy produced by the PV array 1 being part of a string box in the experimental subfield during a maintenance shutdown

It is interesting to know if this loss could be avoided in presence of a distributed ESS. It is necessary to compare the expected PV power production during the scheduled maintenance activity with the PC and EC of the ESS at its actual SOC.

The expected power curve, that is the dashed line in Fig. 94, can be traced running the PV field model with data downloaded from one of the common weather forecast services that provide in advance information on irradiance and temperature with a good accuracy. Just before the shutdown, the actual PC and EC of the ESS are calculated using formulas (20) and (21). The time horizon in such formulas is set equal to 3 hours in order to take into account unforeseen events that could extend the deadline expected for the maintenance activity.

Plots highlight that, in this case, the ESS is able to store all the expected energy produced during the maintenance activity.

This kind of energy assessment can support the scheduling of similar maintenance activities with the purpose to limit the production losses from time to time.

11.3.2 Scenario 2

Fig. 95 shows another operating scenario simulated using data acquired by the datalogger of the PV field during a clear sky day in autumn 2018.

Storage units of the distributed ESS consist of 48 V 200 Ah LA battery packs, the selected string box has 6 power inputs i.e. 6 PV arrays. Each PV array consists of 2 strings in parallel. The SOH of the batteries is 100 %. The charging efficiency η_{ch} is considered as constant equal to 80 % while the SOC_{max} is set at 99 %.

Let us suppose that the PPC fixes a maximum power threshold for the PV plant (for any grid stability reasons) that implies an overall DC power limit of 35 kW for each string box. The extra energy overcoming this threshold can be stored in batteries.

At time t_0 (10:30 AM) the DC power generated by the string box is approaching to such limit, consequently one or more ESS have to be activated in a short time. To comply with the fixed power threshold, it is sufficient to activate only 2 ESS, in particular the ones named ESS 2 and ESS 4 that have higher PC and EC in comparison to the others. The time horizon in (20) is set equal to 5.5 hours in order to include the central part of the day during which high power is expected to take place.

Looking at the power plots in Fig. 95, it is confirmed that the activated battery packs are able to store the extra energy while decreasing the power flowing to string box in order to fulfill the PPC requirements.

In the power plot of PV array 4, the PC of ESS 4 seems to be too low in comparison to the expected maximum power but, in reality, this analysis has to be merged with information regarding the actual SOC as done in Fig. 96.

The increase of SOC_4 from t_0 to 13:00 AM is actually lower than the one calculated for a fixed current $i_{bt,ch,PC}$ at time t_0 since the generated PV power is lower than peak for the most part of the day.

From the recalculation of the PC and EC of ESS 4 at time t_1 13:00 AM, it can be stated that the battery pack is actually able to store the energy produced by the PV array without overcoming the SOC_{max} limit.

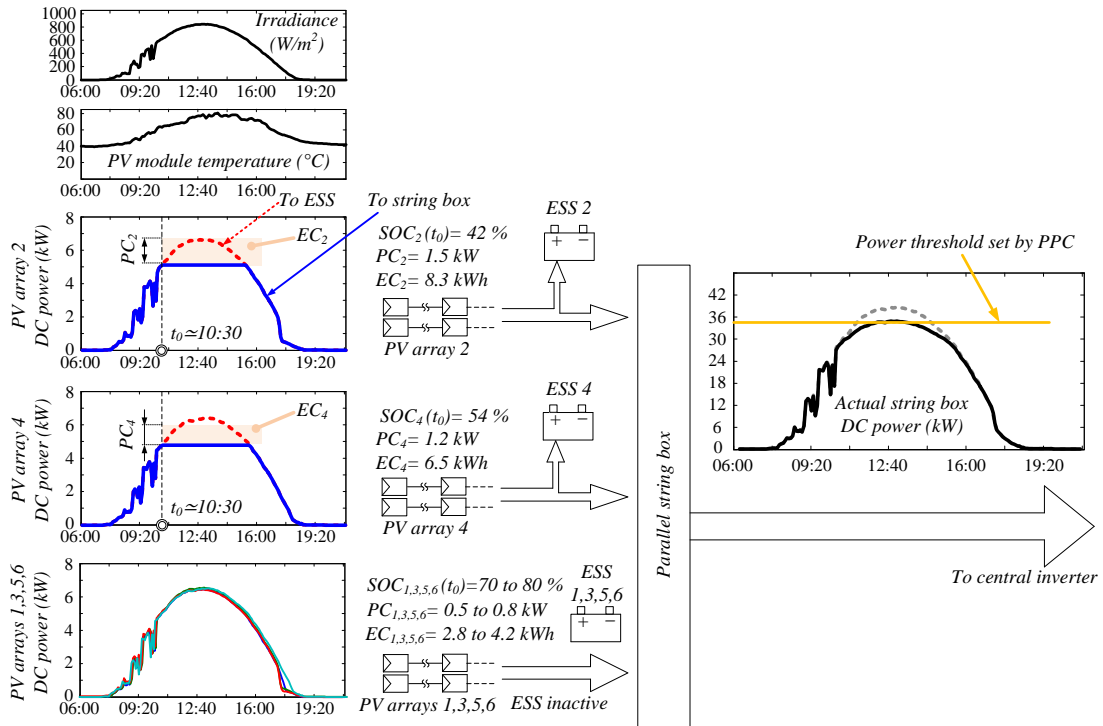


Figure 95. Example of operating scenario in which the distributed ESS is used to store the produced energy in case of power limitation forced by the PPC

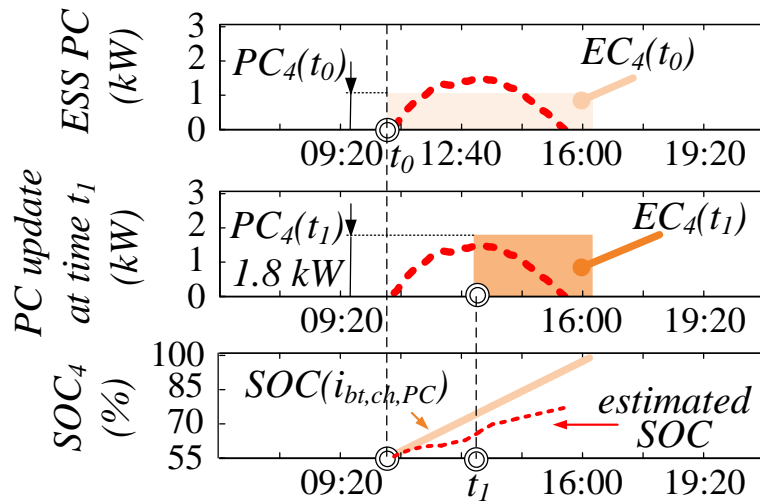


Figure 96. Recalculation of PC and EC of ESS 4 at time t_1 on the basis of the actual SOC value that is continuously estimated by the proposed PI observer algorithm

Finally, the usefulness of the proposed approach is shown applying the same to the case study represented by a real 2 MW PV plant in Central Italy. The calculation of PC and EC for each battery pack and the matching with the power curves of the PV arrays

connected to the distributed ESS allows to establish the optimal energy management strategies.

Chapter 12 - Conclusions and outlook

The massive exploitation of fossil fuels for electricity production in the last century caused their continuous depletion. To face this problem, the main alternative for the future is represented by renewable energy sources.

Among the renewable sources, PV plants are characterized by specific advantages as the possibility to forecast the energy production with good accuracy as well as a full scalability. This latter characteristic implies that similar configurations and technical solutions can be quickly adapted for a wide range of different situations including large or utility-scale PV plants.

Since the main disadvantage of large PV plants is the occupied land, the research activities are oriented to innovative solutions able to increase the energy productivity or, more generally, the performance of the plants. Under this perspective, this thesis investigates on innovative power configurations, in particular on distributed converters which can reduce the mismatch effect leading to the recovery of significant amount of energy and on the development of an integrated state-space average model addressed to large PV plants.

Moreover, the presence of distributed converters makes it possible the creation of a distributed ESS based on multiple battery packs. This thesis also addresses such promising research topic providing extensive results on control strategies to implement for a proper energy management of the PV + ESS system. Matching of renewable energy sources with ESS is also one of the best ways to converge to smart grids.

The benefits related to the presence of ESS for a PV plant strictly depend on the accurate monitoring of SOC and SOH of the battery pack. From these quantities, it is possible to know PC and EC, that are indexes of the maximum power and energy that the battery can deliver in a given time horizon keeping into normal operating zone with respect to safety, too.

Finally, this thesis investigates on the performance optimization of large or utility-scale PV plants through the installation of distributed converters and the integration of

distributed battery packs. This optimization involves the implementation of innovative control strategies supported by suitable modelling approaches.

Validation of the novelties presented in this thesis has been carried out by means of experimental laboratory tests and through the processing of measurements collected in extensive measurement campaigns carried out in two case studies: a 300 MW PV plant in Brazil and in a 2 MW PV plant in Central Italy.

The results of this work can be summarized as follows:

- development of an integrated state-space average model addressed to large PV plants. This model is a useful tool to replace real data in case of missing or wrong measurements provided by dataloggers of the existing plants. It can be also exploited for forecast purpose;
- development of advanced algorithms for the simultaneous estimation of SOC and SOH of battery packs. Such algorithms integrate suitable ECM selected on the basis of proper performance criteria;
- models built for both PV plants and ESS are an optimal trade-off between accuracy and computational effort. This latter parameter is crucial in the field of interest due to the large amount of data to manage;
- performance assessment of distributed converters in comparison to central inverters exploiting real data from large PV plants in operation;
- numerical evaluation of mismatch level in large PV plants;
- integration of models is performed through an innovative approach exploiting the real-time values of PC and EC. This represents a novel approach, thanks to which merging of ESS and PV systems is obtained in a simple but effective way.

Since the validity of the models and algorithms introduced in this thesis has been already confirmed using data from real PV plants over a long time horizon, the implementation of such methods into industrial monitoring systems represents the natural continuation of this work. Several advances are expected to take place for automatic fault detection, energy production forecast, sizing of battery packs and so on.

Appendices

Appendix 1: Matlab code examples, case study 1

A.1.1 String inverter energy and peak power

```
%%%%%%%%%%%% days selection %%%%%%%%%%%%%%
for j=1:1:7;
    if j==1; time_start = '28/10/2018 05:00:00'; time_stop = '28/10/2018 20:00:00';
    else if j==2; time_start = '29/10/2018 05:00:00'; time_stop = '29/10/2018 20:00:00';
    else if j==3; time_start = '30/10/2018 05:00:00'; time_stop = '30/10/2018 20:00:00';
    else if j==4; time_start = '31/10/2018 05:00:00'; time_stop = '31/10/2018 20:00:00';
    else if j==5; time_start = '01/11/2018 05:00:00'; time_stop = '01/11/2018 20:00:00';
    else if j==6; time_start = '02/11/2018 05:00:00'; time_stop = '02/11/2018 20:00:00';
    else time_start = '03/11/2018 05:00:00'; time_stop = '03/11/2018 20:00:00';
        end
    end
    end
    end
    end
    end
    end

formatIn = 'dd/mm/yyyy HH:MM:SS'; %date format adjustment
time_start_num=datenum(time_start,formatIn);
time_stop_num=datenum(time_stop,formatIn);
%%%%%%%%%%%% data extraction from datalogger files %%%%%%%%%%%%%%
[num,text,both]=xlsread('Active Power_28_10_to_03_11',1,'a2:a350000'); %data extraction
text_size=size(text);
for i=1:1:text_size;
    testo=num2str(cell2mat(text(i)));
    C = strsplit(testo,',');
    if length(C)<102;
        testo = strep(testo,',',',',0,');
        C = strsplit(testo,',');
    end
end
```

```

else
end
date_time(i)=C(1); %data extraction, date
STR_INV_02_3_power=C(20); %data extraction, AC power of string inverter no. 3 group 2
STR_INV_02_3_power_num(i)=str2num(num2str(cell2mat(STR_INV_02_3_power)));
i=i+1;
end
STR_INV_02_3_power_num=STR_INV_02_3_power_num';
formatIn = 'mm/dd/yyyy HH:MM:SS';
date_num=datenum(date_time,formatIn); %date format adjustment
[c time_start_rowNum] = min(abs(date_num-time_start_num));
[c time_stop_rowNum] = min(abs(date_num-time_stop_num));
time_start_rowNum;
time_stop_rowNum;
%%%%%%%%%% energy calculation %%%%%%%%%%%
STR_INV_02_3_energy=0;
for k=time_start_rowNum:1:time_stop_rowNum-1;
singola_area=STR_INV_02_3_power_num(k)*(str2num(datestr((date_num(k+1)-
date_num(k)), 'SS'))/3600+str2num(datestr((date_num(k+1)-date_num(k)), 'MM'))/60);
STR_INV_02_3_energy=STR_INV_02_3_energy+singola_area;
End
%%%%%%%%%% peak power calculation %%%%%%%%%%%
STR_INV_02_3_power_subset=STR_INV_02_3_power_num(time_start_rowNum:time_stop_r
owNum);
STR_INV_02_3_peak_power=max(STR_INV_02_3_power_subset);
%%%%%%%%%% plots %%%%%%%%%%%
time_start_plot = time_start;
time_stop_plot =time_stop;
formatIn = 'dd/mm/yyyy HH:MM:SS';
start_plot=datenum(time_start_plot,formatIn);
stop_plot=datenum(time_stop_plot,formatIn);
figure(1);
plot(date_num,STR_INV_02_3_power_num);

```

```

legend('STR_INV 02_3 power'); axis([start_plot stop_plot -inf inf]);
datetick('x',15,'keplimits','kepticks')
title('inverter 02_3 power in QPCA1');
%%%%% message box with results - energy %%%%%%%%%%%
Line1=strcat('Start:',time_start);
Line2=strcat('Stop:',time_stop);
Line3=strcat('String inverter STR_INV 03_2 energy: ',num2str(STR_INV_03_2_energy,7),'
kWh');
h=msgbox({Line1;Line2;Line3} , 'Results data','non-modal');
set(h, 'position', [100 100 1000 450]); %makes box bigger
ah = get( h, 'CurrentAxes' );
ch = get( ah, 'Children' );
set( ch, 'FontSize', 10 ); %makes text bigger
set( h, 'Color',[1,1,1]);
%%%%% message box with results – peak power %%%%%%%%%%%
Line1=strcat('Start:',time_start);
Line2=strcat('Stop:',time_stop);
Line3=strcat('String inverter STR_INV 02_3 peak power:
',num2str(STR_INV_02_3_peak_power,7),' kW');
h=msgbox({Line1;Line2;Line3} , 'Results data','non-modal');
set(h, 'position', [100 100 1000 450]); ah = get( h, 'CurrentAxes' ); ch = get( ah, 'Children' ); set(
ch, 'FontSize', 10 ); set( h, 'Color',[1,1,1]);
% %%%%%%%%%%% results collection %%%%%%%%%%%
STR_INV_02_3_energy_list(j)=STR_INV_02_3_energy;
STR_INV_02_3_peak_power_list(j)=STR_INV_02_3_peak_power;
% %%%%%%%%%%% iteration %%%%%%%%%%%
j=j+1;
end

```

A.1.2 Central inverter energy, peak power and internal temperature

```

%%%%%%%%%% days selection %%%%%%%%%%%
time_start = '16/06/2019 05:00:00';

```

```

time_stop = '16/06/2019 20:00:00';
formatIn = 'dd/mm/yyyy HH:MM:SS';
time_start_num=datenum(time_start,formatIn);
time_stop_num=datenum(time_stop,formatIn);
%%%%%%%% data extraction from datalogger files %%%%%%%%%
CEN_INV1_power=xlsread('Active Power and Inverter Temperature',1,'b2:b350000');
CEN_INV2_power=xlsread('Active Power and Inverter Temperature',1,'d2:d350000');
CEN_INV1_Temperature=xlsread('Active Power and Inverter Temperature',1,'c2:c350000');
CEN_INV2_Temperature=xlsread('Active Power and Inverter Temperature',1,'e2:e350000');
[num,text,both]=xlsread('Active Power and Inverter Temperature',1,'a2:a350000');
date_from_file=text;
i=0;
[m,n] = size(date_from_file);
for i=1:1:m;
    formatIn = 'dd/mm/yyyy HH:MM:SS';
    singolo = datenum(date_from_file(i),formatIn);
    date_num(i)= singolo;
    i=i+1;
end
[c time_start_rowNum] = min(abs(date_num-time_start_num));
[c time_stop_rowNum] = min(abs(date_num-time_stop_num));
%%%%%%%% energy calculation %%%%%%%%%
CEN_INV1_energy=0;
for k=time_start_rowNum:1:time_stop_rowNum;
singola_area=CEN_INV1_power(k)*(str2num(datestr((date_num(k+1)-
date_num(k)), 'SS'))/3600+str2num(datestr((date_num(k+1)-
date_num(k)), 'MM'))/60+str2num(datestr((date_num(k+1)-date_num(k)), 'HH'))/1);
CEN_INV1_energy=CEN_INV1_energy+singola_area;
end
CEN_INV2_energy=0;
for k=time_start_rowNum:1:time_stop_rowNum;

```

```

singola_area=CEN_INV2_power(k)*(str2num(datestr((date_num(k+1)-
date_num(k),'SS'))/3600+str2num(datestr((date_num(k+1)-
date_num(k),'MM'))/60+str2num(datestr((date_num(k+1)-date_num(k),'HH'))/1);
CEN_INV2_energy=CEN_INV2_energy+singola_area;
End
CEN_INV_total_energy=CEN_INV1_energy+CEN_INV2_energy;
% % % % % % % peak power calculation % % % % % % % % % % % % % % % % % %
CEN_INV1_power_subset=CEN_INV1_power(time_start_rowNum:time_stop_rowNum);
CEN_INV2_power_subset=CEN_INV2_power(time_start_rowNum:time_stop_rowNum);
CEN_INV1_peak_power=max(CEN_INV1_power_subset);
CEN_INV2_peak_power=max(CEN_INV2_power_subset);
% % % % % % % internal temperature % % % % % % % % % % % %
CEN_INV1_Temperature_subset=CEN_INV1_Temperature(time_start_rowNum:time_stop_rowNum);
CEN_INV1_Temperature_peak=max(CEN_INV1_Temperature_subset);
CEN_INV1_Temperature_mean=mean(CEN_INV1_Temperature_subset);
CEN_INV2_Temperature_subset=CEN_INV2_Temperature(time_start_rowNum:time_stop_rowNum);
CEN_INV2_Temperature_peak=max(CEN_INV2_Temperature_subset);
CEN_INV2_Temperature_mean=mean(CEN_INV2_Temperature_subset);
% % % % % % % plots % % % % % % % % % % % %
time_start_plot = time_start;
time_stop_plot =time_stop;
formatIn = 'dd/mm/yyyy HH:MM:SS';
start_plot=datenum(time_start_plot,formatIn);
stop_plot=datenum(time_stop_plot,formatIn);
figure(1);
plot(date_num,CEN_INV1_power,'c',date_num,CEN_INV2_power,'g');
legend('CEN_INV1 power','CEN_INV2 power'); axis([start_plot stop_plot -inf inf]);
datetick('x',15,'keeplimits','kepticks'); title('Inverters power');
figure(2);

```

```

subplot(2,1,1); plot(date_num,CEN_INV1_Temperature,'c'); legend('Inverter temperature');
axis([start_plot stop_plot -inf inf]); datetick('x',15,'keeplimits','kepticks'); title('CEN_INV1
Temperature');
subplot(2,1,2); plot(date_num,CEN_INV2_Temperature,'g'); legend('Inverter temperature');
axis([start_plot stop_plot -inf inf]); datetick('x',15,'keeplimits','kepticks'); title('CEN_INV2
Temperature');
figure(3);
[N1,X1] =hist(CEN_INV1_power_subset,100); Bh1 = bar(X1,N1,'facecolor','c','edgecolor','k');
set(get(Bh1,'Children'),'FaceAlpha',0.5); legend('CEN_INV1 power distribution'); xlabel('power
(kW)'); ylabel('minutes (m)'); axis([0 1400 -inf inf]);
figure(4);
[N1,X1] =hist(CEN_INV2_power_subset,100); Bh1 = bar(X1,N1,'facecolor','g','edgecolor','k');
set(get(Bh1,'Children'),'FaceAlpha',0.5); legend('CEN_INV2 power distribution'); xlabel('power
(kW)'); ylabel('minutes (m)'); axis([0 1400 -inf inf]);
figure(5);
[N1,X1] =hist(CEN_INV1_power_subset,100); Bh1 = bar(X1,N1,'facecolor','c','edgecolor','k');
set(get(Bh1,'Children'),'FaceAlpha',0.5); hold on
[N2,X2] =hist(CEN_INV2_power_subset,100); Bh2 = bar(X2,N2,'facecolor','g','edgecolor','k');
set(get(Bh2,'Children'),'FaceAlpha',0.5); legend('CEN_INV1 power distribution','CEN_INV2
power distribution'); xlabel('power (kW)'); ylabel('minutes (m)'); axis([0 1400*2 -inf inf]);
%%%%%% message box with results - energy %%%%%%%%%%%%%
Line1=strcat('Start:',time_start);
Line2=strcat('Stop:',time_stop);
Line3=strcat(' CEN_INV 1 energy: ',num2str(CEN_INV1_energy,7),' kWh');
Line4=strcat(' CEN_INV 2 energy: ',num2str(CEN_INV2_energy,7),' kWh');
Line5=strcat(' CEN_INV total energy: ',num2str(CEN_INV_total_energy,7),' kWh');;
Line6=strcat(' CEN_INV 1 peak power: ',num2str(CEN_INV1_peak_power,5),' kW');
Line7=strcat(' CEN_INV 2 peak power: ',num2str(CEN_INV2_peak_power,5),' kW');
Line8=strcat('CEN_INV1          Temperature,          mean          value:
',num2str(CEN_INV1_Temperature_mean,3),' °C');
Line9=strcat('CEN_INV1          Temperature,          peak          value:
',num2str(CEN_INV1_Temperature_peak,3),' °C');

```



```

time_stop_rowNum;
%%%%%%%%%%%%%%%%%%%%%%%%%%%%%%%%%%%%%%%%%%%%%%%%%%%%%%%%%%%%%%%%%%%%%%%% radiation calculation %%%%%%%%%%%%%%
Irradiation=0;
for k=time_start_rowNum:1:time_stop_rowNum;
singola_area=Irradiance(k)*(str2num(datestr((date_num(k+1)-
date_num(k)), 'SS'))/3600/1000+str2num(datestr((date_num(k+1)-
date_num(k)), 'MM'))/60/1000+str2num(datestr((date_num(k+1)-date_num(k)), 'HH'))/1/1000);
Irradiation=Irradiation+singola_area;
end
%%%%%%%%%%%%%%%%%%%%%%%%%%%%%%%%%%%%%%%%%%%%%%%%%%%%%%%%%%%%%%%%%%%%%%%% message box with results %%%%%%%%%%
Line1=strcat('Start:',time_start);
Line2=strcat('Stop:',time_stop);
Line3=strcat('Irradiation: ',num2str(Irradiation,3),' kWh/m2');
h=msgbox({Line1;Line2;";Line3} , 'Results data', 'non-modal');
set(h, 'position', [100 100 1000 450]); %makes box bigger
ah = get( h, 'CurrentAxes' );
ch = get( ah, 'Children' );
set( ch, 'FontSize', 15 ); %makes text bigger
set( h, 'Color',[1,1,1]);
%%%%%%%%%%%%%%%%%%%%%%%%%%%%%%%%%%%%%%%%%%%%%%%%%%%%%%%%%%%%%%%%%%%%%%%% plots %%%%%%%%%%%%%%
time_start_plot = time_start;
time_stop_plot =time_stop;
formatIn = 'dd/mm/yyyy HH:MM:SS';
start_plot=datenum(time_start_plot,formatIn);
stop_plot=datenum(time_stop_plot,formatIn);
figure(1);
plot(date_num,Irradiance,'b'); legend('Irradiance'); axis([start_plot stop_plot -inf inf]);
datetick('x',15,'keeplimits','kepticks'); title('Irradiance');

```



```

date_from_file=text;
inv4_sb1_current1=xlsread('stringbox_feb_apr_2018','inv4_sb1','d2:d65000');
inv4_sb1_current2=xlsread('stringbox_feb_apr_2018','inv4_sb1','e2:e65000');
inv4_sb1_current3=xlsread('stringbox_feb_apr_2018','inv4_sb1','f2:f65000');
inv4_sb1_current4=xlsread('stringbox_feb_apr_2018','inv4_sb1','g2:g65000');
inv4_sb1_current5=xlsread('stringbox_feb_apr_2018','inv4_sb1','h2:h65000');
inv4_sb1_current6=xlsread('stringbox_feb_apr_2018','inv4_sb1','i2:i65000');
inv4_sb1_current7=xlsread('stringbox_feb_apr_2018','inv4_sb1','j2:j65000');
inv4_sb1_current8=xlsread('stringbox_feb_apr_2018','inv4_sb1','k2:k65000');
[num,text,both]=xlsread('stringbox_feb_apr_2018','inv4_sb1','a2:a65000');
date_from_file_currents_inv4_sb1=text;
[ .....code for the other strings..... ]
formatIn = 'dd/mm/yyyy HH:MM:SS';
date_num=datenum(date_from_file,formatIn);
date_num_currents_inv4_sb1=datenum(date_from_file_currents_inv4_sb1,formatIn);
date_num_currents_inv4_sb2=datenum(date_from_file_currents_inv4_sb2,formatIn);
date_num_currents_inv4_sb3=datenum(date_from_file_currents_inv4_sb3,formatIn);
date_num_currents_inv4_sb4=datenum(date_from_file_currents_inv4_sb4,formatIn);
date_num_currents_inv4_sb4=datenum(date_from_file_currents_inv4_sb4,formatIn);
date_num_currents_inv4_sb5=datenum(date_from_file_currents_inv4_sb5,formatIn);
date_num_currents_inv4_sb6=datenum(date_from_file_currents_inv4_sb6,formatIn);
date_num_currents_inv4_sb7=datenum(date_from_file_currents_inv4_sb7,formatIn);
date_num_currents_inv4_sb8=datenum(date_from_file_currents_inv4_sb8,formatIn);
[c time_start_rowNum] = min(abs(date_num-time_start_num));
[c time_stop_rowNum] = min(abs(date_num-time_stop_num));
time_start_rowNum;
time_stop_rowNum;
[c time_start_rowNum_currents_inv4_sb1] = min(abs(date_num_currents_inv4_sb1-
time_start_num));
[c time_stop_rowNum_currents_inv4_sb1] = min(abs(date_num_currents_inv4_sb1-
time_stop_num));
time_start_rowNum_currents_inv4_sb1;
time_stop_rowNum_currents_inv4_sb1;

```

```

[c   time_start_rowNum_currents_inv4_sb2] = min(abs(date_num_currents_inv4_sb2-
time_start_num));
[c   time_stop_rowNum_currents_inv4_sb2]  = min(abs(date_num_currents_inv4_sb2-
time_stop_num));
time_start_rowNum_currents_inv4_sb2;
time_stop_rowNum_currents_inv4_sb2;
[c   time_start_rowNum_currents_inv4_sb3] = min(abs(date_num_currents_inv4_sb3-
time_start_num));
[c   time_stop_rowNum_currents_inv4_sb3]  = min(abs(date_num_currents_inv4_sb3-
time_stop_num));
time_start_rowNum_currents_inv4_sb3;
time_stop_rowNum_currents_inv4_sb3;
[c   time_start_rowNum_currents_inv4_sb4] = min(abs(date_num_currents_inv4_sb4-
time_start_num));
[c   time_stop_rowNum_currents_inv4_sb4]  = min(abs(date_num_currents_inv4_sb4-
time_stop_num));
time_start_rowNum_currents_inv4_sb4;
time_stop_rowNum_currents_inv4_sb4;
[c   time_start_rowNum_currents_inv4_sb5] = min(abs(date_num_currents_inv4_sb5-
time_start_num));
[c   time_stop_rowNum_currents_inv4_sb5]  = min(abs(date_num_currents_inv4_sb5-
time_stop_num));
time_start_rowNum_currents_inv4_sb5;
time_stop_rowNum_currents_inv4_sb5;
[c   time_start_rowNum_currents_inv4_sb6] = min(abs(date_num_currents_inv4_sb6-
time_start_num));
[c   time_stop_rowNum_currents_inv4_sb6]  = min(abs(date_num_currents_inv4_sb6-
time_stop_num));
time_start_rowNum_currents_inv4_sb6;
time_stop_rowNum_currents_inv4_sb6;
[c   time_start_rowNum_currents_inv4_sb7] = min(abs(date_num_currents_inv4_sb7-
time_start_num));

```

```

[c    time_stop_rowNum_currents_inv4_sb7]    =    min(abs(date_num_currents_inv4_sb7-
time_stop_num));
time_start_rowNum_currents_inv4_sb7;
time_stop_rowNum_currents_inv4_sb7;
[c    time_start_rowNum_currents_inv4_sb8]    =    min(abs(date_num_currents_inv4_sb8-
time_start_num));
[c    time_stop_rowNum_currents_inv4_sb8]    =    min(abs(date_num_currents_inv4_sb8-
time_stop_num));
time_start_rowNum_currents_inv4_sb8;
time_stop_rowNum_currents_inv4_sb8;
inverter_Vdc_subset=inverter_Vdc(time_start_rowNum:time_stop_rowNum);
inv4_sb1_current1_subset=inv4_sb1_current1(time_start_rowNum_currents_inv4_sb1:time_sto
p_rowNum_currents_inv4_sb1);
inv4_sb1_current2_subset=inv4_sb1_current2(time_start_rowNum_currents_inv4_sb1:time_sto
p_rowNum_currents_inv4_sb1);
inv4_sb1_current3_subset=inv4_sb1_current3(time_start_rowNum_currents_inv4_sb1:time_sto
p_rowNum_currents_inv4_sb1);
inv4_sb1_current4_subset=inv4_sb1_current4(time_start_rowNum_currents_inv4_sb1:time_sto
p_rowNum_currents_inv4_sb1);
inv4_sb1_current5_subset=inv4_sb1_current5(time_start_rowNum_currents_inv4_sb1:time_sto
p_rowNum_currents_inv4_sb1);
inv4_sb1_current6_subset=inv4_sb1_current6(time_start_rowNum_currents_inv4_sb1:time_sto
p_rowNum_currents_inv4_sb1);
inv4_sb1_current7_subset=inv4_sb1_current7(time_start_rowNum_currents_inv4_sb1:time_sto
p_rowNum_currents_inv4_sb1);
inv4_sb1_current8_subset=inv4_sb1_current8(time_start_rowNum_currents_inv4_sb1:time_sto
p_rowNum_currents_inv4_sb1);
[ .....code for the other strings..... ]
%%%%%%%%%% time synchronization %%%%%%%%%%%
if length(inv4_sb1_current1_subset)~=length(inverter_Vdc_subset);
inv4_sb1_current1_subset=resample(inv4_sb1_current1_subset,length(inverter_Vdc_subset),
length(inv4_sb1_current1_subset));
inv4_sb1_current2_subset=resample(inv4_sb1_current2_subset,length(inverter_Vdc_subset),

```

```

length(inv4_sb1_current2_subset));
inv4_sb1_current3_subset=resample(inv4_sb1_current3_subset,length(inverter_Vdc_subset),
length(inv4_sb1_current3_subset));
inv4_sb1_current4_subset=resample(inv4_sb1_current4_subset,length(inverter_Vdc_subset),
length(inv4_sb1_current4_subset));
inv4_sb1_current5_subset=resample(inv4_sb1_current5_subset,length(inverter_Vdc_subset),
length(inv4_sb1_current5_subset));
inv4_sb1_current6_subset=resample(inv4_sb1_current6_subset,length(inverter_Vdc_subset),
length(inv4_sb1_current6_subset));
inv4_sb1_current7_subset=resample(inv4_sb1_current7_subset,length(inverter_Vdc_subset),
length(inv4_sb1_current7_subset));
inv4_sb1_current8_subset=resample(inv4_sb1_current8_subset,length(inverter_Vdc_subset),
length(inv4_sb1_current8_subset));
    else
end
[ .....code for the other strings..... ]
%%%%%%%%%% voltage drop calculation %%%%%%%%%%%
R_sb1_DCHV4=xlsread('Resistenze_cavi_distribuzione_DC.xls','inv4','e3');
R_sb2_DCHV4=xlsread('Resistenze_cavi_distribuzione_DC.xls','inv4','e4');
R_sb3_DCHV4=xlsread('Resistenze_cavi_distribuzione_DC.xls','inv4','e5');
R_sb4_DCHV4=xlsread('Resistenze_cavi_distribuzione_DC.xls','inv4','e6');
R_sb5_DCHV4=xlsread('Resistenze_cavi_distribuzione_DC.xls','inv4','e7');
R_sb6_DCHV4=xlsread('Resistenze_cavi_distribuzione_DC.xls','inv4','e8');
R_sb7_DCHV4=xlsread('Resistenze_cavi_distribuzione_DC.xls','inv4','e9');
R_sb8_DCHV4=xlsread('Resistenze_cavi_distribuzione_DC.xls','inv4','e10');
R_DCHV4_inv4=xlsread('Resistenze_cavi_distribuzione_DC.xls','inv4','h3');
inv4_sb1_current_subset=inv4_sb1_current1_subset+inv4_sb1_current2_subset+inv4_sb1_curr
ent3_subset+inv4_sb1_current4_subset+inv4_sb1_current5_subset+inv4_sb1_current6_subset+
inv4_sb1_current7_subset+inv4_sb1_current8_subset;
inv4_sb2_current_subset=inv4_sb2_current1_subset+inv4_sb2_current2_subset+inv4_sb2_curr
ent3_subset+inv4_sb2_current4_subset+inv4_sb2_current5_subset+inv4_sb2_current6_subset+
inv4_sb2_current7_subset+inv4_sb2_current8_subset;

```

$inv4_sb3_current_subset = inv4_sb3_current1_subset + inv4_sb3_current2_subset + inv4_sb3_current3_subset + inv4_sb3_current4_subset + inv4_sb3_current5_subset + inv4_sb3_current6_subset + inv4_sb3_current7_subset + inv4_sb3_current8_subset;$
 $inv4_sb4_current_subset = inv4_sb4_current1_subset + inv4_sb4_current2_subset + inv4_sb4_current3_subset + inv4_sb4_current4_subset + inv4_sb4_current5_subset + inv4_sb4_current6_subset + inv4_sb4_current7_subset + inv4_sb4_current8_subset;$
 $inv4_sb5_current_subset = inv4_sb5_current1_subset + inv4_sb5_current2_subset + inv4_sb5_current3_subset + inv4_sb5_current4_subset + inv4_sb5_current5_subset + inv4_sb5_current6_subset + inv4_sb5_current7_subset + inv4_sb5_current8_subset;$
 $inv4_sb6_current_subset = inv4_sb6_current1_subset + inv4_sb6_current2_subset + inv4_sb6_current3_subset + inv4_sb6_current4_subset + inv4_sb6_current5_subset + inv4_sb6_current6_subset + inv4_sb6_current7_subset + inv4_sb6_current8_subset;$
 $inv4_sb7_current_subset = inv4_sb7_current1_subset + inv4_sb7_current2_subset + inv4_sb7_current3_subset + inv4_sb7_current4_subset + inv4_sb7_current5_subset + inv4_sb7_current6_subset;$
 $inv4_sb8_current_subset = inv4_sb8_current1_subset + inv4_sb8_current2_subset + inv4_sb8_current3_subset + inv4_sb8_current4_subset + inv4_sb8_current5_subset + inv4_sb8_current6_subset;$
 $Vdrop_sb1_DCHV4_subset = inv4_sb1_current_subset * R_sb1_DCHV4;$
 $Vdrop_sb2_DCHV4_subset = inv4_sb2_current_subset * R_sb2_DCHV4;$
 $Vdrop_sb3_DCHV4_subset = inv4_sb3_current_subset * R_sb3_DCHV4;$
 $Vdrop_sb4_DCHV4_subset = inv4_sb4_current_subset * R_sb4_DCHV4;$
 $Vdrop_sb5_DCHV4_subset = inv4_sb5_current_subset * R_sb5_DCHV4;$
 $Vdrop_sb6_DCHV4_subset = inv4_sb6_current_subset * R_sb6_DCHV4;$
 $Vdrop_sb7_DCHV4_subset = inv4_sb7_current_subset * R_sb7_DCHV4;$
 $Vdrop_sb8_DCHV4_subset = inv4_sb8_current_subset * R_sb8_DCHV4;$
 $inv4_current_subset = inv4_sb1_current_subset + inv4_sb2_current_subset + inv4_sb3_current_subset + inv4_sb4_current_subset + inv4_sb5_current_subset + inv4_sb6_current_subset + inv4_sb7_current_subset + inv4_sb8_current_subset;$
 $Vdrop_DCHV4_inv4_subset = inv4_current_subset * R_DCHV4_inv4;$
 $Vdrop_sb1_subset = Vdrop_sb1_DCHV4_subset + Vdrop_DCHV4_inv4_subset;$
 $Vdrop_sb2_subset = Vdrop_sb2_DCHV4_subset + Vdrop_DCHV4_inv4_subset;$
 $Vdrop_sb3_subset = Vdrop_sb3_DCHV4_subset + Vdrop_DCHV4_inv4_subset;$
 $Vdrop_sb4_subset = Vdrop_sb4_DCHV4_subset + Vdrop_DCHV4_inv4_subset;$
 $Vdrop_sb5_subset = Vdrop_sb5_DCHV4_subset + Vdrop_DCHV4_inv4_subset;$


```

Vdrop_sb6_subset=Vdrop_sb6_DCHV4_subset+Vdrop_DCHV4_inv4_subset;
Vdrop_sb7_subset=Vdrop_sb7_DCHV4_subset+Vdrop_DCHV4_inv4_subset;
Vdrop_sb8_subset=Vdrop_sb8_DCHV4_subset+Vdrop_DCHV4_inv4_subset;
sb1_Vdc_subset=inverter_Vdc_subset+Vdrop_sb1_subset;
sb2_Vdc_subset=inverter_Vdc_subset+Vdrop_sb2_subset;
sb3_Vdc_subset=inverter_Vdc_subset+Vdrop_sb3_subset;
sb4_Vdc_subset=inverter_Vdc_subset+Vdrop_sb4_subset;
sb5_Vdc_subset=inverter_Vdc_subset+Vdrop_sb5_subset;
sb6_Vdc_subset=inverter_Vdc_subset+Vdrop_sb6_subset;
sb7_Vdc_subset=inverter_Vdc_subset+Vdrop_sb7_subset;
sb8_Vdc_subset=inverter_Vdc_subset+Vdrop_sb8_subset;
inv4_sb1_str1_power_subset=sb1_Vdc_subset.*inv4_sb1_current1_subset/1000;
inv4_sb1_str2_power_subset=sb1_Vdc_subset.*inv4_sb1_current2_subset/1000;
inv4_sb1_str3_power_subset=sb1_Vdc_subset.*inv4_sb1_current3_subset/1000;
inv4_sb1_str4_power_subset=sb1_Vdc_subset.*inv4_sb1_current4_subset/1000;
inv4_sb1_str5_power_subset=sb1_Vdc_subset.*inv4_sb1_current5_subset/1000;
inv4_sb1_str6_power_subset=sb1_Vdc_subset.*inv4_sb1_current6_subset/1000;
inv4_sb1_str7_power_subset=sb1_Vdc_subset.*inv4_sb1_current7_subset/1000;
inv4_sb1_str8_power_subset=sb1_Vdc_subset.*inv4_sb1_current8_subset/1000;
[ .....code for the other strings..... ]
%%%%%%%%%% energy calculation %%%%%%%%%%%
inv4_sb1_str1_energy=0;
for k=time_start_rowNum:1:time_stop_rowNum;
singola_area=inv4_sb1_str1_power_subset(k-
time_start_rowNum+1)*(str2num(datestr((date_num(k+1)-
date_num(k)), 'SS'))/3600+str2num(datestr((date_num(k+1)-
date_num(k)), 'MM'))/60+str2num(datestr((date_num(k+1)-date_num(k)), 'HH'))/1);
inv4_sb1_str1_energy=inv4_sb1_str1_energy+singola_area;
end
inv4_sb1_str2_energy=0;
for k=time_start_rowNum:1:time_stop_rowNum;
singola_area=inv4_sb1_str2_power_subset(k-
time_start_rowNum+1)*(str2num(datestr((date_num(k+1)-

```

```

date_num(k),'SS'))/3600+str2num(datestr((date_num(k+1)-
date_num(k),'MM'))/60+str2num(datestr((date_num(k+1)-date_num(k),'HH'))/1);
inv4_sb1_str2_energy=inv4_sb1_str2_energy+singola_area;
end
inv4_sb1_str3_energy=0;
for k=time_start_rowNum:1:time_stop_rowNum;
singola_area=inv4_sb1_str3_power_subset(k-
time_start_rowNum+1)*(str2num(datestr((date_num(k+1)-
date_num(k),'SS'))/3600+str2num(datestr((date_num(k+1)-
date_num(k),'MM'))/60+str2num(datestr((date_num(k+1)-date_num(k),'HH'))/1);
inv4_sb1_str3_energy=inv4_sb1_str3_energy+singola_area;
end
inv4_sb1_str4_energy=0;
for k=time_start_rowNum:1:time_stop_rowNum;
singola_area=inv4_sb1_str4_power_subset(k-
time_start_rowNum+1)*(str2num(datestr((date_num(k+1)-
date_num(k),'SS'))/3600+str2num(datestr((date_num(k+1)-
date_num(k),'MM'))/60+str2num(datestr((date_num(k+1)-date_num(k),'HH'))/1);
inv4_sb1_str4_energy=inv4_sb1_str4_energy+singola_area;
end
inv4_sb1_str5_energy=0;
for k=time_start_rowNum:1:time_stop_rowNum;
singola_area=inv4_sb1_str5_power_subset(k-
time_start_rowNum+1)*(str2num(datestr((date_num(k+1)-
date_num(k),'SS'))/3600+str2num(datestr((date_num(k+1)-
date_num(k),'MM'))/60+str2num(datestr((date_num(k+1)-date_num(k),'HH'))/1);
inv4_sb1_str5_energy=inv4_sb1_str5_energy+singola_area;
end
inv4_sb1_str6_energy=0;
for k=time_start_rowNum:1:time_stop_rowNum;
singola_area=inv4_sb1_str6_power_subset(k-
time_start_rowNum+1)*(str2num(datestr((date_num(k+1)-

```

```

date_num(k),'SS'))/3600+str2num(datestr((date_num(k+1)-
date_num(k),'MM'))/60+str2num(datestr((date_num(k+1)-date_num(k),'HH'))/1);
inv4_sb1_str6_energy=inv4_sb1_str6_energy+singola_area;
end
inv4_sb1_str7_energy=0;
for k=time_start_rowNum:1:time_stop_rowNum;
singola_area=inv4_sb1_str7_power_subset(k-
time_start_rowNum+1)*(str2num(datestr((date_num(k+1)-
date_num(k),'SS'))/3600+str2num(datestr((date_num(k+1)-
date_num(k),'MM'))/60+str2num(datestr((date_num(k+1)-date_num(k),'HH'))/1);
inv4_sb1_str7_energy=inv4_sb1_str7_energy+singola_area;
end
inv4_sb1_str8_energy=0;
for k=time_start_rowNum:1:time_stop_rowNum;
singola_area=inv4_sb1_str8_power_subset(k-
time_start_rowNum+1)*(str2num(datestr((date_num(k+1)-
date_num(k),'SS'))/3600+str2num(datestr((date_num(k+1)-
date_num(k),'MM'))/60+str2num(datestr((date_num(k+1)-date_num(k),'HH'))/1);
inv4_sb1_str8_energy=inv4_sb1_str8_energy+singola_area;
end
[ .....code for the other strings..... ]
%%%%%%%%%% plots %%%%%%%%%%%
time_start_plot = time_start;
time_stop_plot =time_stop;
formatIn = 'dd/mm/yyyy HH:MM:SS';
start_plot=datenum(time_start_plot,formatIn);
stop_plot=datenum(time_stop_plot,formatIn);
figure(1);
subplot(3,3,1),plot(Vdrop_sb1_subset),legend('SB1 total DC voltage drop
(V)');massimo=max(Vdrop_sb1_subset);title(strcat('max=',num2str(massimo)));
subplot(3,3,2),plot(Vdrop_sb2_subset),legend('SB2 total DC voltage drop
(V)');massimo=max(Vdrop_sb2_subset);title(strcat('max=',num2str(massimo)));

```

```

subplot(3,3,3),plot(Vdrop_sb3_subset),legend('SB3      total      DC      voltage      drop
(V)');massimo=max(Vdrop_sb3_subset);title(strcat('max=',num2str(massimo)));
subplot(3,3,4),plot(Vdrop_sb4_subset),legend('SB4      total      DC      voltage      drop
(V)');massimo=max(Vdrop_sb4_subset);title(strcat('max=',num2str(massimo)));
subplot(3,3,5),plot(Vdrop_sb5_subset),legend('SB5      total      DC      voltage      drop
(V)');massimo=max(Vdrop_sb5_subset);title(strcat('max=',num2str(massimo)));
subplot(3,3,6),plot(Vdrop_sb6_subset),legend('SB6      total      DC      voltage      drop
(V)');massimo=max(Vdrop_sb6_subset);title(strcat('max=',num2str(massimo)));
subplot(3,3,7),plot(Vdrop_sb7_subset),legend('SB7      total      DC      voltage      drop
(V)');massimo=max(Vdrop_sb7_subset);title(strcat('max=',num2str(massimo)));
subplot(3,3,8),plot(Vdrop_sb8_subset),legend('SB8      total      DC      voltage      drop
(V)');massimo=max(Vdrop_sb8_subset);title(strcat('max=',num2str(massimo)));
figure(2);
subplot(3,3,1),plot(inverter_Vdc_subset),legend('inverter      4      DC      voltage
(V)');massimo=max(inverter_Vdc_subset);title(strcat('max=',num2str(massimo)));
subplot(3,3,2),plot(sb1_Vdc_subset),legend('SB1      DC      voltage
(V)');massimo=max(sb1_Vdc_subset);title(strcat('max=',num2str(massimo)));
subplot(3,3,3),plot(sb2_Vdc_subset),legend('SB2      DC      voltage
(V)');massimo=max(sb2_Vdc_subset);title(strcat('max=',num2str(massimo)));
subplot(3,3,4),plot(sb3_Vdc_subset),legend('SB3      DC      voltage
(V)');massimo=max(sb3_Vdc_subset);title(strcat('max=',num2str(massimo)));
subplot(3,3,5),plot(sb4_Vdc_subset),legend('SB4      DC      voltage
(V)');massimo=max(sb4_Vdc_subset);title(strcat('max=',num2str(massimo)));
subplot(3,3,6),plot(sb5_Vdc_subset),legend('SB5      DC      voltage
(V)');massimo=max(sb5_Vdc_subset);title(strcat('max=',num2str(massimo)));
subplot(3,3,7),plot(sb6_Vdc_subset),legend('SB6      DC      voltage
(V)');massimo=max(sb6_Vdc_subset);title(strcat('max=',num2str(massimo)));
subplot(3,3,8),plot(sb7_Vdc_subset),legend('SB7      DC      voltage
(V)');massimo=max(sb7_Vdc_subset);title(strcat('max=',num2str(massimo)));
subplot(3,3,9),plot(sb8_Vdc_subset),legend('SB8      DC      voltage
(V)');massimo=max(sb8_Vdc_subset);title(strcat('max=',num2str(massimo)));
figure(3);

```

```

plot(date_num_currents_inv4_sb1,inv4_sb1_current1,date_num_currents_inv4_sb1,inv4_sb1_c
urrent2,date_num_currents_inv4_sb1,inv4_sb1_current3,date_num_currents_inv4_sb1,inv4_sb
1_current4,date_num_currents_inv4_sb1,inv4_sb1_current5,date_num_currents_inv4_sb1,inv4
_sb1_current6,date_num_currents_inv4_sb1,inv4_sb1_current7,date_num_currents_inv4_sb1,i
nv4_sb1_current8);
legend('Inv4 SB1 string 1 current (A)','Inv4 SB1 string 2 current','Inv4 SB1 string 3
current','Inv4 SB1 string 4 current','Inv4 SB1 string 5 current','Inv4 SB1 string 6 current','Inv4
SB1 string 7 current','Inv4 SB1 string 8 current');
axis([start_plot stop_plot -inf inf]);
datetick('x',15,'keplimits','kepticks')
title('Inv4 SB1 strings current');
figure(4);
inv4_sb1_strings_energy=[inv4_sb1_str1_energy inv4_sb1_str2_energy inv4_sb1_str3_energy
inv4_sb1_str4_energy inv4_sb1_str5_energy inv4_sb1_str6_energy inv4_sb1_str7_energy
inv4_sb1_str8_energy];
bar(inv4_sb1_strings_energy);
xlabel('Inv4 SB1 strings strings');
ylabel('energy (kWh)');
[ .....code for the other strings..... ]
%%%%%% message box with results - energy %%%%%%%
Line1=strcat('Start:',time_start);
Line2=strcat('Stop:',time_stop);
Line3=strcat('Inverter          4          SB1          total          energy:
',num2str(inv4_sb1_str1_energy+inv4_sb1_str2_energy+inv4_sb1_str3_energy+inv4_sb1_str4_
energy+inv4_sb1_str5_energy+inv4_sb1_str6_energy+inv4_sb1_str7_energy+inv4_sb1_str8_e
nergy,5),' kWh');
Line4=strcat('Inverter          4          SB2          total          energy:
',num2str(inv4_sb2_str1_energy+inv4_sb2_str2_energy+inv4_sb2_str3_energy+inv4_sb2_str4_
energy+inv4_sb2_str5_energy+inv4_sb2_str6_energy+inv4_sb2_str7_energy+inv4_sb2_str8_e
nergy,5),' kWh');
Line5=strcat('Inverter          4          SB3          total          energy:
',num2str(inv4_sb3_str1_energy+inv4_sb3_str2_energy+inv4_sb3_str3_energy+inv4_sb3_str4_

```

```
energy+inv4_sb3_str5_energy+inv4_sb3_str6_energy+inv4_sb3_str7_energy+inv4_sb3_str8_e
nergy,5),' kWh');
```

```
Line6=strcat('Inverter          4          SB4          total          energy:
',num2str(inv4_sb4_str1_energy+inv4_sb4_str2_energy+inv4_sb4_str3_energy+inv4_sb4_str4_
energy+inv4_sb4_str5_energy+inv4_sb4_str6_energy+inv4_sb4_str7_energy+inv4_sb4_str8_e
nergy,5),' kWh');
```

```
Line7=strcat('Inverter          4          SB5          total          energy:
',num2str(inv4_sb5_str1_energy+inv4_sb5_str2_energy+inv4_sb5_str3_energy+inv4_sb5_str4_
energy+inv4_sb5_str5_energy+inv4_sb5_str6_energy+inv4_sb5_str7_energy+inv4_sb5_str8_e
nergy,5),' kWh');
```

```
Line8=strcat('Inverter          4          SB6          total          energy:
',num2str(inv4_sb6_str1_energy+inv4_sb6_str2_energy+inv4_sb6_str3_energy+inv4_sb6_str4_
energy+inv4_sb6_str5_energy+inv4_sb6_str6_energy+inv4_sb6_str7_energy+inv4_sb6_str8_e
nergy,5),' kWh');
```

```
Line9=strcat('Inverter          4          SB7          total          energy:
',num2str(inv4_sb7_str1_energy+inv4_sb7_str2_energy+inv4_sb7_str3_energy+inv4_sb7_str4_
energy+inv4_sb7_str5_energy+inv4_sb7_str6_energy,5),' kWh');
```

```
Line10=strcat('Inverter          4          SB8          total          energy:
',num2str(inv4_sb8_str1_energy+inv4_sb8_str2_energy+inv4_sb8_str3_energy+inv4_sb8_str4_
energy+inv4_sb8_str5_energy+inv4_sb8_str6_energy,5),' kWh');
```

```
h=msgbox({Line1;Line2;Line3;Line4;Line5;Line6;Line7;Line8;Line9;Line10},'Results
data','non-modal');
```

```
set(h, 'position', [100 100 1000 450]); %makes box bigger
```

```
ah = get( h, 'CurrentAxes' );
```

```
ch = get( ah, 'Children' );
```

```
set( ch, 'FontSize', 10 ); %makes text bigger
```

```
set( h, 'Color',[1,1,1]);
```

```
% % % % % % % % results collection % % % % % % % % % % % % % % % % % %
```

```
inv4_sb1_str1_energy_list(j)=inv4_sb1_str1_energy;
```

```
inv4_sb1_str2_energy_list(j)=inv4_sb1_str2_energy;
```

```
inv4_sb1_str3_energy_list(j)=inv4_sb1_str3_energy;
```

```

inv4_sb1_str4_energy_list(j)=inv4_sb1_str4_energy;
inv4_sb1_str5_energy_list(j)=inv4_sb1_str5_energy;
inv4_sb1_str6_energy_list(j)=inv4_sb1_str6_energy;
inv4_sb1_str7_energy_list(j)=inv4_sb1_str7_energy;
inv4_sb1_str8_energy_list(j)=inv4_sb1_str8_energy;
[ .....code for the other strings..... ]
% % % % % iteration % % % % % % % % % % % % % % % %
j=j+1;
    end

```

A.2.2 Irradiance, ambient temperature, module temperature

```

% % % % % days selection and data extraction from datalogger files % % % % % % % % % %
for j=1:1:10;
    if j==1; time_start = '01/04/2018 06:00:00'; time_stop = '01/04/2018 21:00:00';
%   else if j==2; time_start = '02/04/2018 06:00:00'; time_stop = '02/04/2018 21:00:00';
%   else if j==3; time_start = '03/04/2018 06:00:00'; time_stop = '03/04/2018 21:00:00';
%   else if j==4; time_start = '04/04/2018 06:00:00'; time_stop = '04/04/2018 21:00:00';
%   else if j==5; time_start = '05/04/2018 06:00:00'; time_stop = '05/04/2018 21:00:00';
%   else if j==6; time_start = '06/04/2018 06:00:00'; time_stop = '06/04/2018 21:00:00';
%   else if j==7; time_start = '07/04/2018 06:00:00'; time_stop = '07/04/2018 21:00:00';
%   else if j==8; time_start = '08/04/2018 06:00:00'; time_stop = '08/04/2018 21:00:00';
%   else if j==9; time_start = '09/04/2018 06:00:00'; time_stop = '09/04/2018 21:00:00';
%   else if j==10; time_start = '10/04/2018 06:00:00'; time_stop = '10/04/2018 21:00:00';
    end
    end
    end
    end
    end
    end
    end
    end
    end
    end
    end
    end

```

```

        end
formatIn = 'dd/mm/yyyy HH:MM:SS';
time_start_num=datenum(time_start,formatIn);
time_stop_num=datenum(time_stop,formatIn);
d = day(time_start_num);
if d<10;
    d=strcat('0',num2str(d));
else
    d=num2str(d);
end
m = month(time_start_num);
if m<10;
    m=strcat('0',num2str(m));
else
    m=num2str(m);
end
y=num2str(year(time_start_num));
string_nomefile= strcat('stazione-meteo-1_',d,'-',m,'-',y,'.xls');
Irradiance=xlsread(string_nomefile,1,'d2:d65000');
Module_Temperature=xlsread(string_nomefile,1,'c2:c65000');
Ambient_Temperature=xlsread(string_nomefile,1,'b2:b65000');
[num,text,both]=xlsread(string_nomefile,1,'a2:a65000');
date_from_file=text;
formatIn = 'dd/mm/yyyy HH:MM:SS';
date_num = datenum(date_from_file,formatIn);
[c time_start_rowNum] = min(abs(date_num-time_start_num));
[c time_stop_rowNum] = min(abs(date_num-time_stop_num));
time_start_rowNum;
time_stop_rowNum;
%%%%%%%%%% radiation calculation %%%%%%%%%%%
Irradiation=0;
for k=time_start_rowNum:1:time_stop_rowNum-1;

```



```

singola_area=Irradiance(k)*(str2num(datestr((date_num(k+1)-
date_num(k),'SS'))/3600/1000+str2num(datestr((date_num(k+1)-
date_num(k),'MM'))/60/1000+str2num(datestr((date_num(k+1)-date_num(k),'HH'))/1/1000);
Irradiation=Irradiation+singola_area;
end
%%%%%%%%%% module temperature %%%%%%%%%%%
Module_Temperature_subset=Module_Temperature(time_start_rowNum:time_stop_rowNum);
Module_Temperature_peak=max(Module_Temperature_subset);
Module_Temperature_mean=mean(Module_Temperature_subset);
%%%%%%%%%% ambient temperature %%%%%%%%%%%
Ambient_Temperature_subset=Ambient_Temperature(time_start_rowNum:time_stop_rowNum
);
Ambient_Temperature_peak=max(Ambient_Temperature_subset);
Ambient_Temperature_mean=mean(Ambient_Temperature_subset);
%%%%%%%%%% plots %%%%%%%%%%%
time_start_plot = time_start;
time_stop_plot =time_stop;
formatIn = 'dd/mm/yyyy HH:MM:SS';
start_plot=datenum(time_start_plot,formatIn);
stop_plot=datenum(time_stop_plot,formatIn);
figure(1);
subplot(3,1,1); plot(date_num,Irradiance,'b'); legend('Irradiance');
axis([start_plot stop_plot -inf inf]); datetick('x',15,'keeplimits','kepticks'); title('Irradiance');
subplot(3,1,2); plot(date_num,Module_Temperature,'k'); legend('Temperature');
axis([start_plot stop_plot -inf inf]); datetick('x',15,'keeplimits','kepticks');
title('Module Temperature');
subplot(3,1,3); plot(date_num,Ambient_Temperature,'k'); legend('Temperature');
axis([start_plot stop_plot -inf inf]); datetick('x',15,'keeplimits','kepticks');
title('Ambient Temperature');
%%%%%%%% message box with results %%%%%%%%%
Line1=strcat('Start:',time_start);
Line2=strcat('Stop:',time_stop);
Line3=strcat('Irradiation: ',num2str(Irradiation,3),' kWh/m2');

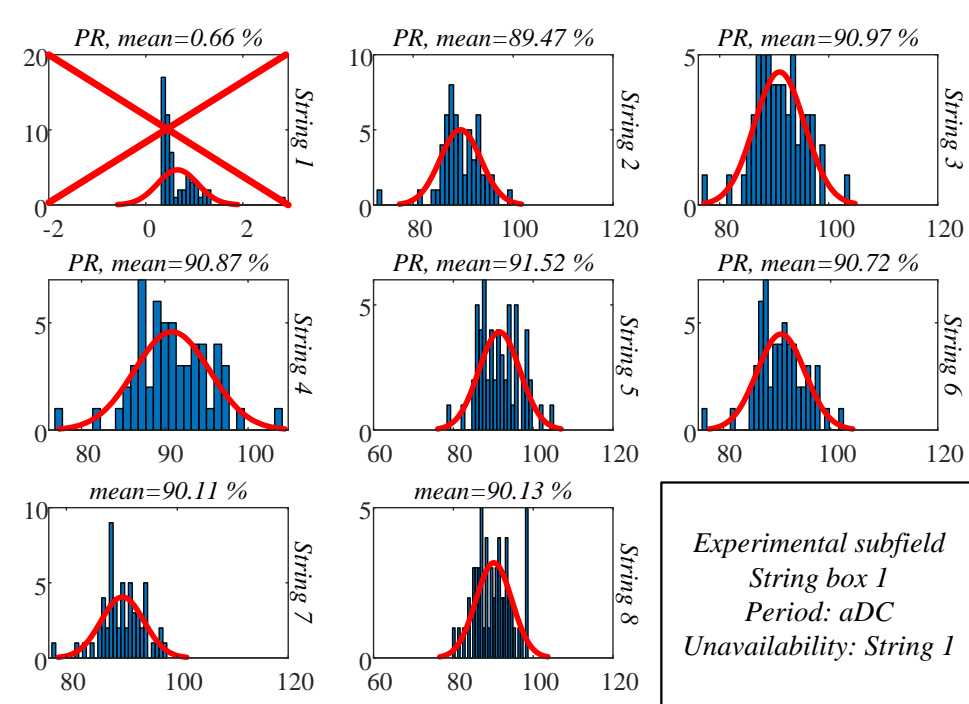
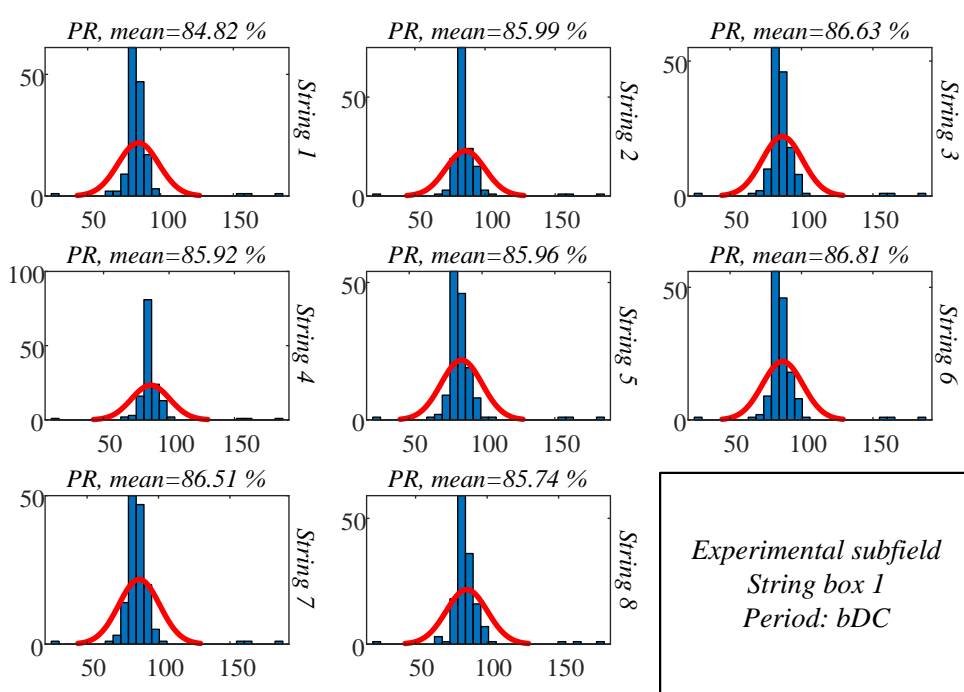
```

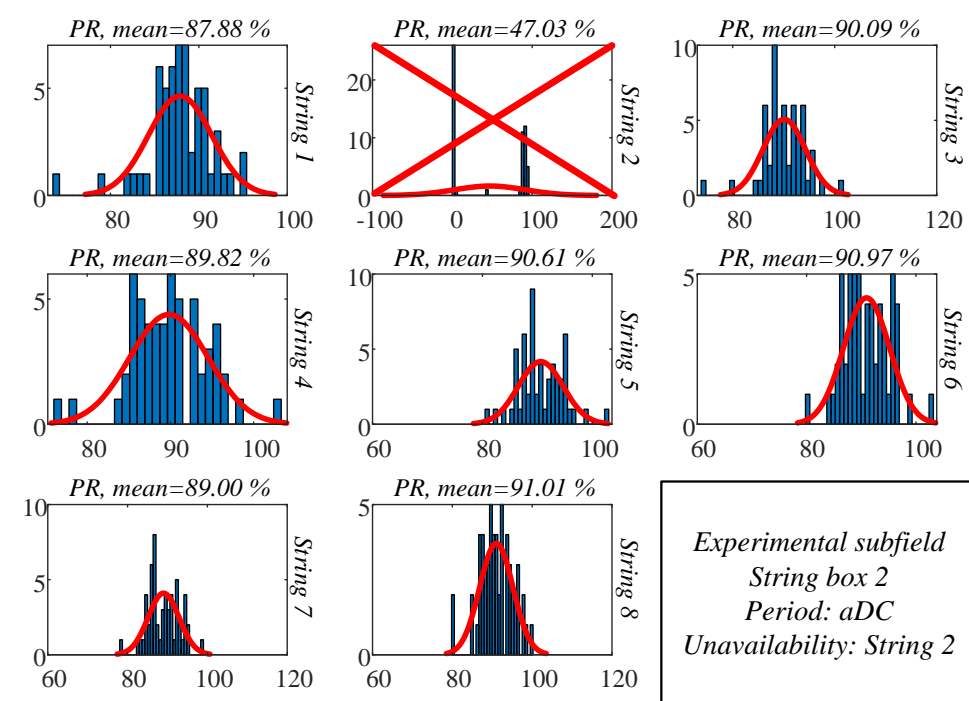
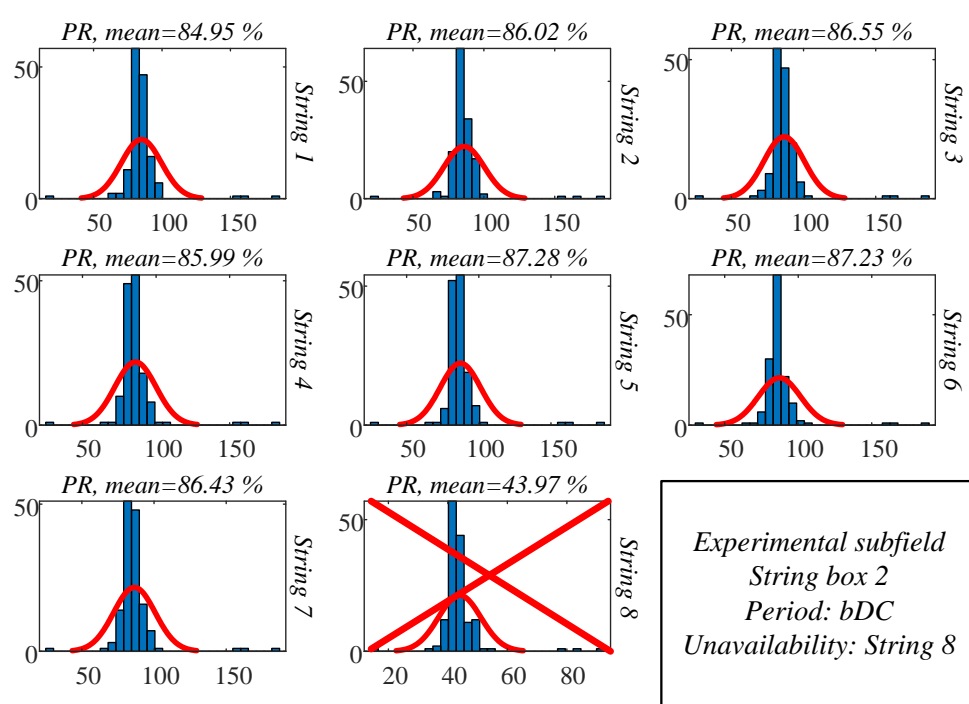
```

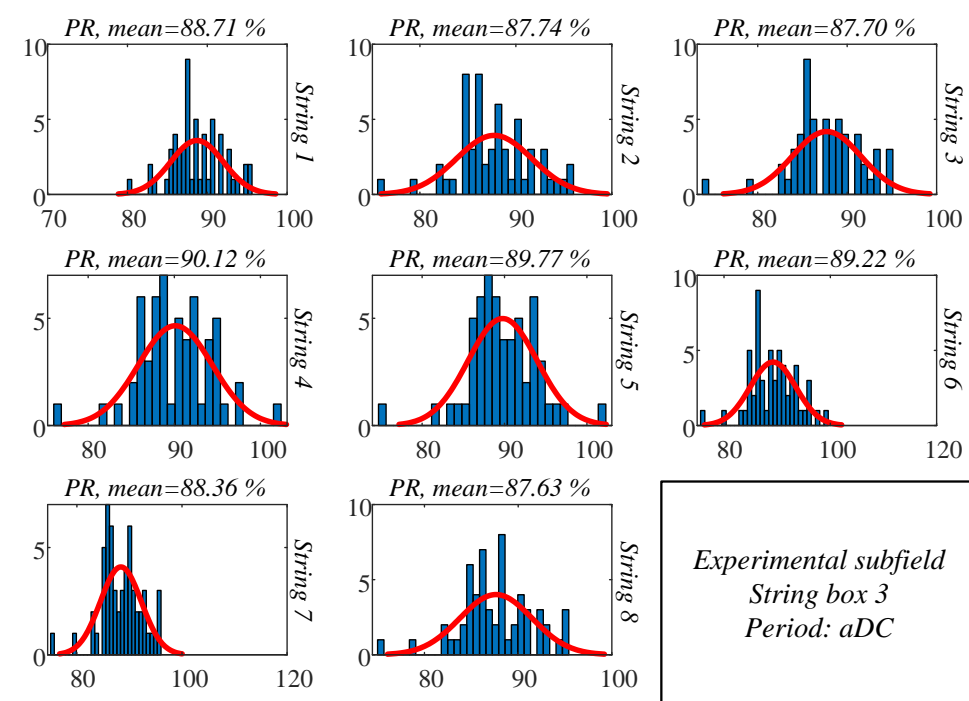
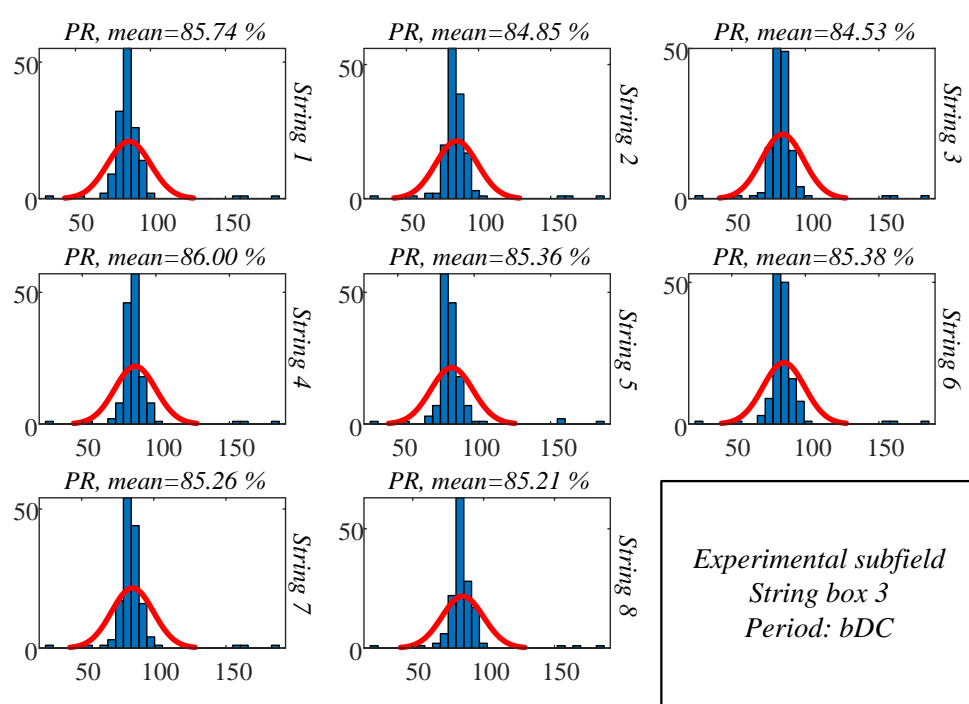
Line4=strcat('Module Temperature, mean value: ',num2str(Module_Temperature_mean,3),'
°C');
Line5=strcat('Module Temperature, peak value: ',num2str(Module_Temperature_peak,3),' °C');
Line6=strcat('Ambient Temperature, mean value: ',num2str(Ambient_Temperature_mean,3),'
°C');
Line7=strcat('Ambient Temperature, peak value: ',num2str(Ambient_Temperature_peak,3),'
°C');
h=msgbox({Line1;Line2;";Line3;";Line4;Line5;";Line6;Line7 } , 'Results data','non-modal');
set(h, 'position', [100 100 1000 450]); ah = get( h, 'CurrentAxes' ); ch = get( ah, 'Children' );
set( ch, 'FontSize', 15 ); set( h, 'Color',[1,1,1]);
% % % % % % % % results collection % % % % % % % % % % % % % % % % % %
Irradiation_list(j)=Irradiation;
Module_Temperature_mean_list(j)=Module_Temperature_mean;
Module_Temperature_peak_list(j)=Module_Temperature_peak;
Ambient_Temperature_mean_list(j)=Ambient_Temperature_mean;
Ambient_Temperature_peak_list(j)=Ambient_Temperature_peak;
% % % % % % % % iteration % % % % % % % % % % % % % % % % %
j=j+1;
end

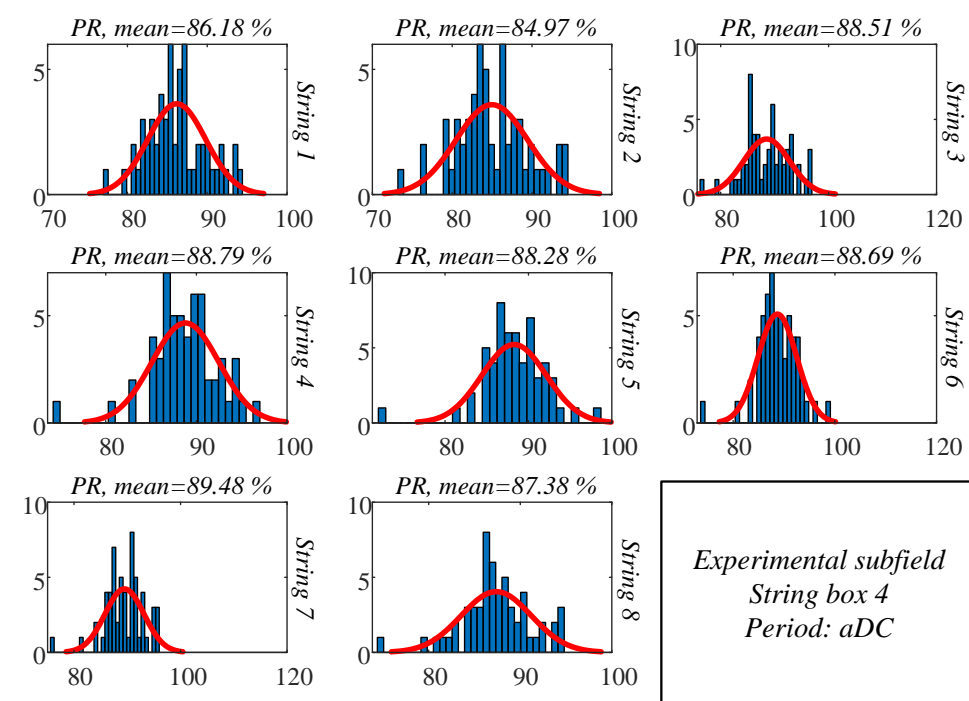
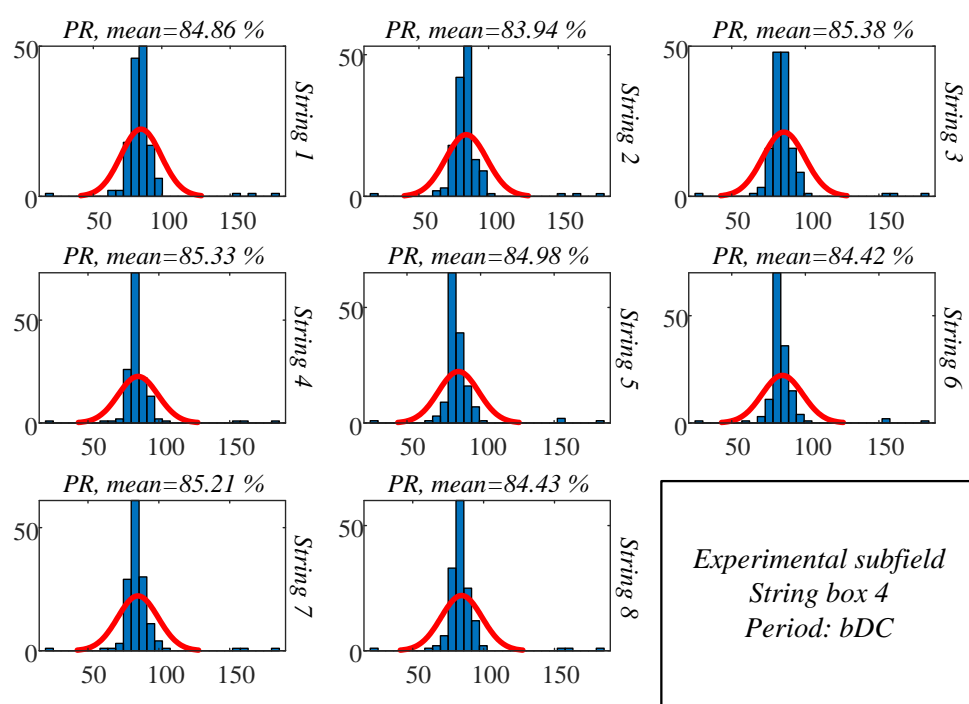
```

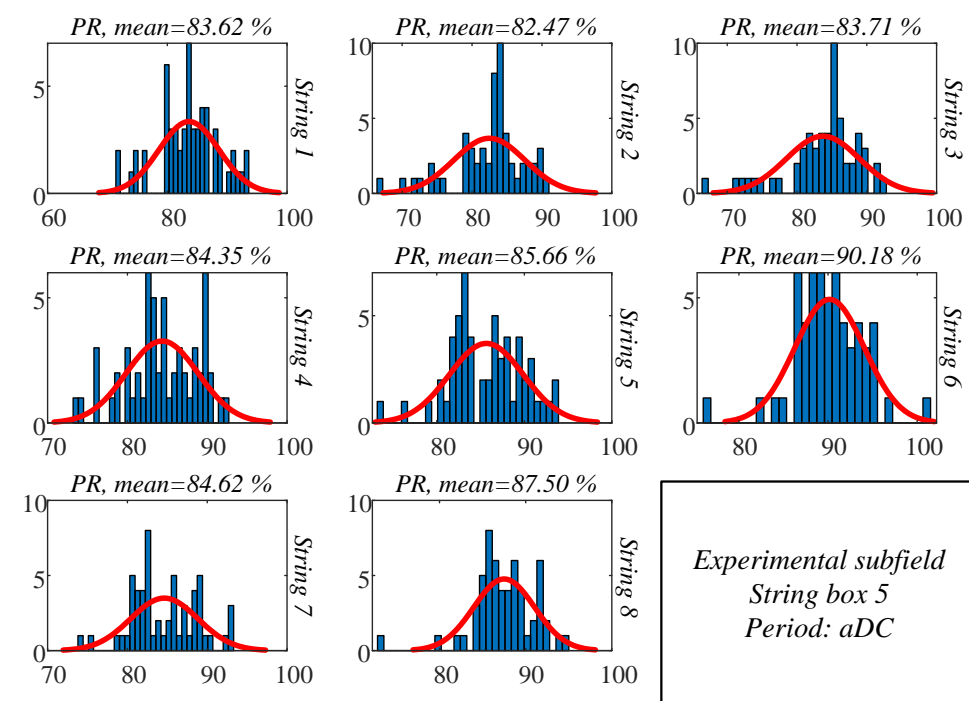
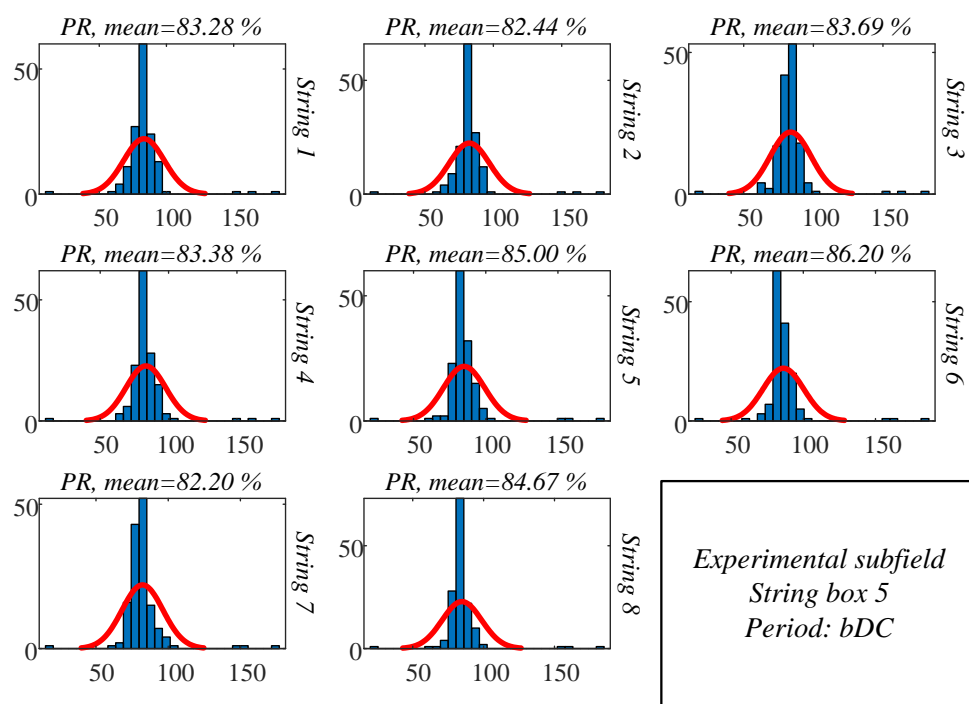
Appendix 3: Strings PR in experimental field of case study 2

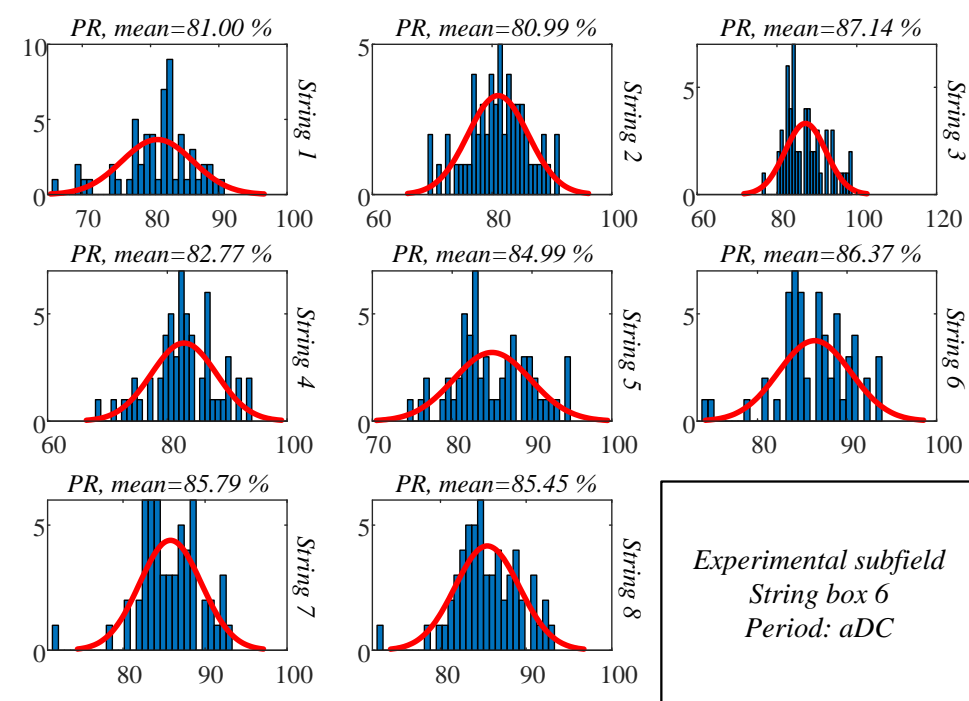
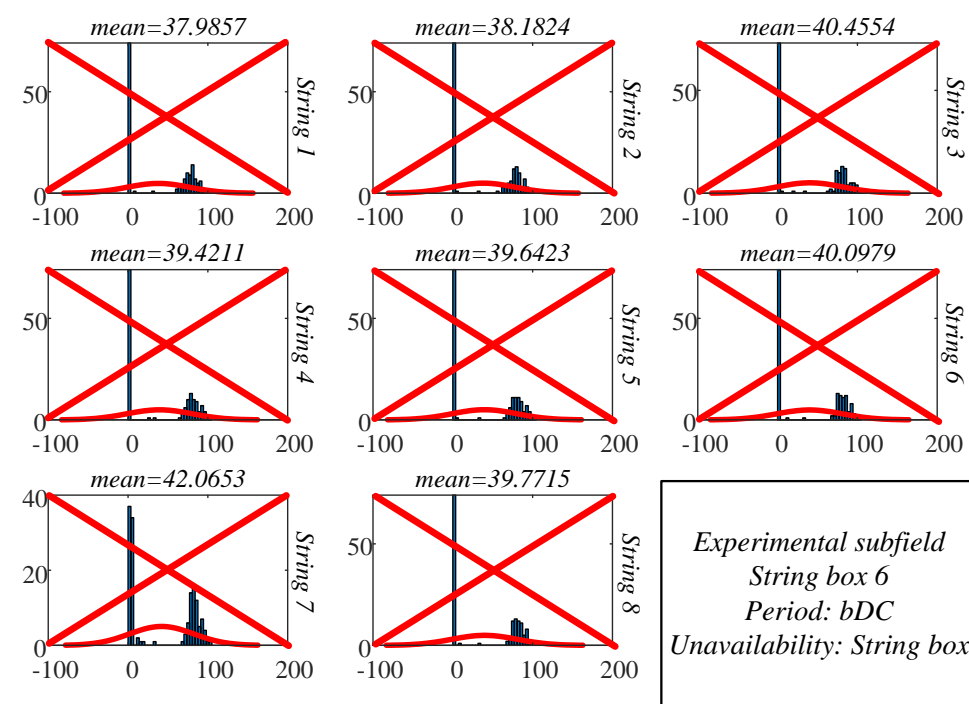


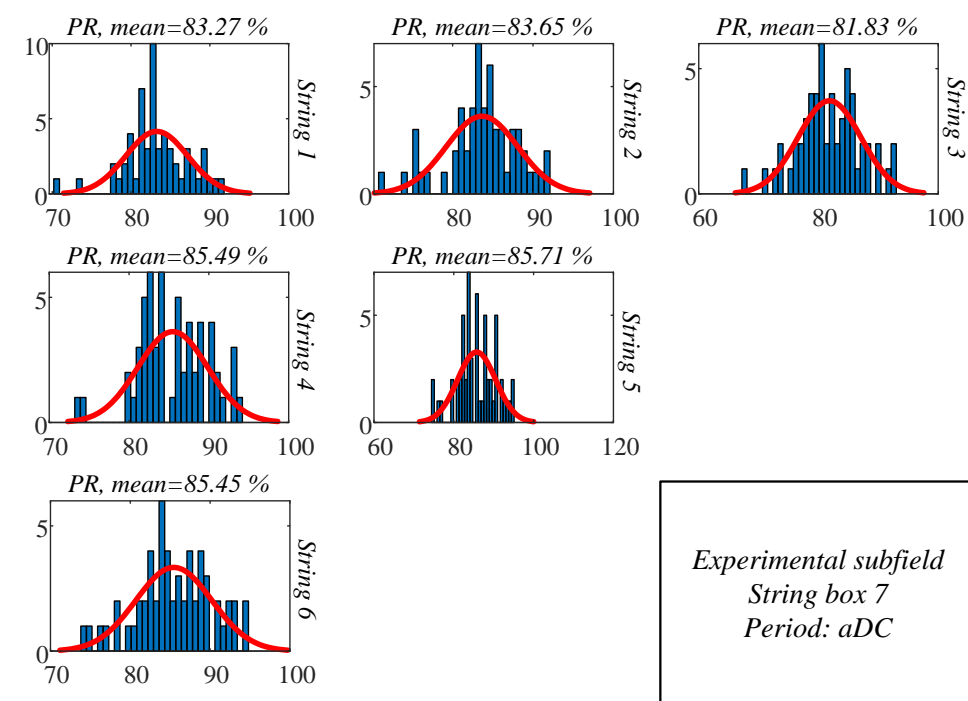
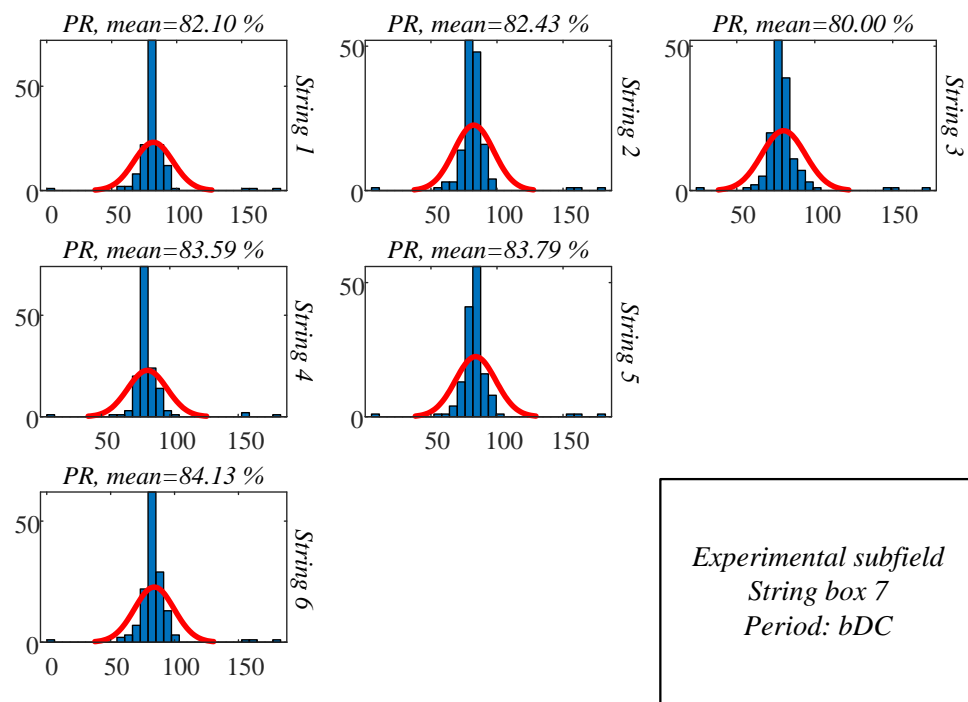


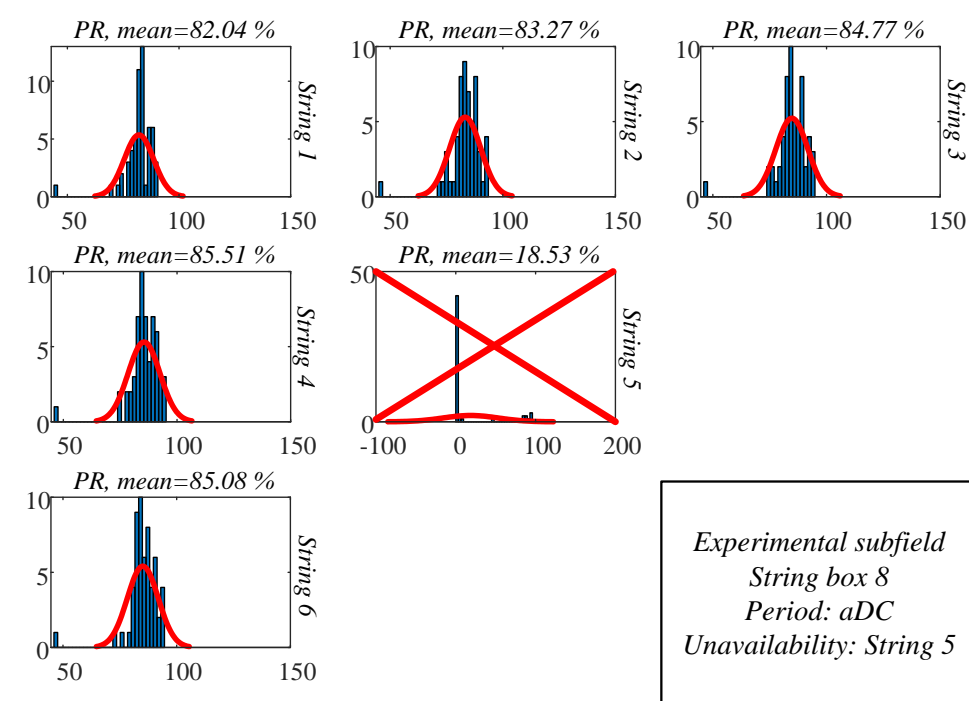
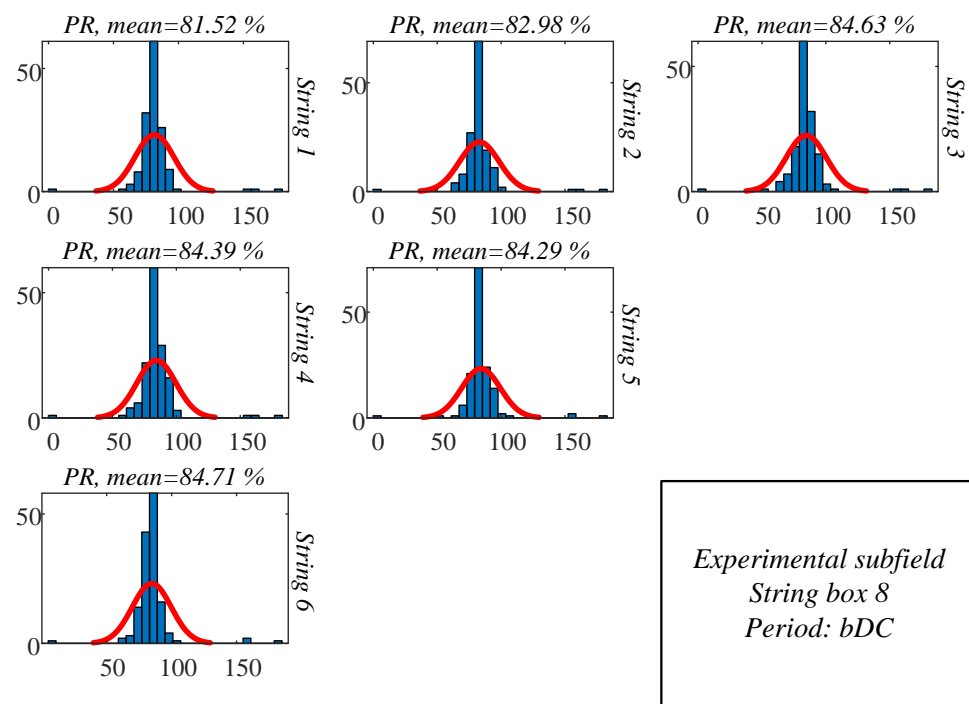












Bibliography

- [1] J. Bebbington, T. Schneider, L. Stevenson, L. Stevenson, A. Fox, “Fossil fuel reserves and resources reporting and unburnable carbon: Investigating conflicting accounts”, Elsevier Critical Perspectives on Accounting, vol. 66, January 2020.
- [2] M. Ourahou, W. Ayrir, B. El Hassouni, A. Haddi, “Review on smart grid control and reliability in presence of renewable energies: Challenges and prospect”, Elsevier Mathematics and Computers in Simulation, vol. 167, pp. 19-31, January 2020.
- [3] IAEA International Atomic Agency Annual Report 2018, link: <https://www.iaea.org/opic/annual-report-2018>, 2018.
- [4] T. H. Bakken, A. Killingtveit, K. Engeland, K. Alfredsen, A. Harby, “Water consumption from hydropower plants – review of published estimates and an assessment of the concept”, Hydrology and Earth System Sciences, vol. 17, pp. 3983-4000, October 2013.
- [5] EU Commission Publications “Fourth report on the State of the Energy Union”, link: https://ec.europa.eu/commission/publications/4th-state-energy-union_en, April 2019.
- [6] IEA Statistics, "Renewables Information: Overview", link: <https://webstore.iea.org/renewables-information-2019-overview>, 2019.
- [7] W. Zappa, M. van den Broek, “Analysing the potential of integrating wind and solar power in Europe using spatial optimisation under various scenarios”, Elsevier Renewable and Sustainable Energy Reviews, vol. 94, pp. 1192-1216, October 2018.
- [8] EU JRC PVGIS Solar Database, link: <https://ec.europa.eu/jrc/en/pvgis>.
- [9] Global Solar Atlas Solar Database, link: <https://globalsolaratlas.info/map>.
- [10] X. Wang, A. Barnett, “The Evolving Value of Photovoltaic Module Efficiency”, MDPI Applied Sciences, vol. 9, no. 1227, March 2019.

- [11] X. Sun, M. R. Khan, C. Deline, M. A. Alam, “Optimization and Performance of Bifacial Solar Modules: A Global Perspective”, Elsevier Applied Energy, vol. 212, pp. 1601-1610, February 2018.
- [12] A. Di Stefano, G. Leotta, F. Bizzarri, “La Silla PV Plant as a Utility-Scale Side-by-Side Test for Innovative Modules Technologies”, in Proc. 2017 European PV Solar Energy Conference and Exhibition EU PVSEC, Amsterdam, The Netherlands, 25-29 September 2017, pp. 1978-1982.
- [13] E. Kandemir, N. S. Cetin, S. Borekci, “A comprehensive overview of maximum power extraction methods for PV systems”, Elsevier Renewable and Sustainable Energy Reviews, vol. 78, pp. 93-112, October 2017.
- [14] W. Xiao, M. S. El Moursi, O. Khan, D. Infield, “Review of grid-tie converter topologies used in photovoltaic systems”, IET Renewable Power Generation, vol. 10, issue 10, November 2016.
- [15] G. Nobile, M. Cacciato, G. Scarcella, G. Scelba, A. G. F. Di Stefano, G. Leotta, P. M. Pugliatti, F. Bizzarri, “Comparison between central and string inverters performance for the utility-scale PV plant in Nova Olinda Brazil”, in Proc. 2018 European PV Solar Energy Conference and Exhibition EU PVSEC, Brussels, Belgium, pp. 1935-1941.
- [16] G. Nobile, M. Cacciato, G. Scarcella, G. Scelba, E. Vasta, A. Di Stefano, G. Leotta, P. M. Pugliatti and F. Bizzarri, "Distributed converters in large PV plants: performance analysis supported by behavioral models", ELECTRIMACS 2019 Springer Lecture Notes in Electrical Engineering, vol. 604, pp. 553-566, April 2020.
- [17] A. Cortés, J. Mazòn, J. Merino, “Strategy of management of storage systems integrated with photovoltaic systems for mitigating the impact of LV distribution network”, Elsevier Electrical Power and Energy Systems, vol. 103, pp. 470-482, December 2018.
- [18] C. K. Das, O. Bass, G. Kothapalli, T. S. Mahmoud, D. Habibi, “Overview of energy storage systems in distribution networks: Placement, sizing, operation

- and power quality”, Elsevier Renewable and Sustainable Energy Reviews, vol. 91, pp. 1205-1230, August 2018.
- [19] C. S. Lai, Y. Jia, L. L. Lai, Z. Xu, M. D. McCulloch, K. P. Wong, “A comprehensive review on large-scale photovoltaic system with applications of electrical energy storage”, Elsevier Renewable and Sustainable Energy Reviews, vol. 78, pp. 439-451, October 2017.
- [20] G. J. May, A. Davidson, B. Monahov, “Lead batteries for utility energy storage: A review”, Elsevier Journal of Energy Storage, vol. 15, pp. 145-157, February 2018.
- [21] A. Al-Akori, “PV Systems for Rural Health Facilities in Developing Areas: A completion of lessons learned”, Report IEA-PVPS, November 2014.
- [22] G. Wang, M. Ciobotaru, V. G. Agelidis, “Power Smoothing of Large Solar Photovoltaic Plant Using Hybrid Energy Storage”, IEEE Trans. Sustainable Energy, vol. 5, issue 3, July 2014.
- [23] A. Seaman, T. Dao, J. McPhee, "A survey of mathematical-based equivalent-circuit and electrochemical battery models for hybrid and electric vehicle simulation”, Journal of Power Sources, vol. 256, pp. 410-423, 2014, June 2014
- [24] G. L. Plett, “High-performance battery-pack power estimation using a dynamic cell model”, IEEE Trans. Vehicular Technology, vol. 53, no. 5, pp. 1586-1593, September 2004.
- [25] A. Jäger-Waldau, EU Commission Publications, “PV Status Report 2019”, link: <https://ec.europa.eu/jrc/en/publication/eur-scientific-and-technical-research-reports/pv-status-report-2019>, 2019.
- [26] IEA, "Renewables 2019 – Market Analysis and Forecast from 2019 to 2024", link: <https://www.iea.org/reports/renewables-2019>, October 2019.
- [27] S. Sharma, K.K. Jain, A. Sharma, “Solar Cells: In Research and Applications - A Review”, Materials Sciences and Applications, vol. 6, pp. 1145-1155, December 2015.

- [28] A. Dolara, S. Leva, G. Manzolini, “Comparison of different physical models for PV power output prediction”, Elsevier Solar Energy, vol. 119, pp. 83-99. September 2015.
- [29] J. S. Stein, “PV Performance Modelling Methods and Practices - Results from the 4th PV Performance Modelling Collaborative Workshop”, Report IEA-PVPS T13-06:2017, March 2017.
- [30] M. Wiesenfarth, S. P. Philipps, A. W. Bett, K. Horowitz, S. Kurtz, “Current Status of Concentrator Photovoltaic (CPV) Technology”, Fraunhofer ISE and NREL Report, April 2017.
- [31] F. Obeidat, “A comprehensive review of future photovoltaic systems”, Elsevier Solar Energy, vol. 163, pp. 545-551, March 2018.
- [32] K. Ishaque, Z. Salam, “A review of maximum power point tracking techniques of PV system for uniform insolation and partial shading condition”, Elsevier Renewable and Sustainable Energy Reviews, vol. 19, pp. 457-488, March 2013.
- [33] Z. Ali, N. Christofides, L. Hadjidemetriou, E. Kyriakides, Y. Yang, F. Blaabjerg, “Three-phase phase-locked loop synchronization algorithms for grid-connected renewable energy systems: A review”, Elsevier Renewable and Sustainable Energy Reviews, vol. 90, pp. 434-452, July 2018.
- [34] S. Nikolovski, “The relay protection Coordination for Photovoltaic Power Plant Connected on Distribution Network”, International Journal of Electrical and Computer Engineering Systems, vol. 5, pp. 15-20, January 2014.
- [35] IEEE Standard “C37.2-2008 Standard Electrical Power System Device Function Numbers, Acronyms, and Contact Designations”, link: https://standards.ieee.org/standard/C37_2-2008.html, October 2008.
- [36] N. AL-Rousan, N. R. M. Isa, M. K. M. Desa, “Advances in solar photovoltaic tracking system: A review”, Elsevier Renewable and Sustainable Energy Reviews, vol. 82, pp. 2548-2569, February 2018.
- [37] F. Bontempo Scavo, G. M. Tina, A. Gagliano, S. Nizetic, “An assessment study of evaporation rate models on a water basin with floating photovoltaic plants”, Wiley International Journal of Energy Research, February 2020.

- [38] Q. Lin, H. Huang, Y. Jing, H. Fu, P. Chang, D. Li, Y. Yao, Z. Fan, “Flexible photovoltaic technologies”, Royal Society of Chemistry Journal of Material Chemistry C, vol. 2, issue 7, pp. 1233-1247, December 2013.
- [39] A. Pyrgou, A. Kylili, P. A. Fokaides, “The Future of the Feed-in Tariff (FiT) scheme in Europe: The case of photovoltaics”, Elsevier Energy Policy, vol. 95, pp. 94-102, August 2016.
- [40] W. Luo, Y. S. Khoo, P. Hacke, V. Neumann, D. Lausch, S. P. Harvey, J. P. Singh, J. Chai, Y. Wang, A. G. Aberle, S. Ramakrishna, “Potential-induced degradation in photovoltaic modules: a critical review”, Royal Society of Chemistry Energy & Environmental Science, vol. 10, issue 1, pp. 43-68, January 2017.
- [41] M. Kontges, S. Kurtz, C. Packard, U. Jahn, K. A. Berger, K. Kato, T. Friesen, H. Liu, M. Van Iseghem “Review of Failures of Photovoltaic Modules”, Report IEA-PVPS T13-01:2014, March 2014.
- [42] R. Evans, M. Boreland, M. A. Green, “A holistic review of mismatch loss: From manufacturing decision making to losses in fielded arrays”, Elsevier Solar Energy Materials and Solar Cells, vol. 174, pp. 214-224, January 2018.
- [43] K. A. K. Niazi, Y. Yang, D. Sera, “Review of mismatch mitigation techniques for PV modules”, IET Renewable Power Generation, vol. 13, issue 12, pp. 2035-2050, August 2019.
- [44] P. Manganiello, M. Balato, M. Vitelli, “A Survey on Mismatching and Aging of PV Modules: The Closed Loop”, IEEE Trans. Industrial Electronics, vol. 62, issue 11, pp. 7276-7286, November 2015.
- [45] A. Al Mansur, Md. Ruhul Amin, K. K. Islam, “Performance Comparison of Mismatch Power Loss Minimization Techniques in Series-Parallel PV Array configurations”, MDPI Energies, vol. 12, no. 874, March 2019.
- [46] A. Massi Pavan, A. Tassarolo, N. Barbini, A. Mellit, V. Lughi, “The effect of manufacturing mismatch on energy production for large-scale photovoltaic plants”, Elsevier Solar Energy, vol. 117, pp. 282-289, July 2015.

- [47] J. Webber, E. Riley, “Mismatch Loss Reduction in Photovoltaic Arrays as a Result of Sorting Photovoltaic Modules by Max-Power Parameters”, *Hindawi International Scholarly Research Notices*, vol. 2013, June 2013.
- [48] S. R. Pendem, S. Mikkili, “Modelling and performance assessment of PV array topologies under partial shading conditions to mitigate the mismatching power losses”, *Elsevier Solar Energy*, vol. 160, pp. 303-321, January 2018.
- [49] A. Peled, J. Appelbaum, “Enhancing the power output of PV modules by considering the view factor to sky effect and rearranging the interconnections of solar cells”, *Wiley Progress in Photovoltaics: Research and Applications*, vol. 25, pp. 810-818, September 2017.
- [50] A. A. Bayod-Rujula, A. Burgio, Z. Leonowicz, D. Menniti, A. Pinnarelli, N. Sorrentino, “Recent Developments of Photovoltaics Integrated with Battery Storage Systems and Related Feed-In Tariff Policies: A Review”, *Hindawi International Journal of Photoenergy*, vol. 2017, March 2017.
- [51] H. Akbari, M. C. Browne, A. Ortega, M. J. Huang, N. J. Hewitt, B. Norton, S. J. McCormack, “Efficient Energy Storage Technologies for photovoltaic systems”, *Elsevier Solar Energy*, vol. 192, pp. 144-168, November 2019.
- [52] J. Hoppmann, T. Schmidt, “The Economic Viability of Battery Storage for Residential Solar Photovoltaic Systems – A Review and a Simulation Model”, *Elsevier Renewable and Sustainable Energy Reviews*, vol. 39, pp. 1101-1118, November 2014.
- [53] D. Akinyele, J. Belikov, Y. Levron, “Battery Storage Technologies for Electrical Applications: Impact in Stand-Alone Photovoltaic Systems”, *MDPI Energies*, vol. 10, no. 1760, November 2017.
- [54] T. Khatib, I. A. Ibrahim, A. Mohamed, “A review on sizing methodologies of photovoltaic array and storage battery in a standalone photovoltaic system”, *Elsevier Energy Conversion and Management*, vol. 120, pp. 430-448, July 2016.
- [55] A. Poullikkas, “A comparative overview of large-scale battery systems for electricity storage”, *Elsevier Renewable and Sustainable Energy Reviews*, vol. 27, pp. 778-788, November 2013.

- [56] Wikipedia, “List of energy storage projects”, link: https://en.wikipedia.org/wiki/List_of_energy_storage_projects.
- [57] DOE OE Global Energy Storage Database, link: <https://www.sandia.gov/ess-ssl/global-energy-storage-database-home/>.
- [58] Philadelphia Solar, Al Badiya Power Generation, link: <https://philadelphia-solar.com/pages/page/9/en/al-badiya-is-a-specialized-power-learn-more>.
- [59] Australian Renewable Energy Agency, Solar Project Nauiyu Daly River, link: <https://arena.gov.au/projects/daly-river-solar-research-project/>.
- [60] L. F. Arenas, C. Ponce de Leon, F. C. Walsh, “Engineering aspects of the design, construction and performance of modular redox flow batteries for energy storage”, Elsevier Journal of Energy Storage, vol. 11, pp. 119-153, June 2017.
- [61] G. Nobile, M. Cacciato, G. Scarcella, G. Scelba, E. Vasta, L. D. Tornello, A. G. F. Di Stefano, G. Leotta, P. M. Pugliatti, F. Bizzarri “A novel model-based approach for the energy management of distributed storage systems in utility-scale PV fields”, in Proc. 2019 IEEE 21st European Conference on Power Electronics and Applications (EPE), pp. 1-10.
- [62] F. Blaabjerg, K. Ma, D. Zhou, “Power Electronics and Reliability in Renewable Energy Systems”, in Proc. 2012 IEEE International Symposium on Industrial Electronics, pp. 19-30.
- [63] N. Zhang, D. Sutanto, K. M. Muttaqi, “A review of topologies of three-port DC-DC converters for the integration of renewable energy and energy storage system”, Elsevier Renewable and Sustainable Energy Reviews, vol. 56, pp. 388-401, April 2016.
- [64] K. Zeb, W. Uddin, M. A. Khan, Z. Ali, M. U. Ali, N. Christofides, H. J. Kim, “A comprehensive review on inverter topologies and control strategies for grid connected photovoltaic system”, Elsevier Renewable and Sustainable Energy Reviews, vol. 94, pp. 1120-1141, October 2018.
- [65] Md. R. Islam, A. M. Mahfuz-Ur-Rahman, K. M. Muttaqi, D. Sutanto, “State-of-the-Art of the Medium-Voltage Power Converter Technologies for Grid

- Integration of Solar Photovoltaic Power Plants”, IEEE Trans. Energy Conversion, vol. 34, no.1, pp. 372-384, March 2019.
- [66] S. Strache, R. Wunderlich, S. Heinen, “A Comprehensive, Quantitative Comparison of Inverter Architectures for Various PV Systems, PV Cells, and Irradiance Profiles”, IEEE Trans Sustainable Energy, vol. 5, issue 3, pp. 813-822, July 2014.
- [67] S. Poshtkouhi, V. Palaniappan, M. Fard, O. Trecases, “A General Approach for Quantifying the Benefit of Distributed Power Electronics for Fine Grained MPPT in Photovoltaic Applications using 3D Modelling”, IEEE Trans. Power Electronics, vol. 27, issue 11, pp. 4656-4666, November 2012.
- [68] Solar Edge website, link: <https://www.solaredge.com/aus/products/power-optimizer#/>.
- [69] Tigo Energy website, link: <https://www.tigoenergy.com/products/#optimization>.
- [70] M. Birane, C. Larbes, A. Cheknane, “Comparative study and performance evaluation of central and distributed topologies of photovoltaic system”, International Journal of Hydrogen Energy, vol. 42, issue 13, pp. 8703-8711, March 2017.
- [71] M. S. Agamy, M. Harfman-Todorovic, A. Elasser, J. A. Sabate, R. L. Steigerwald, Y. Jiang, S. Essakiappan, “DC-DC Converter Topology Assessment for Large Scale Distributed Photovoltaic Plant Architectures”, in Proc. 2011 IEEE Energy Conversion Congress and Exposition (ECCE), pp. 764-769.
- [72] A. Bhattacharjee, N. Kutkut, I. Batarseh, “Review of Multi Port Converters for Solar and Energy Storage Integration”, IEEE Trans. Power Electronics, vol. 34, issue 2, pp. 1431-1445, April 2018.
- [73] N. Muller, S. Kouro, P. Zanchetta, P. Wheeler, G. Bittner, F. Girardi, “Energy Storage Sizing Strategy for Grid-Tied PV Plants under Power Clipping Limitations”, MDPI Energies, vol. 12, no. 1812, May 2019.

- [74] C. Olalla, D. Clement, D. Maksimovic, C. Deline, "A Cell-Level Photovoltaic Model for High-Granularity Simulations", in Proc. 2013 IEEE 15th European Conference on Power Electronics and Applications (EPE), pp. 1-10.
- [75] M. B. H. Rhouma, A. Gastli, L. B. Brahim, F. Touati, M. Benammar, "A simple method for extracting the parameters of the PV cell single-diode model", Elsevier Renewable Energy, vol. 113, pp. 885-894, December 2017.
- [76] C. Koch-Ciobotaru, L. Mihet-Popa, F. Isleifsson, H. Bindner, "Simulation Model developed for a Small-Scale PV System in Distribution Networks", in Proc. 2012 7th IEEE International Symposium on Applied Computational Intelligence and Informatics (SACI), pp. 341-346.
- [77] A. Chouder, S. Silvestre, N. Sadaoui, L. Rahmani, "Modelling and simulation of a grid connected PV system based on the evaluation of main PV module parameters", Elsevier Simulation Modelling Practice and Theory, vol. 20, issue 1, pp. 46-58, January 2012.
- [78] P. Han, Z. Lin, L. Wang, G. Fan, X. Zhang, "A Survey on Equivalence Modelling for Large-Scale Photovoltaic Power Plants", MDPI Energies Journal, vol. 11, no. 1463, June 2018.
- [79] A. Bonfiglio, F. Delfino, M. Invernizzi, R. Procopio, "Criteria for the Equivalent Modelling of Large Photovoltaic Power Plants", in Proc. 2014 IEEE PES General Meeting, Conference & Exposition, pp. 1-5.
- [80] J. Guerrero-Perez, E. De Jodar, E. Gomez-Lazaro, A. Molina-Garcia, "Behavioural modelling of grid-connected photovoltaic inverters: Development and assessment", Elsevier Renewable Energy, vol. 68, pp. 686-696, August 2014.
- [81] Y. Li, X. M. Chen, B. Y. G. Zhao, Z. G. Zhao, R. Z. Wang, "Development of a PV performance model for power output simulation at minutely resolution", Elsevier Renewable Energy, vol. 111, pp. 732-739, October 2017.
- [82] A. Ayad, R. Kennel, "A comparison of quasi-Z-source inverter and conventional two-stage inverters for PV applications", EPE Journal, vol. 27, pp. 43-59, May 2017.

- [83] M. P. Almeida, M. Munoz, I. de La Parra, O. Perpignan, “Comparative study on PV power forecast using parametric and nonparametric PV models”, Elsevier Solar Energy, vol. 155: pp. 854-866, October 2017.
- [84] M. G. Villalva, J. R. Gazoli, E. R. Filho, “Comprehensive Approach to Modelling and Simulation of Photovoltaic Arrays”, IEEE Trans. Power Electronics, vol. 24, issue 5, pp. 1198-1208, May 2009.
- [85] T. Kerekes, E. Koutroulis, D. Sera, R. Teodorescu, M. Katsanevakis, “An Optimization Method for Designing Large PV Plants”, IEEE Journal of Photovoltaics, vol. 3, issue 2, pp. 814-822, April 2013.
- [86] L. Chang, W. Zhang, S. Xu, K. Spence, “Review on Distributed Energy Storage Systems for Utility Applications”, IEEE Trans. Power Electronics and Applications, vol. 2, issue 4, pp. 267-276. December 2017.
- [87] M. Cugnet, M. Dubarry, B. Lyaw, “Secondary batteries – Lead-Acid Systems – Modelling”, Elsevier Reference Module in Chemistry, Molecular Sciences and Chemical Engineering Encyclopedia of Electrochemical Power Sources, pp. 816-828, December 2009.
- [88] C. Zhang, K. Li, S. Mcloone, Z. Yang, “Battery Modelling Methods for Electric Vehicles – A review”, in Proc. 2014 IEEE European Control Conference, pp. 2673-2678.
- [89] A. Coronado-Mendoza, M. A. Perez-Cisneros, J. A. Dominguez-Navarro, V. Osuna-Enciso, V. Zuniga-Grajeda, K. J. Gurubel-Tun, “Dynamic phasors modelling for a single phase two stage inverter”, Elsevier Electric Power Systems Research, vol. 140, pp. 854-865, November 2016.
- [90] A. Hussein, I. Batarseh, "An overview of generic battery models", in Proc. 2011 IEEE Power and Energy Society General Meeting, San Diego.
- [91] S. M. Mousavi, M. Nikdel, “Various battery models for various simulation studies and applications”, Elsevier Renewable and Sustainable Energy Reviews, vol. 32, pp. 477-485, April 2014.
- [92] P. D. Zimmerman, D. E. Zimmerman, G. L. Claypoole, “Apparatus and method for testing remaining capacity of a battery”, U.S. Patent 6823274, Nov. 2004.

- [93] R. E. Kalman, "A new approach to linear filtering and prediction problems", *Trans. ASME Journal of Basic Engineering*, ser. D, pp. 35-45, 1982.
- [94] H. A. Pereira, F. D. Freijedo, M. M. Silva, V. F. Mendes, R. Teodorescu, "Harmonic current prediction by impedance modelling of grid-tied inverters: A 1.4 MW PV plant case study", *Elsevier Electrical Power and Energy Systems*, vol. 93, pp. 30-38, December 2017.
- [95] O. Tremblay, L. Dessaint, "Experimental Validation of a Battery Dynamic Model for EV Applications", *MDPI World Electric Vehicle Journal*, vol. 3, pp. 1-10, May 2009.
- [96] S. Li, B. Ke, "Study of Battery Modelling using Mathematical and Circuit Oriented Approaches", in *Proc. 2011 IEEE Power and Energy Society General Meeting*, pp. 1-8.
- [97] R. A. Jackey, "A Simple, Effective Lead-Acid Battery Modelling Process for Electrical System Component Selection", in *Proc. 2007 SAE World Congress & Exhibition*, paper 2007-01-0778.
- [98] S. Kai, S. Qifang, "Overview of the types of battery models", in *Proc. 2011 IEEE 30th Chinese Control Conference*, pp. 3644-3648.
- [99] X. Hu, S. Li, H. Peng, "A comparative study of equivalent circuit models for Li-ion batteries", *Elsevier Journal of Power Sources*, vol. 198, pp. 359-367, January 2012.
- [100] M. Einhorn, F. V. Conte, C. Kral, J. Fleig, "Comparison, Selection, and Parameterization of Electrical Battery Models for Automotive Applications", *IEEE Trans. Power Electronics*, vol. 28, issue 3, pp. 1429-1437, March 2013.
- [101] H. He, R. Xiong, H. Guo, S. Li, "Comparison study on the battery models used for the energy management of batteries in electric vehicles", *Elsevier Energy Conversion and Management*, vol. 64, pp. 113-121, December 2012.
- [102] W. Wang, H. Chung, J. Zhang, "Near-Real-Time Parameter Estimation of an Electrical Battery Model With Multiple Time Constants and SOC-Dependent Capacitance", *IEEE Trans. Power Electronics*, vol. 29, issue 11, pp. 5905-5920, November 2014.

- [103] J. Li, M. Mazzola, “Accurate battery pack modelling for automotive applications”, Elsevier Journal of Power Sources, vol. 237, Elsevier, pp. 215-228, September 2013.
- [104] M. Chen, A. Rincon-Mora, “Accurate Electrical Battery Model Capable of Predicting Runtime and I–V Performance”, IEEE Trans. Energy Conversion, vol. 21, issue 2, pp. 504-511, June 2006.
- [105] C. M. Sheperd, “Design of Primary and Secondary Cells – Part II. An Equation Describing Battery Discharge”, Journal of the Electrochemical Society, vol. 112, issue 7, pp. 657-664, July 1965.
- [106] N. Kularatna, “Dynamics and Modelling of Rechargeable Batteries”, IEEE Power Electronics Magazine, vol. 1, issue 4, pp. 23-33, December 2014.
- [107] B. S. Bhangu, C. M. Bingham, D. A. Stone, P. Bentley, “Nonlinear Observer techniques for Prediction State-of-Charge and State-of-Health of Lead-Acid Batteries for Hybrid-Electric Vehicles”, IEEE Trans. Vehicular Technology, vol. 54, issue 3, pp. 783-794, May 2005.
- [108] N. Achaibou, M. Haddadi, A. Malek, “Lead acid batteries simulation including experimental validation”, Elsevier Journal of Power Sources, vol. 185, issue 2, pp. 1484-1491, December 2008.
- [109] R. S. Treptow, “The lead-acid battery: its voltage in theory and practice”, Journal of Chemical Education, vol. 79, issue 3, March 2002.
- [110] B. Schweighofer, K. Raab, G. Brasseur, “Modelling of High Power Automotive Batteries by the Use of an Automated Test System”, IEEE Trans. Instrumentation and Measurement, vol. 52, issue 4, pp. 1087-1091, August 2003.
- [111] L. Benini, G. Castelli, A. Macii, E. Macii, M. Poncino, R. Scarsi “Discrete-Time Battery Models for System-Level Low-Power Design”, IEEE Trans. Very Large Scale Integration Systems, vol. 9, issue 5, pp. 630-640, October 2001.
- [112] S. Gold, “A PSPICE Macromodel for Lithium-Ion Batteries”, in Proc. 1997 IEEE Battery Applications and Advances Conference, pp. 215-222.

- [113] A. Salkind, P. Singh, A. Cannone, T. Atwater, X. Wang, D. Reisner, "Impedance modelling of intermediate size lead-acid batteries", Elsevier Journal of Power Sources, vol. 116, pp. 174-184, July 2003.
- [114] D. I. Stroe, M. Swierczynski, A. I. Stroe, V. Knap, R. Teodorescu, S. J. Andreasen, "Evaluation of Different Methods for Measuring the Impedance of Lithium-Ion Batteries during Ageing", in Proc. 2005 IEEE Ecological Vehicles and Renewable Energies International Conference, pp. 1-8.
- [115] H. Wang, G. Li, M. Li, Z. Jiang, X. Wang, Q. Zhao, "Third-order dynamic model of a lead acid battery for use in fuel cell vehicle simulation", in Proc. 2011 IEEE Mechatronic Science, Electric Engineering and Computer Conference, pp. 715-720.
- [116] M. Ceraolo, "New dynamical models of lead-acid batteries", IEEE Trans. Power Systems, vol. 15, issue 4, pp. 1184-1190, November 2000.
- [117] R. Kroeze, P. Krein, "Electrical Battery Model for Use in Dynamic Electric Vehicle Simulations", in Proc. 2008 IEEE Power Electronics Specialists Conference, pp. 1336-1342.
- [118] D. Doerffel, S. A. Sharkh, "A critical review of using the Peukert equation for determining the remaining capacity of lead-acid and lithium-ion batteries", Elsevier Journal of Power Sources, vol. 155, issue 2, pp. 395-400, April 2006.
- [119] M. Swierczynski, D. I. Stroe, A. I. Stan, R. Teodorescu, S. K. Kaer, "Investigation on the Self-discharge of the LiFePO₄/C Nanophosphate Battery Chemistry at Different Conditions", in Proc. 2014 IEEE Transportation Electrification Asia-Pacific Conference, pp. 1-6.
- [120] W. Chang, "The State of Charge Estimating Methods for Battery: A Review", Hindawi International Scholarly Research Notices, vol. 2013, pp. 1-8, July 2013.
- [121] D. Andre, C. Appel, T. Soczka-Guth, D. U. Sauer, "Advanced mathematical methods of SOC and SOH estimation for lithium-ion" Elsevier Journal of Power Sources, vol. 224, pp. 20-27, February 2013
- [122] J. K. Barillas, J. Li, C. Gunther, M. A. Danzer, "A comparative study and validation of state estimation algorithms for Li-ion batteries in battery

- management systems”, Elsevier Applied Energy, vol. 155, pp. 455-462, October 2015.
- [123] J. Xu, C. C. Mi, B. Cao, J. Deng, Z. Chen, S. Li, "The State of Charge Estimation of Lithium-Ion Batteries Based on a Proportional-Integral Observer”, IEEE Trans. Vehicular Technology, vol. 63, no. 4, pp. 1614-1621, May 2014.
- [124] X. Tang, Y. Wang, Z. Chen, “A method for state-of-charge estimation of LiFePO₄ batteries based on a dual-circuit state observer”, Elsevier Journal of Power Sources, vol. 296, pp. 23-29, November 2015.
- [125] M. Cacciato, G. Nobile, G. Scarcella, G. Scelba, “Real-time model-based estimation of SOC and SOH for energy storage systems”, IEEE Trans. Power Electronics, vol. 32, no. 1, pp. 794-803, January 2017.
- [126] M. Cacciato, G. Nobile, G. Scarcella, G. Scelba, A. G. Sciacca, “Energy management optimization in stand-alone power supplies using online estimation of battery SOC”, in Proc. 2016 IEEE 18th European Conference on Power Electronics and Applications (EPE), pp. 1-10.
- [127] A. Li, S. Pelissier, P. Venet, P. Gyan, "Fast Characterization Method for Modelling Battery Relaxation Voltage”, MDPI Batteries Journal, vol. 2, no. 2, April 2016.
- [128] H. R. Eichi, M. Y. Chow, “Modelling and Analysis of Battery Hysteresis Effects”, In Proc. 2012 IEEE Energy Conversion Congress and Exposition (ECCE), pp. 4479-4486.
- [129] J. Meng, D. I. Stroe, M. Ricco, G. Luo, M. Swierczynski, R. Teodorescu, “A Novel Multiple Correction Approach for Fast Open Circuit Voltage Prediction of Lithium-ion Battery”, IEEE Trans. Energy Conversion, vol. 34, issue 2, pp. 1115-1123, June 2019.
- [130] M. U. Cuma, T. Koroglu, “A comprehensive review on estimation strategies used in hybrid and battery electric vehicles”, Elsevier Renewable and Sustainable Energy Reviews, vol. 42, pp. 517-531, February 2015.

- [131] Y. Li, P. Chattopadhyay, A. Ray, C. D. Rahn, "Identification of the battery state-of-health parameter from input-output pairs of time series data", Elsevier Journal of Power Sources, vol. 285, pp. 235-246, July 2015.
- [132] M. Cacciato, G. Nobile, G. Scarcella, G. Scelba, "Real-time model-based estimation of SOC and SOH for energy storage systems", in Proc. 2015 IEEE 6th International Symposium on Power Electronics for Distributed Generation Systems (PEDG), pp. 1-8.
- [133] M. Galad, P. Spanik, M. Cacciato, G. Nobile, "Comparison of common and combined state of charge estimation methods for VRLA batteries", in Proc. ELEKTRO 2016 Conference, pp. 220-225.
- [134] M. Galad, P. Spanik, M. Cacciato, G. Nobile, "Analysis of state of charge estimation methods for smart grid with VRLA batteries", in Electrical Engineering Journal, vol. 99, pp. 1233-1244, July 2017.
- [135] G. Nobile, G. Scelba, M. Cacciato, G. Scarcella, "Losses Minimization in an Integrated Multi-Drives Topology devoted to Hybrid Electric Vehicles", in Proc. 2017 43rd Annual Conference of the IEEE Industrial Electronics Society (IECON), pp. 2059-2066.
- [136] G. Nobile, M. Cacciato, G. Scarcella, G. Scelba "Multi-criteria experimental comparison of batteries circuital models for automotive applications", Communications – Scientific Letters of the University of Zilina, vol. 20, no. 1, pp. 96-103, March 2018.
- [137] R. H. G. Tan, L. Y. H. Hoo, "DC-DC Converter Modelling and Simulation using State-Space Approach", In Proc. 2015 IEEE Conference on Energy Conversion (CENCON), pp. 42-47.
- [138] G. Kanimozhi, J. Meenakshi, V. Sreedevi, "Small Signal Modelling of a DC-DC Type Double Boost Converter Integrated with SEPIC Converter Using State Space Averaging Approach", Elsevier Energy Procedia, vol. 117, 117, pp. 835-846, June 2017.
- [139] S. Chiniforoosh, J. Jatskevich, A. Yazdani, V. Sood, V. Dinavahi, J. A. Martinez, A. Ramirez, "Definitions and Applications of Dynamic Average

- Models for Analysis of Power Systems”, IEEE Trans Power Delivery, vol. 25, issue 4, pp. 2655-2669, October 2010.
- [140] X. Liu, A. M. Cramer, “Three-Phase Inverter Modelling using Multifrequency Averaging with Third Harmonic Injection”, in Proc. 2016 IEEE Energy Conversion Congress and Exposition (ECCE), pp. 111-6.
- [141] Z. Lin, H. Ma, “Modelling and Analysis of Three-phase Inverter based on Generalized State Space Averaging Method”, in Proc. 39th Annual Conference of the IEEE Industrial Electronics Society (IECON), pp. 1007-1012.
- [142] J. W. Kolar, S. D. Round, “Analytical Calculation of the RMS current stress on the DC-link capacitor of voltage-PWM converter systems”, IEEE Proc. Electric Power Applications, vol. 153, pp 535-543, July 2006.
- [143] X. Pei, W. Zhou, Y. Kang, “Analysis and Calculation of the DC-link Current and Voltage Ripples for Three-Phase Inverter With Unbalanced Load” IEEE Trans. Power Electronics, vol. 30, issue 10, pp. 5401-5412, October 2015.
- [144] R. H. G. Tan, V. K. Ramachandramurthy, “A Comprehensive Modelling and Simulation of Power Quality Disturbances Using MATLAB/SIMULINK”, Intech Power Quality Issues in Distributed Generation, Chapter 3, pp. 83-107, October 2015.
- [145] G. Nobile, M. Cacciato, G. Scarcella, G. Scelba “Performance Assessment of Equivalent-Circuit Models for Electrochemical Energy Storage Systems”, in Proc. 2017 43rd Annual Conference of the IEEE Industrial Electronics Society (IECON), pp. 2799-2806.
- [146] G. Nobile, M. Cacciato, G. Scarcella, G. Scelba, L. Salvo “Performance Assessment of a novel Integrated Multi- Drives Topology for Automotive Applications”, in Proc. 2018 International Symposium on Power Electronics, Electrical Drives, Automation and Motion (SPEEDAM), pp. 570-576.
- [147] G. Nobile, M. Cacciato, G. Scarcella, G. Scelba, “Losses Minimization Control for an Integrated Multi-Drives Topology devoted to Hybrid Electric Vehicles”, IEEE Trans. Industrial Electronics, vol. 66, issue 11, pp. 8345-8360, November 2019.

- [148] Y. Mahmoud, E. F. El-Saadany, “Enhanced Reconfiguration Method for Reducing Mismatch Losses in PV Systems”, *IEEE Journal of Photovoltaics*, vol. 7, no. 6, pp. 1746-1754, November 2017.
- [149] K. Lappalainen, S. Valkealahti, “Effects of irradiance transition characteristics on the mismatch losses of different electrical PV array configurations”, *IET Renewable Power Generation*, vol. 11, issue 12, pp. 248-254, April 2017.
- [150] Z. Corba, B. Popadic, V. Katic, B. Dumnic, D. Milicevic, “Future of High Power PV Plants – 1500V inverters” in *Proc. 19th IEEE International Symposium Power Electronics*, October 2017.
- [151] L. Scarpa, P. M. Tumino, M. Nunnari, G. Chicco, F. Spertino, “Technical Solutions and Standard Upgrade for Photovoltaic Systems Operated over 1500 Vdc” in *Proc. 4th IEEE International Forum on Research and Technology for Society and Industry*.
- [152] A. N. Jimenez, R. Bkayrat, “Utility scale 1500 Vdc PV power plant architecture evolution: advantages and challenges” in *Proc. 2015 Integration of Renewable Energy into High and Medium Voltage Systems Conference and Exhibition*.
- [153] E. Gkoutioudi, P. Bakas, A. Marinopoulos, “Comparison of PV Systems with Maximum DC Voltage 1000V and 1500V”, in *Proc. 39th IEEE Photovoltaic Specialists Conference*, pp. 2873-2878.
- [154] R. Inzunza, R. Okuyama, T. Tanaka, M. Kinoshita, “Development of a 1500 Vdc Photovoltaic Inverter for Utility-Scale PV Power Plants” in *Proc. 2nd IEEE International Future Energy Electronics Conference*, pp. 1-4.